DEVELOPMENT OF A BROADBAND MULTI-CHANNEL NIRS SYSTEM FOR

QUANTIFYING ABSOLUTE CONCENTRATIONS OF HEMOGLOBIN

DERIVATIVES AND REDUCED SCATTERING COEFFICIENTS

by

DHEERENDRA KASHYAP

Presented to the Faculty of the Graduate School of

The University of Texas at Arlington in Partial Fulfillment

of the Requirements

for the Degree of

DOCTOR OF PHILOSOPHY

THE UNIVERSITY OF TEXAS AT ARLINGTON

August 2007

ACKNOWLEDGEMENTS

Sundar Victor, Suresh, Amith, and former and present members of biomedical optics lab at UTA. Their efforts have really made a difference.

Thanks a lot for everything. I would like to acknowledge and thank my parents, sister and my wife for their help throughout my career. Their unwavering faith and confidence in my abilities and in me is what has shaped me to be the person I am today I also extend my gratitude to all my friends for being friends and for the support they have lent me. My very special thanks to the GOD, whom I owe everything I am today. Thank you for everything.

April 30, 2007

ABSTRACT

DEVELOPMENT OF A BROADBAND MULTI-CHANNEL NIRS SYSTEM FOR

QUANTIFYING ABSOLUTE CONCENTRATIONS OF HEMOGLOBIN

DERIVATIVES AND REDUCED SCATTERING COEFFICIENTS

Publication No. _____

Dheerendra Kashyap, PhD.

The University of Texas at Arlington, 2007

Supervising Professor: Dr Hanli Liu

Near infrared spectroscopy (NIRS) has been widely applied to investigate hemoglobin oxygenations of muscles, brain and breast tumors. Steady state reflectance techniques developed previously have been restricted to determination of relative concentrations. To overcome these limitations, this dissertation describes the development, validation and applications of broadband, steady-state, optical spectroscopic systems and algorithms to quantify absolute concentrations of hemoglobin derivatives and reduced light scattering coefficients using (1) thin optical probes with small (100 μm – 1 mm) source-detector separations and (2) a large separation (< 4 cm) probe..

v

A recently developed mathematical model by Zonios and Dimou for reflectance at small source-detector separations was used to develop techniques to quantify chromophore concentrations and light scattering coefficients (Chap. 2). Blood-intralipid phantom models were used to determine empirical coefficients to model reflectance spectra. This technique was further applied to quantify hemodynamic changes during formalin- induced pain behaviors in rats (Chap. 3).

To overcome limitations in penetration depth and investigated tissue volume, another approach to quantify concentrations of chromophores in tissues at large source-detector separations was also developed. This novel approach uses the process of second differential spectroscopy to quantify concentrations of deoxygenated hemoglobin with respect to the tissue water content. Based on such quantification, an adaptation of the ant colony optimization algorithm was utilized to quantify absolute concentrations of other constituent tissue chromophores. The developed techniques were validated with the reflectance measurements from blood-intralipid phantoms and further applied to monitoring of ex vivo human prostate lesions and of rat brain tumor growth in vivo (Chap. 4).

In the second stage of my doctoral development, a multi-channel, broadband, steady-state, NIRS imaging system was developed to determine spatial distributions of hemoglobin concentrations and reduced light scattering coefficients. The imager was calibrated with laboratory phantoms to eliminate deterministic instrumentation bias of CCD-spectrometers, optical fibers, and multiplexer channels. Calibration procedures also include determinations of the source strength and boundary coefficients in order to

obtain accurate image reconstructions. A multi-wavelength, spectrally constrained reconstruction algorithm was developed to obtain tomographic maps of hemoglobin derivative concentrations and reduced scattering coefficients, using laboratory tissue phantoms. The developed imaging system and reconstruction algorithms were validated with both static and dynamic multi-tube phantoms.

TABLE OF CONTENTS

Appendix

LIST OF ILLUSTRATIONS

xviii

LIST OF TABLES

CHAPTER 1

INTRODUCTION

<u>1.1 Background</u>

Near Infrared Spectroscopy (NIRS) is one of the simplest techniques used for studying physiological properties of biological tissues. Light incident on tissues, undergoes multiple scattering and absorption. It can be detected in transmission or reflectance geometry a few centimeters away from the source on the tissue, carrying quantitative information. Light in the visible region (400-650 nm) is strongly attenuated in tissues, whereas the attenuation in the near infrared (700-900 nm) region is relatively less by tissue chromophores, such as oxygenated hemoglobin (HbO) and deoxygenated hemoglobin (Hb), thus permits the study of their variations in this wavelength region.

NIRS has been widely applied to investigate hemoglobin oxygenations of muscles [1-3], brain [4, 5] and animal tumors [6-9]. The quantification of chromophore concentrations requires the ability to separate the effects of absorption and scattering. The coefficients of absorption μ_a and of reduced scattering μ_s' are typically determined by a series of reflectance or attenuation measurements performed either in time [10, 11] (fast pulse), frequency [12-14] (sinusoidal modulation of intensity), or steady state domains [15-17]. All three techniques have their own advantages and shortcomings. Steady state techniques with a single source and detectors at multiple distances are

relatively inexpensive and better suited for the quantification of optical properties over large continuous wavelength ranges. Typically, measurements are performed with a set of small (~ 1 transport mean free path) and large (> many transport mean free paths) source detector separations. The variations in optical properties are assumed to be insignificant over the ranges of volume probed.

Time and frequency-domain techniques are well suited for deeper investigations (~.1 cm) of biological tissues. Additionally, they can be performed with only one or a few source–detector separations, which make these techniques more robust for use in studying heterogeneous samples. Although these techniques are more robust, they require sources to be pulsed or modulated rapidly. Additionally, covering a large wavelength range requires a tunable laser or an extensive collection of laser diodes, both of which can be expensive, difficult to maintain, and results in slower acquisition times. Quantification of chromophore concentrations can be significantly affected by the use of a limited number of wavelengths, which can be a major drawback, as discussed by Hull et al [18]. In contrast, steady-state techniques are relatively inexpensive, simple in design and construction and are more readily suited for the determination of μ_a and μ_s' over large, continuous ranges of wavelengths than are other techniques. Broad band light source, broadband data acquisitions accomplished with the use of white light source and CCD array spectrometers significantly decrease the acquisition time per wavelength and permits rapid data acquisitions that enable the development of miniature size real time monitoring systems.

Steady state reflectance measurements with large (~1 cm) separations have been previously used to monitor the changes in tumor oxygenation under gas intervention using NIRS [12, 19]. Needle like probes with very small source detector separations (< 0.5 cm) have also been employed previously by our group and other groups to differentiate between deep brain structures [20] and monitor oxygenation levels during gas interventions in animal tumors [9, 21]. Techniques developed previously with steady state domain methods have been restricted to the determination of relative concentrations of tissue chromophores or require reflectance or transmittance measured at multiple source detector separations for quantification of chromophore concentrations. Development of steady state techniques to quantify chromophore concentrations with single source detector separation would result in significant simplification of instrumentation hardware.

1.2 Overview of Dissertation

In this context, this dissertation describes the development, validation and applications of multi wavelength broad band algorithms to quantify reduced scattering coefficients and absolute concentrations of tissue chromophores such as hemoglobin derivatives with small (100μm-1mm) and large single source detector separations(<0.5cms).In the second stage of development, hardware and image reconstruction algorithms to quantify spatial distributions of chromophores and scattering coefficients were developed.

Chapter-2 describes the development and validation of techniques for quantifying concentrations of hemoglobin derivatives and reduced scattering

coefficients with small source detector separations. On a sub-millimeter scale, it is reasonable to assume that investigated tissue volume is fairly homogenous. Therefore, quantifying one set of chromophore concentrations and scattering coefficients sufficiently characterizes the optical properties of investigated tissue volume.

In the first stage of development, a recently developed mathematical model for diffuse reflectance at small source detector separations [22] was used to develop techniques to quantify chromophore concentrations and reduced scattering coefficients. Measurements made with tissue like blood-intralipid phantom models were used to determine empirical coefficients. The empirical coefficients were used to determine reflectance spectra. A method to determine concentrations of chromophores and reduced scattering coefficients from measured reflectance was developed. Developed techniques were validated through measurements made from blood-intralipid phantoms.

Chapter-3 describes the application of this technique to quantify and monitor hemodynamic changes during formalin induced pain behaviors in rats. Adult male Sprague Dawley rats were anesthetized. Dilute formalin was injected into one of the paws. Blood hemoglobin concentrations, reduced scattering coefficients and mean particle sizes were quantified throughout the evolution of pain response.

Smaller source detector separations resulted in a restricted investigation of tissue volume and reduced penetration depth. The penetration depth achieved with small source detector separation is in the range of a few millimeters [23]. Use of large source–detector separation, allows for centimeter-scale mean probing depths that cannot be achieved with short source-detector separations. This advantage for deeply probing

studies will be significant for many clinical purposes. To overcome fore mentioned limitations, chapter-4 in the dissertation describes the technique to quantify concentrations of chromophores and scattering coefficients in tissues at large source-detector separations. The developed technique used the approach of second differential spectroscopy [24] to arrive at relative concentrations of deoxygenated hemoglobin, relative to water concentrations. Further, an adaptation of ant colony optimization algorithm [25] utilized concentrations of deoxygenated hemoglobin as initial information, to quantify absolute concentrations of other constituent tissue chromophores. Developed techniques were validated with reflectance measurements from tissue simulating phantoms of blood and intralipid.

The developed algorithms were used to quantify tissue chromophores such as oxygenated hemoglobin, deoxygenated hemoglobin, and water content and reduced scattering coefficients in prostate lesions. Tissue chromophores and scattering coefficients were determined at superficial and deeper regions to investigate the extent of spatial heterogeneities. The technique was also applied to monitor changes in hemodynamic parameters during tumor growth. Glioma cells were injected into the right caudate nucleus of Fisher rats. Changes in concentrations of total hemoglobin, oxygen saturation were monitored from tumor implantation till the animal was sacrificed. The surgical procedures and experimental procedures are described in detail in chapter-4.

The developments and algorithms described with the use of large source-detector separations were limited to quantification of global values of hemoglobin

derivatives, without spatial information. Larger the spread of distances probed, more likely that heterogeneities, such as those found in biological tissues, becomes significantly large and cannot be ignored. Therefore, volume averaged values of chromophore concentrations and scattering coefficients do not sufficiently represent optical properties of tissues investigated with large source-detector separations. To quantify and localize spatial heterogeneities of hemoglobin derivatives and scattering coefficients, chapter-5 describes the second stage of developmental process in which, a multi-channel broad band NIRS imaging system was developed. Finite element approximations of diffusion theory were used to develop reconstruction algorithms to quantify spatial distribution of hemoglobin derivatives and reduced scattering coefficients. Calibration techniques were devised to eliminate deterministic instrumentation bias and determine the source strength for image reconstruction. The developed techniques and instrumentation were validated with static and dynamic blood-intralipid phantoms.

<div align="center">1.3 Hypotheses and Specific aims</div>

This dissertation aims to develop a system that encompasses development of hardware and necessary algorithms for the quantification of hemoglobin derivatives and reduced scattering coefficients in tissues. Quantification of optical properties in terms of concentration of constituent chromophores and scattering coefficients are accomplished with the use of large and small source detector separations.

In this context, the overall hypothesis of the dissertation can be stated as:

<div align="center">6</div>

Overall Hypothesis: Broadband NIRS is a portable and real time tool that can be used to quantify absolute concentrations of hemoglobin derivatives and reduced scattering coefficients.

The proof of this hypothesis is accomplished through a set of more specific hypotheses and their simplified specific aims. Specific hypothesis 1 addresses the quantification of chromophore concentrations and scattering coefficients at small source detector separations. Smaller separations (100μm-1mm) results in superficial penetration depth of 1 to 3mm [23]. At this small scale, heterogeneities in investigated tissue volume are relatively small; hence chromophore concentrations quantified are a true representation of optical properties. The penetration depth scales with source-detector separation. Large source-detector separations (>0.5cm<5cm) result in mean penetration depths in the range of 1-2cm [26, 27]. Specific hypothesis 2 addresses the quantification of chromophore concentrations and scattering coefficients at large source-detector separations. Greater the spread of distances probed, more likely that heterogeneities, such as those found in tissues, become significantly large and cannot be ignored. Therefore, bulk values of chromophore concentrations and scattering coefficients do not sufficiently represent optical properties of tissues investigated with large source-detector separations. Evaluating the extent and location of heterogeneities in chromophore concentrations and scattering coefficients are accomplished with use of multiple sources and detectors. Quantification and spatial localization of distributions of chromophores are accomplished through specific hypothesis 3. Spatial distributions of

7

hemoglobin derivatives and reduced scattering coefficients are evaluated through the development of hardware and algorithms for image reconstruction.

The hypotheses and specific aims are:

Hypothesis 1: Quantifications of hemoglobin derivatives in tissues at millimeter scale can be determined by using sub millimeter source detector separations and spectroscopic techniques that span visible and NIR wavelength ranges. (Chapters 2 &3)

Aim 1: Determine constants (mathematical model of reflectance) k_1 and k_2 through experimental calibrations with blood-intralipid phantoms for quantification of hemoglobin derivatives and reduced scattering coefficients.

Aim 2: Demonstrate the utility of the method to characterize and quantify hemodynamic changes in rat hind paws during formalin induced pain behaviors.

Hypothesis 2: Broadband (600-850nm) near infrared spectroscopic technique can be used to quantify absolute concentrations of hemoglobin derivatives with large source-detector separations. (Chapter 4)

Aim 3: Develop a multi wavelength steady state spectroscopy algorithm for absolute quantification of hemoglobin derivatives and reduced scattering coefficients.

Aim 4: Validate the developed technique with blood Intralipid phantoms.

Aim 5: Evaluate the feasibility of the technique to monitor and quantify changes in hemodynamic parameters during the growth of orthotropic tumors in rat caudate nucleus.

Aim 6: Investigate feasibility of the technique to quantify hemoglobin derivative concentrations and reduced scattering coefficients in prostate lesions.

Hypothesis 3: Spatial distribution of hemoglobin derivative concentrations and reduced scattering coefficients can be extracted from multi wavelength, multi source-detector broadband steady state diffuse reflectance measurements. (Chapter 5)

Aim 7: Design and develop a multi channel broadband NIRS imaging system for monitoring hemodynamic changes in animal models.

Aim 8: Calibrate the imager with laboratory phantom models to eliminate effects of inhomogeneity of spectrometer channels, fibers and multiplexer channels and determine the source strength for image reconstruction.

Aim 9: Use a multi channel, multi wavelength reconstruction algorithm to obtain tomographic maps of absolute concentrations of hemoglobin derivatives and reduced scattering coefficients from laboratory phantom models.

The set of specific hypothesis and their aims are directed at quantification of chromophores and scattering coefficients beginning from small or minute volumes to large volumes in tissues. The determination of constants (mathematical model of

9

reflectance) k_1 and k_2 through experimental calibrations with blood-intralipid phantoms provides a quantitative relationship between reflectance measured with an optical probe and optical properties of media. Optical properties are predominantly determined by chromophore concentrations and scattering coefficients. The source-detector separations in the optical probe were 100μm-1mm. These separations result in superficial penetration depth of 1 to 3mm [23]. The utility of developed techniques are demonstrated through an application. The technique was applied to quantify hemodynamic changes in formalin induced pain behaviors.

Investigation of deeper regions and larger volumes of tissues requires that the scaling of source-detector separations. The second hypothesis and its aims are directed to quantify chromophore concentrations at separations of >0.5cm<5cm. Diffusion model [26] of photon transport was used to develop spectroscopic techniques to quantify volume averaged chromophore concentrations and scattering coefficients. The third hypothesis was directed to quantify these spatial heterogeneities in hemoglobin derivatives, other tissue chromophores and reduced scattering coefficients that are encountered in biological tissues as a result of increased investigated tissue volume. Multi source-detector NIRS system and multi-wavelength image reconstruction algorithms were developed to quantify spatial distributions of hemoglobin derivatives, other chromophores such as lipids, water and scattering coefficients. Tomographic maps of chromophore concentrations and reduced scattering coefficients are obtained.

In summary, hypothesis 1, 2 and 3 addresses quantifications of chromophore concentrations and reduced scattering coefficients in minute and large volumes.

Hypothesis 1 and its aims were directed towards the quantification optical properties at minute scale. Hypothesis 2 and its aims were directed towards the quantification of optical properties on a larger scale. Spatial heterogeneities in hemoglobin derivatives, other tissue chromophores and reduced scattering coefficients that are encountered in biological tissues as a result of increased investigated tissue volume were quantified through aims for hypothesis 3. The instrumentation developed for quantifications of chromophores and reduced scattering coefficients was portable in addition to having acquisition times suitable for online monitoring.

The developed broadband system enhances the potential of accurate quantifications of non-hemoglobin and oxygen level independent tissue absorbers that would remain uncharacterized with sparse wavelength reconstruction techniques. The ability to quantify water fractions and scattering has dramatic implications in terms of the value of these parameters with respect to tumor prognosis. The developed techniques and development would be readily applicable to in vivo monitoring of oxygenation in tumors for cancer prognosis and therapy monitoring. The NIRS imager built will be used to study hemodynamics of animal brain tumors with modifications.

CHAPTER 2

QUANTIFICATION OF HEMOGLOBIN DERIVATIVES WITH SINGLE VERY
SHORT SOURCE DETECTOR SEPARATION

The diffusion approximation of radiative transport theory has been widely used in recent years for modeling the propagation of near-infrared (NIR) light (650-900 nm) through turbid media, including biological tissues, and for quantifying optical properties of tissues. The solutions of diffusion equations have been validated by experimental measurements and Monte Carlo simulations under the conditions that 1) ρ (source-detector separation) is much larger than the transport mean free path (mfp or referred to as Z_0 later), and 2) absorption coefficients (μ_a) of the measured tissue are much smaller than its reduced scattering coefficients (μ_s') [26, 28]. The reduced scattering coefficients (absorption coefficients) are a measure of mean distance traveled by the photon before being scattered (absorbed).The major chromospheres that absorb light in biological tissues are oxygenated and deoxygenated hemoglobin (HbO and Hb respectively) with distinct optical spectra in the visible and the NIR wavelength ranges.

In optical fiber probes with a short separation, source-detector separations are of the order of 100 μm-1mm. Such a separation range violates fundamental assumptions of the diffusion approximation since 100 μm -1 mm separations are in the same order of mean free path of photons [26]. Also, increased absorption coefficients due to hemoglobin absorption at the visible range [29] in blood-perfused tissues make

magnitudes of absorption and scattering coefficients comparable. Hence, the diffusion model of photon transport is not valid when either short source-detector separations are used or visible light is employed. Several approaches have been suggested to quantify optical reflectance at short source-detector separations [17, 22, 30]. An example was a previous study reported by our group [17] that determined blood oxygen saturation of tissues using optical reflectance measured at short source-detector separations.

In this chapter, a steady-state, spectroscopic reflectance measurements at single short source-detector separation are used to quantify chromophore concentrations and reduced scattering coefficients of the tissues under study. This method is particularly promising for quantifying concentrations of hemoglobin derivatives and light scattering parameters in tissues under regular and dynamic conditions. For such applications, the method presented here permits rapid data acquisition and robust resolution of contributions from tissue absorbers: i.e., oxygenated and deoxygenated hemoglobin.

My approach is based on a recently published analytical model by Zonios and Dimou that expresses the reflectance measured with optical probes having short source-detector separations. I have developed a semi-empirical approach in tandem with a heuristic ant colony optimization algorithm to quantify concentrations of hemoglobin derivatives and non-hemoglobin tissue absorbers with acceptable levels of accuracy. One unique feature of this development is the use of broadband white light source for the acquisition of spectral reflectance. The instrumentation is straightforward and is particularly easy to replicate.

2.1 Mathematical model for small source-detector separation

Several approaches have been suggested and used to quantify optical properties of turbid media using short source-detector separations. Semi-empirical and theoretical models have been used to quantify diffuse reflectance measured from optical probe geometries. Such approaches have been reported to quantify oxygen saturation and reduced scattering coefficients [17, 30, 31]. In a recent development, Zonios and Dimou presented a model to quantify and relate the optical reflectance measured with optical probes having short source-detector separations to the reduced scattering coefficients and absorption coefficients of the medium [22].

The semi-empirical model presented by Zonios and Dimou is introduced in Equation (2.1) as follows [22]:

$$R_p(\lambda) = \frac{1}{k_1 \dfrac{1}{\mu_s'(\lambda)} + k_2 \dfrac{\mu_a(\lambda)}{\mu_s'(\lambda)}} \tag{2.1}$$

where $R_p(\lambda)$ is the optical reflectance measured by the optical probe at a particular measurement wavelength λ, k_1 and k_2 are parameters depending on geometrical characteristics of the optical probe as well as on the refractive indices of tissues and the surrounding medium, $\mu_s'(\lambda)$ is the reduced scattering coefficient, and $\mu_a(\lambda)$ is the absorption coefficient at wavelength λ. In principle, k_1 and k_2 of a selected probe need to be calibrated experimentally using tissue phantoms. The accuracy of calibration, effects of scattering coefficients on calculated k_1 and k_2 will be discussed in section 2.6. Absorption and reduced scattering coefficients are functions of deoxygenated

hemoglobin concentration *[Hb]*, oxygenated hemoglobin concentration *[HbO]*, melanin

concentration, C_{mel}, and water fraction, as described in Equations (2.2) and (2.3).

The spectral dependence of $\mu_a(\lambda)$ for blood-perfused tissues can be written as

$$\mu_a(\lambda) = [HbO]\varepsilon_{HbO}(\lambda) + [Hb]\varepsilon_{Hb}(\lambda) + \varepsilon_{H_2O}\%H_2O + [C_{mel}]\varepsilon_{mel}(\lambda), \quad (2.2)$$

where λ is the wavelength in nanometers; $\varepsilon_{HbO}(\lambda)$, $\varepsilon_{Hb}(\lambda)$, and $\varepsilon_{H_2O}(\lambda)$ are

extinction coefficients of HbO, Hb and water, respectively. The spectral dependence of

$\mu_s'(\lambda)$ can be approximately written as

$$\mu_s'(\lambda) = \left(1 - \frac{d_0^{1/2}}{d_S^{1/2}} \frac{\lambda - \lambda_{min}}{\lambda_{max} - \lambda_{min}}\right)\mu_S'(\lambda_{min}), \quad (2.3)$$

where the maximum and minimum wavelengths were originally selected as λ_{max}=900

nm and λ_{min}=450 nm, respectively, d_S represents the effective scatterer size, and d_0 is a

constant and equals 0.0625 μm. Effective scatterer size depends closely on the tissue

being probed. Intralipid has an effective scatterer size of 0.5 μm. It is clear that

Equation (2.3) describes a linear dependence of reduced scattering coefficients on the

wavelength. It is a reasonable approximation which is supported by numerical

calculations from Mie theory for spherical scatterers with Gaussian distribution in size

[32]. Maximum (λ_{max}) and minimum (λ_{min}) wavelengths chosen span the visible and NIR

wavelength ranges and model the linear dependence of reduced scattering coefficients

on the wavelength.

2.2 Experimental calibration for k_1 and k_2

2.2.1 Experimental setup for tissue phantoms

In vitro tissue phantoms were prepared using intralipid (Baxter Healthcare Corporation, Deerfield, IL) and hemoglobin from equine blood (Hemostat Inc, San Francisco, CA). The blood and intralipid were diluted with water. Simultaneous measurements were made on a dilute solution of Intralipid and animal blood (horse) with an ISS Oximeter (ISS Inc, Champaign, IL) and our thin optical fiber probe [16, 31]. The ISS Oximeter gives us a measure of reduced scattering coefficients and hemoglobin derivative concentrations. Optical reflectance in the visible and NIR wavelength range is measured using our optical probe [17]. An intralipid solution is a very good choice for a tissue phantom as it closely simulates light scattering properties of tissue with an estimated g (cosine of mean scattering angle) > 0.9 and a mean particle size of 0.5 μm [33]. A rectangular plastic container with dimensions of 10 cm x 8 cm x 14 cm (height x width x length) as shown in Figure 2.1 was used to hold the testing intralipid solution. The probes were inserted from the top into the solution during the measurement, so there was no intralipid-container or intralipid-air interface for the probe. The thin probe tip was facing vertically down towards the bottom of the container, 2-3 cm below the solution surface, and 4-5 cm away from the walls of the container. Integration times of spectral acquisition were varied from 50 ms to 125 ms to study its effect on determined calibration factors. To prevent saturation of the CCD detector, neutral density filters were used in the range of O.D. equal to 0.5 and 1.0. The

lowest integration time for measurement was chosen to ensure that measured intensities were greater than 500 counts [16].
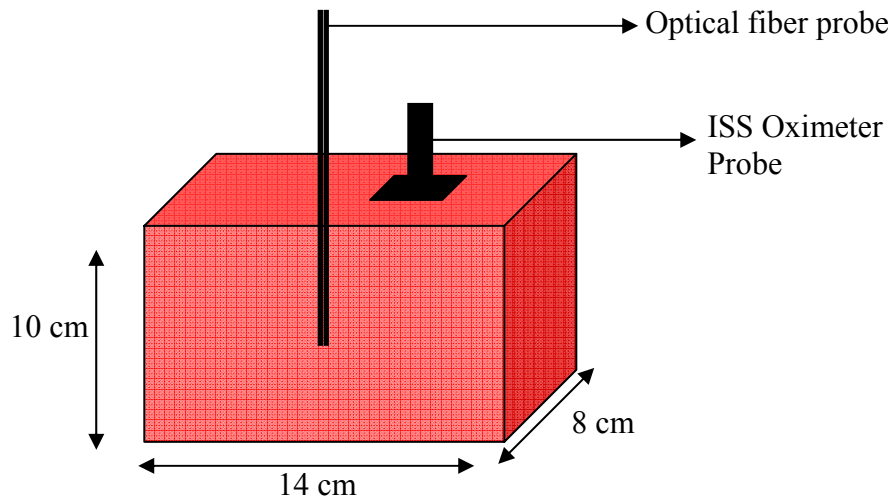
Figure 2.1 Schematic diagram of phantom, illustrating positions of the thin fiber probe and ISS Oximeter probe. The thin probe tip was facing vertically down towards the bottom of the container, 2-3 cm below the solution surface, and 4-5 cm away from the walls of the container. The probe position of ISS Oximeter is also shown. The dimensions are not to scale.

The Intralipid stock solution was 20% by volume, and the diluted Intralipid solutions ranged in concentration from 0.5%-2.0%, depending on the reduced scattering coefficient desired. In general, the reduced scattering coefficients, μ_s', found in tissues vary between 5 and 25 cm^{-1}; however, larger values of μ_s' have been reported in brain tissues [34, 35]. The reflectance spectra were taken at different Intralipid concentrations and different blood concentrations (as listed in Table 2.1). μ_s' values at wavelengths of 750 nm and 830 nm and hemoglobin derivative concentrations were obtained from the ISS Oximeter. All reflectance measurements were calibrated by making measurements with a standard reflectance white sample (WS-1, Ocean Optics, Dunedin, FL, USA). This standard sample had a reflectance > 98% throughout the wavelength range (350-

1100nm) [36]. The blood concentration predominantly determined the absorption properties of the phantom.

2.2.2 Determination of k_1 and k_2

The parameters of k_1 and k_2 in Equation (2.1) were determined using the least squares approach by using Moore-Penrose pseudo inverse. Equation (2.1) can be rewritten as

$$\frac{\mu_s^{'}(\lambda)}{R_p(\lambda)} = k_1 + k_2\mu_a(\lambda), \tag{2.4}$$

Equation (2.4) is valid for every wavelength in the spectrum. In a matrix form, Equation (2.4) can be rewritten as

$$[K] = [\mu_a]^{-1}\left[\frac{\mu_s^{'}}{R_p}\right], \tag{2.5}$$

$$\text{with } [K] = \begin{bmatrix} k_1 \\ k_2 \end{bmatrix}, \quad [\mu_a] = \begin{bmatrix} 1 & \mu_a(\lambda_{i=1}) \\ \cdots & \\ \cdots & \\ 1 & \mu_a(\lambda_{i=N}) \end{bmatrix}, \quad \left[\frac{\mu_s^{'}}{R_p}\right] = \begin{bmatrix} \frac{\mu_s^{'}(\lambda_{i=1})}{R_p(\lambda_{i=1})} \\ \cdots \\ \cdots \\ \frac{\mu_s^{'}(\lambda_{i=N})}{R_p(\lambda_{i=N})} \end{bmatrix}. \tag{2.6}$$

Equation (2.6) defines the individual terms in Equation (2.5). λ is a wavelength in the VIS /NIR wavelength range. N is the total number of wavelengths at which the reflectance was measured with the thin optical probe.

2.2.3 Calculation of absorption and reduced scattering coefficients

Absorption coefficients at all wavelengths in the visible and NIR range were calculated from the measured blood hemoglobin concentrations and published hemoglobin extinction coefficients [29]. To calculate reduced scattering coefficients the wavelength range is divided into two regions, Region-1 (500-600 nm) and Region-2 (600-850 nm), respectively. Reduced scattering coefficients in the visible wavelength range were determined from the approximations given by Flock et al [33]. To calculate the reduced scattering coefficients in Region-2 the following procedure was adopted:

1. Scaling factors, K_{scale}, are calculated to scale the measured reflectance from the thin optical probe at the measurement wavelengths given by the ISS Oximeter (750nm and 830 nm), as shown in Equations (2.7) to (2.9).

$$K_{750nm} = \frac{R_p(750nm)}{\mu_s'(750nm)},$$
(2.7)

$$K_{830nm} = \frac{R_p(830nm)}{\mu_s'(830nm)},$$
(2.8)

$$K_{scale} = \frac{K_{830nm} + K_{750nm}}{2},$$
(2.9)

where R_p(750nm) and R_p(830nm) are the reflectance measured from the thin optical probe; μ_s'(750nm) and μ_s'(830nm) are reduced scattering coefficients measured by the ISS Oximeter. K_{750nm} and K_{830nm} are scaling factors between the measured reflectance and reduced scattering

19

coefficients at respective wavelength. K_{scale} is the mean of K_{750nm} and K_{830nm}.

2. Reduced scattering coefficient at any wavelength between 600 and 850 nm in Region-2 can be expressed as shown in Equation (2.10).

$$\mu_s'(\lambda) = \frac{R_p(\lambda)}{K_{scale}} \qquad (2.10)$$

where $R_p(\lambda)$ is the reflectance measured by the thin optical probe.

3. Fit a polynomial through the reduced scattering coefficients determined in Region-1 and Region-2 to smooth the transition between them. This polynomial is used to calculate the reduced scattering coefficients in the entire wavelength range from 500 to 850 nm.

Reduced scattering and absorption coefficients calculated as described in the previous paragraph were used in the determination of k_1 and k_2, based on Equations (2.5) and (2.6). Multiple sets of k_1 and k_2 were determined at various total hemoglobin concentrations and reduced scattering coefficients. The average set over all multiple cases was chosen as the calibrated k_1 and k_2 and used for all further computations.

2.2.4 Simpler and better technique to quantify k_1 and k_2

A better and simpler technique can be made to quantify k_1 and k_2. This technique was graphical and hence gave the capability of visually evaluating the accuracy and convergence of the determined parameters. As seen in Equation (2.4), k_1 and k_2 can be determined by obtaining a least squares linear fit that best fits $\mu_s'(\lambda) \big/ R_p(\lambda)$ vs $\mu_a(\lambda)$, as illustrated in Figure 2.2. In this case, k_1 forms the y-intercept and k_2 the

slope of the line. k_1 has the same unit as the y-axis in Figure 2.2(a) which is cm^{-1}; k_2 which forms the slope, is a ratio and has no unit. A non-monotonic nature is seen in Figure 2.2, and it will be discussed in Section 2.6.

Figure 2.2 Linear fit with a least square regression line to determine values of k_1 and k_2. k_1 forms the y-intercept and k_2 the slope of the line. The measurements were made with 7-fiber array probe. a) Linear fit for data measured using a phantom with [Hb_{Total}]=28 µM and μ_s'(750nm)=7.5 cm^{-1}, giving rise to k_1= 35.64 and k_2 = 12.41. b) Linear fit for data measured using a phantom with [Hb_{Total}]=37 µM and μ_s'(750nm)=13.5 cm^{-1}, having k_1= 37.96 cm^{-1} and k_2 = 14.42.

The accuracy of both measurements and calculations of the optical coefficients is critical to the accuracy of quantifications for parameters k_1 and k_2. As shown in Figures 2.2(a) and 2.2(b), each blood-intralipid concentration gives a set of k_1 and k_2 with experimental variation. In principle, the set of k_1 and k_2 for a selected probe should be unique, independent of blood concentrations and light scattering properties. Thus, I calculated multiple sets of k_1 and k_2 from various blood-intralipid phantoms that had different total hemoglobin concentrations and reduced scattering coefficients. The averaged set of k_1 and k_2 over all the cases was chosen as the calibrated k_1 and k_2.

After having determined k_1 and k_2, a comparison between the measured and predicted reflectance by the mathematical model in the VIS/NIR wavelength region can be obtained, as shown in Figure 2.3(a). It shows good agreement between the actual measurement and calculated curve using the calibrated k_1 and k_2, while some deviations from the model are seen at smaller wavelengths (500-525 nm). These deviations will be discussed in Section 2.7.

In another way for comparison, Figure 2.3(b) shows a correlation plot between the calculated versus actual reflectance measured with the 7-fiber-array-probe. It is desired that the experimentally calibrated constants (k_1 and k_2) produce a correlation as close as possible to a straight line of unit gradient and zero intercept. The goodness of match is apparent from Figure 2.3(b) having a slope 1.03 and an intercept of 0.01.
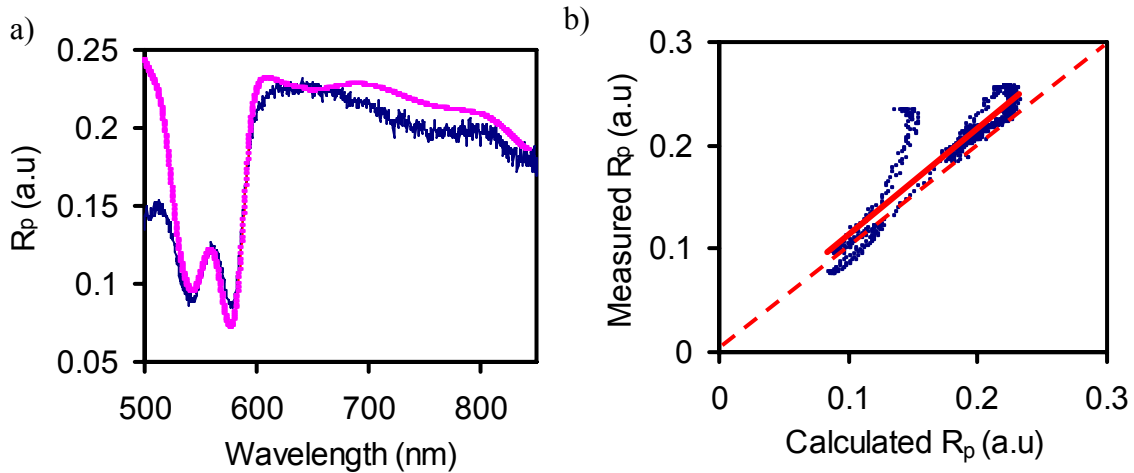
Figure 2.3 Comparison between values of reflectance predicted by the model and measured from the phantoms with 7-fiber-array probe. (a) Spectra predicted by the model (pink curve) and measured from a phantom (blue curve) with $[Hb_{Total}]$=56μM and μ_s'(750 nm)=13.5 cm^{-1}.(b) Correlation plot between the predicted and measured reflectance spectrum, having slope= 1.03, intercept = 0.01, and R^2=0.85). A unity line (red dashed line) in each is placed to indicate the desired ideal result.

2.2.5 Measurements based on different integration times

Measurements were made at different integration times on blood-intralipid phantoms. The reduced scattering coefficients and total hemoglobin concentrations measured by the ISS Oximeter are tabulated in Table-2.1. Reflectance measured from the thin optical probe at 50, 75, 100 ms were used for calibration (Calibration Set). Neutral density filters as mentioned earlier in Section 2.2.1 were used to scale the reflectance to prevent saturation of spectrometer.

Table 2.1 Calibration Set: Total hemoglobin concentrations and reduced scattering coefficients of blood intralipid phantoms. Measurements made at integration times listed in this table were used to calibrate the optical probe.

Integration Time (ms)	$[Hb_{Total}]$ µM	Intralipid concentration	μ_s' (750nm) cm^{-1}	μ_s' (830nm) cm^{-1}
50	31,48	0.5%	5.8	4.5
	20,28,37,56	0.8%	8.2	7.5
	33,48	1.25%	14.2	13.5
75	20,28,37,56	0.8%	8.2	7.5
	17,33,48,	1.25%	14.2	13.2
100	28,37,56	0.8%	8.2	7.5
	33,48	1.25%	14.2	13.5

Table 2.2 Test Set: Total hemoglobin concentrations and reduced scattering coefficients of phantoms. Measurements made at 125 ms integration time are listed in this table and were used to verify quantifications of hemoglobin derivative concentrations and reduced scattering coefficients.

Integration Time (ms)	$[Hb_{Total}]$ µM	Intralipid concentration	μ_s' (750 nm) cm^{-1}	μ_s' (830 nm) cm^{-1}
125	31,48	0.5%	5.8	4.5
	28,37	0.8%	8.2	7.5
	33,48	1.25%	14.2	13.5

Data measured at 125 ms was used to verify the ability of the technique to quantify hemoglobin derivatives (Hb and HbO) and reduced scattering coefficients. Data segregated as the test set was not used for calibration. Calibration factors (k_1 and k_2) determined from the calibration set at three integration times was verified by the data obtained at 125 ms (Test set). Table 2.2 lists all total hemoglobin concentrations and reduced scattering coefficients used in the test set.

2.3 Inverse calculations

Determination of diffuse reflectance from Equations (2.1), (2.2) and (2.3) is straight forward if concentrations of tissue chromophores and tissue scattering properties are known. The inverse calculation deals with determination of tissue chromophore concentrations and effective scatterer sizes from measurements of diffuse reflectance on the tissue surface. The mathematical problem of inversion can be transformed into a problem of function minimization using an optimization algorithm. The algorithm searches for a set of values (chromophore concentrations and effective scatterer sizes) from the given solution space that best fit the measurement of spectral diffuse reflectance using least squares analysis. It can be expressed as follows:

$$\chi^2 = \sum_{i=1}^{M} \left[R_p(\lambda_i)^{(measured)} - R_p(\lambda_i)^{(predicted)} \right]^2, \qquad (2.11)$$

where M is the number of wavelengths, $R_p(\lambda_i)^{(measured)}$ and $R_p(\lambda_i)^{(predicted)}$ are the reflectance values measured by the thin optical probe and calculated by using the prediction of hemoglobin concentrations and scattering coefficients selected from the optimization algorithm at wavelength λ_i.

24

2.3.1 Ant colony optimization

Evolutionary algorithms are widely utilized in the field of optimization. The algorithms work on a population of values rather an initial guess, making the solution independent of an initial guess. These algorithms do not need the existence or calculations of derivatives. Their inherent characteristics make them suitable to search for global minimums, rather than being stuck in local minima.

The ant colony optimization algorithm (ACO), introduced by Marco Dorigo [25], is a probabilistic evolutionary technique for solving computational problems which can be reduced to finding good paths through graphs. They draw inspiration from the behaviors of ants in finding paths from the colony to food. Ants, to begin with, wander randomly and upon finding food return to their colony laying down pheromone trails. If other ants find such a path, they are likely not to keep traveling at random, but to instead follow the trails, returning and reinforcing it if they eventually find food. With passage of time, pheromone trails begin to evaporate, thus reducing its attractive strength. The greater the time it takes for an ant to travel down the path again, the more time the pheromones have to evaporate. A short path, in comparison, gets marched over faster, and thus the pheromone density remains high as it is laid on the path as fast as it can evaporate. If there were no evaporation at all, the paths chosen by the first group of ants would tend to be excessively attractive to the following ones. It can be said that when one ant finds a good (short) path from the colony to a food source, other ants are more than likely to follow that path, and positive feedback eventually leaves all ants following a single path.

The idea of the ant colony algorithm is to mimic this behavior with "simulated ants" walking around the graph representing the problem to solve. Pheromone evaporation has also the advantage of avoiding the convergence to a locally optimal solution. In the absence of evaporation, exploration of the solution space would be constrained. Ant colony optimization algorithms have been used to produce near-optimal solutions to real world problems [37, 38]. They have an advantage over simulated annealing and genetic algorithm approaches when the objective function and weight of various parameters effecting this objective function may change dynamically; the ant colony algorithm can be run continuously and adapt to changes in real time. I am using a similar approach in this dissertation to transform mathematical problems of inversion to programming problems.

2.3.2 Mathematical formulation

A system with real valued properties is considered as g_m, $m = 0, 1, 2, \ldots, P\text{-}1$, where P is the number of properties. In my study, the properties determine the optical reflectance at individual wavelengths in the spectrum ($R_p(\lambda)$). These properties correspond to the objectives of the system to be optimized. Specifically, these properties (x_j) of the system are dependent on D number of real valued parameters as indicated in Equation (2.12):

$$x_j ; \quad j = 0, 1, 2, \ldots , D\text{-}1. \tag{2.12}$$

In my study, these properties (x_j) correspond to the concentrations of tissue chromophores and parameters that represent the wavelength dependence on reduced scattering coefficients. A practically realizable system requires that the values x_j be

26

bounded. In a similar manner, physiological ranges of concentrations and scattering coefficients can be written as in Equation (2.13), where x_{jl} and x_{jh} are the lower and upper bounds respectively.

$$x_j \in [x_{jl}, x_{jh}] \qquad (2.13)$$

Optimization of the system implies the variation of D-dimensional variation of parameter vector, as shown in Equation (2.14), until the properties of g_m (i.e., $R_p(\lambda)$) are optimized.

$$\bar{x} = (x_0, x_1, x_2 \ldots . . x_{D-1}) \qquad (2.14)$$

Optimization problem can be reformulated as a minimization problem and stated as in Equation (2.15)

$$\min f_m(\bar{x}) \qquad (2.15)$$

where $f_m(x)$ represents the function by which the property g_m is calculated, and its optimization is represented as the minimization of $f_m(x)$. This function corresponds to Equation (2.11), where the differences between the predicted and measured reflectance are minimized to arrive at optimal values of concentrations and scattering coefficients.

The ant colony algorithm begins from a randomly chosen location $\bar{x}_N$, which is any location in the D-dimensional parameter space. $\bar{x}_N$ can be written as

$$\bar{x}_N = (x_0 = \alpha_0, x_1 = \alpha_1, \ldots \ldots \ldots x_{D-1} = \alpha_{D-1}), \qquad (2.16)$$

where α_0, α_1, ….. α_{D-1} are some constants. $\bar{x}_N$ represents a D-dimensional vector and is the initial nesting location.

Let us consider that there are *n* number of ants in the ant colony, such that

27

$$a_i, \ i \in [1...n].$$ (2.17)

Each of these ants a_i explore p locations in the D-dimensional parameter space in the neighborhood of $\bar{x}_N$ such that

$$\bar{x}_{N,i} = \bar{x}_N + \gamma_i (x_{jh} - x_{jl})$$ (2.18)

where $\bar{x}_{N,i} \in [x_{jl}, x_{jh}]$ and γ_i is a randomly generated number between [0,1]. In addition, the best parameter vector $x_{best,i}$ is evaluated for ants in order to keep track of the progress that is made during the minimization process. $x_{best,i}$ is the D-dimensional parameter that has the least $f_m(\bar{x}_{N,i})$.

In another level of exploration of the parameter space, each of these ants, a_i, explores locations in the neighborhood of $\bar{x}_{N,i}$ such that

$$\bar{x}_{N,i,local} = \bar{x}_{N,i} + \gamma_{i,local} (x_{jh} - x_{jl})$$ (2.19)

$\bar{x}_{N,i,local}$ are D-dimensional vectors generated by using randomly generated factors $\gamma_{i,local}$, which are smaller in magnitude compared to γ_i. $\gamma_{i,local}$ is a randomly generated factor between [0,1]. Again the best parameter vector $x_{best,i,local}$ is evaluated for ants in order to keep track of the progress that is made during the minimization process. $x_{best,i,local}$ is the D-dimensional parameter that has the least $f_m(\bar{x}_{N,i})$ in all generated vectors. At the beginning of next iteration of the algorithm, nest location is moved to $x_{best,i,local}$, D-dimensional vector.

$$x_N = x_{best,i,local}$$ (2.20)

28

Iterations are made until $f_m(\bar{x}_{N,i})$ decreases below a specified threshold. Alternatively, iterations could be terminated after a preset number of them. Stopping criteria may vary depending upon the specific application and set of constraints to be satisfied. Stopping criteria for this particular application is to be described in the following sub-section.

2.3.3 Stopping criteria

The iterations were terminated when the decrease in objective function values were less than 1% in successive iterations. This ensured convergence of the solution. A maximum of 100 iterations were set to prevent from infinite looping. The computation time per measurement spectrum was less than 30 seconds on an average windows PC (Intel Pentium M Processor, 1.73 GHz, 512MB RAM). If the program failed to reach the conditions for convergence in the preset iterations, a flag was set up to indicate the non-convergence, and mean squared error was reported.

2.4 Instrumentation

The experimental setup used for reflectance measurements is shown in Figure 2.4. A CCD spectrometer (USB2000, Ocean Optics, Dunedin, FL, USA), capable of collecting spectra in the 350-1050 nm range was used for diffuse reflectance measurements.

Illumination was provided by a tungsten-halogen light source (HL-2000, Ocean Optics, Dunedin, FL, USA). All spectra were referenced to a reflectance calibration standard (WS-1, Ocean Optics, Dunedin, FL, USA). Diffuse reflectance spectra were calibrated by being divided by the reflectance spectrum of the calibration standard. A

typical integration time for spectral collection was 10-125 ms depending upon specific applications. Signal to noise ratio (SNR) was measured by making measurements of reflectance with the light source turned off (dark signal) which corresponds to noise in our measurements. Signal intensity is the reflectance intensity measured from a phantom or specimen, usually depending on the spectral wavelength. The SNR (signal intensity/dark signal intensity) was typically greater than 100:1 in the major spectral range in our measurements.
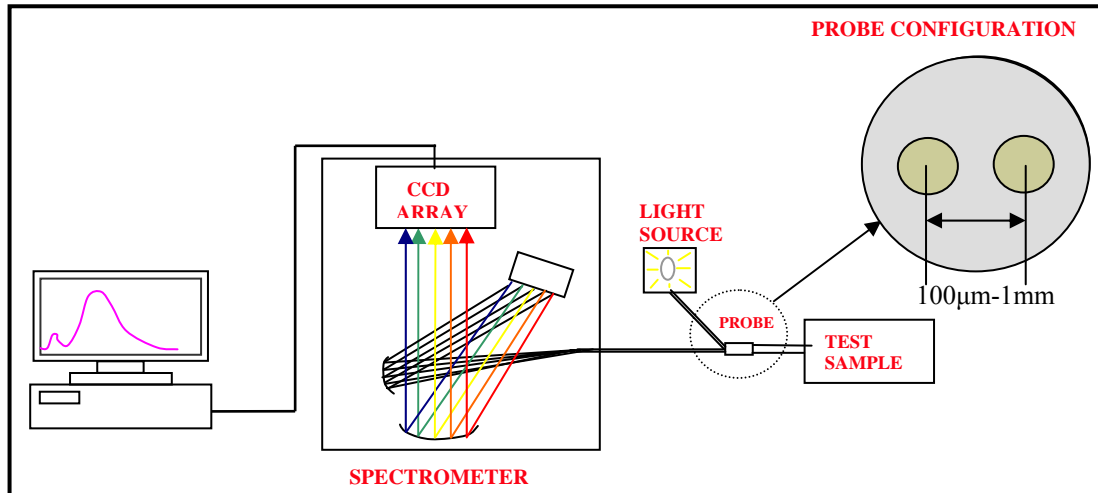
Figure 2.4 Schematic diagram of experimental setup used for the measurement of reflectance spectra. Source-detector separations varied between 100 μm and 400 μm for different thin probes used in the applications.

2.4.1 Optical probes

Three different thin fiber probes have been utilized in our research development: one is a 7-fiber-array probe, the other two are single source-detector fiber probes. The fiber-array probe was utilized for prostate and kidney ex vivo measurements, whereas the two single source-detector probes were used in my in vivo pain study using rats (See

Chapter 3). Constants k_1 and k_2 are determined for all three thin fiber optic probes, respectively, by making measurements on blood intralipid phantoms. Detailed analysis to study the effect of parameters such as integration time, including and excluding information from the wavelength range of 500-560nm are made using the 7-fiber-array probe.

2.4.1.1 7-fiber-array probe

The design of 7-fiber-array probe was made with future applications in mind. Although the present applications require the use of only one source detector separation, provisions for multiple source detectors were made. The source-detector separations considered in this chapter are in the scale of 100 μm – 700 μm. Within this range of source-detector separation the diffusion approximation is not valid [16, 17, 22, 31]. Separations in this range allow light reflected back from superficial surfaces to carry quantitative information more about the tissue surfaces. The validity of my semi-empirical approach for thin optical probes has been verified using Monte Carlo simulations by our group [17, 31, 34] and others [22]. The penetration depth of the probes scales with the corresponding source-detector separation [27]. The geometry for the 7-fiber-array probe is illustrated with a cross-sectional view in Figure 2.5(a). The fibers 3 and 5 have bee used for prostate and kidney applications (not shown in my dissertation). The fibers are centrally located on the probe array. This ensures easy positioning of the optical probe for measurements.

The diameter of each optical fiber in the array is 100 μm plus the additional room for cladding and epoxy coating. The distance between fibers 3 (for light delivery)

and 5 (for detection) is about 300 μm (see Figure 2.5(a)). The 'look ahead distance' with this source-detector separation is of the order of 1-2 mm. The 'look ahead distance' as a function of source-detector separations was investigated in previous studies by our group [23]. Such an optical probe can be designed with flexibility of selected source-detector separations, based on the particular application.
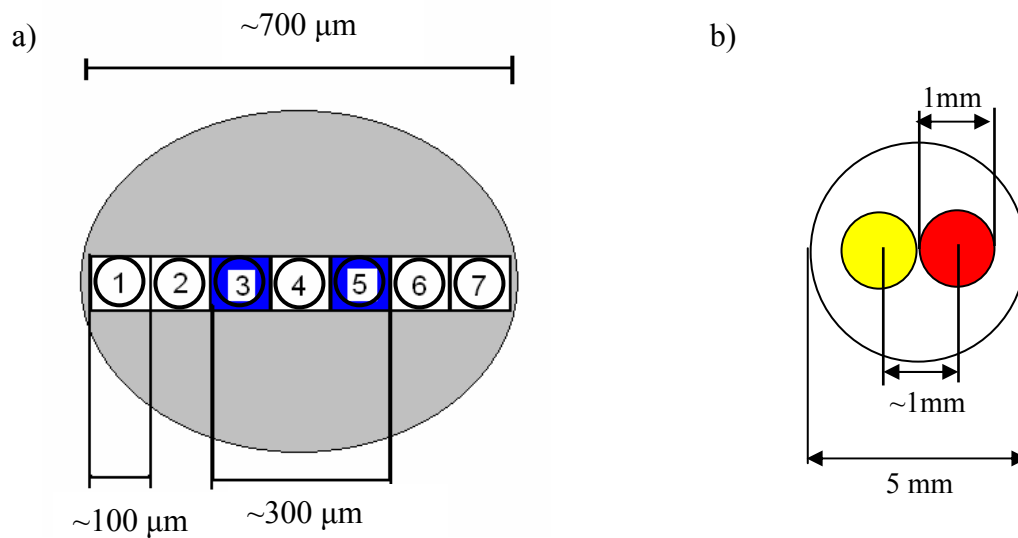
Figure 2.5 a) Cross sectional view of an optical probe, with a 7-fiber array, used for reflectance measurements from prostate and renal lesions ex vivo. Locations of the source and detector are illustrated, i.e., fibers 3 and 5. b) Cross sectional view of an optical probe, with a single source-detector, used for reflectance measurements in my in vivo pain study using rats.

2.4.1.2 Single source-detector optical fiber probes

Two single source-detector probes were used in my in vivo pain study using rats to be described in Chapter 3. These thin fiber optic probes were obtained from TechEn Inc, Boston, MA. The geometry of the probes is illustrated with a cross-sectional view in Figure 2.5(b). It consisted of 1-mm core diameter optical fibers for light delivery and

collection. The center to center distance between the fibers was approximately 1 mm. The outer diameter of the optical fiber was 5 mm.

2.5 Results

Constants k_1 and k_2 were determined at various total hemoglobin concentrations and reduced scattering coefficients using the simpler and better technique described in Section 2.2.4. Absorption and reduced scattering coefficients were evaluated as described earlier in Section 2.2.3. After multiple sets of k_1 and k_2 were obtained from a variety of blood-intralipid solutions, the average values of k_1 and k_2 are obtained for all further computations. The range of variation of k_1 and k_2 for the 7-fiber-array optical probe obtained at 50 ms integration time is tabulated in Table 2.3. Additionally, multiple sets of k_1 and k_2 were determined with integration times of 75 ms and 100 ms and are included in Appendix A. The averaged k_1 and k_2 values with three different integration times are all in good agreement with one another.

Table 2.3 Range of variation of k_1 and k_2 for 7-fiber-array optical fiber probe computed using measurements from blood-intralipid phantoms. Measurements were made at an integration time of 50 ms

	$[Hb_{Total}]$ μM	Intralipid concentration	μ_s' (750 nm) cm^{-1}	μ_s' (830 nm) cm^{-1}	k_1	k_2
Measurement-1	31	0.5 %	5.8	4.5	33.8	12.6
Measurement-2	48	0.5 %	5.8	4.5	39.4	15.2
Measurement-3	20	0.8 %	8.2	7.5	39.0	13.2
Measurement-4	28	0.8 %	8.2	7.5	40.9	15.4
Measurement-5	37	0.8 %	8.2	7.5	35.6	12.3
Measurement-6	56	0.8 %	8.2	7.5	38.1	12.8
Measurement-7	33	1.25 %	14.2	13.2	30.2	12.3
Measurement-8	48	1.25 %	14.2	13.2	32.1	14.7
		Average			34.7±.4.2	12.6±1.3

2.5.1 Integration time

In vitro measurements were made using a diluted solution of intralipid and animal blood (horse) to simultaneously measure reduced scattering coefficients using the ISS Oximeter and optical reflectance with the thin optical probe (see Figure 2.1). Integration times of 50, 75, 100 ms were used for the CCD spectrometer to determine constants k_1 and k_2 as mentioned before.

Figure 2.6(a) presents a comparison between the constants obtained at different integration times for the 7-fiber-array probe. A single factor ANOVA was performed to test for differences among k_1 values determined at 50, 75, 100 ms. The same test was repeated for values of k_2 determined at 50, 75, 100 ms. Values of k_1 determined at 50, 75, 100 ms were not significantly different ($F(2,14)=3.61$, $p=0.054$). Similarly, values of k_2 were not significantly different ($F(2,14)=0.27$, $p=0.76$) at three different integration times.

The effect of changes in the values of k_1 and k_2 on predicted spectra were visually inspected, as shown in Figure 2.6(b). Another way to quantitatively compare the measured and predicted spectra, which were obtained using the calibrated k_1 and k_2 with different integration times, was done by calculating Pearson product moment correlation coefficient (R) [39]. In all cases with three different integration times, $R^2 > 0.89$, reinforcing the results obtained through statistical analysis that the calculated spectra are insensitive to variations in parameters k_1 and k_2 due to changes in integration times. The mean of R^2 values and their standard deviations at each integration time are tabulated in Table 2.4.
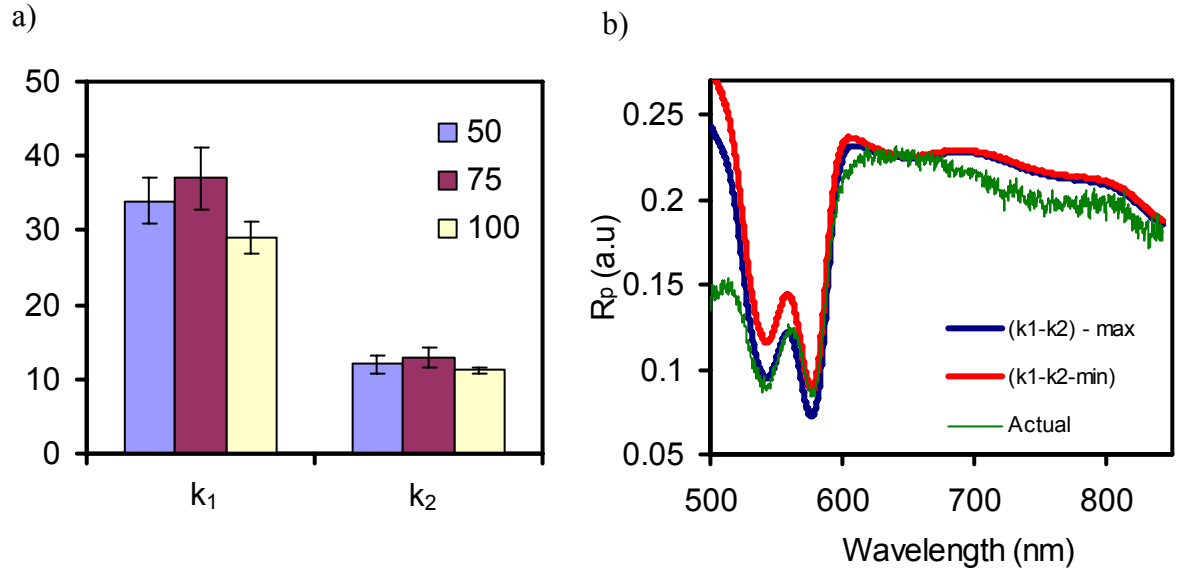
Figure 2.6 (a) Constants k_1 and k_2 determined at three integration times 50, 75, 125 ms for the 7-fiber-array probe. (b) Comparisons between spectra predicted with maximum values of constants k_1 and k_2 (red curve), minimum values of constants k_1 and k_2 (blue curve) and actual measurement of a reflectance spectrum (dark green) from 7-fiber-array probe.

Table 2.4 Mean and standard deviations of R^2 values with different integration times and respective k_1 and k_2 values for 7-fiber-array optic probe.

Integration time (ms)	k_1	k_2	R^2
50	34.7±4.2	12.6±1.3	0.92±0.03
75	38.5±3.7	14.3±1.2	0.94±0.02
100	30.2±4.9	10.2±1.5	0.93±0.01
Mean of k_1 and k_2	34.9±3.9	12.9±1.5	

As mentioned in Section 2.4.1, the fiber-array probe was utilized for prostate and kidney ex vivo measurements, whereas the two single source-detector probes were used in my in vivo pain study using rats (See Chapter 3). The respective sets of calibrated k_1, k_2 for those probes are tabulated in Table 2.5. The reflectance calculated

with calibrated k_1, k_2 are in very good agreement ($R^2 = 0.99$) with the actual spectral measurements using blood-intralipid phantoms.

Table 2.5 Sets of k_1 and k_2 for optical probes used for reflectance measurements from prostate, renal lesions and rat hind paws.

Probe	k_1	K_2
Prostate-renal (7-fiber-array probe)	34.7	12.6
Rat-probe-1	28.6	14.3
Rat-probe-2	30.2	10.2

2.5.2 Blood-intralipid phantom verifications

The phantom measurements not used for the calibration set were utilized to verify the correctness of the developed method by quantifying the hemoglobin derivative concentrations and reduced scattering coefficients of the phantoms. The measurements made at an integration time of 125 ms were used for the test set. The corresponding hemoglobin concentrations and reduced scattering coefficients are tabulated in Table 2.2. The Intralipid stock solution was 20% by volume, and diluted Intralipid solutions ranged in concentration from 0.5% - 1.5%, depending on the reduced scattering coefficient desired. Reflectance spectra were used to determine total hemoglobin concentration, oxygen saturation, reduced scattering coefficients and effective scatterer size.
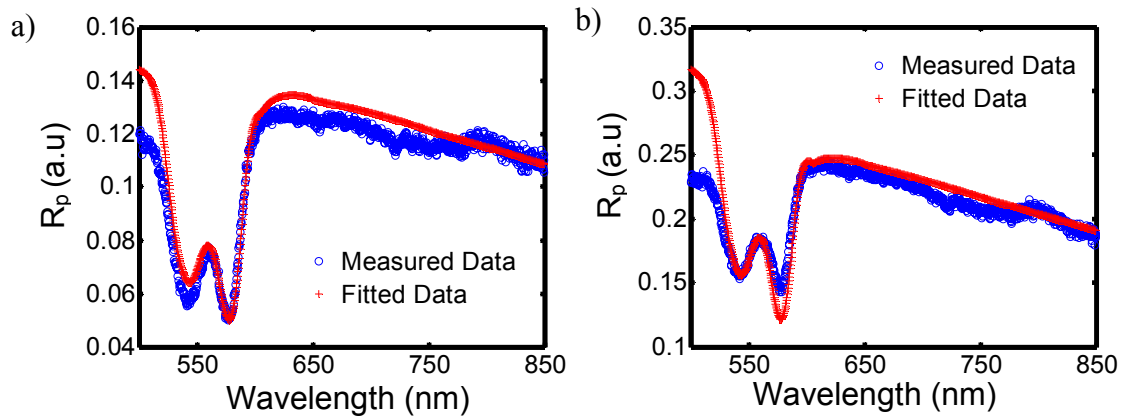
Figure 2.7 Two diffuse reflectance spectra measured with 7-fiber-array optical probe taken on blood intralipid phantom with (a) $\mu_s'(750 \text{ nm})$=7.8 (8.2) cm^{-1}, $\mu_s'(830\text{nm})$=6.5 (7.3) cm^{-1}, $[HbO]$=30.7 (28.0) μM; (b) $\mu_s'(750\text{nm})$=4.8 (5.6) cm^{-1}, $\mu_s'(830\text{nm})$=4.2 (4.8) cm^{-1}, $[HbO]$=30.7 (28.0) μM. The values in parentheses indicate the expected parameters obtained from the ISS Oximeter. The blue curves indicate the measured data, and the red curves are the best fits using the calibrated k_1 and k_2. The best fits give rise to the calculated hemoglobin derivative concentrations and reduced scattering coefficients, as listed above.

Figures 2.7(a) and 2.7(b) depict comparison between the calculated spectra and actual measurements for the 7-fiber-array optical probe. The deviation in reflectance values between those predicted by the model and those measured by the probe were less than ±5% in the wavelength range of 525 nm – 850 nm. Large deviations (>20%) were observed at smaller wavelengths (500-525 nm). Possible causes for these deviations will be discussed in Section 2.6. Spectrum shown in Figure 2.7(a) corresponds to measurement 2 listed in Table 2.7 and the spectrum in Figure 2.7(b) to measurement 4.

Table 2.6 Comparison of calculated and measured hemoglobin derivative concentrations and reduced scattering coefficients with 7-fiber-array probe. The ISS Oximeter was used as the gold standard for all measurements.

Measurement	μ_s' (750nm) cm^{-1}		μ_s' (830nm) cm^{-1}		Oxygen Saturation (%)		[HbO] μM		Scatterer-size, μm	
	ISS	Calculated	ISS	Calculated	ISS	Calculated	ISS	Calculated	Pub.	Calculated
1	8.2±1	7.8	7.3±1	6.5	98±3	99	37.0±5	32.2	0.5	0.48
2	8.2±1	8.9	7.3±1	8.1	98±3	99	28.6 ±5	30.7	0.5	0. 64
3	5.6±1	4.8	4.8±1	4.2	98±3	99	48.4±5	52.7	0.5	0.56
4	5.6±1	4.8	4.8±1	3.7	97±3	99	31.2±5	28.2	0.5	0.41
5	14.2±1	15.2	13.5±1	14.7	97±3	99	33.0±5	29.6	0.5	0.68
6	14.2±1	14.1	13.5±1	13.8	97±3	99	48.2±5	44.2	0.5	0.38

Table 2.7 Relative errors in hemoglobin derivatives and reduced scattering coefficients. All values in the table indicate relative errors in percentage.

Measurement	μ_s' (750nm)	μ_s' (830nm)	Oxygen Saturation	[HbO]	Scatterer-size
1	4.8	16.4	1.0	13.5	4.0
2	8.5	9.8	1.0	6.9	28.0
3	21.4	22.0	1.0	8.3	12.0
4	21.4	19.1	2.0	9.6	18.0
5	6.5	8.8	2.0	9.0	36.0
6	1.0	1.0	2.0	8.2	24.0

The fitted parameters (hemoglobin derivative concentrations and reduced scattering coefficients) were compared with the expected values taken from the simultaneous measurements with the ISS Oximeter. All parameters derived from the described algorithm are tabulated in Table 2.6. It can be seen that the derived and expected parameters are in good agreement. The mean particle size for intralipid was obtained from published literature [33]. The relative errors between the calculated and expected parameters are tabulated in Table 2.7. Mean values indicated by the ISS Oximeter were used for comparisons and computation of relative errors.

The Pearson coefficient, R, of correlation (between the measured and calculated spectra) was calculated [39], and R^2 values for all cases are greater than 0.89. These coefficients for all spectra used for verification are tabulated in Table 2.8. In another way for comparison, as mentioned in Section 2.2.4 and depicted in Figure 2.3(b), correlation were plotted between the calculated versus actual reflectance. It is desired that the calculated spectrum that fits the experimental spectrum with a minimum χ^2 (Equation 2.11) produces a correlation as close as possible to a straight line of unit gradient and zero intercept. The slope and intercept of correlation plots for six spectra used for verifications are tabulated in Table 2.8. The goodness of match is reflected by (1) the lowest value of slope (i.e., R) 0.89 and the highest intercept of 0.03, and (2) the mean squared error, χ^2.

$$Mean\ sqaured\ error = \frac{\sum_{i=1}^{M}\left[R_p(\lambda_i)^{(measured)} - R_p(\lambda_i)^{(calculated)}\right]^2}{M}, \quad (2.21)$$

where $R_p(\lambda_i)^{(measured)}$ is the experimentally measured spectrum, $R_p(\lambda_i)^{(calculated)}$ the calculated spectrum and M is the number of wavelengths. The mean squared errors for all spectra used for verification are tabulated in Table 2.8.

Table 2.8 SlopeR^2 values spectra measured and calculated spectra for blood-intralipid phantoms listed in Table 2.7.

Spectra	Slope	Intercept	Mean squared error, χ^2	R^2
1	0.89	0.030	0.0003	0.89
2	0.93	0.006	4.03E-05	0.92
3	0.87	0.040	0.0003	0.89
4	0.86	0.027	0.0001	0.90
5	0.86	0.003	0.0005	0.92
6	0.97	0.010	0.004	0.92

<u>2.6 Discussion</u>

The study in this chapter described the use of a simple analytical model for diffuse reflectance at short source-detector separations that can be used to quantify optical properties of biological tissues. This model is one of the simplest models as compared to other models available in the literature for describing diffuse reflectance at short source-detector separations [30]. In principle, the Oximeter by itself has an error range. All concentrations and scattering coefficients calculated from the algorithm (Table 2.6) are likely within the error ranges of the ISS Oximeter [40]. Table 2.7 indicates that the maximum error in quantification of $\mu_s'(750$ nm$)$ and $\mu_s'(830$ nm$)$ is 22%. This can be attributed to low scattering properties (5.6 cm^{-1} for 750 nm and 4.8 cm^{-1} for 830 nm, see Table 2.6). The error in quantification of particle sizes is also large (a maximum error of 24%). One of the possible reasons is that all computed particle sizes were compared to those published in literature. The differences in optical properties and particle sizes in intralipid are well documented by earlier investigators [33, 41]. These variations can lead to large errors in quantification of particle sizes. Such variations in intralipid property can lead to large errors in comparison between the calculated and expected particle sizes.

One-time phantom calibration required by the model and described in detail in this chapter does not constitute a serious disadvantage. It can be noted that any analytical model requires verification to ascertain its validity. The model with the calibration method described here can be used with all common fiber optic probe

geometries after initial calibration process. Once the probe is calibrated for a given application, no further calibration or adjustment to the model is required.
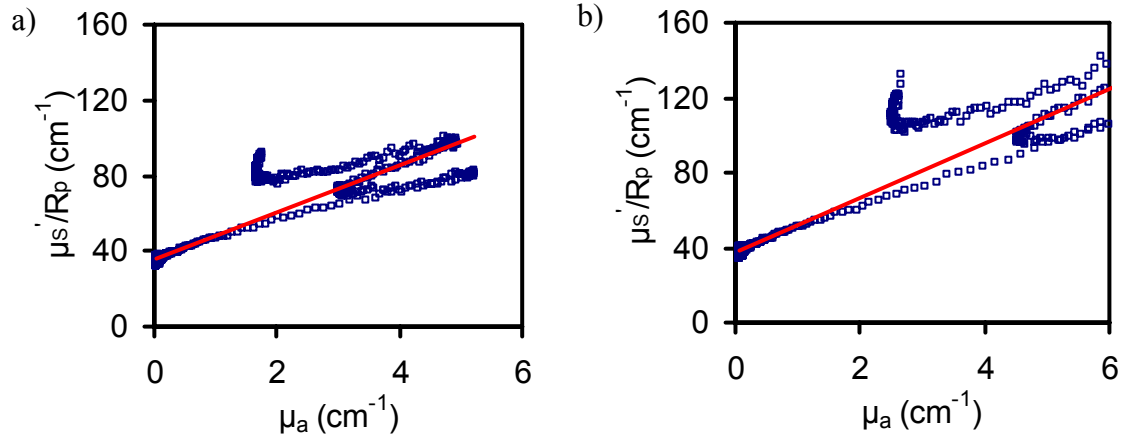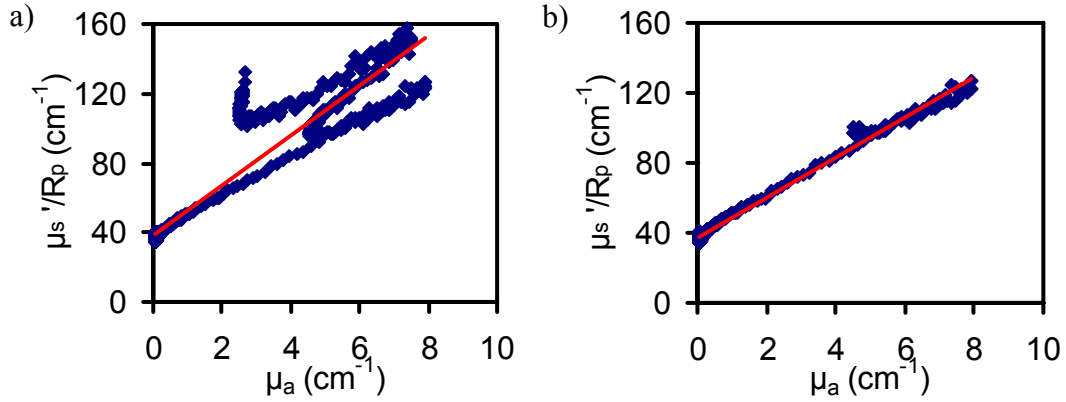

Figure 2.8 Linear fit with a least squares regression line to determine the values of k_1 and k_2. k_1 forms the y-intercept and k_2 the slope of the line. Measurements were made with 7-fiber-array probe. a) Linear fit for data measured using a phantom with $[Hb_{Total}]=28$ μM and $\mu_s'(750nm)=7.5$ cm^{-1}, leading to $k_1= 14.41$ and $k_2= 37.97$ with $R^2=0.90$. Wavelengths of 500-850 nm were considered. b) Linear fit for data measured using a phantom with $[Hb_{Total}]=28$ μM and $\mu_s'(750nm)=7.5$ cm^{-1}, giving rise to $k_1= 11.56$ and $k_2= 36.67$ with $R^2=0.99$. Wavelengths at 560-850 nm were considered.

2.6.1 Non-monotonic curves of $\mu_s(\lambda)/R_p(\lambda)$ vs $\mu_a(\lambda)$

Linear fits with a linear, least squares regression line are used to determine constants k_1 and k_2 from $\mu_s'(\lambda)/R_p(\lambda)$ vs $\mu_a(\lambda)$ plot. Figure 2.2 shows a non-monotonic trend between the two quantities. The reason for this behavior of the plot can be attributed to the non-monotonic behavior of hemoglobin absorption between the wavelengths of 500-560 nm. As an example, Figure 2.8(a) shows a $\mu_s'(\lambda)/R_p(\lambda)$ vs $\mu_a(\lambda)$ plot including the data at wavelengths 500-560 nm. The non-monotonic behavior is clearly apparent. In Figure 2.8(b), the data from wavelengths of 500-560 nm was excluded, and the non-monotonic behavior is significantly removed.
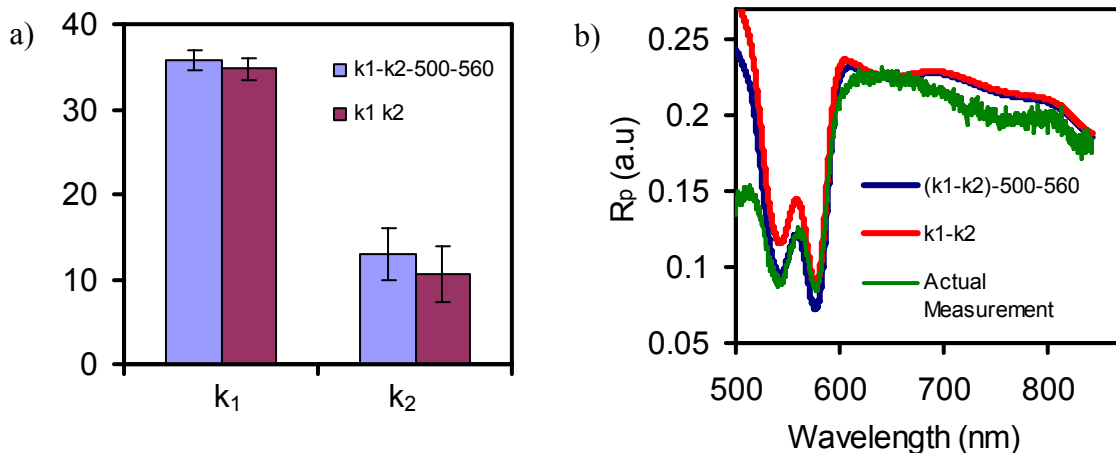
Figure 2.9 a) Constants k_1 and k_2 calculated by including and excluding data between 500-560 nm for the 7-fiber-array probe. b) Comparisons of reflectance spectra calculated by excluding and including the data from wavelengths of 500-560 nm. The green plot indicates the measured reflectance from the optical probe. The blue plot indicates the reflectance spectrum calculated using information from 500-560 nm. The red plot indicates the reflectance excluding data from 500-560 nm.

Investigations were made to study the effect of omission of this wavelength range on the quantification of reflectance spectra. The values of k_1 and k_2 were recalculated for the 7-fiber-array probe in all cases with and without the data from the wavelengths of 500-560 nm. A t-test was done to compare if including and excluding data from wavelengths of 500-560 nm could make significant difference when quantifying k_1 and k_2. The results show that both k_1 ($p=0.66$) and k_2 ($p=0.28$) did not exhibit significant differences between the two cases. The mean and standard deviations for k_1 and k_2 are shown in Figure 2.9(a). The reason for this behavior of the plot can be attributed to non-monotonic nature of spectra (500-600 nm) of hemoglobin absorption [29]. Figure 2.9(b) compares spectra calculated by excluding and including the data from wavelengths of 500-560 nm that caused non-monotonic behavior shown in Figure 2.8(a). Visual inspection on the spectra calculated by either including or excluding the

42

data at 500-560 nm did not show much difference. Further comparison between the two cases was done by calculating Pearson correlation coefficient (R) [39] between the calculated spectra with k_1 and k_2 that were obtained from excluding and including data at 500-560 nm (e.g., Figure 2.9(b)). Although the values of R^2 were totally acceptable in both cases, R^2 values including the data taken from 500-560 nm were better, as listed in Table 2.9. The two values of R^2 were significantly different. (p=0.02). This seems to suggest that in spite of non-monotonic plot as seen in Figure 2.8(a) the values of k_1 and k_2 determined by including information from 500-560 nm represent the actual measurement of reflectance better (in terms of R). Actually, Figure 2.9(b) illustrates clearly that the calculated curve obtained with inclusion of 500-560 nm data fits better to the actual measurement in the 520-580 nm region (blue curve in Figure 2.9(b)).

Table 2.9 Mean and standard deviations of R^2 values with and without data from 500-560 nm.

	R^2
With data taken at 500-560 nm	0.92±0.03
Without data taken at 500-560 nm	0.88±0.05

2.6.2 Sensitivity of reflectance with respect to k_1 and k_2

Following a similar approach as Kumar and Schmitt [42], one can define the sensitivity of the reflectance, $R_p(\lambda)$ to k_1 and to k_2 ($S_{k_1}(\lambda)$ and $S_{k_2}(\lambda)$) as $S_{k_1} = -\dfrac{\partial(\ln R_p)}{\partial k_1}$

and $S_{k_2} = -\dfrac{\partial(\ln R_p)}{\partial k_2}$, respectively [28]. After a few mathematical simplifications from Equation (2.4), we arrive at

$$S_{k_1}(\lambda) = -\frac{1}{R_p(\lambda)}\frac{\partial R_p(\lambda)}{\partial k_1} = -\frac{1}{k_1 + k_2\mu_a(\lambda)} \qquad (2.22)$$

$$S_{k_2}(\lambda) = -\frac{1}{R_p(\lambda)}\frac{\partial R_p(\lambda)}{\partial k_1} = \frac{\mu_a(\lambda)}{k_1 + k_2\mu_a(\lambda)} \qquad (2.23)$$

$S_{k_1}(\lambda)$ and $S_{k_2}(\lambda)$ represent sensitivity of measured reflectance to parameters k_1 and k_2 at

a particular wavelength λ, respectively.
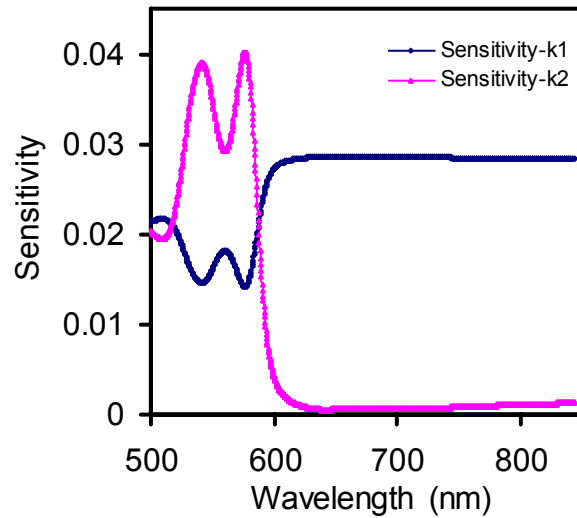
Figure 2.10 a) Sensitivity of parameters k_1 and k_2 in the visible and NIR
wavelength range. The reflectance measured by an optical probe is more sensitive
to value of k_2 in the visible wavelength range and more sensitive to k_1 in the NIR
wavelength range.

Figure 2.10 shows changes in respective sensitivities with respect to

wavelength. Oxygen saturation has been assumed to be 90% to calculate sensitivities.

Sensitivity of k_2 is higher than that of k_1 in the visible wavelength range (500-600nm)

where as in the NIR range (600-850nm) sensitivity to k_1 is higher and remains almost

constant. Looking at the sensitivity of k_1 and k_2, it can be thought that value of k_2 is

predominantly determined by reflectance in the visible range and that of k_1 by reflectance in the NIR range. This sensitivity analysis indicates that k_2 is more sensitive to changes in μ_a which is orders of magnitude higher in the visible wavelength range. In the NIR range the reflectance depends predominantly on μ_s' [31] . k_1 is more sensitive to changes in NIR wavelength range and in turn sensitive to changes in μ_s'. In the NIR wavelength range it can be seen that sensitivity of k_2 is orders of magnitude lower.

2.6.3 Scattering coefficients and mean particle size

Several previous investigations from our group and others in the field have focused on quantifying particle sizes based on spectra of reduced scattering coefficients [43-45]. Limitations and non-uniqueness in the quantification of particle sizes were shown by our group [43]. This publication used simulations from Mie theory and data from latex microsphere suspensions which indicated non-uniqueness in slope of reflectance spectra with respect to sizes of microspheres. The problem gets more complicated in real tissues. Presence of several refractive indices at various membrane interfaces in different cell organelles [46] further complicates the problem.

The mathematical model (Equation 2.3) adapted in this investigation to model wavelength dependence of scattering coefficients does not account for the change in refractive indices, which plays a major role in the determination of scattering coefficients and its wavelength dependence. Improving the model for reduced scattering coefficients as a function of incident wavelength and refractive index ratios of boundaries will improve the quantification of mean particle sizes and reduce the uncertainty in their quantifications. Particular attention will be necessary for mean sizes

greater than 0.2μm which are similar to sizes seen in normal tissues [45]. This uncertainty in quantification of particle sizes may lead to large deviations in particle sizes and quantified scattering coefficients.

2.7 Conclusions

This chapter described the use of recently developed analytical model [22] for diffuse reflectance at short source-detector separations. Constants k_1 and k_2 were determined through experimental calibrations with blood-intralipid phantoms for three thin fiber optical probes with short source-detector separations: one 7-fiber-array probe and two single source-detector fibers. The calibrated k_1 and k_2 for the two single source-detector probes were utilized in my in vivo pain study using rats to quantify appreciate hemoglobin concentrations and light scattering coefficients of the animals in response to farmalin-induced pain (See Chapter 3).

k_1 and k_2 were determined at integration times of 50, 75 and 100 ms for the 7-fiber array probe. The values of constants k_1 and k_2 determined at these three integration times did not show significant differences at 0.05 level of significance, indicating that the determined k_1 and k_2 are independent of integration time.

Sensitivity of reflectance with respect to k_1 and k_2 was investigated. k_1 was found to be more sensitive to reflectance in the $600 - 850$ nm range and hence to μ_s', as described in Section 2.6.2. On the other hand, k_2 was found to be more sensitive to reflectance in wavelength range of 500-600 nm and hence more sensitive to changes in μ_a, as mentioned in Section 2.6.2.

An ant colony optimization algorithm was used to quantify concentrations of hemoglobin derivatives and reduced scattering coefficients. The maximum error in quantification of hemoglobin derivative concentrations was less than 15% (Table 2.7). The calculated reduced scattering coefficients were within ± 1 cm^{-1} from the measured values given by the ISS Oximeter (Table 2.6). Overall all concentrations and scattering coefficients calculated were within error ranges of the instrument taken as gold standard.

The probes calibrated can directly be used to quantify optical properties and concentrations of hemoglobin derivatives. The constants calculated are valid for the life of the optical probe and measurement system. As an example, the model and developed algorithms to quantify hemoglobin derivative concentrations and scattering coefficients are applied to quantify hemodynamic changes during formalin-induced pain behaviors and to be described in detail in the following chapter.

CHAPTER 3

NON-INVASIVE OPTICAL MONITORING OF PERIPHERAL HEMODYNAMIC
CHANGES DURING FORMALIN INDUCED PAIN RESPONSE

Changes in peripheral circulation occur in response to noxious peripheral stimulations. Formalin pain model, a well characterized model, enables assessments of animal response to moderate and continuous pain generated by tissue injury. Characterization of peripheral blood flow changes in previous investigations was limited to quantification of relative changes. In this study, changes in peripheral circulation as a result of noxious stimulations are quantified with spectral alterations in NIRS. The quantifications are not limited to change in relative perfusion units, rather elicit changes in oxygen saturations, increase of oxygenated and total hemoglobin concentrations. Reflectance signals were measured simultaneously on hind paws during formalin-induced pain when and after 50 μl of formalin was injected subcutaneously into one hind paw of the anesthetized rat. A portable spectrometer was used to monitor the site and the temporal evolution of signal changes during the development of formalin-induced hyperalgesia. Applying a recently developed mathematical model [22], significant increases in blood volume and oxygenated hemoglobin concentrations induced by the noxious stimulation were detected in the ipsilateral side, but no significant changes in light scattering were observed. This study aptly demonstrates that NIRS is a real-time, non-invasive method to characterize and quantify temporal changes

48

in blood circulation during formalin induced pain behaviors, potentially useful in understanding different pain mechanisms and quantifying peripheral blood volume changes in response to pain.

<u>3.1 Background</u>

The formalin pain model, which is predominantly used with rats and mice, involves moderate, persistent pain generated by injured tissue. In this way it differs from most traditional tests of nociception, such as tail-flick test, flinch-jump test, hot-plate test, and pinch test, which rely upon brief stimuli of threshold intensity. The formalin pain model enables assessments of animal response to moderate, continuous pain generated by tissue injury. It is believed that the test provides a more valid model for clinical pain than the tests with phasic mechanical or thermal stimuli. A formalin injection may induce a state that is a better approximation to clinical conditions than what is possible with an acute cutaneous stimulation as in threshold or reflex tests [47].

This pain model is evoked by a subcutaneous injection of dilute formalin in the paws. The ensuing stimulation of nociceptors results in a biphasic pattern of `pain' behavior. The first phase (Phase 1) lasts for about 5 min and is presumed to be a result from ongoing stimulation of nociceptors [48]. Experiments indicate that formalin predominantly evokes activity in C fibers, and not in Aδ afferents [49]. After 10 minutes of quiescent period (interphase), a second phase (Phase 2) of behavior lasts for about 45 minutes. Phase 2 is generated by ongoing stimulation of nociceptors, by inflammatory mediators, and/or by a first phase-induced spinal cord (functional changes in the dorsal horn) hyper-excitability, also termed central sensitization [50].

Experimental results have suggested that substance P and bradykinin participate in the early phase or phase 1, while histamine, serotonin, prostaglandins and bradykinin play a role in the late phase [47].

The next section gives background information about pain mechanisms, such as its perception, conduction through neuronal pathways, chemical mediation of pain responses and neurogenic inflammation. The next section attempts to explain mechanisms that lead to increase in blood flow in response to peripheral inflammation and pain. The role of axonal reflexes and dorsal root reflexes in the pain response has been elicited. The contribution of each of them to pain response has been mentioned.

3.1.1 Perception of pain

Pain is an unpleasant sensory and emotional experience associated with actual or potential tissue damage. Even though pain is mediated by nervous system, distinction between pain and the neural mechanisms of nociception – the response to actual or perceived tissue damage- is critical both experimentally and clinically. Certain tissues are equipped with specialized receptors, known as nociceptors. Nociceptors are activated by noxious insults to peripheral tissues. Nociception will not necessarily lead to the experience of pain. This is another example of the fact that perception is a product of brain abstraction of sensory input [51].

3.1.2 Classification of pain

Pain can be classified into two broad classes, nociceptive and neuropathic. Nociceptive pain results from direct activation of nociceptors in the skin or soft tissue in response to tissue injuries and usually arises from accompanying inflammation.

Neuropathic pain is a result of direct injury to nerves in the peripheral or central nervous system.

3.1.3 Nociceptors

Noxious stimulus to subcutaneous tissues activates several classes of nociceptor terminals, peripheral endings of primary sensory neurons whose cell bodies are located in the dorsal root ganglia and trigeminal ganglia. Thermal nociceptors are stimulated by extreme temperatures. They are comprised of thinly myelinated Aδ fibers that transmit at 5-30 m/sec. Mechanical nociceptors are activated by pressure applied to the skin and similar conduction speeds. Polymodal nociceptors are activated by high intensity mechanical, thermal or chemical stimuli such as formalin. These nociceptors have small diameter non-myelinated C fibers, having slow conduction speeds of 1.0 m/sec.

These three classes of nociceptors are widely distributed in skin and deep soft tissues and often work together. Taking an example of simple 'Thumb hit', 'first' sharp pain is felt immediately, followed by a prolonged aching. This first sharp pain is transmitted by Aδ fibers and the subsequent slow dull pain is transmitted by C fibers that are activated by polymodal nociceptors. The mechanisms by which noxious stimuli depolarize free sensory endings are still a matter of debate. In pathological situations, activation of nociceptors can lead to two types of abnormal pain states, hyperalgesia – a state in which subjects exhibit excessive response to noxious stimuli and allodynia- a state in which pain results from normally innocuous stimuli.

3.1.4 Conduction of nociception

Nociceptive afferent fibers terminate mainly in the dorsal horn of the spinal cord. Based on cytological features, the dorsal horn can be divided into six classes. Distinct functions are conveyed by different classes of primary afferent neurons terminating in the dorsal horn. Hence, there is a close correlation between functional and anatomical organization of the dorsal horn. Nociceptive neurons are located in the superficial dorsal horn in the marginal layer and substantia gelatinosa. Most of these neurons in the marginal layer respond exclusively to noxious stimulation and project to higher brain centers. Nociceptive information is carried from the spinal cord to brain through five major ascending pathways: spinothalamic, spinorecticular, spinomesencephalic, cervicothalamic and spinohypothlamic tracts [51].

3.1.5 Origins of hyperalgesia

Noxious stimuli when applied repeatedly, cause proximally located nociceptors that were unresponsive to become responsive. This phenomenon is termed as sensitization. Axonal reflexes are thought to be responsible for this mechanism and are similar to the spread of vasodilatation in the proximity of cutaneous injury [52]. This sensitization is a result of variety of chemical mediations by chemicals released from damaged cells and tissues in the vicinity of injury or inflammation. Chemical mediators that are released are primarily bradykinin, prostaglandins, leukotrienes, acetylcholine, serotonin and substance P. Each of them is released from a different group of cells. All of them act to lower the threshold of activation of nociceptors. Histamine released from damaged mast cells, activates the polymodal nociceptors. Bradykinin results in the

activation of Aδ and C fibers and also increases the synthesis of prostaglandins. Regulation of chemical environment occurs through the synthesis of chemical mediators in the cell body of neurons, transportation to the peripheral terminal for storage and release upon depolarization of the terminal. A cutaneous injury results in the release of neuroactive peptides- substance P and calcitonin gene related peptide (CGRP) as shown in Figure 3.1[51]. These peptides contribute to the spread of edema by acting directly on venules to produce vasodilatation. Additionally, they mediate the release of histamine from mast cells which results in lowering of activation threshold for nociceptors.
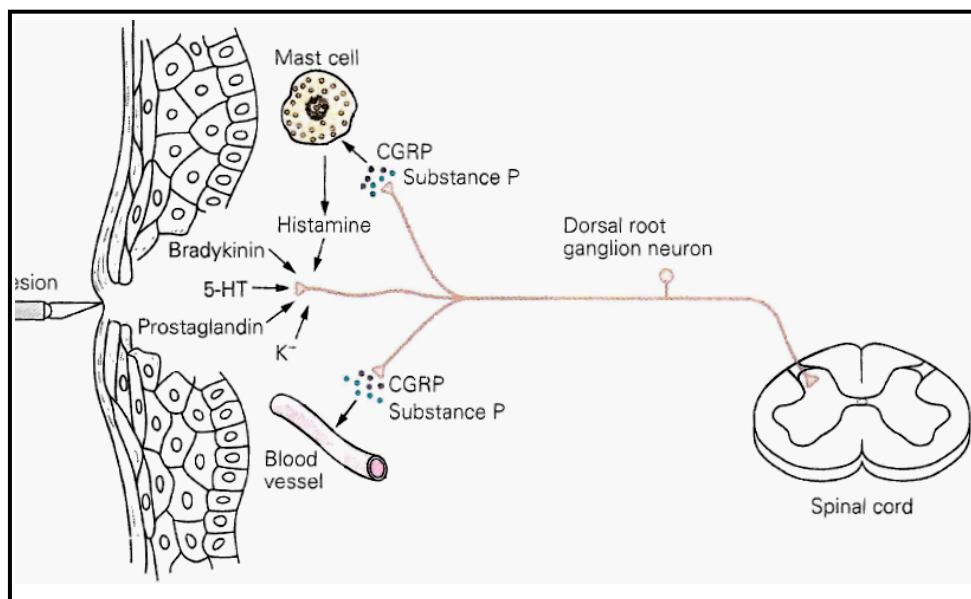
Figure 3.1 Role of dorsal root ganglion cells: Nerve endings of ganglion cells release chemical mediators, such as prostaglandins (substance P) and CGRP. Substance P acts on the mast cells to mediate the release of histamine. Substance P causes plasma extravasation and CGRP causes peripheral dilation of blood vessels. (Courtesy: Principles of Neural Science by Kandel, Schwartz, Jessel).

The cardinal signs of inflammation are redness (rubor), heat (calor), swelling (tumor) and pain (dolor). Heat and redness are produced as a result of dilation of

peripheral blood vessels and swelling is a consequence of plasma extravasation. CGRP causes dilation of peripheral blood vessels [53]; resulting edema causes further release of bradykinin. Vasadilatory action of CGRP is due to the dilation of arterioles. Extravasation is a process in which proteins and cells leak out of post capillary venules with fluid. This occurs due to an increase in spaces between endothelial cells due to endothelial cell contraction caused by substance P [54]. This information is mediated primarily by neuronal activity and referred to as neurogenic inflammation.

3.1.6 Dorsal root reflexes

Inflammation might lead to an increase in dorsal root reflexes triggered by peripheral stimulation by several mechanisms. Inflammation causes upregulation of GABAergic mechanisms in the dorsal horn [55]. Increased release of GABA from GABAergic interneurons of the dorsal horn results in more primary afferent depolarization (PAD) and triggering of secondary dorsal root reflexes. Another mechanism responsible would be increased activity of Na^+-K^+-Cl^- co-transporter. This co-transporter is regulated by second messenger systems that are controlled by a variety of neurotransmitters, hormones and growth factors. Second messenger systems control the equilibrium potential and the size of PAD and the strength of presynaptic inhibition by changing the activity of the transporters [56].

3.1.7 Overcoming limitations in previous investigations

Several investigations have been made to study and characterize blood flow changes in response to formalin induced pain [57, 58]. Laser Doppler flow (LDF) imaging has been used to characterize changes in blood flow [50, 59, 60]. Although

LDF produces images of the paw to indicate the specific site of increase in perfusion, it has certain limitations. The LDF images are not quantitative and are limited to relative changes of perfusion from a baseline to a transient condition. It is not sensitive to changes in oxygen saturation in microcirculation. Additionally, the technique is limited in its sensitivity to blood hemoglobin related changes and cannot address changes in optical scattering. In the course of my doctoral research, I have developed and validated a simple, low-cost, broadband, optical sensing methodology using a thin optical probe to obtain tissue reflectance, as given in Chapter 2. Such a simple and economical approach, which uses a recently developed mathematical model [22] to quantify concentrations of hemoglobin derivatives, other non-oxygen dependent tissue absorbers and reduced scattering coefficients, may be a good tool to be used for monitoring peripheral hemodynamic changes to formalin induced pain response. The rest of this chapter will focus on the direction and demonstrate that the optical tissue reflectance using a thin fiber probe is a valuable monitoring means to study peripheral noxious stimulation..

3.2 Instrumentation

The experimental setup used for measurements of reflectance spectra is shown in Figure 3.2. A multi-channel (8 channels) CCD spectrometer (Ocean Optics, Dunedin, FL, USA), capable of collecting spectra in the 350-1050 nm range, was used for diffuse reflectance measurements. Light was delivered and collected by means of a fiber optic probe (TechEn Inc, Boston, MA) which consisted of bifurcated fiber bundles for light delivery and collection. There were two fiber probes used, and each of the two fiber

probes was placed in light contact with each of the two hind paws. The two probes were a few mm in diameter for the probe tips. The probes were placed such that there was a good contact between the skin and probe surface but not too much pressure to cause pressing or indentation of skin on the hind paw. Excessive pressing of skin can result in local occlusion of blood flow to skin regions. Flat probes were used to ensure proper contact and free of movements during injection of formalin. The arrangement becomes apparent from Figure 3.2.
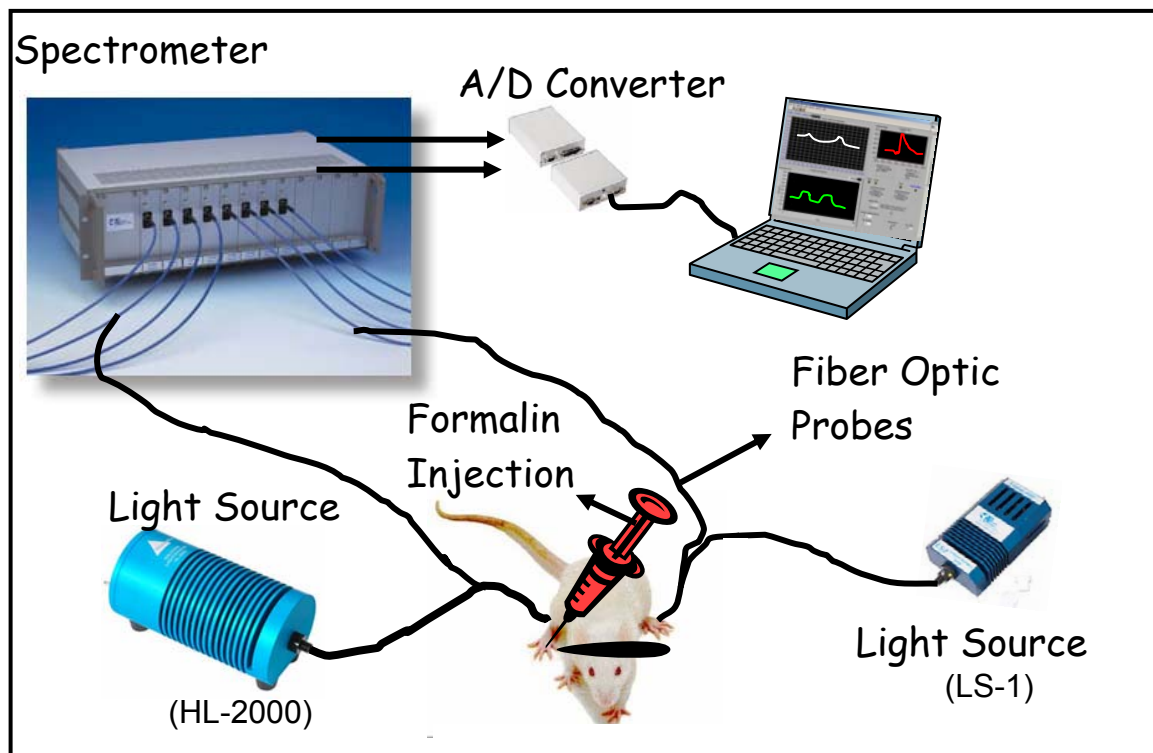
Figure 3.2 Schematic of experimental setup for investigating changes of hemodynamics during formalin induced pain behaviors. The set up shows the multi-channel spectrometer, light sources and laptop for data acquisitions. Two of bifurcated optical fiber probes were used; for each probe, each branch of the bifurcated cables was for light delivery and collection. The source-detector separation should be in 100-400 microns.

Illumination was provided by a tungsten-halogen light source (HL-2000, Ocean Optics, Dunedin, FL, USA) on one hind paw, and on the other paw with another light source (LS-1, Ocean Optics, Dunedin, FL, USA). Neutral density filters (Thor Labs Inc, www.thorlabs.com) were used to achieve extension of dynamic ranges to prevent saturation of the CCD detectors. Changes in optical densities of filters were incorporated into calculations. All spectra were referenced to a reflectance calibration standard (WS-1, Ocean Optics, Dunedin, FL). Typical integration time for spectral collection was 10-15 ms depending upon the specific animal. Signal to noise ratio were typically greater than 100:1 (Ratios of measured intensity to dark signal intensity).

3.3 Animal preparation and experimental protocols

The animal preparation and animal measurement were carried by Dr. Yuanbo Peng's group from the Department of Psychology at UT Arlington. My major responsibility for this research project was to setup the instrument, assure good contacts between the probes and animals, acquire data continuously during and after the formalin injection, perform data analysis, and interpret the data.

Adult male Sprague Dawley rats were initially anesthetized with sodium pentobarbital (50 mg/ kg, i.p.). A catheter was placed into the jugular vein for continuous administration of anesthetic. Controlled ventilation was administered through a tracheal cannula following tracheostomy. Continuous anesthesia was accomplished by administering a mixture of 1 ml (50 mg) of sodium pentobarbital in 9 ml 0.9% NaCl at a rate of 1.2 ml per hour (i.e. 6 mg/h). Musculature paralysis was achieved by an intravenous placing of a continuous injection of 0.5 ml pancuronium

bromide every 2 hours. The end tidal CO_2 was maintained at around 30 mmHg. The animal's body temperature was maintained at 37.8°C by a feedback controlled electric heating blanket. Schematic diagrams depict experimental setup (Figure 3.2) and arrangements of optical probes for the study. Rat was held in a stereotaxic frame to prevent movement during recording. The probes were placed on the paw so as to facilitate the injection of formalin into the plantar surface of the hind paw without any movement of probe. The probes were placed on the bare surface (hairless) just above the digits. Adequate support was provided for the paws to facilitate placements of the optical probes. We tried to minimize any artifacts due to movement of the probes relative to the paw skin surface.

3.3.1 Baseline measurements

After completing all preliminary animal preparations, baseline measurements of reflectance spectra were made for five minutes. The measurements were made only after the eye blink and tail pinch responses were eliminated. Measurements were made with a sampling time of 1 second. All measurements were made in dark surroundings to eliminate ambient light contamination. To eliminate any contribution of ambient light, dark signals were measured and subtracted in post data analysis. Vital signs were monitored throughout the experiment [61].

3.3.2 Formalin induced pain response

After five minutes of baseline measurements, 50µl of formalin was injected subcutaneously into the right hind paw of the anesthetized rat. The injection was into the plantar surface of the hind paw. Care was taken to ensure that there was no

movement of optical probes on either paw. Measurements of reflectance spectra were made continuously till one hour after the injection of formalin. Thereafter the animal was sacrificed by an overdose of anesthesia.

All procedures used in this study were approved by the Animal Care and Use Committee of UTA and followed guidelines for treatment of animals of the International Association for the Study of Pain [62].

3.4 Theory

Melanin, like skin pigment, and hemoglobin derivatives, namely oxygenated hemoglobin and deoxygenated hemoglobin, have been assumed as significant absorbers in the visible and NIR wavelength ranges. The selection of tissue chromophores of significant absorption are based on their specific absorption coefficients obtained from literature [29, 63, 64].

The spectral dependence of absorption coefficient (μ_a) for blood perfused tissues is described in Equation (2.2) in Chapter 2. In my computations, 80% of water has been assumed based on data from Woodward et al [65]. The approximation of spectral dependence of reduced scattering coefficients (μ_s') is described in Equation (2.3) in Chapter 2.

After computing μ_s' and μ_a using the developed methods described in Chapter 2, reflectance as a function of wavelength in the spectrum is given by a recently developed mathematical model [22], which relates μ_s' and μ_a to the measured reflectance $R_p(\lambda)$ in Equation (2.1). In this equation, k_1 and k_2 are parameters depending on geometrical characteristics of the optical probe and are determined experimentally using tissue like

blood-intralipid phantoms (see details in Chapter 2). The set of k_1 and k_2 for the optical probes used in this study have been tabulated in Table 2.5 in the previous chapter. [HbO], [Hb] and [Hb_{Total}] and scattering parameters can be determined from Equation (2.1) after k_1 and k_2 are fully calibrated. Indeed, this chapter focuses on an application of a new methodology that I have developed and validated, as described in detail in Chapter 2.

3.5 Results

Temporal changes in concentration of hemoglobin derivatives and reduced scattering coefficients during formalin induced pain responses were quantified. Reduced scattering coefficients and effective scatterer size give information about change in structure in response to stimuli. Measurements were made on both paws with optical probes with short source-detector separation. Injection of 50μL formalin was made on the right paw after baseline measurement of 5 minutes. Experimental protocol and time points of formalin injections have been listed in Table 3.1 Time points of formalin injections varied from subject to subject due to practical issues. If movements of the probe were suspected during the baseline measurements, the baseline measurements were restarted and measured again. In all subjects, measurements were made until one hour after the injection of formalin on hind paw.

Table 3.1 Experimental protocol for formalin induced pain response. The formalin injection was made after a baseline measurement of five minutes. All units are in seconds. Zero indicates start of measurement. Spectral measurements are made for an hour after formalin injection.

Subject	Baseline (sec)		Formalin Injection (sec)		Baseline period for comparison (sec)	Response period for comparisons(sec)
	Start	End	Start	End		
1	0	300	300	350	0-300	600-900
2	0	1650	1650	1675	1350-1650	1950-2250
3	0	300	300	350	0-300	600-900
4	0	700	700	750	400-700	1000-1300
5	0	750	750	800	450-750	1050-1350

3.5.1 Temporal changes in spectra during pain response

Raw spectra measured on the ipsilateral and contralateral sides are compared on various time points before and after the injection of formalin on the hind paws of a representative rat. The spectra from ipsilateral and contralateral sides are shown in Figures 3.3(a) and 3.3(b), respectively. Spectra measured on the contralateral side (Figure 3.3(b)) change marginally before and after the injection of formalin. On the ipsilateral side (Figure 3.3(a)), there was an overall and continuous decrease in the spectral profiles after the injection of formalin. [Hb], [HbO], [Hb_{Total}], μ_s' and effective scatterer size were further determined from the spectra using the algorithms I developed, and the respective data are given in the next sub-section.
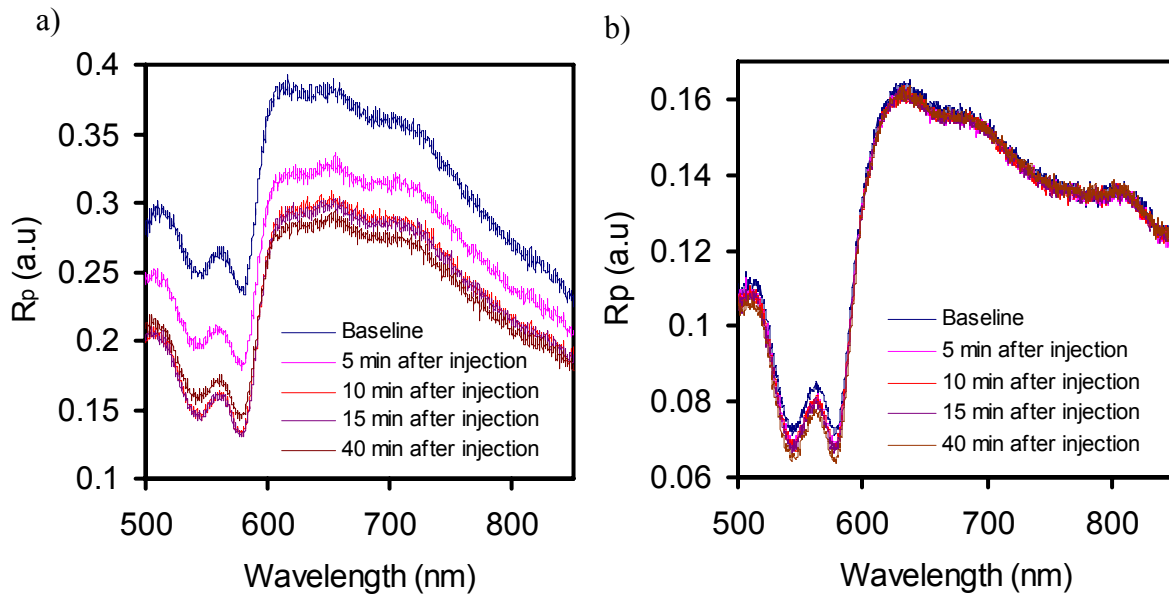
Figure 3.3 Temporal changes in measured spectra (500-850nm) on the ipsilateral (a) and contralateral (b) sides as a result of formalin injection.

3.5.2 Temporal changes in [Hb], [HbO] and [Hb$_{Total}$]

The temporal changes in [Hb], [HbO] and [Hb$_{Total}$] on the ipsilateral and contralateral sides during the pain response are depicted in Figure 3.4. All concentrations are absolute concentrations in μM. Two colored bars in Figure 3.4 indicate two temporal regions chosen for a 5-minute baseline starting 5 minutes before the injection of formalin and 5-minute response period starting 5 minutes after the injection of formalin. [Hb], [HbO] and [Hb$_{Total}$] are compared for differences between these two regions. Actual time points selected as baseline and response periods are indicated Table 3.1. Average values in both of the selected periods are compared for differences using 2 way ANOVA (Section 3.5.3).
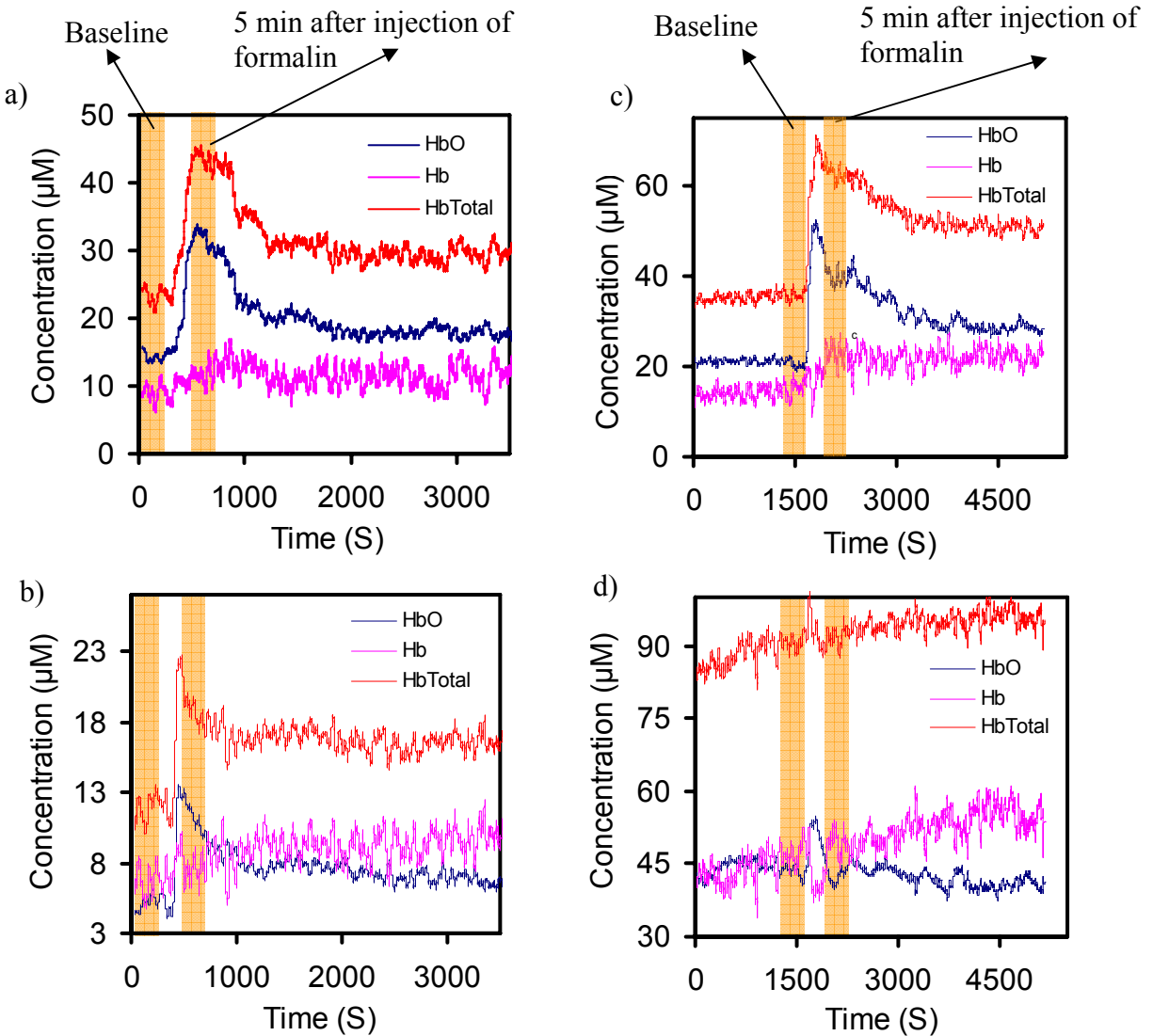
Figure 3.4 Temporal changes in hemodynamic parameters as a result of injection of formalin measured by an optical thin probe. The time points of injection on each subject have been tabulated in Table 3.1. Representative traces are shown for two animals. All concentrations are in µM. (a) Subject-1 on ipsilateral side, (b) Subject-1 on contralateral side, (c) Subject-2 on ipsilateral side, (d) Subject-2 on contralateral side.

$[Hb_{Total}]$ and $[HbO]$ on the ipsilateral side (Figure 3.4(a) and Figure 3.4(c))

followed very similar trends across subjects (n=5). The general trends observed are that

both of $[Hb_{Total}]$ and $[HbO]$ remained constant with minimal variations during the

baseline or absence of stimulus, had a rapid and sudden increase at the instant of injection, followed by a gradual decrease, and settled at an elevated levels. On the contralateral side, the temporal changes of $[Hb_{Total}]$ and $[HbO]$ showed significant inter-subject variations, as seen from the two representative samples (Figure 3.4(b) and Figure 3.4(d)). In some subjects, concentrations of $[HbO]$ and $[Hb_{Total}]$ showed trends very similar to those on the ipsilateral sides, in that they increased immediately after the injection and remained elevated throughout the measurement. In some cases, they did not have any acute changes, irrespective of the formalin injection. Overall, values of $[HbO]$ and $[Hb_{Total}]$ on contralateral side did not show any consistent pattern of behavior in a group of 5 rats (n=5).
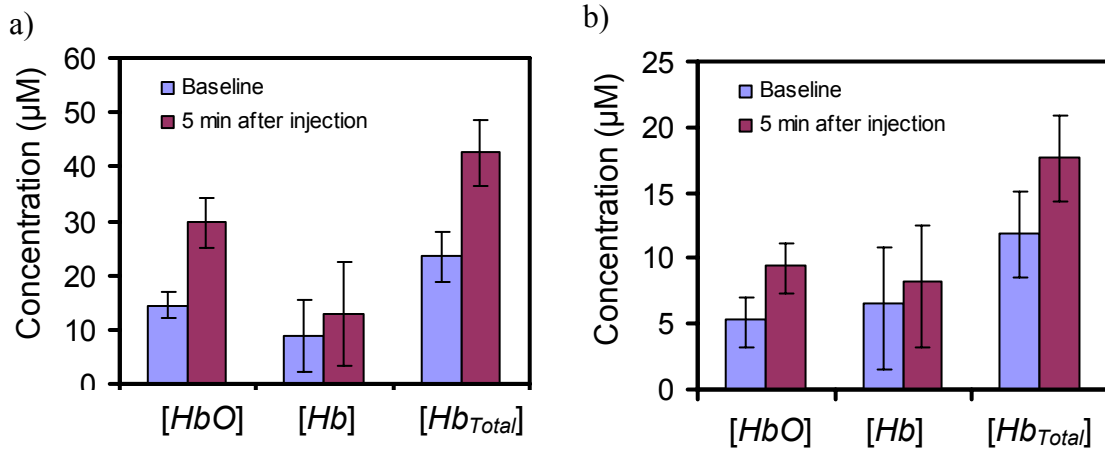
Figure 3.5 Comparisons of hemodynamic parameters for Rat-1 given in Table 3.2 for (a) ipsilateral side and (b) contralateral side. All values of $[Hb]$, $[HbO]$ and $[Hb_{Total}]$ are in μM and compared before and five minutes after injection of formalin in right paw.

Figure 3.5 compares values of $[HbO]$, $[Hb_{Total}]$ and $[Hb]$ for a representative case (Rat-1 in Table 3.2) on the ipsilateral (Figure 3.5(a)) and contralateral (Figure 3.5(b)) sides. The concentrations determined during the baseline measurements and those

measured 5 minutes after the injection of formalin were compared for differences. Conducting repeated t-test to test for differences between the parameters ([Hb], [HbO] and [Hb_{Total}]) measured during the baseline and response periods may artificially amplify the significance. To avoid this artificial amplification of significance a two-way ANOVA was done to compare absolute concentrations on each paw before and after the injections of formalin [39]. In this representative case, [HbO], [Hb_{Total}] and [Hb] showed significant increases on the ipsilateral sides ($p<0.001$). In this representative case, [HbO], [Hb_{Total}] and [Hb] showed significant increases on the contralateral side ($p<0.001$), showing similar responses to the ipsilateral side. However, the response pattern on the contralateral side was not consistent from subject to subject in the group of five subjects (n=5). The p values for all cases and parameters are tabulated in Table 3.2.

3.5.3 Two way ANOVA

A two way ANOVA was conducted to test for differences in hemodynamic parameters and scattering coefficients before and after the administration of formalin injection. Time period starting 5 minutes before the injection of formalin to the point of injection was chosen as the baseline. The period for 'after injection' was between 5 and 10 minutes after the injection. A test for significant differences between before and after injection of formalin was conducted. The results (SPSS outputs) for each case are attached in Appendix B. The results in terms of p values are tabulated in Table 3.2.

Table 3.2 *p* values to determine significant differences: Differences between baseline period (before injection of formalin) and five minutes after the injection of formalin. Two-way ANOVA was done to compare absolute concentrations on each paw before and after the injections of formalin.

	$[Hb]$	$[HbO]$	$[Hb_{Total}]$	Oxygen Sat	Melanin	μ_s' (500 nm)	Scatterer-size
Contralateral							
Rat-1	0.05 >	0.001 >	0.001 >	0.001 >	0.981	0.678	0.858
Rat-2	0.001>	0.104	0.082	0.05<	0.938	0.951	0.973
Rat-3	0.001 <	0.001<	0.001 <	0.01>	0.971	0.674	0.987
Rat-4	0.349	0.078	0.05 >	0.05<	0.990	0.970	0.999
Rat-5	0.001 <	0.001 <	0.001 <	0.001 >	0.804	0.001 <	0.647
Ipsilateral							
Rat-1	0.001 >	0.001 >	0.001 >	0.361	0.990	0.745	0.91
Rat-2	0.001 >	0.001 >	0.001 >	0.001 >	0.989	0.217	0.941
Rat-3	0.001 >	0.001 >	0.001 >	0.001 >	0.979	0.877	0.880
Rat-4	0.264	0.001 >	0.001 >	0.001 >	0.896	0.001>	0.911
Rat-5	0.001 >	0.001 >	0.001 >	0.001 >	0.983	0.001 >	0.904

3.5.4 Oxygen saturation and scattering parameters (μ_s' (500 nm) and effective scatterer size)

Oxygen saturation is another important parameter that reflects metabolic activity in response to stimuli. It is the fraction of $[HbO]$ in $[Hb_{Total}]$. Like other hemodynamic parameters, oxygen saturations determined on the ipsilateral and contralateral side exhibited a lot of inter-subject variations. In general, oxygen saturation increased after formalin injections in most cases and decreased immediately (within five minutes). The variation of oxygen saturation did not show any particular trend with injection of formalin (Table 3.2).

The temporal changes in scattering parameters, i.e., μ_s' (500 nm) and effective scatterer size, did not exhibit any particular consistent trends across subjects on either

side. Scattering parameters were compared between the baseline and five minutes after the injection of formalin. The corresponding p values have been tabulated in Table 3.2.
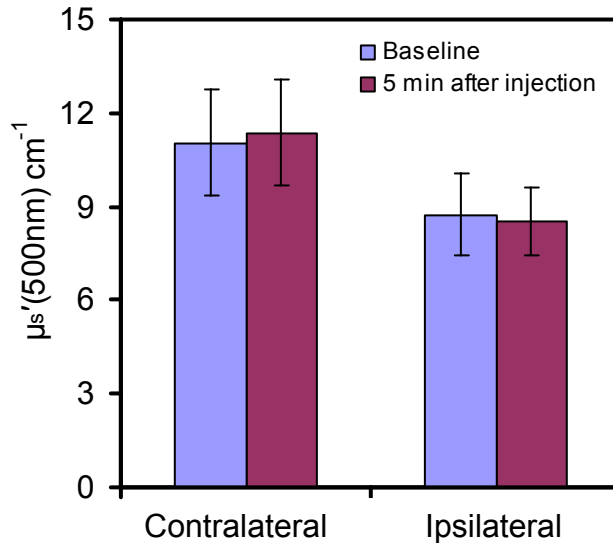
Figure 3.6 Comparisons of μ_s' (500 nm) for Rat-1 given in Table 3.2 for ipsilateral side and contralateral side. All values of μ_s' (500 nm) are in cm^{-1} and compared before and five minutes after injection of formalin in right paw.

Figure 3.6 compares values of μ_s' (500 nm) for a representative case (Rat-1 in Table 3.2) on the ipsilateral and contralateral sides. The μ_s' (500 nm) values determined during the baseline measurements and those measured 5 minutes after the injection of formalin were compared for differences: they did not show significant differences on ipsilateral (p=0.257) and contralateral sides (p= 0.678) of the paws.

3.5.5 Averaged hemodynamic parameters across 5 subjects

All above analysis were performed on individual spectrum basis, and the comparisons of [Hb_{Total}], [HbO] and [Hb] and scattering coefficients were based on the averaged respective values over two selected time periods (before and 5 minutes after

the injection). In this sub-section, all temporal profiles of [Hb_{Total}], [HbO] and [Hb] are normalized to their respective baseline values to remove the effect of their individual magnitudes before comparison. This facilitates comparison of measured responses to formalin injection across 5 subjects. This is done to investigate whether and where (in time period) the differences in parameters are significant between the ipsilateral and the contralateral side as a group. To get uniformity for comparison, some simplifications with regards to data was made. 300 seconds (5 minutes) prior to the injection of formalin was used as baseline. Measurements made up to an hour after the injection was considered.

A t-test (2-paired, unequal variance) was made to test for significant differences at each time instant. Value of $p<0.05$ indicates that the differences were significant at the particular time instant. The $p<0.05$ value represents the significance level, at which differences are significant between ipsilateral and contralateral sides at every time instant. The averages (n=5) of normalized [Hb_{Total}] and [HbO] on ipsilateral and contralateral sides are shown in Figures 3.7(a) and 3.7(c), respectively. The corresponding plots for p values are shown in Figures 3.7(b) and 3.7(d), respectively.

The averages of [Hb_{Total}] and [HbO] increased to about 200% of their baseline values on the ipsilateral side, while [Hb_{Total}] and [HbO] on the contralateral side showed marginal (15%) increases. Figures 3.7(b) and 3.7(d) indicate that there are greatly significant differences in concentrations of [Hb_{Total}] and [HbO] between 750-1250 seconds using $p<0.01$, as shown by two pink arrows. About 15 minutes (~1250 seconds) after the injection the differences were not significant using $p<0.01$.
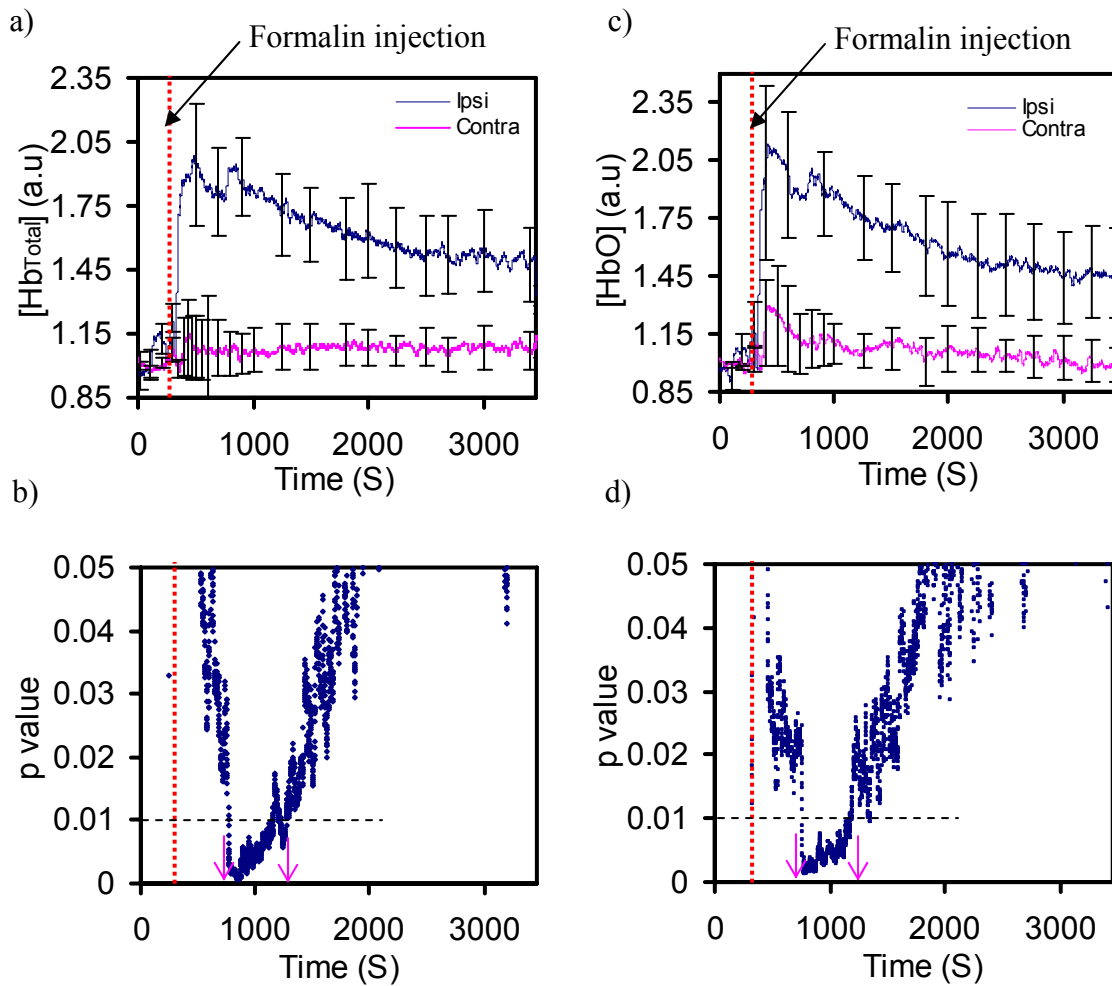
Figure 3.7 Comparisons of temporal profiles of (a) [Hb_{Total}] and (b) [HbO], averaged over 5 rats, on the ipsilateral (injection-side) and contralateral (control) side. Concentrations were normalized to the mean of baseline values on the individual basis. 0-300 seconds were during the baseline measurements. The dashed red line indicates the time point of formalin injection. Error-bars indicate the standard error of mean (SEM). Temporal profiles of p values for (c) [Hb_{total}] and (d) [HbO] are calculated between ipsilateral and contralateral sides.
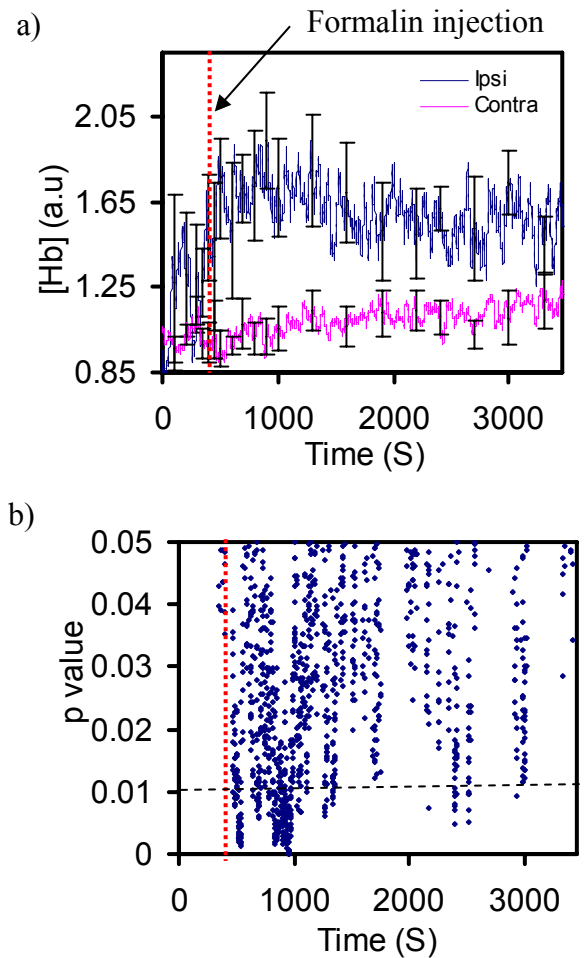
Figure 3.8 Comparisons of temporal profiles of (a) [*Hb*] between the ipsilateral (Injection-side) and contralateral side. Error bars indicate the standard error of mean (SEM) for 5 animals. Concentrations are normalized to mean of baseline values. (b) A temporal profile of *p* values for *[Hb]*.

The average of [*Hb*] over 5 subjects is shown in Figure 3.8(a), while Figure 3.8(b) indicates the significance level of the differences between ipsilateral and contralateral sides at each time instant. [*Hb*] showed an increase in response to injection of formalin on the ipsilateral side. Unlike the cases in [*Hb$_{Total}$*] and [*HbO*] where p<0.05 values clearly exist between the ipsilateral and contralateral sides during 750-1250

seconds, the averages of [*Hb*] on the ipsilateral and contralateral sides have mixed *p* values. Some of them are *p* < 0.01, but some of them are *p* > 0.01, during the response time of 750-1250 seconds, as shown in Figure 3.8(b).
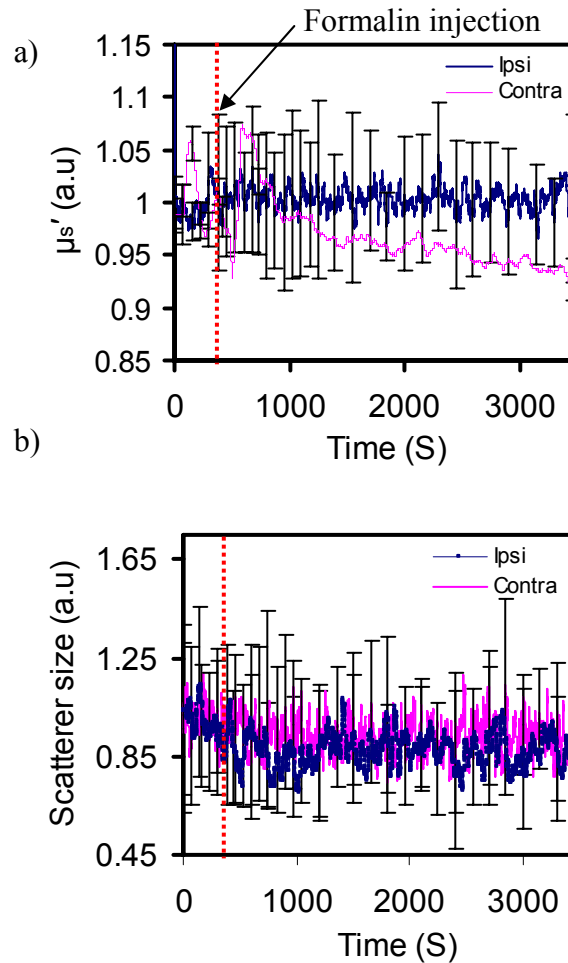
Figure 3.9 Comparisons of temporal profiles of (a) μ_s' (500 nm) and (b) effective scatterer size on the ipsilateral (Injection-side) and contralateral side. All parameters are normalized to mean baseline values and averaged over 5 animals. The error bars indicate the standard error of mean (SEM) for the ipsilateral side over 5 animals.

There were no significant differences of scattering parameters, μ_s' (500 nm) and effective scatterer size, between the ipsilateral and contralateral sides during the pain response as demonstrated in Figures 3.9(a) and 3.9(b). The change in μ_s' (500 nm) on the ipsilateral side was <5% (Figure 3.9(a)) in response to the injection formalin. The averaged values of scattering parameters, both μ_s' (500 nm) and effective scatterer size remained within a standard deviation during the course of the response.

3.6 Discussion

In this Chapter, changes in hemoglobin derivative concentrations during response to formalin induced pain were quantified. This approach leads to more quantitative information on [Hb_{Total}], [HbO], and [Hb] on each side of the paws. The technique is also sensitive to reduced scattering coefficients, hence being able to decouple chromophore concentrations from scattering coefficients. Besides, my approach elicits blood oxygen saturation and reduced scattering coefficients. Overall, use of a broad spectrum (500-850 nm), instead of sparse wavelength sampling, enhances the separation of chromophore absorptions from light scattering and also minimizes inter chromophore crosstalk.

Quantification of [Hb_{Total}] and hence blood volume changes [66] would enhance our knowledge of physiology of pain responses. This knowledge could lead to development of better pain management approaches during chronic pain due to several causes such as trauma, injuries or caused by particular pathologic states. In particular, understanding blood volume changes would lead to development of better drug delivery methods and better anesthetics for alleviation and management of pain.

3.6.1 Effective scatterer sizes

Inflammation is generally accompanied by stretching of skin and other related structures. Figure 3.9(b) seems to indicate that no significant differences in effective scatterer sizes were observed during the pain response. Intuitively, this seems contradictory to previously known phenomenon of pain response to cutaneous injection of formalin. The changes in effective scatterer sizes are natural to any inflammatory response. Limitations of investigation modality could be a possible reason for this observation. Several previous investigations from our group and others in the field have focused on quantifying scatterer sizes based on spectra of reduced scattering coefficients [43-45]. Limitations and non-uniqueness in the quantification of particle sizes were shown by our group [43]. The previous studies stated with simulations from Mie theory [43] and data from latex microsphere suspensions [44] that there exists non-uniqueness in slope of reflectance spectra with respect to sizes of microspheres. The problem gets more complicated in tissues due to several refractive indices at membrane interfaces that are seen in different cell organelles [46]. The mathematical model, (Equation (2.3), adapted in this investigation to model wavelength dependence of scattering coefficients does not account for change in refractive indices, which plays a major role in the determination of scattering coefficients and its wavelength dependence. Improving the model for reduced scattering coefficients as a function of incident wavelength and refractive index ratios of boundaries will improve the quantification of mean effective scatterer sizes. Particular attention has to be paid to sizes greater than 0.2 μm which are similar to sizes seen in normal tissues [45]. This

uncertainty in quantification of effective scatterer sizes may explain large deviations seen for effective scatterer sizes in our study.

3.6.2 Ipsilateral side

The blood volume changes seen were very consistent in all animal subjects on the ipsilateral side. All animals exhibited a rapid increase in blood volume or $[Hb_{Total}]$, followed by a gradual decrease to a plateau region where the total hemoglobin concentration remains elevated from the baseline values. Figures 3.4(a), 3.4(c), and 3.7(a) are evidences of the stated observation. Peripheral vasodilatation and plasma extravasation occurs in response to pain and inflammation through inflammatory mediators and neuronal responses (dorsal root reflexes), as described in detail in section 3.1. Increases in blood volume could be attributed to this peripheral dilatation of blood vessels. This observation is consistent with several previous investigations of formalin induced pain with LDF, which indicated increases in blood flow [48, 57, 58, 67]. Although LDF measures increases and decreases in blood flow, it remains one of the only related measurements that are comparable to the current study. Although the changes or increases in blood flow do not necessarily mean increases in blood volume or hemoglobin concentrations, increases in hemoglobin concentrations can be related to changes in blood flow by using a model, with assumptions valid in physiology [68].

3.6.3 Contralateral side

Blood volume changes on the contralateral side showed a lot of inter subject variations as seen from Figures 3.4(b) and 3.4(d). $[Hb_{Total}]$, $[HbO]$ and $[Hb]$ are generally increased when compared with baseline values; however, the increases were

not significant across all subjects (Table 3.2). The magnitude of increases in averaged values of [Hb_{Total}] and [HbO] was significantly (*p* values from Figure 3.7(b) and Figure 3.7(d) respectively) lower on the contralateral side than those on the ipsilateral side. The differences were significant only for a certain period of time (about 15 minutes, based on p<0.01) after the injection of formalin. Previous investigations with formalin induced pain model [57-59, 67, 69, 70] have shown that physiological responses are seen in the first fifteen minutes.

3.6.4 Origin and evolution of response

The comparison of changes in [Hb_{Total}], [HbO] and [Hb] profiles between the contralateral and ipsilateral side enables the investigation of origin and temporal evolution of pain responses. The initial simultaneous increase of [Hb_{Total}] in the contralateral and ipsilateral side may be an evidence of central mediation of pain responses. As mentioned in section 3.1, vasoactive substances are released from the afferent fibers which cause peripheral vasodilatation. The increase seen in contralateral side may be a result of release of vasoactive peptides, as a result of stimulation in the dorsal root ganglion. The activity of dorsal root ganglion cell causes release of vasoactive peptides from terminals, which could be attributed to the increase in hemoglobin concentrations seen in both paws. Previous investigators have measured changes in cutaneous blood flow that occur at the site of injection and at a distance 1-2.5 cm from the injection using LDF. These studies seem to indicate that redness near the site of injection is due to the action of formalin on sensory nerve terminals or to

axon reflexes, whereas the surrounding flare could be a result of dorsal root reflexes [56].

3.6.5 Effect of factors such as heart-rate, metabolic activity and CO_2 production

To reduce the effect of CO_2 production in the changes of hemodynamic parameters, end tidal CO_2 was maintained at around 30 mmHg. The heart rate and temperature were monitored continuously during experiment. It is known that temperature plays a very major role in the peripheral circulation changes. To minimize effects due to temperature changes, temperature was maintained constant using a feedback controlled electric heating blanket. Also, increase in metabolic activity during pain does bring about changes in peripheral circulation. The rate of increase in blood hemoglobin concentrations observed in my experiments is more rapid than those known to occur by metabolic activity. Changes due to metabolic activity are generally slower in comparison with stimulus of chronic pain [71]. Most of the increases in blood concentrations observed in my study are noticed in the first fifteen minutes ($p<0.01$) after the injection. Actual physiological cause of this increase in concentration of hemoglobin derivatives as seen in this study or the increase in blood flow as seen by LDF-based studies are still a matter of debate. In this context, my study is complimentary to previous studies to enhance physiological information about pain responses.

3.6.6 Sampling rate

The sampling rate chosen for my experiment was 1 Hz so as to monitor changes in a temporal resolution of seconds. The hardware permitted a more rapid data

acquisition in the range of 10 Hz. Increase in sampling rate can bring about a better temporal resolution for measuring pain responses. Howecer, a greater sampling rate will result in an increase in volume of data collected, hence an increase in un-necessary computational burden. Since hemodynamic changes that my study aims to quantify are usually slow in nature [72, 73]. Most imagers built to study hemodynamic changes work on a sampling rate of around 1 Hz [72-75].

<div align="center">3.7 Conclusions</div>

In conclusion, a novel optical non-invasive technique is presented, which could be a valuable tool for the quantitative, objective evaluation of changes in hemoglobin concentrations caused by peripheral noxious stimulation. The technique developed has the ability to decouple effects in absorption from those in scattering. Hemodynamic parameters were quantified during the temporal evolution of formalin-induced pain response. Significant ($p<0.001$) increases in [Hb_{Total}], [HbO] and [Hb] after injection of formalin were seen in the ipsilateral side (Table 3.2). Temporal profiles of [Hb_{Total}], [HbO] and [Hb] were normalized to their respective baseline values to remove the effect of their individual magnitudes before comparison as mentioned in Section 3.5.5. Significant differences in concentrations of [Hb_{Total}] and [HbO] were seen between the ipsilateral and contralateral sides during the time period of 750-1250 seconds using $p<0.01$, as shown by two pink arrows in Figure 3.7(b) and Figure 3.7(d) respectively. About 15 minutes (~1250 seconds) after the injection the differences were not significant using $p<0.01$. Unlike the cases in [Hb_{Total}] and [HbO] where p<0.05 values clearly exist between the ipsilateral and contralateral sides during 750-1250 seconds, the

averages of [*Hb*] on the ipsilateral and contralateral sides have mixed p values. Some of them are $p < 0.01$, but some of them are $p > 0.01$, during the response time of 750-1250 seconds, as shown in Figure 3.8(b). Moreover, I did not observe any significant changes in light scattering before and after the injection, averaged over 5 experimental animals on either side of the paws.

CHAPTER 4

QUANTIFICATION OF HEMOGLOBIN DERIVATIVES WITH SINGLE LARGE
SOURCE DETECTOR SEPARATION

4.1 Introduction

Near infrared spectroscopy is a technique for characterizing turbid media that has been increasingly used in diagnostic applications. When quantification of chromophore concentrations is needed, it is required to separate the effects of light absorption from those of light scattering. The coefficients of absorption (μ_a) and of reduced scattering (μ_s') can be determined by a series of reflectance measurements performed in one of the three domains, namely, time [76], frequency [13, 14], and steady state [26] domain.

All the three techniques have their own advantages and shortcomings. Steady state techniques use a single source and detectors at multiple distances and are relatively inexpensive and better suited for quantification of optical properties over continuous large wavelength ranges (600-900nm). Typically, measurements are performed with a set of small (~ 1 transport mean free path) and large (many transport mean free paths) source detector separations. The small source-detector separations range from 1-5mm, while the larger source-detector separations refer to separations in the range of 1-5 cm. The variations in optical properties are assumed to be insignificant over the ranges of tissue volume probed.

Time and frequency-domain techniques are better suited for more quantitative investigations of biological tissues. The quantification of optical properties can be performed with only one or a few source–detector separations, which makes them easier for use in studying heterogeneous samples and reporting their volume-averaged optical properties. These techniques require sources that can be pulsed or modulated rapidly, and covering multiple wavelengths in the range of 600-900 nm requires a tunable laser or an extensive collection of laser diodes, both of which can be expensive, difficult to maintain, and slow to cover the entire spectrum.

Previous chapters (2&3) described the development and applications of techniques to quantify optical properties at a minute scale with source-detector separations being a few hundred microns. Investigations of larger tissue volumes or increase in penetration depths require that source–detector separations be scaled up to 1 cm – 4 cm. This chapter reports the development of a multi wavelength algorithm to quantify absolute concentrations of tissue chromophores, such as HbO and Hb, with a single large source-detector separation (~1 – 4 cm) using steady state reflectance measurements. The method has inherent advantages of a broad wavelength coverage and increased penetration depth. The variations in optical properties are assumed to be insignificant over the ranges of volume probed. The assumption does not hold in all biological tissues. An approach to quantification of spatial extent of heterogeneities is further developed in Chapter 5.

In my study, I used single, large source–detector separation (~ 1 - 4 cm), unlike spatially resolved steady state measurements (multiple source-detector separations). The

instrumentation for our development is relatively straight forward, particularly easy to replicate or add additional channels, and relatively inexpensive. The technique I developed uses the second-differential NIRS to determine relative concentrations of deoxygenated hemoglobin to tissue water by fitting spectral features of these two chromophores in the 710-780 nm spectral region [24]. The absolute concentration of deoxygenated hemoglobin can then be calculated, as the concentration of tissue water is known in the accuracy of few percent [65]. The deoxygenated hemoglobin concentration is used as priori information to inversely solve the diffusion model. A heuristic ant colony optimization algorithm [25, 37, 38, 65] was used to determine the concentration of oxygenated hemoglobin and reduced scattering coefficients. A description and mathematical formulation of the algorithm has been described in Sections 2.3.1 and 2.3.2, respectively. Unlike other steady state approaches that use multiple source-detector separations to quantify chromophore concentrations [26], my technique presented here uses only a single source-detector separation. Second differential NIRS has been used by other groups to estimate path length in continuous wave diffuse optical tomography [24]. The path length information was used to reconstruct images of a target medium [77]. My developed technique is validated by making measurements from tissue simulating blood intralipid phantoms [17], and simultaneous measurements using an ISS Oximeter have been considered as gold standard in the validation experiments.

After having validated the developed technique using phantoms, feasibility of my technique to monitor and quantify changes in hemodynamic parameters during the

growth of orthotropic brain tumors in rats was evaluated. [*Hb*] and [*HbO*] were monitored from tumor implantation till the animal was sacrificed (see Section 4.4.2). Moreover, the heterogeneities in the investigated volume are significant due to presence of various tissue types. This violates the assumption of insignificant change in optical properties within the optically interrogated tissue volume. The effect of this heterogeneity on the measured spectra and quantified [*Hb*] and [*HbO*] will be discussed in Section 4.5.

As a second application, the feasibility of my developed technique to quantify hemoglobin derivatives, water content and reduced scattering coefficients of ex vivo human prostate lesions was investigated. Chromophore concentrations and reduced scattering coefficients were evaluated in superficial and deeper regions of the prostate glands (see Section 4.4.3). In addition, estimates of absolute concentrations determined from the algorithm were compared with those reported by other recent in vivo studies for the human prostate using the time-resolved measurements [78]. In the last part of this chapter, effects of presence of heterogeneities in biological tissues on measured spectra and its deviation from those predicted by theory are discussed (Section 4.5.3).

<u>4.2 Theory</u>

The diffusion approximation of radiative transport theory has been widely used in recent years for modeling the near-infrared (NIR) light (650-900 nm) propagation through biological tissues[26], and quantifying optical properties of tissues. Solutions of diffusion equations have been validated by experimental measurements and Monte Carlo simulations under the conditions that, 1) ρ (source-detector separation) is much

larger than the transport mean free path (referred to as z_0 later) and 2) absorption coefficients (μ_a) of the measured tissue are much smaller than its reduced scattering coefficients(μ_s').

The major chromospheres that absorb light in biological tissues are HbO and Hb concentrations with distinct optical absorption spectra in the visible and the NIR wavelength ranges. When source-detector separations are of the order of a few centimeters, sufficient photons can be transmitted or backscattered through blood perfused turbid media and can be detected in the NIR wavelength range. The detected signal depends strongly on [Hb] and [HbO] with characteristic spectral features in the NIR wavelength range. The spectral dependence of μ_a for blood perfused tissues can be written as

$$\mu_a(\lambda) = [HbO].\varepsilon_{HbO}(\lambda) + [Hb].\varepsilon_{Hb}(\lambda) + \varepsilon_{H_2O}.\%H_2O \qquad (4.1)$$

'λ' is the wavelength in nanometers, [HbO] and [Hb] are molar concentrations (μM) of HbO and Hb, respectively. $\varepsilon_{HbO}(\lambda)$, $\varepsilon_{Hb}(\lambda)$ and $\varepsilon_{H_2O}(\lambda)$ are the extinction coefficients of HbO, Hb [29] and water [79]. [79], respectively The equation is very similar to Equation (2.2). The contribution of melanin to μ_a can be added to Equation (4.1) when melanin is appropriate to be included. In most of tissue cases, the contribution from melanin in this wavelength range (600-850 nm) is not significant and therefore excluded [63, 80].

The spectral dependence of μ_s' can be approximated as

$$\mu_S'(\lambda) = -c.\lambda + d \qquad (4.2)$$

where c and d are tissue dependent parameters [32]. λ is the wavelength in nm.

The diffusion approximation [26] allows the determination of optical properties of tissues from steady state diffuse reflectance R, where R is the diffuse photon flux escaping from the tissue boundary interface (at $z = 0$). The reflectance is given in Equation 4.3 as

$$R(\rho, z_o) = \frac{I_0}{4\pi}\left(z_0(\mu_{eff} + \frac{1}{r_1})\frac{\exp(-\mu_{eff}r_1)}{r_1^2} + (z_0 + 4AD) \times (\mu_{eff} + \frac{1}{r_2})\frac{\exp(-\mu_{eff}r_2)}{r_2^2}\right) \quad (4.3)$$

where, $r_1 = \sqrt{(z_0^2 + \rho^2)}$, $r_2 = \sqrt{((z_0 + 4AD)^2 + \rho^2)}$, $D = \frac{1}{3(\mu_a + \mu_s')}$, $\mu_{eff} = \sqrt{\mu_a/D}$,

$z_0 = \frac{1}{\mu_a + \mu_s'}$, ρ is the source-detector separation, and A is a constant related to the total

internal refraction and depends on the refractive index of the medium. Equation 4.3 has been shown to be consistent with spatially resolved Monte Carlo simulations with large source-detector separations. An improved solution is available for more accurate characterization of tissue optical properties [28]. , as given below:

$$R_{imp} = 0.118\phi(\rho, z_0) + 0.306R(\rho, z_0) \quad (4.4)$$

$$\phi(\rho, z_0) = \frac{1}{4\pi D}\left[\frac{\exp(-\mu_{eff}r_1)}{r_1} - \frac{\exp(-\mu_{eff}r_2)}{r_2}\right]. \quad (4.5)$$

Equations 4.1-4.5 provide a straight forward way of calculating the diffuse reflectance at a source-detector separation ρ if the concentration of hemoglobin derivatives and reduced scattering coefficients are known. Equation (4.1) relates the tissue chromophore concentrations to μ_a, similarly Equation (4.2) relates μ_s' to tissue related parameters. Equation (4.3) provides a relationship between reflectance at the

tissue-air interface and tissue optical properties (μ_a, μ_s'). In my study, Equation 4.3 is used to generate forward data, i.e., reflectance spectra for given [*Hb*], [*HbO*] and μ_s'.

4.2.1 Attenuation spectra

Equation (4.6) below defines a term known as attenuation, A. It is the logarithm of reciprocal of reflectance, R.

$$A = -\log_{10} R.$$ (4.6)

Figure 4.1 displays the attenuation spectra computed for the common tissue chromophores Hb, HbO and water. Concentrations of 100 μM were used to calculate the attenuation spectra. Firstly, Equation (4.3) was used to calculate the reflectance, R, at a source-detector separation of 1-4 cm, followed by taking logarithm of reciprocal of the reflectance, as for attenuation.
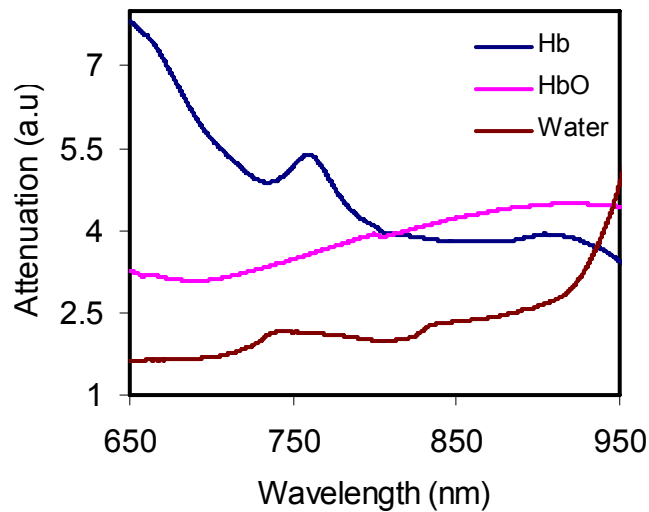
Figure 4.1 Attenuation spectra of common tissue chromophores Hb, HbO and water. Concentrations of 100 μM were used to compute the attenuation spectra. A source-detector separation of 3.5 cm was used.

The attenuation spectrum of HbO in Figure 4.1 appears to be smooth at the wavelength range of 710-780 nm and devoid of any bumps that can be seen in the attenuation spectra of Hb and water in the same wavelength range. The attenuation spectrum of HbO exhibits a linear dependence on the wavelength in this wavelength range. It is intuitive that a second derivative of HbO with respect to wavelength would not be significant in this wavelength range (710-780 nm) in comparison with Hb and water.

4.2.2 Second Differential NIRS

The approach of using spectral features of second derivatives of attenuation spectra was presented by Matcher et al [24]. A numerical second derivative of attenuation spectra in Figure 4.1 is determined. My way of obtain the second differential at a point is as follows: (1) fitting a third order polynomial through 5 data points in the spectrum, i.e., the point, the following two points and preceding two points; (2) then computing the second differential based on the polynomial at that point. This procedure is repeated for all spectral points in the wavelength range of 650-975 nm. The second derivative spectra of Hb, HbO and water have been obtained through this way and shown in Figure 4.2(a). The wavelength range of 710-780 nm as mentioned earlier is of particular interest. Figure 4.2(b) shows a magnified version of Figure 4.2(a) for the wavelength range of 710-780 nm. The distinct spectral features at 720 nm for water and 760 nm for Hb are clearly seen corresponding to the features present in the in vitro spectra of water and Hb. The second-differential spectrum for HbO is essentially featureless and should not, therefore, affect the subsequent analysis.

This feature allows the quantification of [*Hb*] relative to concentrations of tissue water. The concentration of tissue water is generally known within accuracies of a few percent [65], so this information can used to obtain the absolute concentration of Hb ([*Hb*]).

a)

b)
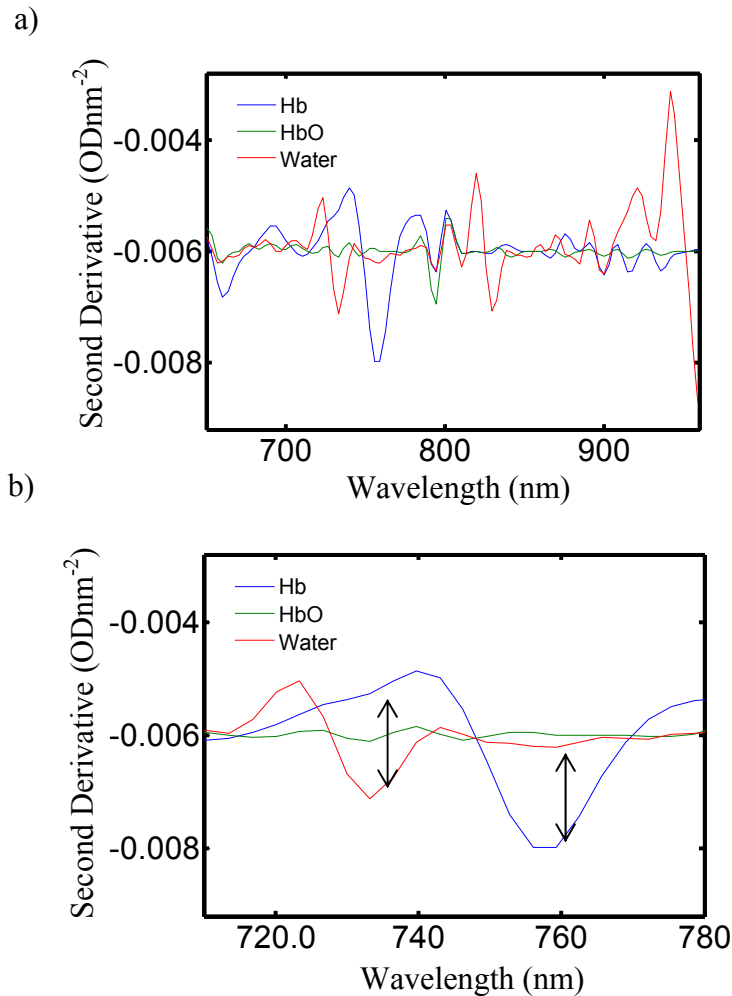
Figure 4.2 (a) Second derivatives of attenuation spectra of common tissue chromophores Hb, HbO and water in the wavelength range of 650-975 nm. (b) Second derivative spectra in the wavelength range of 700-780 nm. The green HbO plot in (b) is devoid of features, unlike Hb (blue) and water (red) plots, indicating minimal contribution from the second derivative of HbO. Notice that Hb has a deep trough at ~760 nm, while water has a trough at ~730 nm.

Concentrations of deoxygenated hemoglobin relative to tissue water is determined by fitting spectral features of Hb and H_2O from 710 nm to 780 nm [24]. The second differential of the measured attenuation spectrum is fit with the reference second differential spectra of Hb and H_2O to obtain the relative concentrations of [*Hb*] to tissue water. The reference second differential spectra are calculated using Equations 4.1-4.3 and Equation 4.6. The fitting parameter is the ratio ([Hb]/%[H_2O]) which is concentration of Hb relative to water content in the tissue.
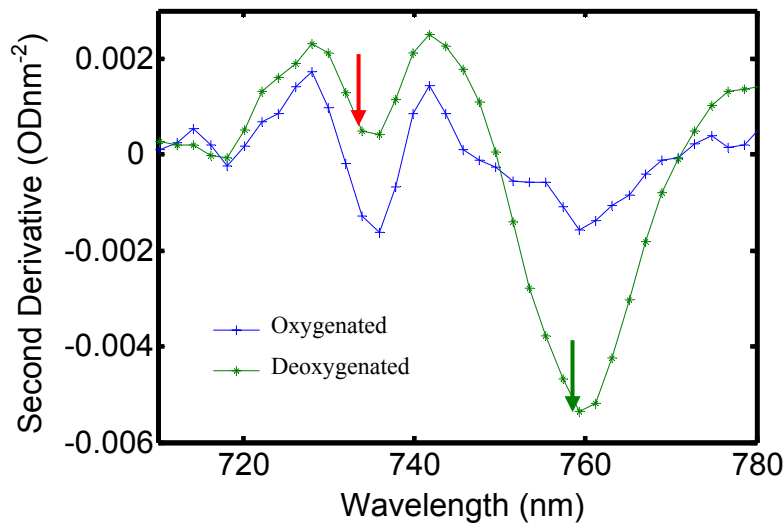
Figure 4.3 Illustration of the second derivatives of attenuation spectra at different blood oxygen saturation levels. Oxygenated ([*Hb*] = 1.3μM, [HbO]=50 μM, [H_2O] = 80%) and Deoxygenated ([Hb]= 21μM, [HbO]=50 μM, [H_2O] = 80%). The differences in the peaks at 760 nm are clearly evident from the figure.

Figure 4.3 shows spectra with different blood oxygen saturation levels that were computed using Equations 4.1-4.3 and Equation 4.6. Concentrations of chromophores used for the computation were [*Hb*]=1.3μM, [HbO] = 50μM, %H_2O = 80% for the oxygenated blood and [Hb]=21μM, [HbO]=50μM, [H_2O]=80% for the deoxygenated

spectrum, respectively. The differences between the oxygenated spectra and deoxygenated spectra are apparent. The trough at 760 nm for the deoxygenated blood (green curve) is very deep, as pointed by the green arrow, and in the same plot the trough at 730-740nm (shown by the red arrow) is clearly seen, indicating in the existence of water. Complimentary features are seen for the more oxygenated blood (blue plot), where the Hb trough reduced greatly and water trough increased largely comparison to the green curve. The oxygenated blood (blue plot) contains contributions from the water feature and that from Hb. As HbO contributes minimally to the second derivative spectra, predictably no features are observed. By taking the ratios of the two troughs, absolute [Hb] can be calculated provided the water concentration is known. This is implemented by fitting the ratio of [Hb]/%[H_2O] to the second differential of the attenuation spectrum between 710-780 nm using Hb and water reference spectra. Multiplying the concentration ratio of Hb to H_2O by concentration of H_2O to obtain the absolute [Hb].

The procedure to fit the second derivative of the attenuation spectrum to determine the ratio of [Hb] to H_2O concentration is elaborated below.

1. Start from an initial guess of [Hb] and %[H_2O].

2. Use Equation (4.1) to compute $\mu_a(\lambda)$ in the wavelength range 710-780 nm.

3. Assume an arbitrary scattering spectrum for μ_s' as mentioned in Matcher et al [24]. Intralipid reduced scattering $\mu_s'(\lambda)$ calculated from

89

approximations based on Flock et al were used as arbitrary scattering spectrum.

4. Use Equation (4.3) to calculate the reflectance spectrum for the assumed initial guess of concentrations and determine attenuation spectrum by using Equation (4.6).

5. Calculate the numerical second differential of the attenuation spectrum as described in previous paragraphs.

6. Eliminate spurious contributions from noise in the measured spectra by smoothing with a Savitzky-Golay filter [81].

7. The Matlab^{TM} function 'lsqnonlin.m' is used to iteratively update the initial guess of [Hb] and %[H_2O] to minimize differences between the measured second differential spectra and the computed second differential spectra as shown in Equation (4.7).

$$\sum_{\lambda=710nm}^{\lambda=780nm} \left(S_a^{computed}(\lambda) - S_a^{measured}(\lambda) \right)^2 \qquad (4.7)$$

where $S_a^{computed}(\lambda)$ is the computed second differential of attenuation spectrum and $S_a^{measured}(\lambda)$ is the second differential of the measured attenuation spectrum.

8. Multiply the ratio of [Hb] to H_2O concentration by concentration of H_2O to get the absolute [Hb].

The determined absolute [Hb] is used as a priori information in the optimization algorithm to determine reduced scattering coefficients and concentration of oxygenated

90

hemoglobin. The spectrum measured from tissue phantoms and tissue generally has some noise associated with the acquisition. To eliminate erroneous contribution to second derivatives, a Savitzky-Golay filter is used to smooth the data [81] as mentioned earlier.

4.2.3 Optimization Algorithm

The inverse problem is treated as an optimization problem, and hence the solution lies in determining those values of [HbO], [H_2O], c, and d that minimize the error, χ^2, in the objective function, as given below in Equation 4.8.

$$\chi^2 = \sum_{i=1}^{M}\left[R(\lambda_i)^{(measured)} - R(\lambda_i)^{(predicted)}\right]^2 \qquad (4.8)$$

The absorption and scattering properties are determined from estimated values of [Hb], [HbO], c, and d. $R(\lambda)^{(measured)}$ is a reflectance spectrum measured from a test sample or tissue, while $R(\lambda)^{(predicted)}$ is a reflectance spectrum calculated from the estimated values of μ_a and $\mu_s^{'}$ at each wavelength of λ. Ant Colony optimization algorithm [25, 37, 38] is used to iteratively determine the parameters of [Hb], [HbO], [H_2O], c, and d to optimally match the calculated and measured reflectance. The basic principle and theoretical basis of the ant colony algorithm has been described in detail in Chapter 2.

In order to circumvent photometric calibration difficulties, two normalization approaches were used (Figure 4.4(a) and Figure 4.4(b)). In the first approach the measured spectral reflectance curves were normalized to scale of 0-1. Similarly, in the second approach (Figure 4.4(b)), the measured spectral reflectance were normalized

with respect to the reflectance at $\lambda=600$ nm. The first normalization approach is used to obtain an estimate of μ_s' (i.e parameters c, d) and blood oxygen saturation. The parameter [Hb] already determined using the second differential spectroscopy is used as a priori information in this step. [Hb] is allowed to vary in a $\pm$ 10 % from the concentrations determined from second differential spectroscopy. The estimates obtained using the first normalization approach serve as initial guesses or a priori information in the next step. [Hb], [HbO], water content and μ_s' (i.e parameters c, d) are allowed to vary in a $\pm$ 15 % from those determined from previous steps. Using the second normalization approach and information from the previous steps as mentioned, [Hb], [HbO], water content and μ_s' (i.e parameters c, d) are further refined.
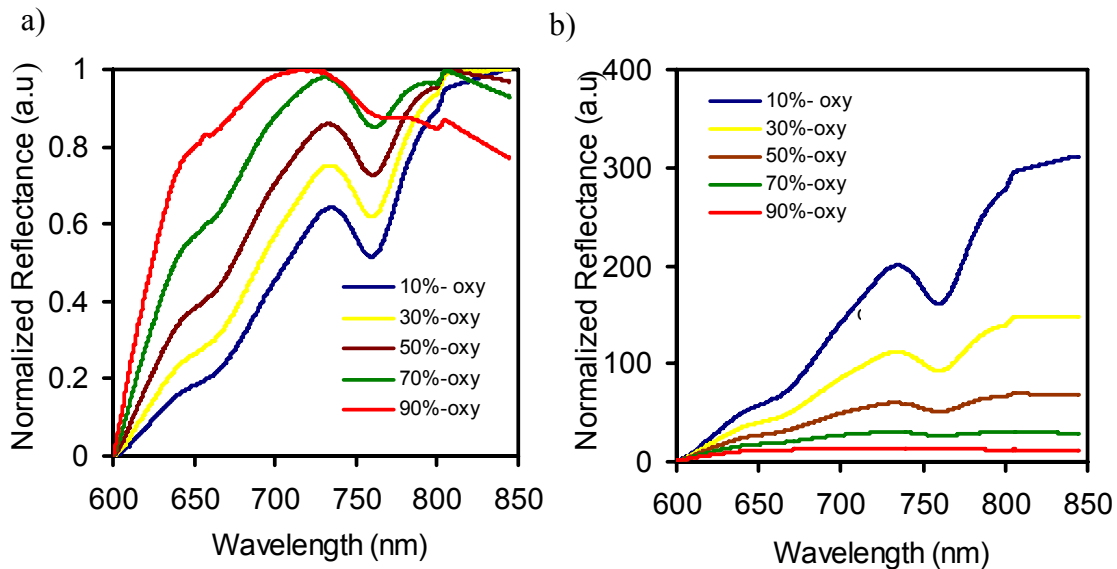
Figure 4.4 Two normalization approaches: a) the first normalization approach where the measured reflectance is normalized between 0 and 1. Lowest value is set to 0 and other values are correspondingly scaled. b) the second normalization approach where the measured reflectance is normalized with respect to reflectance at $\lambda=600$ nm.

A step wise description of all procedures followed to determine absolute concentrations of Hb, HbO and μ_s' (i.e parameters c, d) is given below.

- Raw reflectance spectra were measured from in vitro experiments.

- To eliminate spectral effects from the fiber, light source and instrument response, the measured spectra are divided by a calibration spectrum taken from a standard reflectance sample, which gives the reflectance R.

- A logarithm of reciprocal of R gives the attenuation. Evaluating the same at all spectral points yields corresponding attenuation spectra.

- Obtain the second differential of attenuation spectra in the wavelength range of 710-780 nm and fit with the reference spectra of water and deoxygenated hemoglobin to obtain relative concentrations of deoxygenated hemoglobin as mentioned in Section 4.2.2.

- Use the deoxygenated hemoglobin concentration in the optimization algorithm to determine the concentration of oxygenated hemoglobin and reduced scattering coefficients as mentioned in Section 4.2.3.

4.3 Experimental setup

4.3.1 Liquid phantom experiments

Figure 4.5 shows the schematic for the experimental set up used for making reflectance measurements on blood intralipid phantoms. Light from the light source (Illumination Technologies, Inc. Model 3900 DC regulated, Light Feedback Fiber Optic Light source) is delivered via an optical fiber (Illumination Technologies, 3 mm core diameter, SMA) to the surface of the sample and collected at some distance away. The

collected light is delivered to the CCD array spectrometer (Ocean Optics Inc, Florida, S2000 Spectrometer (350-1050nm) 200μm slit width) with an optical fiber (Innova Quartz Inc, Phoenix, Arizona, 3-mm core diameter, SMA). The spectrometer records a total of 2048 points with a spectral resolution of 3 nm. The source-detector separation, ρ, used in the measurements was 3.5 cm.
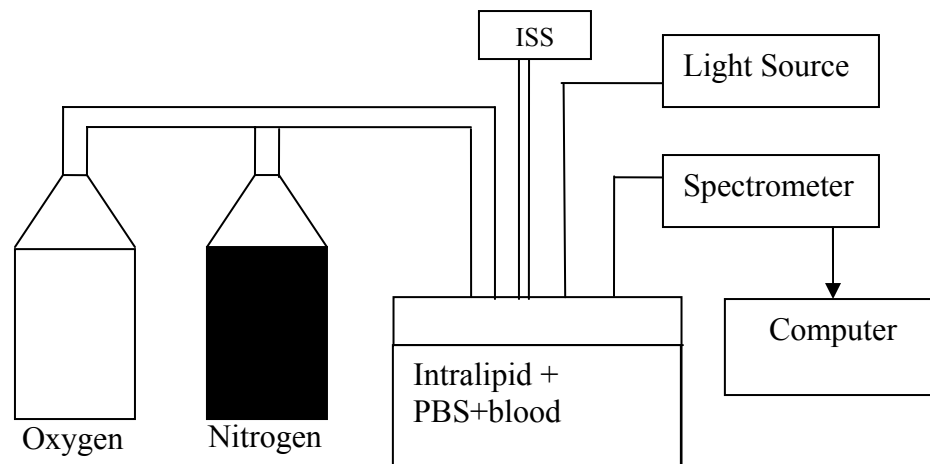
Figure 4.5 Schematic diagram of the experimental setup used for in vitro measurement of reflectance spectra from a liquid tissue phantom. The source-detector separation was 3.5 cm for an old experimental setup. The oxygen and nitrogen gases were used to oxygenate and de-oxygenate the phantom.

The calibration measurement is made by shining light from the source fiber on a standard reflectance sample (WS-1, Ocean Optics, Dunedin, FL, USA) and by collecting the reflected light with the detector fiber. Relative reflectance is calculated to be the sample spectrum divided by the calibration spectrum. Both measurements use the same delivery fiber, collection fiber, and detector apparatus. This calibration procedure is necessary to eliminate the spectral responses of delivery and collection fibers, light source and CCD detector [82].

The tissue phantom contained a mixture of defibrinated horse blood (Hemostat Labs Inc, Dixon,CA) and an aqueous scattering suspension (Intralipid-20%) dissolved in PBS (Phosphate buffered saline). The ingredients and their respective proportions to prepare PBS are listed in Appendix C.. Before the addition of Intralipid, the hemoglobin concentration was measured with a co-oximeter. The volume and the concentration of intralipid in the aqueous suspension were varied according to the scattering coefficients desired. The total hemoglobin concentrations and reduced scattering coefficients were measured using an ISS Oximeter.
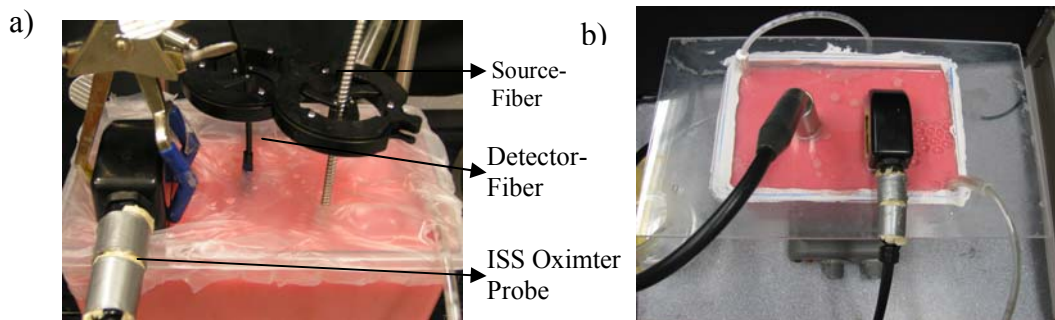
Figure 4.6 Photograph of tissue-phantom experiment setup showing the arrangement of source and detector fibers and the ISS Oximeter probe. (a) an old experimental setup; (b) an improved new experimental setup to prevent errors due to possible oxygen leakage from the ambient air into the phantom container.

The water content in the phantoms is calculated as follows. Table 4.1 gives a list of ingredients and their respective amounts that are used in the blood intralipid phantom. The volume blood used to prepare the phantom was 100 ml. It is assumed that 1% intralipid is used to prepare the phantom. The fraction of lipid in intralipid [83] was

assumed to be 1% and blood was assumed to consist of 80% water [65]. The water content in the phantoms is given by

$$\%[H_2O] = \frac{weight \ of \ H_2O}{Total \ weight} \times 100 = 0.97*100 \ \%, \quad (4.11)$$

Table 4.1 List of ingredients and their respective weights in the blood intralipid phantom

Ingredient	Weight (g)
Water	2910
NaH2PO4- H2O	0.9
Na2HPO4	3.508
NaCl	26.3
KCl	0.6
Blood	20
Intralipid	30
Total weight	2991.0

Optical measurements were performed as indicated in Figure 4.6(a) and Figure 4.6(b), with source and detector fibers placed at the surface of liquid phantom. Nitrogen was bubbled to deoxygenate the blood through the intralipid blood suspension. Air or oxygen was bubbled to re-oxygenate the intralipid suspension. The experimental setup in Figure 4.6(a) could lead to errors in measurements due to possible oxygen leakage from ambient air coming in contact with the liquid phantom surface. This error source was removed in the improved experimental setup (Figure 4.6(b)). An air tight lid was placed with the probes fit into holes that were perfectly cut through the lid. All crevices were sealed with vacuum grease. The bubbled gas is vented out into a beaker of water. The geometry for the new fiber probe is shown in Figure 4.9.

4.3.2 Monitoring of brain tumors

This part of experiments was performed and data collected by Mr. Vikrant Sharma, who worked under the collaboration between our research laboratory and Dr. Giller from Baylor University Medical Center at Dallas. My work is to analyze the collected animal data to test the feasibility of my algorithm.
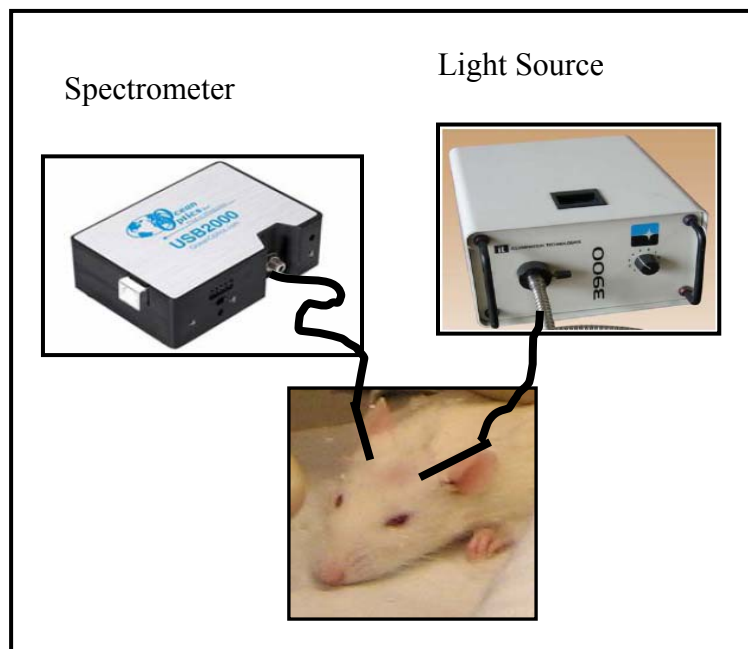
Figure 4.7 Schematic of experimental setup for rat brain tumor measurements. Optical probes were placed on the rat head to interrogate the brain tumor region.

9L/LacZ glioma tumor cell lines ($10\neg6$ cells in 10 μL) were implanted in right caudate nucleus of adult male Fisher C rats (250-300 gm), as described in detail previously [84]. Optical measurements were performed as indicated in Figure 4.7. Light was delivered through a broadband light source (Illumination Technologies) and

collected using the same spectrometer as one for the phantom study (USB 2000, Ocean Optics Inc.). The source and the detector fiber were placed on the rat's head separated by a distance of 1.7cm. The fibers were placed so as to interrogate the region of brain tumor. Measurements were taken progressively on the rat head for several days after implantation of the tumor [6].

The rats were anesthetized with 0.3ml pentobarbital, (~100 mg/ml) and maintained under general gaseous anesthesia with isoflurane in air (~1.3% isoflurane at $1dm^3$/min air) through a mask placed over the animal's mouth and nose. Hair on the head was shaved to improve optical contact for transmitting light. Body temperature was maintained by a warm electric blanket and was monitored by a rectal thermal probe connected to a digital thermometer (Digi-Sense, model 91100-50, Cole-Parmer Instrument Company, Vernon Hills, IL).

4.3.3 Laparoscopic Prostatectomy

This part of measurements was performed and data collected by Ms. Disha Peswani, who worked on ex vivo optical reflectance measurements from human kidney and prostate for her thesis. My work is to analyze the collected human prostate data to test the feasibility of my algorithm.
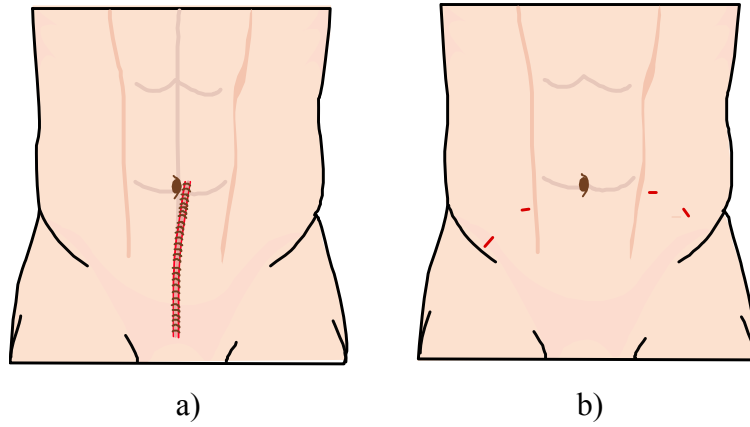
Figure 4.8 Schematic of locations of incisions for (a) open and (b) laparoscopic prostatectomy.

The human surgical procedures were performed to remove the prostate with cancer before the optical measurements. Radical prostatectomy is a surgical procedure performed under general anesthesia and the procedure takes from 1.5-4 hours. The patient is either unconscious during the prostatectomy or remains awake but numb from waist below. Figure 4.8(a) shows the location of incision for traditional radical prostatectomy. Typically in radical prostatectomy procedures, the incision begins below the navel and extends to just above the pubic bone. In a variation of this procedure, a smaller, curved incision is made between the anus and the base of the scrotum; the prostate is then removed from underneath the pubic bone. A nerve sparing radical prostatectomy is typically employed in an attempt to preserve the man's erectile function [85]. The importance of preservation of neurovascular bundle is also emphasized. More recently, radical prostatectomy is most often done using the laparoscopic approach (Figure 4.8(b)). The detailed information on laparoscopic prostatectomy can be found in refs. [86], [87].,[88] and [89].

4.3.4 Ex-vivo measurements on human prostate gland

Human prostates were obtained after laparoscopic prostatectomy as described in the earlier section. Diffuse optical reflectance measurements were made on excised prostrate gland using a custom-designed optical probe shown in Figure 4.9(a). The geometry of source and detector fibers is shown in Figure 4.9(b). The optical probe had a source to deliver light to the tissue surface and three detectors at distances of 0.95 cm, 1.5 cm and 2.2 cm to collect reflected light from the tissue. The probe was placed in contact with the prostate tissues as shown in Figure 4.10.
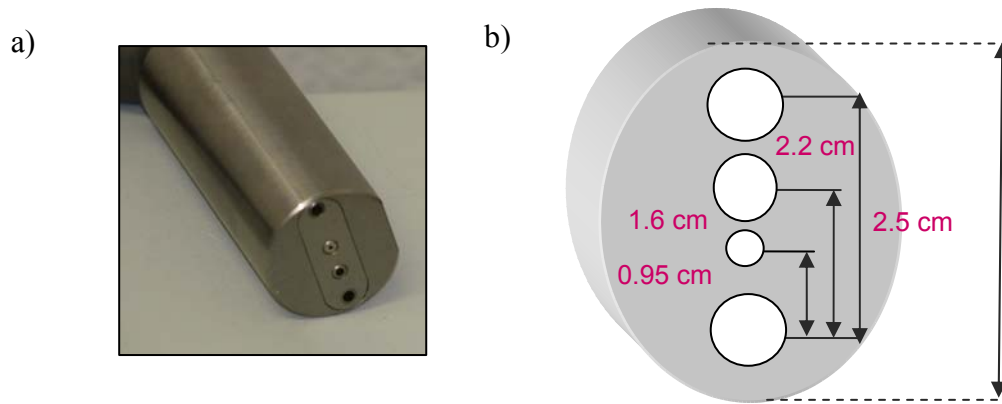
Figure 4.9 Custom designed multi separation probe for reflectance measurements Diameters are progressively increased to provide for decreased light intensity at large separations. a) Photograph depicting the custom designed probe b) geometry of probe depicting source-detector separation.

Figure 4.10 Multi separation probe for reflectance measurements Probe is placed on the gland surface. The seminal vesicles are seen attached to the prostate gland.

Measurements made at 0.95 cm and 1.5 cm are utilized for data analysis. The signal intensity from 2.2 cm channel was too small to characterize the excised prostate tissues. Larger separations result in deeper penetration depths and thus larger probed tissue volumes. The penetration depth of light with a source-detector separation of 0.95cm can be estimated to be about 0.5 cm and with 1.5 cm separation about 0.75 cm [2]. These characteristics were used to probe tissue volume differentially to elicit heterogeneities in hemodynamic parameters.

I have developed data-acquisition Labview^{TM}-based software that can be used to collect multi-channel reflectance spectra simultaneously. The acquired spectra were used to determine the hemoglobin concentrations and scattering coefficients for the investigated regions. Hemoglobin derivative concentrations, water fractions and reduced scattering coefficients from different regions of the prostate were determined

using diffusion theory with a heuristic optimization algorithm as described in earlier sections. Such tissue parameters were investigated at different depths in the prostate glands. Histological examinations of some prostate specimens were made to determine the location and extent of tumors in the excised prostate gland, but they were not the focus of my study and thus are not shown in this dissertation.

4.4 Results

The measured light intensity or raw light reflectance obtained from in vitro or in vivo samples is divided by the calibration spectrum taken from the standard reflectance sample (Equation 4.8) at each wavelength λ. This eliminates spectral response due to optical fibers, light source and instrument response [82]. $I_{Sample}(\lambda)$ and $I_{Standard\_Reflectance}(\lambda)$ are intensities measured from the tissue and calibration sample, respectively.

$$R(\lambda) = \frac{I_{Sample}(\lambda)}{I_{Standard\_Reflectance}(\lambda)} \tag{4.9}$$

Equation (4.9) is the expression for reflectance R measured from the optical fiber probe. The source-detector separation in this case is large (~1-4 cm), and in the animal case the separation was 1.7 cm. Another related quantity in tissue spectroscopy is the attenuation. It is given in Equation 4.10.

$$A = \log_{10}(\frac{I_{Standard\_Reflectantance}}{I_{Sample}}) = -\log_{10} R \tag{4.10}$$

4.4.1 Blood intralipid liquid phantoms

Figures 4.11(a) and 411(b) display the raw spectra and the corresponding attenuation spectra, respectively, taken from an oxygenated and deoxygenated state of a blood intralipid phantom. The reflectance spectrum measured from the oxygenated state shows significantly higher intensities in range of 600-800 nm than those obtained in the deoxygenated state. These features are typical spectral features of HbO and Hb. The behavior is vice-versa in the wavelengths of 800-950 nm. The attenuation spectra being reciprocals of corresponding reflectance spectra show complimentary behaviors.

a)

b)
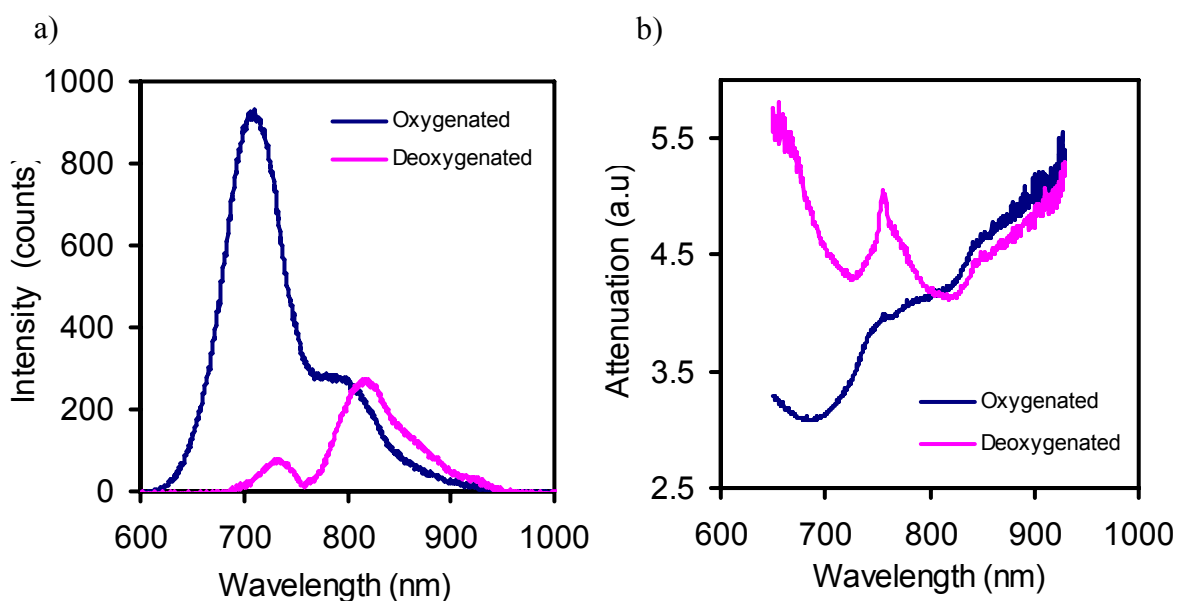
Figure 4.11 Reflectance (a) and attenuation (b) spectra acquired from blood-intralipid phantoms. The oxygenated state and deoxygenated state have high (95%) and low (37%) blood oxygen saturation levels.

The second derivatives of the attenuation spectra are determined as described in section 4.2.2. The second differential spectrum from the measurements is fit with

103

reference spectra calculated from Equations 4.1-4.3 and Equations 4.6 to obtain concentrations of Hb relative to tissue water.
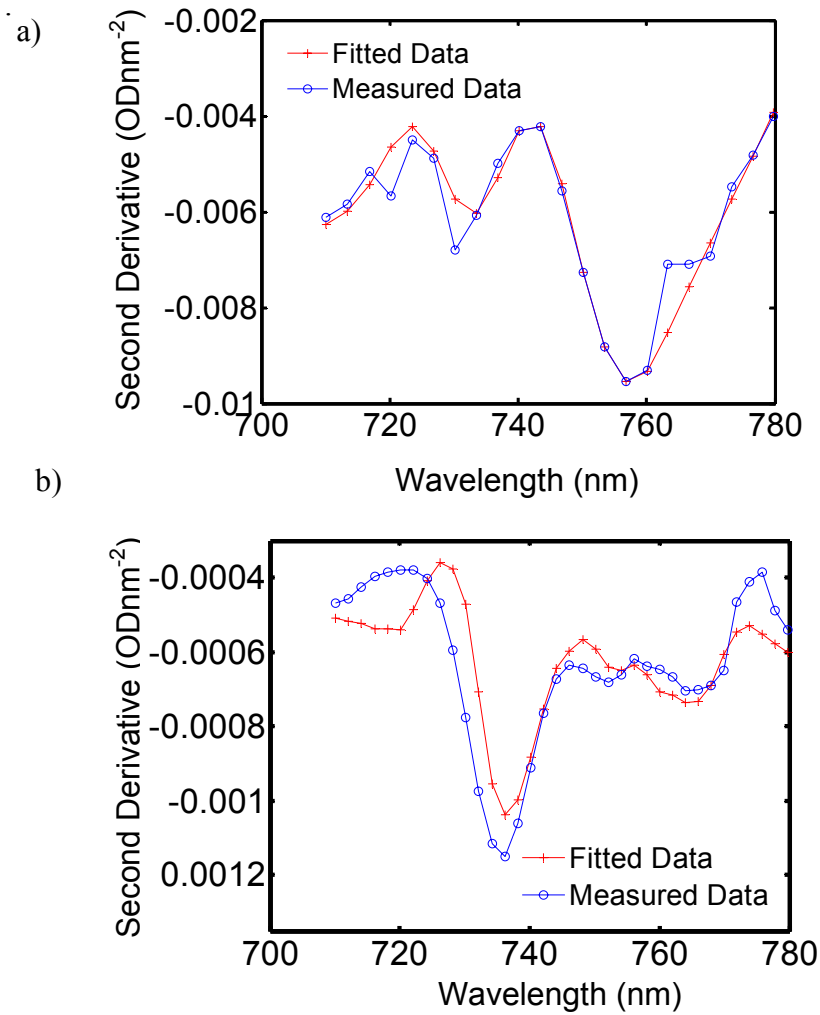
Figure 4.12 Comparison of measured second derivatives of the attenuation spectra and their corresponding fits to determine relative concentrations of Hb with respect to water. The line with blue circles indicates the measured data from the phantoms and red line with plus signs indicates its corresponding best fit. (a) is for a deoxygenated state with [Hb]=25 μM (26.7μM) (b) is for an oxygenated state of [Hb]=1.3 μM (2.3μM). Values in parentheses indicate concentrations measured by the ISS Oximeter. Values outside represent Hb concentrations determined from the second differential spectroscopy. Water content was calculated to be 97% in phantoms by volumetric measurements.

Second derivative spectra for the corresponding deoxygenated state and oxygenated state of the phantom are shown in Figure 4.12(a) and Figure 4.12(b) respectively. The magnitude of the second derivative is lower by a factor of 10 for the oxygenated state as compared with deoxygenated state. The distinct spectral feature of Hb (a trough at 760 nm) is seen in Figure 4.12(a) but not present in Figure 4.12(b). [*Hb*] determined from fitting the second differential spectra are used as a priori information for the optimization algorithm

Figure 4.13 displays a comparison of normalized diffuse reflectance (using the 2nd normalization method) measured from a couple of phantoms and their best fits using Equations 4.1-4.3 to fit for hemoglobin derivative concentrations and reduced scattering coefficients. The oxygenation dependent spectral features are clearly seen. Figure 4.13(a) shows the typical spectral features for a deoxygenated state and Figure 4.13(b) for an oxygenated state. The optimization algorithm described in Section 4.2.3 is used to calculate [*HbO*], μ_s' (i.e., parameters *c, d*) and refine the water content that was assumed during the second differential spectroscopy. The [*Hb*] information is used as a priori information to calculate the other parameters. The values determined from our algorithm and those measured by the ISS Oximeter are consistent, as listed in the legend of Figure 4.13. A detailed comparison between the measured and calculated [*Hb*] and [*HbO*] in the form of correlation plots appears in Figure 4.15.

a)

b)
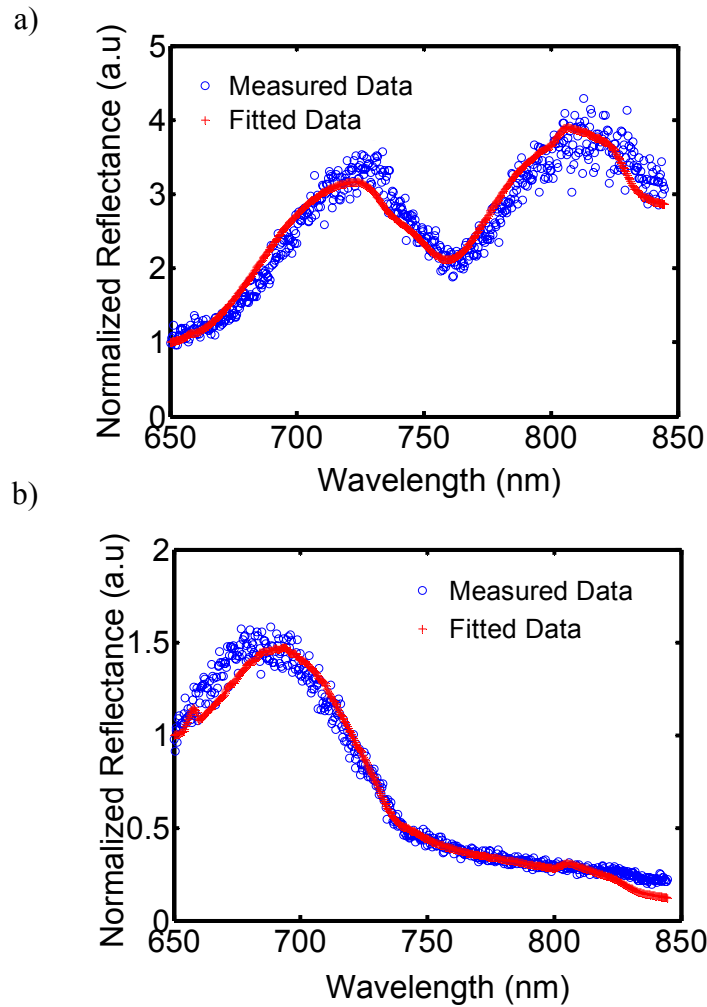
Figure 4.13 Normalized diffuse reflectance spectra. This is based on the 2nd
normalization method: the reflectance values are normalized to one at λ=600 nm.
(a) A spectrum for oxygen saturation of 96.% with [Hb]=1.3 μM, [HbO]=42.5
μM, and μ_s'(750 nm)=6.2 cm^{-1} (5.8 cm^{-1}). (b) A spectrum for oxygen saturation of
37.3 % with [Hb]=25 μM, [HbO]=15.0 μM, and μ_s'(750nm)=6.2 cm^{-1} (5.8 cm^{-1}).
Blue dots indicate the measured data from the phantoms and red curves indicate
the best fits computed from the optimized hemoglobin derivative concentrations
using our algorithm. Hemoglobin concentrations and μ_s' values measured by the
ISS Oximeter are indicated in parentheses.
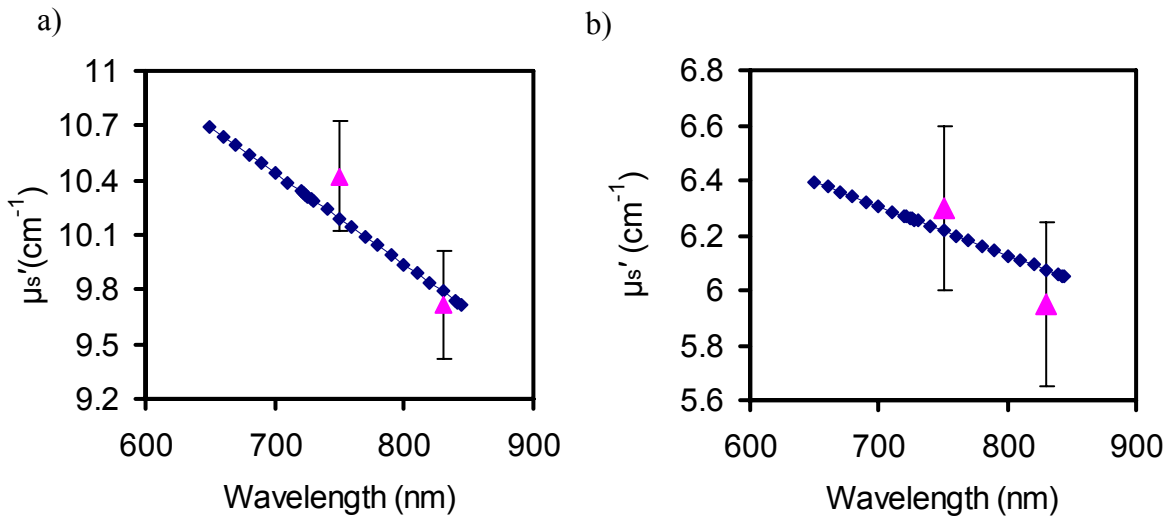
Figure 4.14 Broadband μ_s' spectra for two blood-intralipid phantoms. Triangles represent discrete μ_s' values measured by the ISS Oximeter, Diamonds are the best fits obtained from my algorithm. (a) Spectrum of μ_s' with $\mu_s'(750nm)=10.1$ cm^{-1} (10.6 cm^{-1}) and $\mu_s'(830nm)=9.9$ cm^{-1} (9.7 cm^{-1}). (b) Spectrum of μ_s' with $\mu_s'(750nm)=6.2$ cm^{-1} (6.3 cm^{-1}) and $\mu_s'(830nm)=6.1$ cm^{-1} (5.9 cm^{-1}). The error bars shown are the derived standard deviations from the ISS Oximeter measurements.

Figure 4.14 shows the least-squares fit to the μ_s' values, obtained from my algorithm, and those measured by the ISS Oximeter on the blood-intralipid phantom. As expected, the wavelength dependence of μ_s' in the NIR wavelength range is fairly smooth, weak, and possibly predictable. It is evident that the determined values of the reduced scattering coefficients lie within the error ranges of the ISS oximeter. The error bars are derived standard deviations from the ISS Oximeter measurements
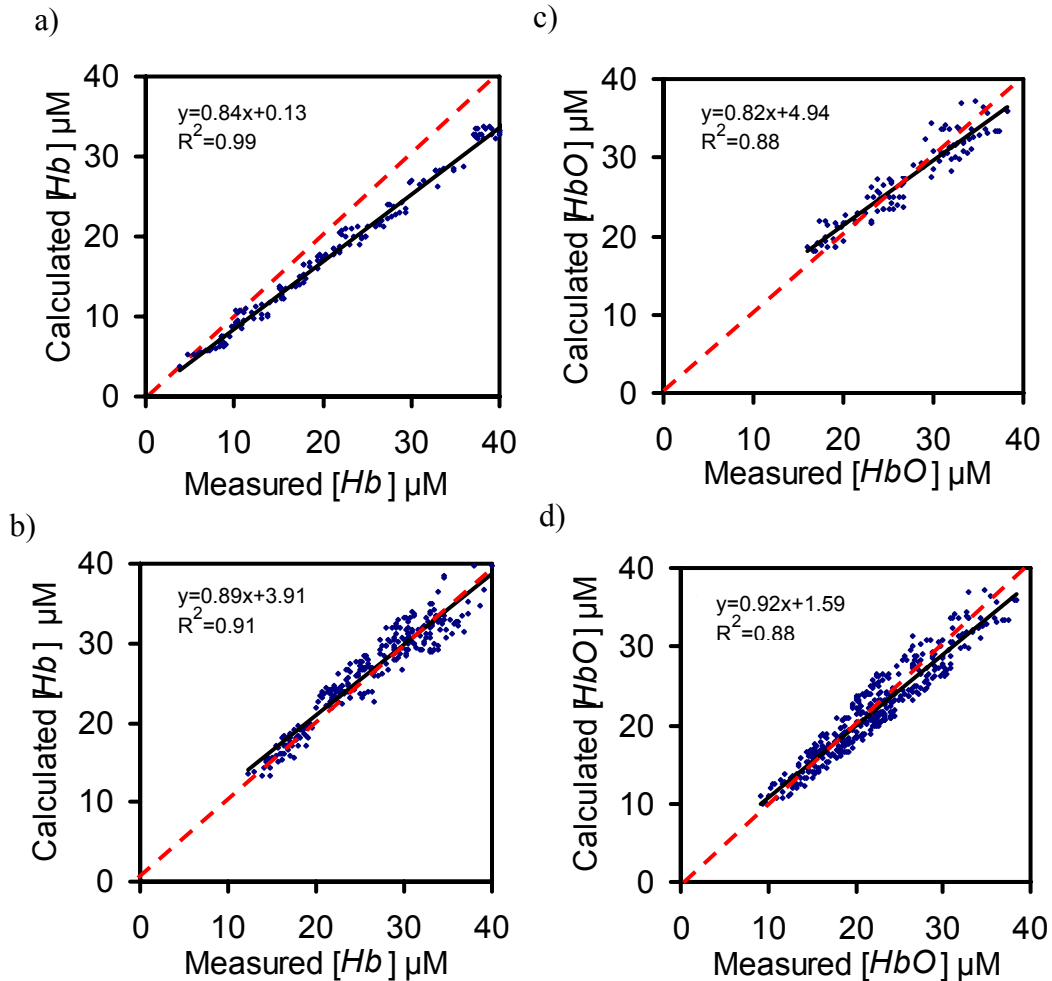
Figure 4.15 Correlation plots of the calculated (from my algorithm) versus ISS Oximter measured [HbO] and [Hb] from multiple sets of blood-intralipid phantoms. The individual dots indicate the data, and the solid black lines are the resulting linear regression lines for correlation comparison. A unity line (red line) in each panel is placed to indicate the desired ideal result. (a) Correlation plot for [Hb] (slope= 0.84, intercept = 4.98) with an old experimental setup. (b) Correlation plot for [Hb] (slope= 0.88, intercept = 3.1) with the new experimental setup. (c) Correlation plot for [HbO] (slope= 0.82, intercept = 4.9) with an old experimental setup. d) Correlation plot for [HbO] (slope= 0.91, intercept = 1.5) with the new experimental setup.

Figure 4.15 shows results in the form of correlation plots between the [Hb] and

[HbO] calculated from the developed algorithm versus those measured by the ISS

Oximeter. Figure 4.15(a) and Figure 4.15(c) show the correlation plots for the

measurements made with an old experimental setup (Figure 4.6(a)). Figure 4.15(b) and Figure 4.15(d) show the correlation plots for the measurements made with a new experimental setup (Figure 4.6(b)). It is desired that the developed algorithm produces a correlation plot as close as possible to a straight line with a unit slope and zero intercept. The correlation plots provide a simple and established metric to evaluate the algorithm. The calculated [*Hb*] and [*HbO*] from the measurements made using either an old or improved experimental setup correlated well with the ISS Oximeter readings, as listed in the figures. The relative errors in all measurements of [*Hb*], [*HbO*] and reduced scattering coefficients were less than 15% with the old and new experimental setup. It is seen that the slopes are better, i.e., closer to unity, for both [*Hb*] and [*HbO*] when the improved experimental setup was utilized. This improvement is due to the reduction in erroneous oxidation of deoxygenated blood from oxygen in ambient air in the old experimental setup. The oxidation of the liquid phantom by ambient air was reduced in the new setup as mentioned in Section 4.3.1.

The advantage of using tissue-equivalent phantom data to validate the algorithms is that one can also gauge the extent to which the algorithm is model specific, e.g., one can test whether a favored algorithm performs equally well when applied to data generated using a different set absorption and reduced scattering coefficients. My analysis has been repeated for a range of concentrations of [*Hb*] and [*HbO*] as well as reduced scattering coefficients using a wide range of tissue like phantoms. All sets of concentrations of [*Hb*] and [*HbO*] have been tabulated in Appendix D.

4.4.2 Hemodynamic monitoring of brain tumors in vivo

Several reflectance spectra of the brain tumors at various stages of growth are shown in Figure 4.16. The measurements of reflectance spectra were made as mentioned earlier in this section. The fitted data are obtained using the developed algorithm. The plots with blue dots are experimental data, and red curves are full-spectrum fits.

It is evident from Figures 4.16(a), 4.16(b), and 4.16(c) that the peak in the wavelength range of 800-850 nm increases with respect to the peak at 700-750 nm. This becomes clear after inspection on Figure 4.4, where the simulations were carried out at different oxygenation states. A decrease in blood oxygen saturation brings about the noticed spectral changes. Specific absorption of Hb is significantly higher than HbO in the wavelength range 600-800 nm, after which the specific absorption of HbO is higher than that of Hb [29]. Thus, we can conclude that the rat brain has been gradually deoxygenated for the cases shown in Figures 4.16(a), 4.16(b), and 4.16(c).
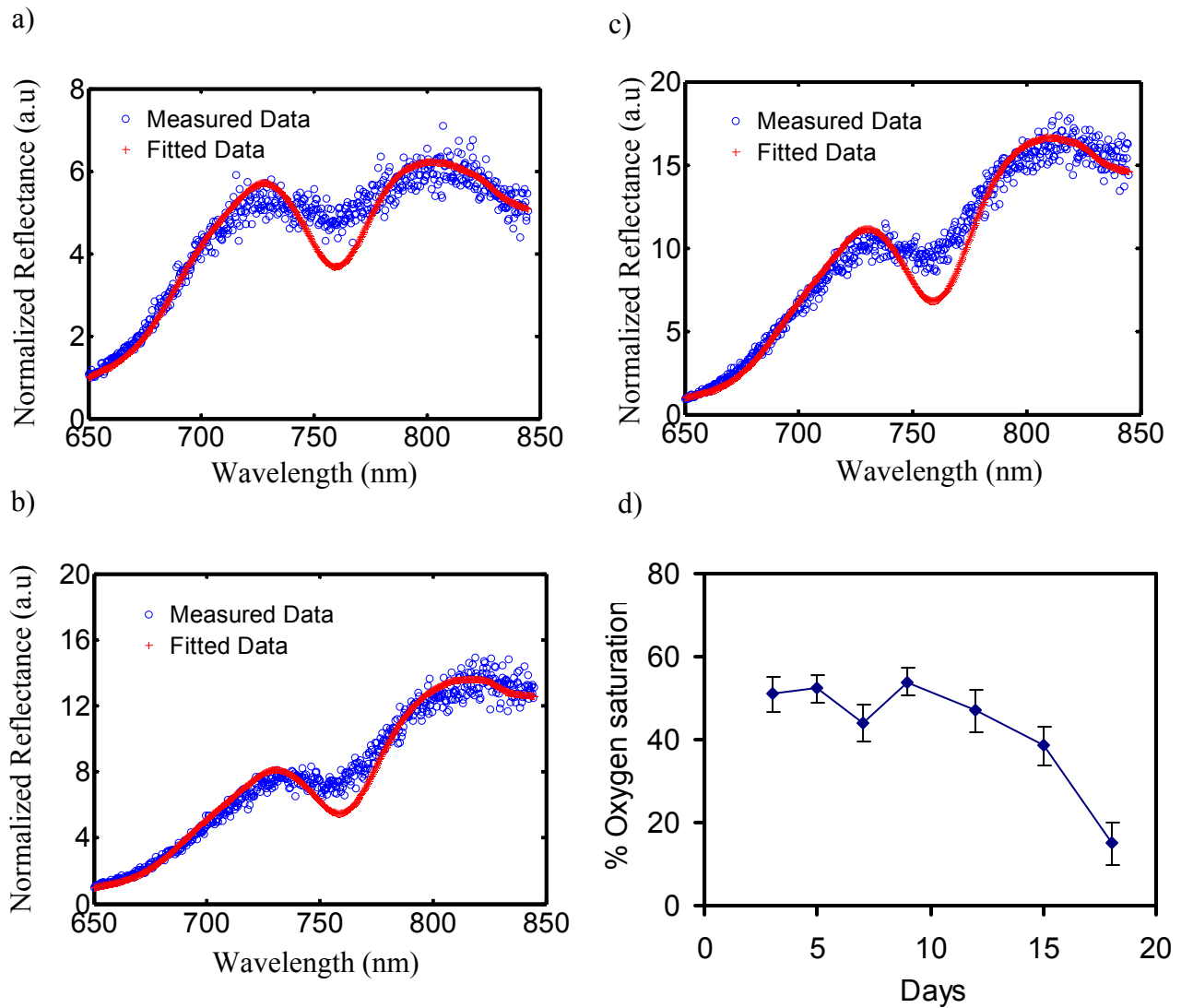
Figure 4.16 Normalized diffuse reflectance spectra acquired from an implanted brain tumor with a source detector separation of 1.7 cm. Reflectance values are normalized to the reflectance at $\lambda = 600$nm. Blue dots indicate the measured data from the animals and red curves indicate the best fitted spectra computed from the optimized hemoglobin derivative concentrations using my algorithm. (a) Day-3 after tumor implantation: Spectrum for an oxygen saturation of 55-60%, (b) Day-15: Spectrum for an oxygen saturation of 37.3%, c) Day-18: Spectrum for an oxygen saturation of 15%, and d) Oxygen saturation monitored throughout the growth of tumor. The decrease in oxygen saturation with tumor progression is clearly evident.
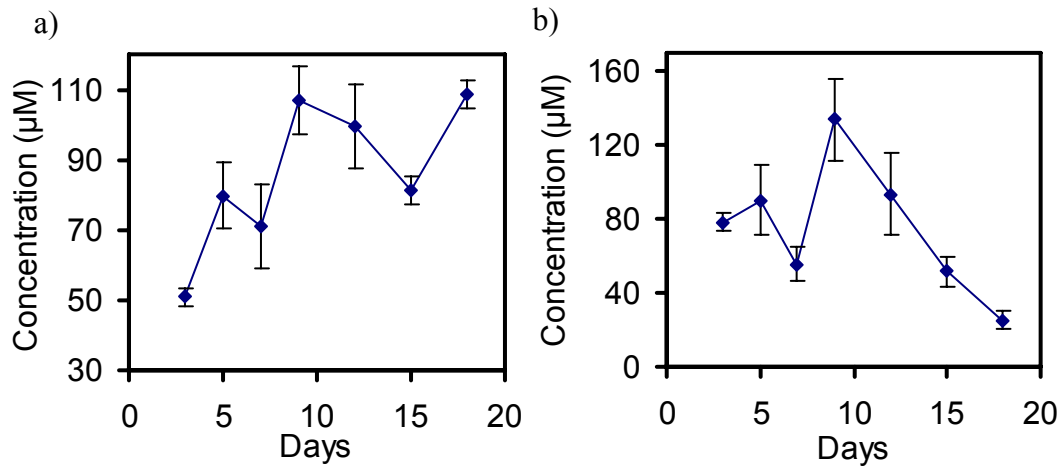
Figure 4.17 [*HbO*] and [*Hb*] concentrations measured with the tumor grown in a rat brain. a) [*HbO*] b) [*Hb*]. The increase in [*Hb*] and decrease in [*HbO*] are clearly seen.

As seen in our previous tumor studies [9, 90, 91] and investigations from other groups [92], an implanted tumor in the right caudate nucleus was seen to become increasingly hypoxic. The blood oxygen saturation, as determined by our algorithm, decreased from a value of 60% during the initial stages of tumor growth to almost 15% just prior to the sacrifice of the animal. Other indicators behaved consistently as the rats appeared increasingly sick with tumor growth. A reduction in animal's body weight was also observed.

Figure 4.17(a) and Figure 4.17(b) show a decrease in [*HbO*] and an increase in [*Hb*], respectively, during tumor progression. A steady trend of decrease in [*HbO*] with simultaneous increase in [*Hb*] is observed with tumor growth. Further investigations using more animals are needed and currently undertaken by my colleagues in the laboratory to confirm/investigate these observations. The results given in this study mainly demonstrate the feasibility of the developed technique for detecting changes in

oxygen saturation levels, [*Hb*] and [*HbO*], potentially serving as physiological markers for tumor prognosis and for cancer therapy monitoring.

4.4.3 Evaluation of heterogeneities in hemodynamic parameters in prostate lesions

Hemodynamic characterization of excised prostates was made to evaluate extent of heterogeneities with respect to penetration depth. Hemoglobin concentrations and oxygen saturations were evaluated at different depths. Shallow depths were probed using a shorter source-detector separation (0.95 cm), which preferentially investigates shallower depths in comparison with a separation of 1.5 cm [2]. My analysis will show that hemoglobin concentrations and light scattering in superficial regions of the prostrate glands were significantly higher in comparison with those determined at deeper regions of prostates.
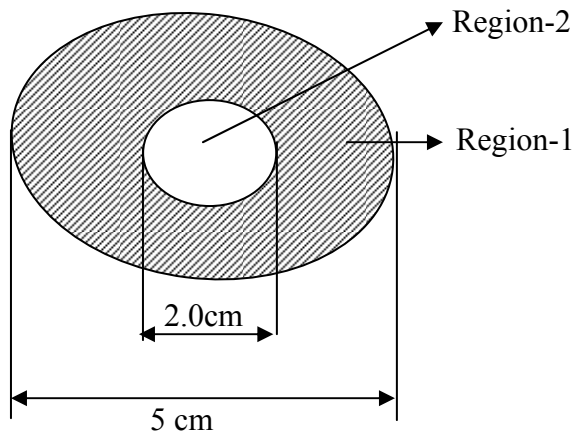
Figure 4.18 Locations of diffuse reflectance measurements on the excised specimen of human prostate gland: 29 measurements were made around the surface of the prostate gland, which is labeled as Region-1 all around the prostate gland. 5 measurements were made from Region-2, which is a randomly designated area at the top of the prostate gland. Regions 1& 2 were investigated for differences in [*Hb*], [*HbO*] and reduced scattering coefficients.

Figure 4.18 displays the locations of Regions 1 and 2 that are used for quantifications of hemoglobin concentrations and light scattering given in Figures 4.19-4.22 and in Table 4.1. A total of 29 spectral measurements were made around the surface of the prostate gland, which is labeled as Region-1 all around the prostate gland (Figure 4.18) with the optical probe shown in Figure 4.9 at distributed locations. Another set of 5 measurements were made from Region-2, which is a randomly selected region at the top of the excised prostate gland, by placing the optical probe as shown in Figure 4.10 at different orientations within Region-2.
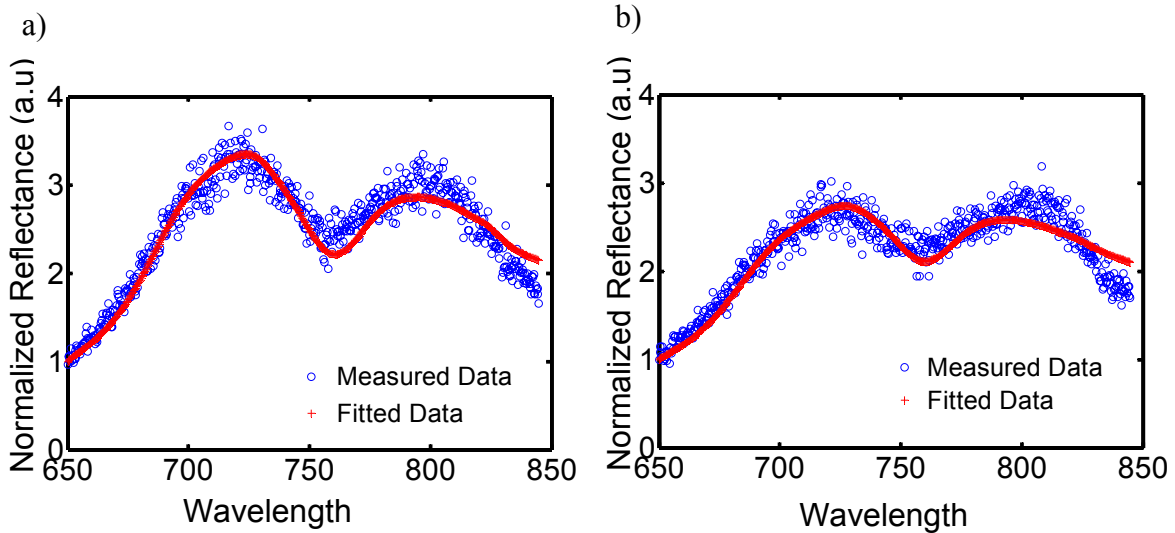
Figure 4.19 Normalized diffused reflectance spectra from non-hypoxic and hypoxic lesions. Reflectance values are normalized to reflectance at $\lambda = 600$ nm (Normalization method II). (a) It is taken from a non-hypoxic lesion with an oxygen saturation of 65%. b) It is from a hypoxic lesion with an oxygen saturation of 49%.

Figure 4.19 displays two representative reflectance spectra from non-hypoxic and hypoxic lesions measured on the same excised prostate.. Two spectral peaks can be seen in the spectrum near 720 nm and 800 nm. The increase in the level of peak

between 700-750 nm indicates an increase in oxygen saturation and decrease in [*Hb*], whereas an increase in the level of peak between 750-845 nm indicates a decrease in oxygen saturation and corresponding increase in [*Hb*].

Figure 4.20 and Figure 4.21 attempts to illustrate heterogeneities in [*HbO*] (Figure 4.20(a)), [*Hb*] (Figure 4.20(c)), oxygen saturations (Figure 4.20(b)), μ_s'(750nm) (Figure 4.20(d)), and [*Hb$_{Total}$*] (Figure 4.21) with respect to penetration depths in an excised human prostate gland. Two locations of measurements (considered as Region 1 and Region 2) were measured on the prostate gland, and the corresponding data are tabulated in the Appendix D. Oxygen saturations in Region 1 were lower for both separations in comparison to those seen at Region 2, but the differences were not significant (p=0.432). Oxygen saturations were higher in superficial regions in comparison with the deeper regions for both regions. These findings are in line with the reports given in previous studies [78]. Moreover, [*HbO*] and [*Hb*] concentrations in superficial regions, from both Regions 1 and 2, were significantly greater (p<0.01) when compared with those from deeper regions. The values of reduced scattering coefficients were significantly higher in superficial regions as compared with the deeper regions, for both Regions 1 and 2.

Figure 4.22 summarizes the comparisons of [*Hb*], [*HbO*], oxygen saturations, water content and μ_s' (750nm) at separations of 0.95 cm and 1.5 cm for overall 34 measurements taken from the same excised prostate specimen. The averages of parameters at each source-detector separation include both regions 1 and 2 since overall there is no significant difference between the two regions, except for [*Hb*] (p=0.005)

and [Hb_{Total}] (p=0.006) with ρ=0.95 cm. [Hb] concentrations measured at ρ=0.95 cm are not averaged but indicated separately for Regions 1 and 2. All hemoglobin concentrations and scattering coefficients measured at the two penetration depths are tabulated in Table 4.1. This Table shows clearly that [HbO], [Hb], [Hb] measured at Region-1, [Hb] measured at Region-2, [Hb_{Total}] measured at Region-1 and [Hb_{Total}] measured at Region-2 and μ_s' are significantly different between the superficial and deeper regions ($p < 0.002$), while percentages of hemoglobin oxygen saturation and water do not exhibit depth-dependent differences. This analysis has been repeated on two more specimens of excised human prostate with consistent results.

Table 4.2 Optical properties and hemoglobin concentrations taken at different source-detector separations from an ex-vivo human prostate specimen (n = 34 for all except for region specific concentrations: n = 5 for Region-2 and n = 29 for Region-1)

Separation	0.95 cm	1.5 cm	p values
Region-1 [Hb] (μM)	47±6	26±11	0.0008
Region-2 [Hb] (μM)	92±11	33±6	0.0003
[HbO] (μM)	172±30	37±16	2.23E-5
Region-1 [Hb_{Total}] (μM)	206±54	67±21	0.0005
Region-2 [Hb_{Total}] (μM)	301±37	64±25	1.59E-5
% Oxygen Saturations	79±4	58±7	0.001
% Water	72±4	71±4	0.613
μ_s'(λ=750nm) cm^{-1}	11±1.4	5±1.2	1E-5
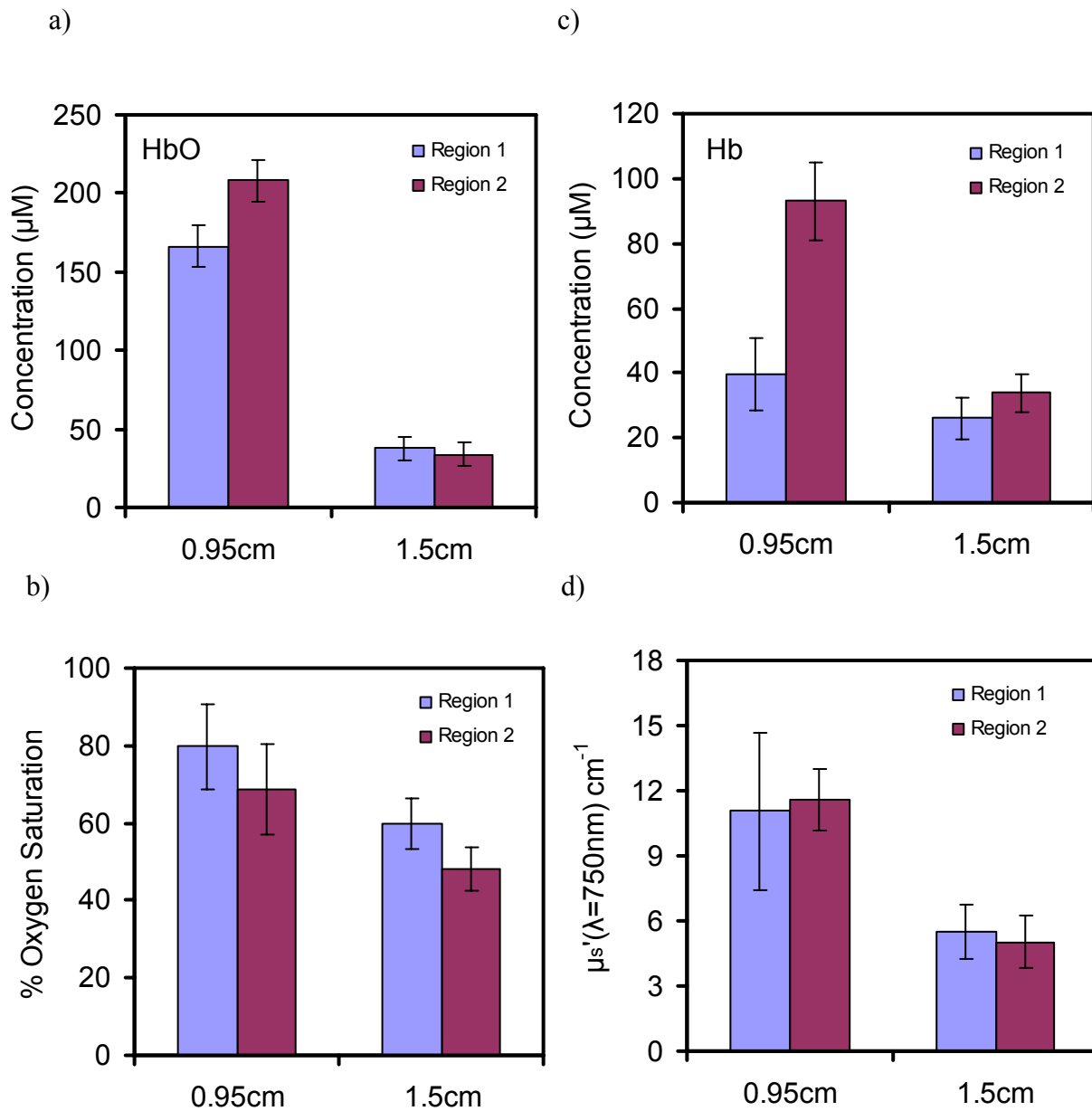
Figure 4.20 Comparison of hemodynamic parameters at superficial and deeper regions: (a) [*HbO*], b) [*Hb*], c), Oxygen Saturation, and d) μ_s' (750nm). Regions 1 and 2 refer to separate lesions on the prostate gland. The location of each measurement is tabulated in the Appendix D. Optical reflectance was measured at source-detector separations of 0.95 cm and 1.5 cm.
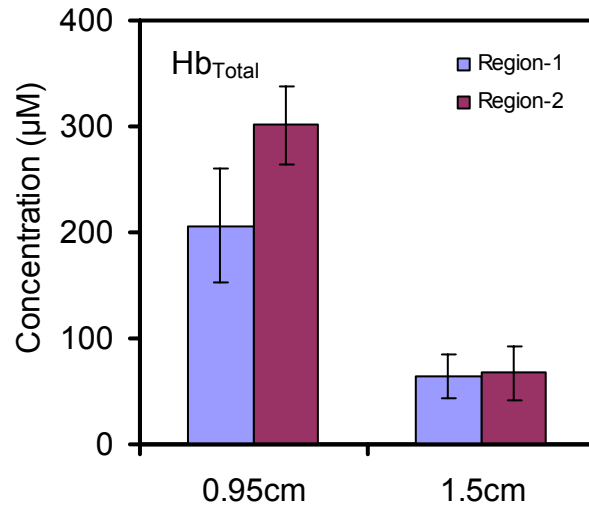
Figure 4.21 Comparison [Hb_{Total}] at superficial and deeper regions. Regions 1 and 2 refer to separate lesions on the prostate gland. The location of each measurement is tabulated in the Appendix D. Optical reflectance was measured at source-detector separations of 0.95 cm and 1.5 cm.
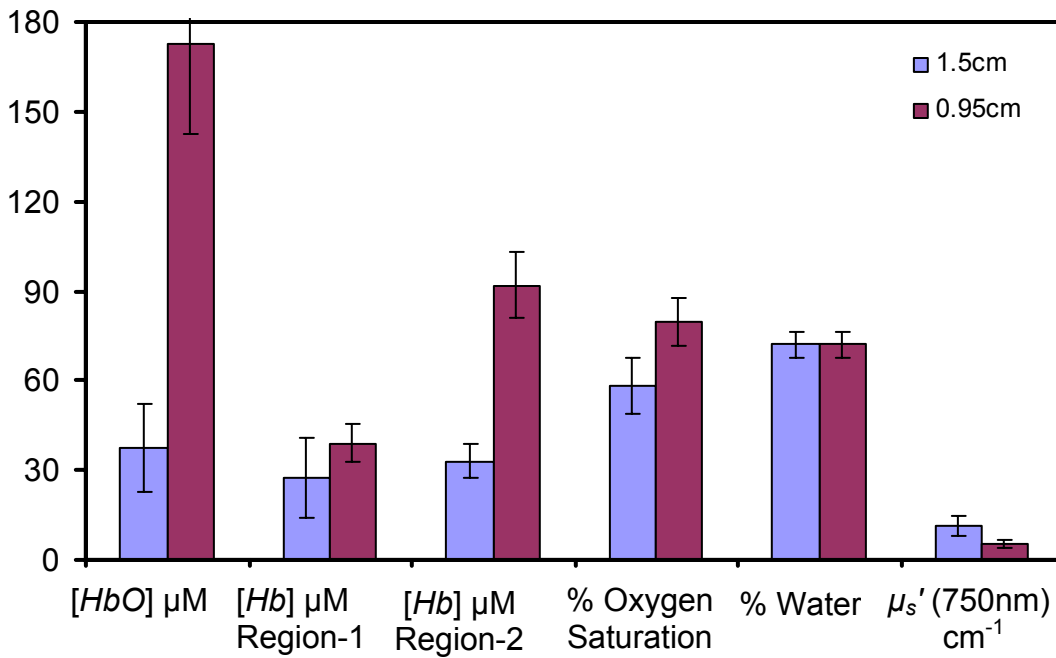
Figure 4.22 Comparison of [HbO], [Hb], oxygen saturation, water content and μ_s'(750nm) taken from an excised human prostate at superficial (0.95 cm) and deeper (1.5cm) regions. The mean and standard deviations of all parameters are tabulated in Table 4.1. The range in the graph has been selected for viewing all the parameters.

4.5 Discussion

The developed algorithm demonstrated that the steady state measurements in 650-850 nm can accomplish the goal of quantification of optical properties in tissues. Use of spectral dependence of absorption and scattering is the single most important requirement for this study. Fitting a wavelength-dependent function of concentration of absorbing chromophores to the reflectance values yields hemodynamic and light scattering parameters for the measured tissue.

4.5.1 Effect of filtering used to calculate second derivative

Second differential spectroscopy has been used to arrive at an initial guess of deoxygenated hemoglobin concentrations. Smoothing of data using Savitzky-Golay filtering [81] was taken to eliminate spurious introduction of noise into the second derivative spectra, but the smoothing can lead to loss of high frequency component of the data. This loss is very minimal in the wavelength range considered for the calculation of the second derivative. Loss of spectral resolution due to smoothing of the data is obvious, but it does not affect the second differential spectroscopic estimates of [*Hb*], as shown by Matcher et al [24]. Wavelength dependence of scattering coefficients in this range is weak and a decreasing linear function. Hence scattering does not contribute to the second derivative spectra. This is of significant advantage, as this decouples the effects of absorption and scattering, enabling the computation of [*Hb*]. Advantage gained by using the second derivative spectroscopy to determine absolute concentration of deoxygenated hemoglobin far outweighs the marginal loss in accuracy in the quantification of second derivative. To correct for this inaccuracy, deoxygenated

hemoglobin concentrations are allowed to vary in a certain small range (10%) around the initial values during the computation for concentration of oxygenated hemoglobin and reduced scattering coefficients. The results and correlation plots (Figures 4.14 and 4.15) obtained from the measurements on blood-intralipid phantoms illustrate the accuracy of this method.

4.5.2 Deviation of measured spectra from spectra modeled diffusion theory

Figure 4.16 shows reflectance spectra measured from rat brains with tumors implanted in right caudate nucleus. Careful visual inspection on the modeled and measured spectra brings up certain systematic deviations. The modeled spectra deviate from the actual measurements in the wavelength range of 740-760 nm. This behavior is likely to be an actual divergence from assumptions of diffusion model. Such deviation appears when the diffusion model's assumptions are not sufficiently fulfilled. The tissue heterogeneity, i.e., the layered superficial structure, the mix of deeper fat globules and fibrous tissue and more importantly the presence of blood vessels such as capillaries, arterioles and venules could be all possible sources of deviation from the model. These deviations between the diffusion model and reality of heterogeneous tissues have been investigated previously by other investigators, who have demonstrated spectral broadening of the measured spectra due to the presence of embedded blood vessels. For example, a previous investigation was carried out on tissue like phantom models by Liu et al [93]. This point becomes clearer if we compare the animal data with the spectra (Figure 4.13) measured from the blood-intralipid phantoms, where there is no spectral broadening seen. In the tissue-like phantoms the distribution of blood is homogenous

and hence consistent with the assumptions used in diffusion theory, as opposed to the real living tissues where heterogeneity of tissue components exists, giving rise to possible spectral broadening in the reflectance spectra.

4.5.3 Evaluation of heterogeneities in hemodynamic parameters in prostate lesions

Reliable estimation of optical parameters is a critical issue in the dosimetry for photo dynamic therapy (PDT) in particular and for all other therapeutic interventions in general and could play a very important role in its development into a modality for treatment of prostate cancer. This study with the use of steady state NIRS was able to generate estimations of μ_s', $[Hb]$, $[HbO]$ and oxygen saturation for excised prostates, and thus providing an insight into variation of vasculature with respect to depth in the prostate gland. In addition, the instrumentation requirements are fairly simple and economical, needing only two fixed fibers and a spectrometer for a single measurement. While my study in this particular area is very preliminary, I have demonstrated the feasibility of the technique to quantify μ_s', $[Hb]$, $[HbO]$ and oxygen saturation in excised prostate tissues, and particularly showing high heterogeneity in both vasculature and light scattering with respect to depth in the prostate gland. Future investigations from more human specimens are needed and currently undertaken by my colleagues in the laboratory to confirm/investigate my observations.

4.6 Conclusion

Multi-wavelength, steady state reflectance techniques have been described for quantification of tissue chromophores and scattering coefficients. The beneficial aspects and shortcomings of the technique have been mentioned. With broadband, steady state spectroscopy, the wavelength coverage is continuous. This technique requires only a single source–detector separation, making it suitable to report volume-averaged values of optical properties for heterogeneous tissues. Furthermore, the source–detector separation can be large (1-4 cm, even 5-6 cm if stronger light sources are used), allowing for mean probing depths to be in centimeters that cannot be achieved with multi-source-detector, steady state techniques [26]. This advantage permits to probe deep tissues and thus is significant for many clinical purposes. The developed technique was validated by making simultaneous measurements with the ISS Oximeter. The calculated concentrations of Hb and HbO correlated well with the expected values. The μ_s' values calculated from the algorithm were within $\pm\ 1\ cm^{-1}$ of those measured by the ISS Oximeter.

The feasibility of using the technique that I developed in this study to quantify optical properties of human prostate lesions and during the growth of orthotropic brain tumors in rats has been demonstrated, with spectral acquisition time of less than 500 ms. The total hemoglobin content, oxygen saturation, and water fraction of prostate lesions and rat brain tumors in vivo have been quantified and shown to have physiological meanings for respective applications. This technique is relatively inexpensive and could prove valuable in improving accuracy and for developing online monitoring techniques.

One deficiency of my method is the inability to quantify water content or percentage in tissues because of the intrinsic approach of the second derivative method. With the second derivative spectra of the NIR reflectance from tissues, [*Hb*] can be quantified only by having known or assumed water percentage. This being the case of tumors, water content or percentage can be a sensitive parameter and can serve as a physiological parameter for monitoring tissue/tumor status. Further study should be carried out in order to overcome this shortcoming of the method.

CHAPTER 5

BROADBAND NIRS MULTI-CHANNEL IMAGING SYSTEM FOR SPATIAL
DISTRIBUTION OF HEMOGLOBIN DERIVATIVES

5.1 Introduction

Chapters 2 and 4 described the methods to quantify optical properties of tissue at small (100 μm – 1 mm) and large (1-4 cm) source-detector separations. In Chapter 4 spatial heterogeneities in hemoglobin derivative concentrations and reduced scattering coefficients were ignored, and volume-averaged parameters were computed. This approach is not accurate in real biological tissues when the investigated volumes are large as measured with large source-detector separations. To address this requirement, this chapter describes the design and development of a steady-state, broadband, NIRS imaging system to evaluate the spatial extent of heterogeneities in chromophore concentrations and reduced scattering coefficients.

NIRS based approaches have been used to monitor hemoglobin concentrations and their changes in biological tissues [3, 31, 71] and to characterize malignant and normal tissues based on the high intrinsic contrast available from heme in blood [12, 94-96], leading to images that are related to patho-physiologic processes of tissues such as angiogenesis and hypoxia. The common spectroscopic imaging methods utilize a minimum of two wavelengths, one above and one below the isobestic wavelength of deoxygenated hemoglobin and oxygenated hemoglobin, Hb and HbO, respectively.

DOT (Diffuse Optical Tomography) imagers have been built in the steady state domain [97, 98], time domain [99-101] and frequency domain [102]. These imagers have been earlier designed and used to detect malignancy in animal and human breast tumors [103], detect brain activity [27], and abnormality in bones [104, 105]. The reconstruction of chromophores and scattering properties depends upon the spectral decomposition of the images acquired at a few discrete wavelengths. Sparse spectral sampling together with an image reconstruction problem, which is ill posed, amplifies errors in quantification of spatially resolved parameters [74].

It is believed that better accuracy can be achieved with additional numbers of wavelengths to improve spectroscopic information [18]. The extreme extension of this is to take a broadband approach, where light with a broad spectral width is transmitted into the tissue and a spectrum is detected by the use of the combination of a spectrograph and CCD array detectors. With multispectral data, other chromophores, such as water, lipid, and cytochrome, can be analyzed together with hemoglobin. Moreover, the microscopic scattering particle size [106], density, and distribution can be investigated from the reduced scattering coefficient spectrum [44].

The design presented in this chapter aims to overcome the drawback of sparse wavelength sampling by utilizing a broadband white light source that provides a wide continuous spectrum in the wavelength range of 650-1000 nm. This study focuses on the advantage of a spectrally constrained approach for image reconstruction, which follows recent pioneering developments proposed by Corlu et al [107] and Srinivasan et al [74]. Corlu et al and Srinivasan et al showed that incorporation of spectral

constraints into the reconstruction process improves the uniqueness of image formation by using continuous-wave data and frequency domain data, respectively. My approach given in this Chapter examines the use of a multiple set of discrete wavelengths from a continuous band of wavelengths for the improved accuracy in quantification of chromophores and reduced scattering coefficients.

Specifically, I firstly describe the design, construction and operation of a broadband NIR tomography system in Section 5.2. Each of the eight source optodes transmits broadband NIR light at 650–1000 nm in an alternating pattern, and the spectra from a circular tissue phantom are simultaneously obtained from each of the eight detector optodes, which are co-located with the source optodes (probes). Section 5.3 provides a description of design and construction of hemodynamic phantoms for validation of the developed hardware system and reconstruction algorithms. Section 5.4 describes the methodologies adopted for image reconstructions. In Section 5.5, phantom studies to validate and characterize the imager are presented.

5.2 Instrumentation

The intended function of the instrumentation is to measure the complete spectrum over the wavelength range 650–1000 nm from eight transmitting fibers and eight receiving fibers placed alternately around the phantom. The 8 transmitting and receiving fibers are bifurcated so that the number of fiber optodes is only 8. The system uses parallel detection so that each transmitting fiber is illuminated in sequence, and spectra from all eight receiving fibers are collected and sent to an 8-channel spectrometer simultaneously.

Figure 5.1 shows a schematic diagram of the 8-channel imager. The imager consists of four major functional components: 1) one broadband CW light source, 2) optical multiplexer to multiplex the light into 8 channels, 3) 8-channel CCD array spectrometer to detect the light reflected from the surface of the sample, and 4) 8 optical fiber bundles with bifurcated fibers for each. Light is transmitted from the light source to the optical multiplexer, which multiplexes the light source into eight light. Light from each of the 8 channels are delivered in sequence to the surface of a circular phantom by the optical fibers and collected by the detection fibers around the phantom and then delivered to the 8-channel CCD spectrometer.
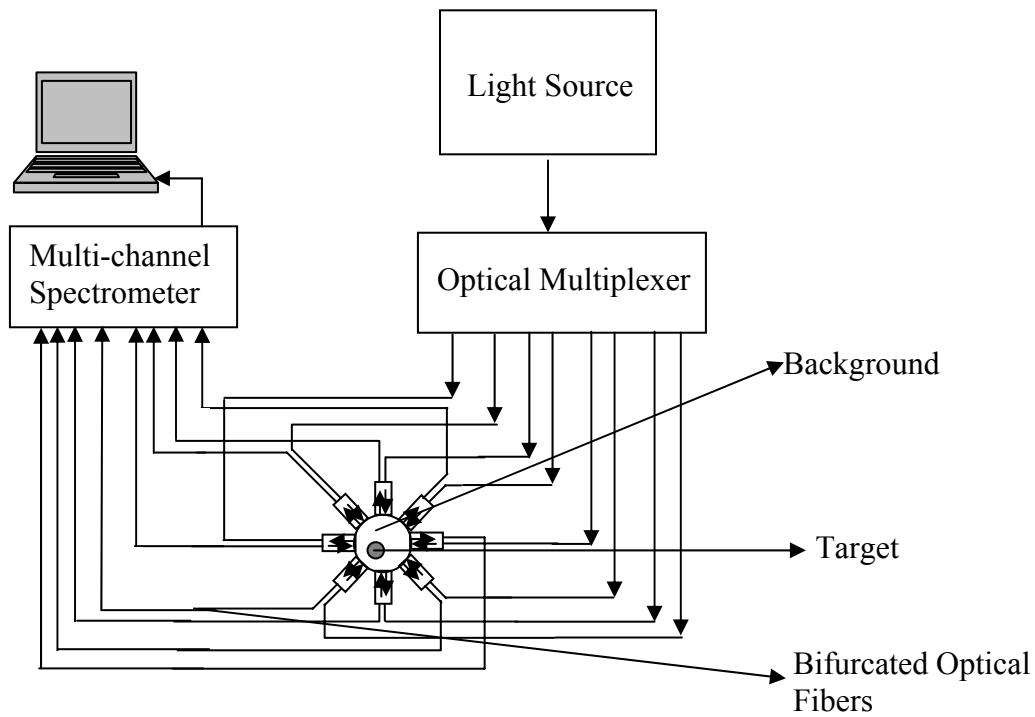
Figure 5.1 Schematic of 8-channel NIRS imaging system depicting the light source, optical multiplexer and 8-channel CCD spectrometer.

127

5.2.1 Light source

The imaging system uses a fiber-optic illuminator (Illumination Technologies, Inc. Model 3900 DC regulated, Light Feedback Fiber Optic Light source.) as the light source. It is a self-contained unit, in which a built-in regulated and power factor corrected, 24-V dc supply powers a 150-W, broadband, quartz–tungsten halogen lamp, emitting light in the region of 250–2500 nm. Light from the light source is delivered via an optical fiber (Illumination Technologies,,3mm core diameter, SMA) to the optical multiplexer.

5.2.2 Optical multiplexer

The Fiber Optic Multiplexer (Avantes Inc. FOM-VIS-NIR (200-1100 nm), 1 x 16 channels, for 1-mm fiber core) is an instrument that can optically couple 1 input channel to 16 different output channels. The multiplexer consists of a precisely controlled stepper motor and a rotator block. The optical path is coupled through multiple COL-UV collimating lenses. This multiplexer is software controlled and interfaces to a PC through the RS-232 protocol. The software enables full control of the switching order, switching time and delay time. The device has a working wavelength range of 350-2000 nm with a 1-mm diameter for the fiber core. Switching delay between adjacent positions is of the order of 60 ms.

5.2.3 Light delivery and collection

Light from the light source is delivered via an optical fiber to the optical multiplexer. A set of eight bifurcated optical fibers deliver light from the optical multiplexer output channels to the surface of the sample and collect light from the

surface of the sample. The collected light is delivered to the 8-channel CCD array spectrometer (Ocean Optics Inc, Florida, S2000 Spectrometer (350-1050 nm), 200-µm slit width) with the bifurcated fibers. The eight sets of fibers deliver and collect light from the sample. The arrangement becomes apparent from the photograph of the phantom and fiber assembly, as shown in Figure 5.2.
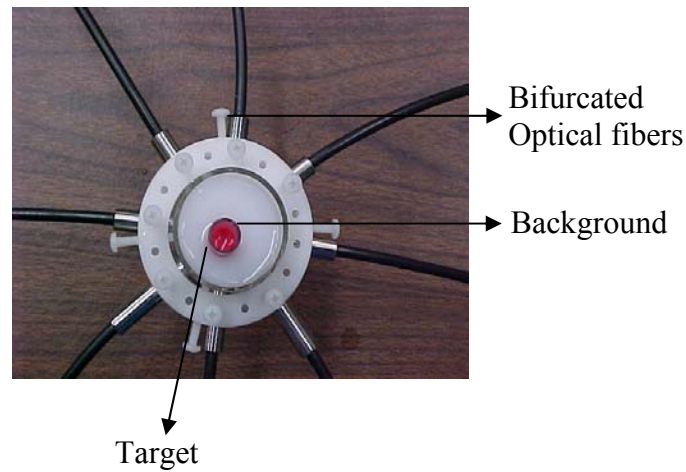
Figure 5.2 Photograph of a typical phantom used for evaluating the imager and reconstruction algorithms. The optical fiber arrangement around this phantom is also depicted. The eight fibers are spaced equally around the circumference. The fibers are held in place by a fiber holder.

Optical fibers play an important role in the performance of the system. It is desirable to deliver light with minimum attenuation in fibers and gather a maximum possible fraction of light that is reflected or transmitted through the specimen so as to achieve a highest feasible SNR. The geometry of optical fibers used in the system is illustrated in Figure 5.3.

The core diameter of the optical fibers was 1 mm. The active diameter at the common end of the bifurcated fiber bundles is larger than that at the bifurcated end. The active diameters at the SMA terminated ends (going to light source or spectrometer channels) are restricted to a 1mm. The active diameters at the SMA end are restricted to cater to the slit height of spectrometer entrances and the core diameter of multiplexer fibers (1mm). The numerical aperture (NA) of the fiber bundles are designed to be 0.22.
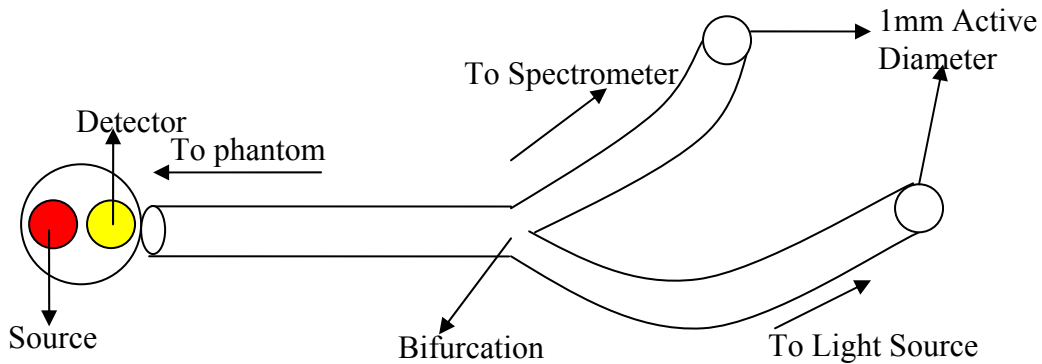
Figure 5.3 A bifurcated optical fiber for light delivery and collection. It illustrates the geometry of the source and detector fibers in the bifurcated fiber bundle. Single borosilicate fibers with diameters of 1 mm are used. At the common end the source and detector fibers appear to be next to one another as shown. The bifurcated ends are terminated with SMA terminations. The overall length of the fiber bundle is ~10 feet.

5.2.4 Measurement sequence

To start with, the multiplexer brings the light to channel-1 or the source fiber of bifurcated fiber-1. Spectral measurements are made from all channels of the spectrometer. In the next step, multiplexer switches the light source to the next fiber. All measurements are accomplished with an in house Labview™ program. The

software automates the sequencing of multiplexer switching and spectrum acquisition for the spectrometer channels. Same protocol of measurement is repeated for the multiplexer cycles through all fibers to complete one set of measurement. Spectral acquisition times are of the order of 1 second per channel, resulting in a total acquisition time of 10 seconds for one set of measurements. All spectra measured simultaneously from 8 channels (i.e. 8 detector probes) are stored in the desktop computer for post measurement analysis.

5.3 Laboratory phantoms for image reconstruction

Two types of phantoms were designed and built to validate the developed instrumentation and image reconstruction algorithms. Static phantoms with a single inclusion/heterogeneity/target were first used to validate the newly developed system. Multi-tube phantoms were built to model and mimic the flow of blood in blood vessels as seen in real tissue vasculature [108]. These phantoms are more realistic and resemble tissue vasculature. Phantoms have the ability to change or modulate their optical properties in response to oxygenation levels. Intralipid and animal blood suspensions were used as tissue simulating liquids. The defibrinated horse blood (Hemostat Inc, San Francisco, CA) was used in all of my experiments.

5.3.1 Static phantoms

The simple tissue-simulating phantom was built in a cylindrical glass tube of 15 cm×5.5 cm (length x diameter) with a wall thickness of 0.2 cm. The tissue vasculature was simulated by a single cylindrical glass tube of 20 cm × 1 cm (length x diameter) placed inside the large glass tube, resembling a group of vessels, containing a solution

of intralipid and blood with a higher concentration compared with the solution in the background (Figure 5.2). The inner tube was made longer than the outer tube to facilitate addition and removal of blood-intralipid mixture from the tube. The inner cylindrical tube was surrounded by a blood and intralipid solution in the outer glass tube. The blood-intralipid solution in the inner tube (20cm × 1cm) is covered and maintained airtight with a paraffin film to prevent it from getting oxygenated. Stock solution of 20% Intralipid was diluted from 20% to 1% or 0.5 % to yield optical properties similar to those of tissues [33, 41]. The blood- intralipid solution was oxygenated and deoxygenated as described previously (Section 4.3.1) by bubbling oxygen or nitrogen, respectively. The ISS Oximeter was used to measure the reduced scattering coefficients and concentrations of hemoglobin derivatives in the blood-intralipid solution for verification of the results. For the ISS oximeter measurement, the oxygenation and deoxygenation of blood-intralipid solution was carried in a different container. The solutions were then transferred to the respective tubes. A photograph of this phantom is shown in Figure 5.2.

5.3.2 Multi tube phantoms

Multi-tube phantoms [108] The phantom was designed and built as a part of Master's thesis by Mr. Raghavendra Ranga. The vasculature is mimicked in a more realistic manner by using transparent tygon tubes with practically smallest possible diameters.

The tissue vasculature is simulated by imbedded small tubes that were placed parallel to the horizontal axis of the outer glass tube, resembling a group of vessels,

located off the central axis of the glass tube as shown in Figure 5.4(a) to Figure 5.4(c). The small tubes were transparent tygon tubes (Cole Parmer, IL) with 3.23-mm outer diameter and 1.3-mm inner diameter. These small tubes were surrounded by the blood-intralipid solution within the outer glass tube as shown in Figure 5.4(b), in the way similar to the earlier phantom model. A manifold at one end of the glass tube distributed the fluid from a single, 9.5-mm tygon tube into the multiple, small tygon tubes that were imbedded within the phantom. Similarly, another manifold at the other end of the phantom reunited the small tubes into one single big tube and collected the fluid into the reservoir.

A peristaltic pump (Master Flex Cole Parmer, IL) was connected to the tube and used to circulate a 50% diluted animal blood solution across the phantom. The blood was diluted with PBS (Phosphate buffered saline) to achieve desired blood concentrations. PBS maintains the osmolarity of blood. This is essential to prevent hemolysis and to maintain the vitality of blood. It must be noted that no intralipid was added to the blood that was circulated through the small imbedded tubes. A sampling port was provided to sample the blood solution periodically in order to check its oxygen saturation and possible hemolysis. The oxygenator/deoxygenator also served as the reservoir for the phantom. The blood was oxygenated/deoxygenated by bubbling oxygen/nitrogen in the reservoir. The reservoir was maintained airtight with rubber corks to eliminate oxygenation of blood from the oxygen in ambient air. The reservoir was constantly stirred with a magnetic stirrer to ensure homogeneity in the blood solution. Blood was drawn from the sampling port to monitor the oxygenation level and

to measure the hemoglobin concentrations using a Co-Oximeter (IL 682 Co Oximeter System, GMI Inc, Ramsey, MN).

The arrangement of optical fibers was similar to the static phantom model, as described in the previous sub-section. The arrangement of fibers becomes apparent in Figure 5.4(a) and Figure 5.4(c). The blood from the reservoir was pumped by the peristaltic pump through the 9.5-mm tube and the manifold into the phantom through the small tygon tubes. A flow rate was set high initially to prime all the tubes with the animal blood. The flow rate was subsequently adjusted such that the outflow was approximately 5 ml per minute. The flow was determined by collecting fluid in a measuring cylinder.

Defibrinated blood diluted with PBS has an oxygen saturation of ~75%. This (oxygenated) blood was first pumped into the phantom, followed by the measurements using the imaging system, as described in Section 5.2. Then the blood was deoxygenated till the oxygen saturation dipped to 45% and then pumped into the tubes again. The deoxygenated blood was pumped till all the earlier oxygenated blood in the tubes was flushed out. This was ascertained by checking oxygen saturation levels at the exit of phantom. The measurements were repeated with deoxygenated blood in the small tubes. The blood was partially re-oxygenated by bubbling oxygen gas or air and pumped into the imbedded tubes until earlier deoxygenated blood was flushed out. The measurements were made then with this partially re-oxygenated blood using the identical method. The oxygen gas was bubbled further in the reservoir to fully
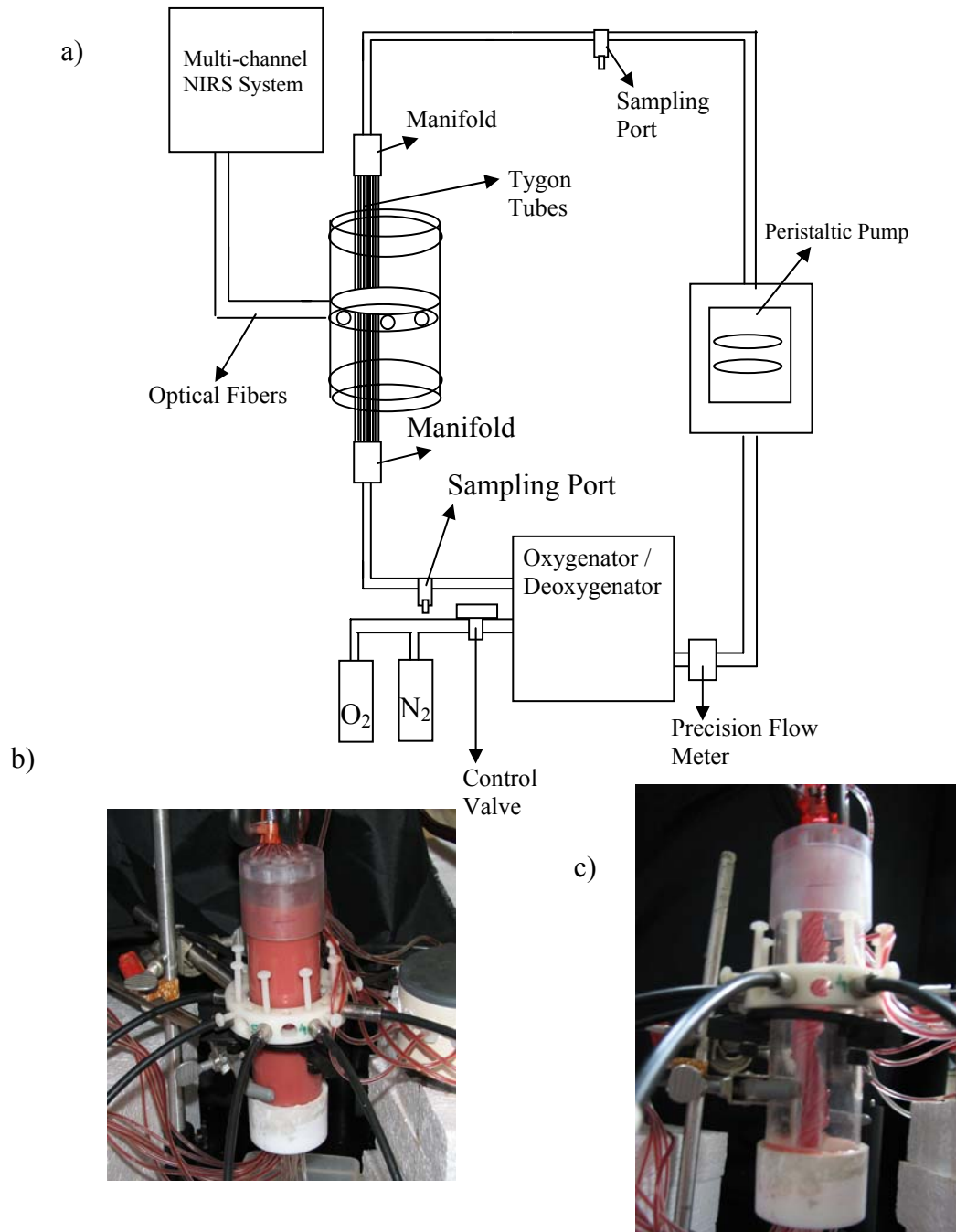
Figure 5.4 (a) Schematic diagram of a multi-tube hemodynamic phantom for image reconstruction. The tygon tubes carry blood within them. The bunch of small tygon tubes are placed slightly offset from the center of the large tube. Oxygenated and deoxygenated blood is pumped into the tubes. (b) A photograph depicting the surrounding blood-intralipid solution and the bifurcated optical fibers held by the fiber holder. (c) A photograph depicting the inner bundle of tygon tubes inside the outer transparent tube with the bifurcated optodes attached.

oxygenate the blood to an oxygen saturation level greater than 95%. This blood was again pumped into the tubes for repeated measurements.

At the end of the experiment, the diluted isopropyl alcohol (5ml in 1L water) was used to cleanse the tubes and manifolds. This dilute alcohol was pumped through the system repeatedly to remove any blood cells that might be stuck to the tubes. Thereafter, the tubes were pumped with hot water to ensure complete cleansing of the phantom. The blood waste disposal was collected and stored in a safety jar for future biohazard collection using the protocol approved by the Department of Environmental Health and Safety at University of Texas at Arlington.

<u>5.4 Image reconstruction</u>

In optical tomography, we aim to update D (Diffusion Coefficient) and μ_a distributions through the solution of Equation (5.1), the steady-state diffusion equation, so that a weighted sum of the squared difference between computed and measured intensities at the detectors can be minimized.

$$\nabla \bullet D(r)\nabla\Phi(r) - \mu_a(r)\Phi(r) = -S(r), \qquad (5.1)$$

where $\Phi(r)$ is the photon density, $S(r)$ is the light source term, $\mu_a(r)$ is the absorption coefficient, and $D(r)$ is the diffusion coefficient, which can be written as:

$$D(r) = \frac{1}{3\left(\mu_a(r) + \mu_s'(r)\right)}, \qquad (5.2)$$

where r is the position vector, $\mu_s'(r)$ is the reduced scattering coefficient. A point source, $S = S_0\delta(r - r_0)$, is used in which S_0 is the source strength and $\delta(r - r_0)$ is the Dirac delta function for the source S_0 at location r_0.

5.4.1 Finite element model of the diffusion equation

A finite-element-based model of the diffusion equation is used for image reconstruction, and its development has been described in detail in a Master's thesis of Aditya Apte [109]. The image reconstruction algorithm is based on steady-state diffusion equation [109], as given in Equation (5.1). The equation can be re-written as shown in Equation (5.3):

$$\nabla(k\nabla u(r)) - \mu_a u(r) = 0,\tag{5.3}$$

where $u = u_s$ at the source, $k = \dfrac{1}{3(\mu_a + \mu_s')}$, and u is equivalent to photon density Φ.

μ_a and μ_s' are the absorption and reduced scattering coefficients at the particular measurement wavelength. A finite element approximation to Equation (5.3) can be expressed as [109]

$$(K_k(k) + K_a(\mu_\alpha))u = 0\tag{5.4}$$

This equation is subject to the boundary condition that $u_j = u_s$, where u_s is the source strength and j is a node on the boundary $\partial\Omega$ where the source is located. Equation (5.4) is used to iteratively update an initial guess of optical property distribution to minimize an objective function composed of a weighted sum of squared differences between the computed and measured data on the boundary detectors. K_k and K_a are assembled from the element matrices according to standard finite element procedures.

$$K_k = \sum (K_e)_k,\tag{5.5}$$

137

$$K_a = \sum (K_e)_{\mu_a} .\tag{5.6}$$

Before applying the boundary conditions, we have

$$KU = 0 .\tag{5.7}$$

Since we know the source strength by assuming a point source, we can partition U as

$$U = \begin{Bmatrix} U_s \\ U_f \end{Bmatrix}\tag{5.8}$$

where subscript *s* indicates a specified or known photon density at the particular node, and *f* indicates a free or unknown photon density at this particular node. Partitioning *K* accordingly leads Equation (5.7) to

$$\begin{bmatrix} K_{ss} & K_{sf} \\ K_{fs} & K_{ff} \end{bmatrix} \begin{Bmatrix} U_s \\ U_f \end{Bmatrix} = \begin{Bmatrix} 0 \\ 0 \end{Bmatrix} .\tag{5.9}$$

Then U_f can be computed from

$$K_{ff} U_f = -K_{fs} U_s .\tag{5.10}$$

The global matrix *K* can be assembled from the following equation:

$$K = \sum (K_e)_k + \sum (K_e)_{\mu_a} ,\tag{5.11}$$

where

$$(K_e)_k = \int_{V_e} k[\phi]^T [\phi] dxdy ,\tag{5.12}$$

$$(K_e)_{\mu_a} = \int_{V_e} \mu_a [\phi]^T [\phi] dxdy ,\tag{5.13}$$

where $[\phi]$ = shape function matrix. Within an element, k, μ_a are assumed to be constant. Then we have

138

$$(K_e)_k = k(\overline{K_e})_k,\tag{5.14}$$

$$(K_e)_{\mu_a} = \mu_a(\overline{K_e})_{\mu_a}.\tag{5.15}$$

As there are several elements having the same properties in geometry, it leads to

$$K = \sum_{i=1}^{N_p}[\mu_{a_i}K_a\{i\} + k_iK_k\{i\}],\tag{5.16}$$

where N_p is the number of "design" regions. $K_a\{i\}$ and $K_k\{i\}$ are matrices with the same dimension as that of the global matrix, K. Equations (5.12) and (5.13) use triangular elements in the two dimensional geometry.
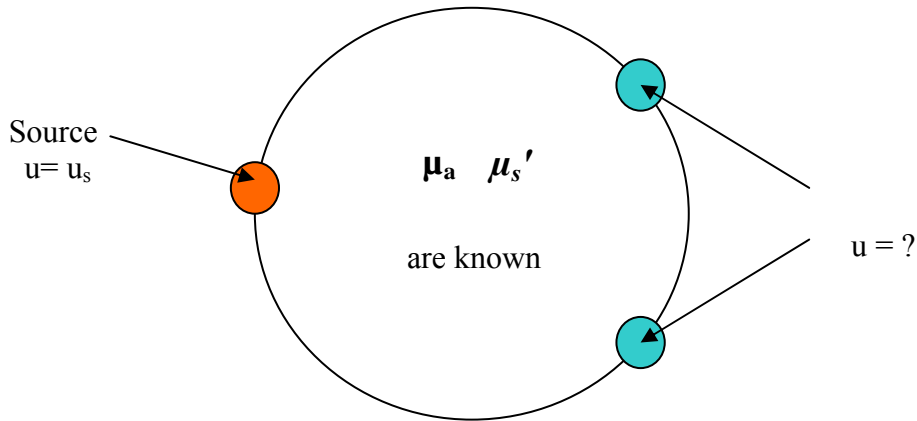
Figure 5.5 Illustration of forward problem. Optical properties of the medium inside the boundary are known. Light intensities at the detectors on the boundary are computed or measured, as mentioned in Section 5.4.2.

5.4.2 Forward problem

The forward problem is illustrated in Figure 5.5. In the forward problem, the spatial distribution of optical properties (μ_a and μ_s' at every node) is known, as illustrated in Figure 5.5. The source photon densities, $u=u_s$, at source nodes are assumed

to be known. Equation (5.10) is used to determine the photon density at the detectors on the boundary. The term U_f refers to photon densities at all the nodes and is determined by using Equation 5.17.

$$U_f = -\left[K_{ff}\right]^{-1} K_{fs} U_s \qquad (5.17)$$

5.4.3 Inverse problem
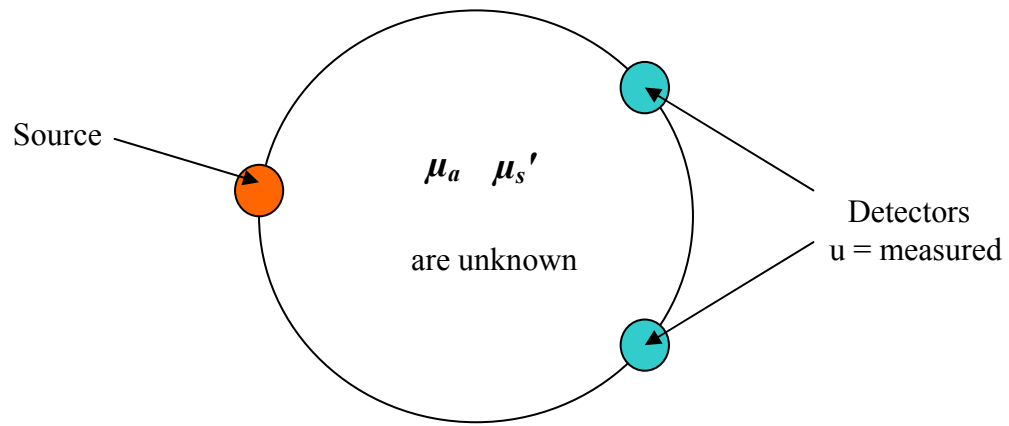
Figure 5.6 Illustration of inverse problem. Optical properties of the medium inside the boundary are unknown. Light intensities are measured at the boundary by the detectors (known). Initial guesses of optical properties are updated by minimizing squared differences between the computed and measured intensities at the detectors.

The inverse problem is illustrated through a diagram in Figure 5.6. Determination of spatial distribution of optical properties with known intensities determined by the detectors on the boundary constitutes the inverse problem.

$$\chi^2 = \sum_{j=1}^{m} \sum_{i=1}^{n} \left(u_{ij}^{measured} - u_{ij}^{calculated}\right)^2 , \qquad (5.18)$$

where $u_{ij}^{measured}$ is the photon density measured by detector i due to source j, and $u_{ij}^{calculated}$ is the corresponding calculated photon density. The photon densities at the detectors are calculated as described in the previous section. m is the number of sources and n the number of detectors on the periphery. An initial guess of spatial distribution of optical properties is iteratively updated; a weighted sum of the squared difference between the computed and measured data, Equation (5.18), is the objective function and needs to be minimized.

5.4.4 Single wavelength image reconstruction

In this approach, the initial guess of spatial distribution of optical properties is iteratively updated when the objective function (Equation 5.18) is minimized using the optical measurements taken with a single wavelength $\lambda = \lambda_1$. The chromophore concentrations can be extracted from μ_a, μ_s', which are determined using two or more wavelengths independently, as described in the previous section. It can be seen that this approach leads to an increased number of unknowns. In principle, there are two unknowns for every node, i.e., μ_a and μ_s'; at every measurement wavelength. As the number of detectors that can be used is finite, the problem becomes highly undetermined. This leads to an inherent problem of non-uniqueness in the computed spatial distribution of optical properties.

5.4.5 Hyper radial basis functions

In my method, following the previous approach used in our group [109] [109], the spatially varying absorption and reduced scattering coefficients at each

measurement wavelength are modeled as hyper radial basis functions (HRBF) as shown in Equation (5.19) and Equation (5.20).

$$\mu_a = C_{a0} + \sum_{i=1}^{N} C_{ai} e^{-\left[\frac{(x_c - x_{ai})^2}{\sigma_{axi}} + \frac{(y_c - y_{ai})^2}{\sigma_{ayi}}\right]} \tag{5.19}$$

$$\mu_s' = C_{s0} + \sum_{i=1}^{N} C_{si} e^{-\left[\frac{(x_c - x_{ai})^2}{\sigma_{axi}} + \frac{(y_c - y_{ai})^2}{\sigma_{ayi}}\right]} \tag{5.20}$$

'Ca_0' and 'Cs_0' are background absorption and scattering coefficients, Ca_i, Cs_i are absorption and scattering coefficients of the ith perturbed region, X_c, Y_c are center co-ordinates of the assumed heterogeneity at which optical properties are determined, 'Xa_i' and 'Ya_i' are the coordinates of the ith perturbed region, and lastly 'N' is the number of the perturbed regions.

'Ca_0', 'Cs_0', 'Ca_i', 'Cs_i', 'Xa_i', 'Ya_i' are fitted at each measurement wavelength by least squares minimization and then formulate the hyper radial basis functions (HRBF). Optical properties at individual nodes are not calculated separately but assumed to vary having the shape of HRBF (see Equations (5.19) and (5.20), thus bringing a huge reduction in the number of fitted parameters to be optimized for image reconstruction.

The reconstruction of optical properties yields the location, size and extent of spatial heterogeneities in optical properties at each measurement wavelength. The algorithm and the ability of this technique to reconstruct optical heterogeneities are mentioned in detail elsewhere [109]. The entire domain is divided into background and perturbed regions to reconstruct the quantities of [*Hb*], [*HbO*], lipid concentration,

water percentage, and Mie scattering coefficients using the spectral constraints to be described in Section 5.4.6.

5.4.6 Non-uniqueness in steady-state, single-wavelength reconstructions

Previous investigations by other groups have elicited the inherent non-uniqueness in the steady state or continuous wave optical tomography [110]. Different optical property distributions can lead to the same light intensity distribution in the detectors at the boundary. Single wavelength reconstructions (described in the earlier sub-section) or determinations of optical property distributions are not unique. To overcome this problem of non-uniqueness, several approaches such as use of spectral constraints while combining information from multiple measurement wavelengths have been suggested and used [74, 107]. My reconstruction algorithm developed uses the similar method to reconstruct the spatial distribution of optical properties, as described in details in the following sub-section.

5.4.7 Spectral constraints with multiple measurement wavelengths

An alternative approach to estimating optical properties at each measurement wavelength and then spectrally reconstructing images of chromophore concentrations can be spectrally constrained to directly reconstruct the spatial distributions of [*HbO*], [*Hb*], water content, scatter amplitude, and scatter power, thus resulting in a reduction of parameter space from 16 images (μ_a and μ_s' at 8 wavelengths) to 5 parametric images. Increase in measurement wavelengths does not result in increase of parameter space. Unlike the conventional DOT, where absorption and scattering are reconstructed separately at each wavelength and then spectrally deconvolved to obtain chromophore

concentrations, the spectral constraints in the current approach are incorporated into the reconstruction algorithm to directly determine [*HbO*], [*Hb*], water, scatter amplitude, and scatter power, thus reducing the number of fitted parameters and increasing the computational efficiency.

Srinivasan et al presented a method to directly incorporate the spectral constraints into image reconstruction. I have adopted this method in my image reconstructions. The method presented by Srinivasan et al is introduced as follows: The update in the optical properties is related to the difference between the measured and the calculated data as

$$\partial \phi = J \; \partial \mu, \tag{5.21}$$

where $\partial \phi$ refers to the change in boundary data ($u_{ij}^{calculated} - u_{ij}^{measured}$), J is the Jacobian, the matrix containing the sensitivity of the boundary detector data to a change in optical properties defined by $J = \left[J_{\mu_a} ; J_k \right]$, $\partial \mu$ is the change in optical properties defined by $\partial \mu = \left[\partial \mu_a ; \partial k \right]$. k is the diffusion coefficient defined by $k = \dfrac{1}{3(\mu_a + \mu_s')}$. $J_{\mu_a} = \partial \phi / \partial \mu_a$ and $J_\kappa = \partial \phi / \partial \kappa$ are the sensitivities of the boundary detector data to a change in μ_a and k respectively.

The optical absorption coefficient and reduced scattering coefficients of the tissues are dependent on the wavelength as mentioned in earlier in Chapters 2-4. The wavelength-dependent, tissue absorption can be written as

$$\mu_a(\lambda) = \sum_i \varepsilon_i(\lambda) C_i, \tag{5.22}$$

where c_i is the concentration and $\varepsilon_i(\lambda)$ is the extinction coefficient of the ith chromophore at wavelength λ. The wavelength-dependent, reduced scattering coefficient of tissues is assumed to take a simplified Mie-scattering form [111]:

$$\mu_s^{'}(\lambda) = a\lambda^{-b}, \tag{5.23}$$

where a and b are the scatter amplitude and scatter power, respectively.

In the approach of Srinivasan et al, measurements at all wavelengths are coupled together [74], and the relations of Equations (5.21), (5.22) and (5.23) are combined to get a new set of relations, which can be written at any wavelength λ as

$$\partial\phi_\lambda = J_{c,\lambda}\partial c + J_{a,\lambda}\partial a + J_{b,\lambda}\partial b, \tag{5.24}$$

where

$$J_{c,\lambda} = J_{\mu,\lambda} \otimes \left[\varepsilon_\lambda^{c_1,c_2,c_3,c_4}\right], \tag{5.25}$$

$$J_{\mu,\lambda} = \left.\frac{\partial\phi}{\partial\mu_a}\right|_\lambda, \tag{5.26}$$

$$J_{a,\lambda} = J_k\left(-3k^2\right)\left(\lambda^{-b}\right)_\lambda, \tag{5.27}$$

$$J_{b,\lambda} = J_k\left(-3k^2\right)\left(\mu_s^{'}\right)\left(-\ln\lambda\right)_\lambda, \tag{5.28}$$

$$J_k = \left.\frac{\partial\phi}{\partial k}\right|_\lambda, \tag{5.29}$$

Equations (5.25) to (5.29) define the terms in Equation (5.24). $\left[\varepsilon_\lambda^{c1,c2,c3,c4}\right]$ is a matrix of extinction coefficients of chromophores, namely Hb, HbO, H_2O [79] and lipids [112] The derivation of expression for $J_{a,\lambda}$, $J_{b,\lambda}$ is mentioned in Appendix F. The method to numerically calculate sensitivity factors $J_\mu = \partial\phi/\partial\mu$ and $J_\kappa = \partial\phi/\partial\kappa$ is

described in a previous work from our group [109]. The overall system of equations is assembled by substituting the relations from Equations. (5.25) to (5.28) into Equation (5.24) and writing Equation (5.24) in a matrix form as

$$\begin{pmatrix} \partial\phi_{\lambda1} \\ \partial\phi_{\lambda2} \\ \partial\phi_{\lambda3} \\ \\ \partial\phi_{\lambda n} \end{pmatrix} = \begin{bmatrix} J_{c1,\lambda1} & J_{c2,\lambda1} & J_{c3,\lambda1} & J_{c4,\lambda1} & J_{a,\lambda1} & J_{b,\lambda1} \\ J_{c1,\lambda2} & J_{c2,\lambda2} & J_{c3,\lambda2} & J_{c4,\lambda2} & J_{a,\lambda2} & J_{b,\lambda2} \\ ... & ... & ... & ... & ... & ... \\ ... & ... & ... & ... & ... & ... \\ J_{c1,\lambda n} & J_{c2,\lambda n} & J_{c3,\lambda n} & J_{c4,\lambda n} & J_{a,\lambda n} & J_{b,\lambda n} \end{bmatrix} \begin{pmatrix} \partial c_1 \\ \partial c_2 \\ \partial c_3 \\ \partial c_4 \\ \partial a \\ \partial b \end{pmatrix}, \qquad (5.30)$$

The left hand side vector of Equation (5.30) indicates the size of matrix for one detector at all n measurement wavelengths. It is a matrix of change in boundary data ($u_{ij}^{calculated} - u_{ij}^{measured}$) as mentioned earlier in this Section at all measurement wavelengths. The right hand side vector in Equation (5.30) indicates the size for one triangular element at all measurement wavelengths. The column matrix indicates the updates (or small changes) in concentrations of chromophores and scattering parameters (a and b) for the triangular element. The next paragraph mentions the size of these vectors for my image reconstruction.

The size of the vector on the left hand side is equal to the number of measurement wavelengths multiplied by the number of measurements per wavelength. Experimental setup shown in Figure 5.1 has eight sources and detectors. Due to saturation of detectors located adjacent to the source, intensities measured from only five detectors are used for reconstruction. A total of 40 (5 detectors x 8 sources) measurements per wavelength are used for image reconstruction. The size of the left

146

hand vector in my reconstruction was 40 (measurements per wavelength) x 8 (number of wavelengths used for reconstruction).

The size of the right-hand side vector is equal to the number of chromophores and scatter parameters times the number of elements in the finite element mesh used for image reconstruction times the number of wavelengths used for reconstruction. Spatial distributions of four chromophores Hb, HbO, H_2O and lipid are reconstructed in my study. Image reconstructions in my dissertation are made with 200 triangular elements. The size of the right hand vector in my reconstruction was 200 (number of triangular elements) x 6 (4 chromophores + 2 scattering parameters) x 8 (number of wavelengths used for reconstruction).

The individual Jacobian matrices for each chromophore were computed as mentioned below. The sensitivity factors $J_{\mu_a} = \partial\phi / \partial\mu_a$ and $J_{\kappa} = \partial\phi / \partial\kappa$ at every measurement wavelength are numerically determined for each triangular element as described in Master's thesis of Aditya Apte [109] Jacobian matrices for each chromophore are computed by taking a Kronecker product with the matrix of extinction coefficients of chromophores as shown in Equation (5.25).

$$
\begin{pmatrix} \partial\phi^1_{\lambda 1} \\ \cdots \\ \partial\phi^1_{\lambda n} \\ \cdots \\ \partial\phi^m_{\lambda 1} \\ \cdots \\ \partial\phi^m_{\lambda n} \end{pmatrix} =
\begin{bmatrix}
J^{1,1}_{c1,\lambda 1} & \cdots & J^{1,1}_{c4,\lambda 1} & \cdots & J^{1,1}_{b,\lambda 1} & \cdots & J^{1,p}_{c1,\lambda 1} & \cdots & J^{1,p}_{c4,\lambda 1} & \cdots & J^{1,p}_{b,\lambda 1} \\
\cdots & & \cdots & & \cdots & & \cdots & & \cdots & & \cdots \\
J^{1,1}_{c1,\lambda n} & \cdots & J^{1,1}_{c4,\lambda 1} & \cdots & J^{1,1}_{b,\lambda n} & \cdots & J^{1,p}_{c1,\lambda n} & \cdots & J^{1,p}_{c4,\lambda n} & \cdots & J^{1,p}_{b,\lambda n} \\
J^{2,1}_{c1,\lambda 1} & \cdots & J^{2,1}_{c4,\lambda 1} & \cdots & J^{2,1}_{b,\lambda 1} & \cdots & J^{2,p}_{c1,\lambda 1} & \cdots & J^{2,p}_{c4,\lambda 1} & \cdots & J^{2,p}_{b,\lambda 1} \\
\cdots & & \cdots & & \cdots & & \cdots & & \cdots & & \cdots \\
J^{2,1}_{c1,\lambda m} & \cdots & J^{2,1}_{c4,\lambda m} & \cdots & J^{2,1}_{b,\lambda n} & \cdots & J^{2,p}_{c1,\lambda n} & \cdots & J^{2,p}_{c4,\lambda n} & \cdots & J^{2,p}_{b,\lambda n} \\
\cdots & & \cdots & & \cdots & & \cdots & & \cdots & & \cdots \\
\cdots & & \cdots & & \cdots & & \cdots & & \cdots & & \cdots \\
J^{m,1}_{c1,\lambda 1} & \cdots & J^{m,1}_{c4,\lambda 1} & \cdots & J^{m,1}_{b,\lambda 1} & \cdots & J^{m,p}_{c1,\lambda 1} & \cdots & J^{m,p}_{c4,\lambda 1} & \cdots & J^{m,p}_{b,\lambda 1} \\
\cdots & & \cdots & & \cdots & & \cdots & & \cdots & & \cdots \\
J^{m,1}_{c1,\lambda n} & \cdots & J^{m,1}_{c4,\lambda n} & \cdots & J^{m,1}_{b,\lambda n} & \cdots & J^{m,p}_{c1,\lambda n} & \cdots & J^{m,p}_{c4,\lambda n} & \cdots & J^{m,p}_{b,\lambda n}
\end{bmatrix}
\begin{pmatrix} \partial c^1_1 \\ \partial c^1_2 \\ \partial c^1_3 \\ \partial c^1_4 \\ \partial a^1 \\ \partial b^1 \\ \partial c^2_1 \\ \cdots \\ \cdots \\ \partial b^p \end{pmatrix},
$$

…………………… (5.31)

where ϕ^m_λ denotes the mth detector's reading at wavelength λ, and $J^{m,p}_{c,\lambda}$ represents the Jacobian for the mth detector at wavelength λ due to change in c component (chromophore or light scattering) at the p triangular element.

Equation (5.31) shows the assembly of equations for n wavelengths, m measurements per wavelength and p triangular elements. In Equation (5.31), the number of unknowns is greater than the number of equations. The total number of unknowns in this problem are the number of triangular elements times the number of chromophores plus the scattering parameters. In this particular application, number of measurements = 40 (measurements per wavelength) x 8 (number of wavelengths for reconstruction) = 320, whereas the total number of unknowns = number of elements x (number of chromophores (4) + 2 scattering parameters) = 200 x 6 = 1200. It is obvious that the problem is undetermined. Hence, image reconstruction described here uses a

non-linear least square minimization function (Matlab[TM] function-"lsqnonlin.m") that iteratively updates the optical property parameters (concentrations of chromophores and scattering parameters) based on a least-squares-error given by Equation (5.18). The summation now is over all the measurement wavelengths and given in Section 5.8. The Jacobian matrices that are required for the least squared minimization are computed as described in the earlier paragraphs.

5.5 Optimal selection of measurement wavelengths

A white light broadband source provides a wide continuous spectrum of wavelengths in the NIR range from which some wavelengths can be chosen for image reconstruction. Previous studies have reported the criticality of measurement wavelengths in reducing chromophore cross-talk and unique separation of effects of absorption from those of scattering [107, 110]. It would not be optimal to choose all wavelengths, as this would increase the computational burden to unmanageable levels. It would be helpful to develop a technique to choose measurement wavelengths from the available wavelength range that best fit the criteria mentioned earlier. To address this requirement, this section presents an algorithm to search for optimal wavelength sets from the available wavelength range (650-930 nm) that best fit the criteria of reduction of chromophore cross-talk and unique separation of absorption and scattering effects.

5.5.1 Criteria and metrics for wavelength selection

Two conditions have been derived by Corlu et al [107] for selection of measurement wavelengths based on uniqueness criteria. Suppose there are n chromophores (c_i) and m measurement wavelengths (λ_k), uniqueness of the inverse problem requires the unique separation of absorption and scattering parameters and separation of absorption of contributing chromophores.

According to Corlu et al,, R, is defined as a parameter that evaluates the ability of a measurement wavelength set to separate effects of scattering from those of absorption. Choices of measurement wavelength sets that maximize R, define the first criterion for selecting optimal wavelengths. κ is defined as a parameter that evaluates the ability of a measurement wavelength to minimize the cross talk within the absorption chromophores. Wavelength choices that minimize κ define our second criterion for selecting optimal wavelengths. The method to determine R and κ is described in ref. [107] and with more details in ref. [113].

It is intuitive that the ratio κ/R could be considered as a parameter that collectively evaluates the ability of a measurement wavelength set to uniquely and simultaneously reconstruct concentrations and scattering parameters. The smaller the ratio κ/R is, the better the ability of the wavelength set is to uniquely separate the effects of absorption and scattering and thus to minimize inter-chromophore cross-talk. This criterion is used to search for an optimal set of measurement wavelengths with a heuristic search algorithm.

5.5.2 Differential evolution algorithm for wavelength selection

Differential evolution algorithm is a very simple, population-based, stochastic function minimization algorithm which is very powerful at the same time [114]. This algorithm is used to search for a set of optimal measurement wavelengths that minimize the ratio κ/R thereby satisfying the criterion for unique separation of absorption and scattering and for the smoothness of contribution of absorbing chromophores.

Hb, HbO, water, lipid were selected as chromophores with significant absorption in the NIR range. The search space for the algorithm spanned wavelengths in the range of 650-930 nm. Optimal wavelengths sets were determined by increasing number of measurement wavelengths from 4 to 32 in steps of 2.

5.5.3 Effect of increasing measurement wavelengths on uniqueness criteria

The residual norm R and κ were evaluated for all optimal wavelength sets obtained from the search algorithm. Figures 5.6(a), 5.6(b) and 5.6(c) show the variations of R, κ and the ratio κ/R with increase in the number of measurement wavelengths. The increase in the residual norm R and decrease in value of κ are apparent from Figures 5.7(a) and 5.7(b), respectively. A consequent decrease in κ/R ratio is seen with the increase in number of measurement wavelengths (Figure 5.7(c)). It can be seen from Figure 5.7(c) that the rate of decrease of the ratio decreases to a trickle when the measurement wavelengths increase beyond 10. This shows that an increase in the number of measurement wavelengths beyond a certain critical number of wavelengths results only in a marginal increase in accuracy outweighed by the increase in computational load.
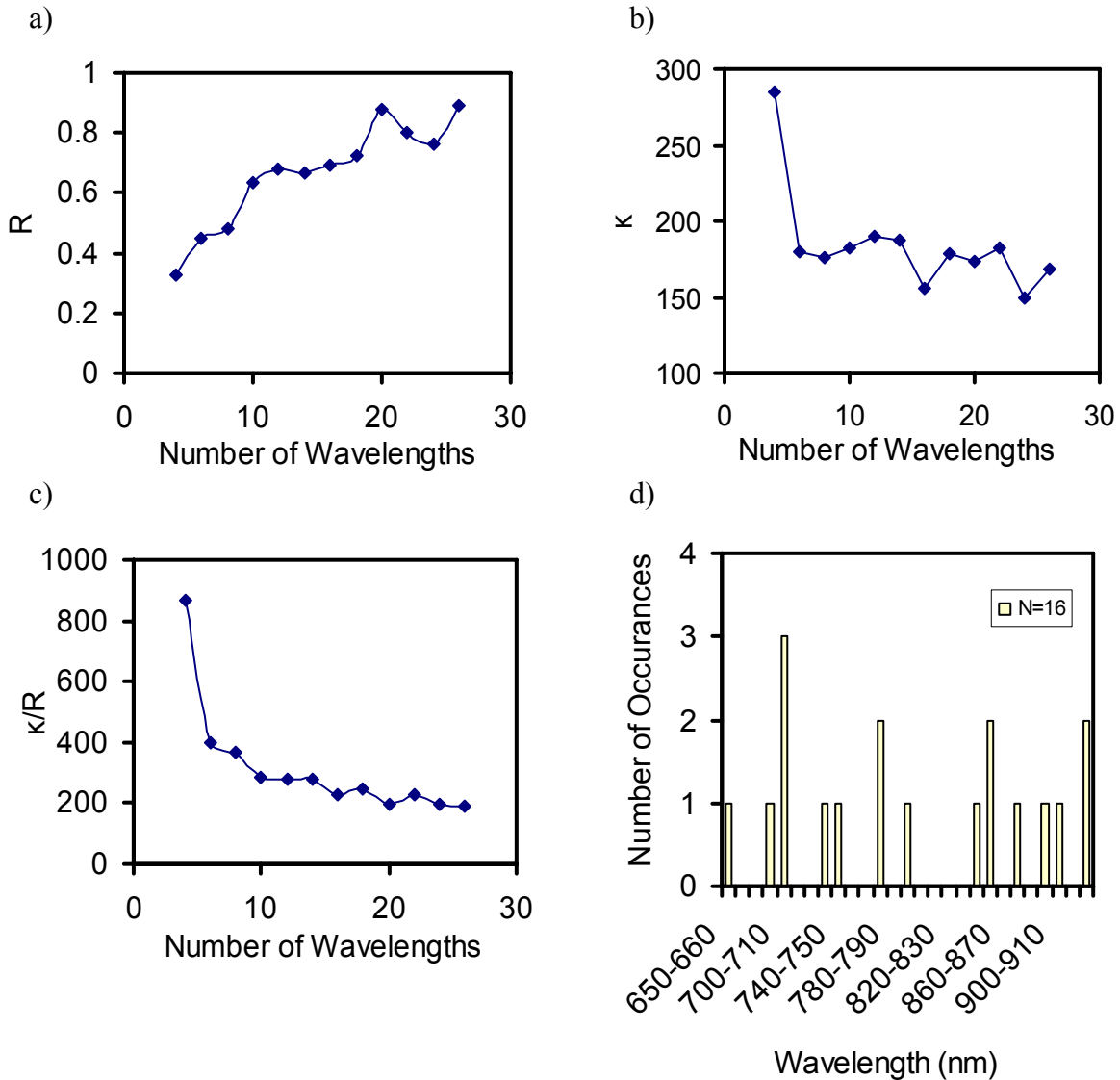
Figure 5.7 The values of κ, R were evaluated for optimum wavelength sets determined by our heuristic search algorithm. The ratio of κ/R was also evaluated for the multiple numbers of wavelengths. a) Plot of R showing the increase of R with increase in the number of wavelengths. b) Plot κ showing the decrease of κ residue with the increase in the number of wavelengths. c) Plot the ratio of κ/R showing the decrease of κ/R with increase in the number of wavelengths. d) distribution plot of optimum wavelengths selected for $N = 16$.

Figure 5.7(d) shows the spread of measurement wavelengths in the wavelength range

selected. Optimum measurement wavelength set obtained spans the range of the

152

spectrum selected. The distribution of wavelengths was not even. The number of optimal wavelengths from particular wavelength regions, such as 700-710 nm and 920-930 nm, had predominantly more number of wavelengths (Figure 5.7(d)). This characteristic was also observed with optimal measurement wavelength sets with $N > 6$, where N is the number of measurement wavelengths. In spite of repetitions of some wavelength regions, more wavelength regions were sampled with an increase in number of wavelengths. This result has significant importance as it emphasizes the need for broad band or white light sources.

5.5.4 Wavelengths chosen for image reconstruction

Eight wavelengths were chosen for my image reconstruction. Reconstructions made from the measurements did show an increase in accuracy after utilizing 8 wavelengths. Specifically, all reconstructions were carried out with the following set of wavelengths: 652, 717, 726, 774, 817, 827, 886, and 927 nm. All reconstructions that were carried to obtain tomographic maps used this set of wavelengths in my study.

5.6 System calibration

Calibration procedures are necessary to reduce the deterministic bias of instrumentation system on the measured signal. System calibration is aimed to eliminate the influence of the variation among all components of the imaging system, such as optical fibers, spectrometer channels and multiplexer channels.

5.6.1 Optical fibers

Manufacturing limitations in the manufacture of optical fibers render variations from one fiber to the other. To compensate for differences in detected spectral intensities from different optical fibers, all fibers are calibrated with respect to fiber-1.

A fiber (Innova Quartz Inc, Phoenix, Arizona, 3mm core diameter, SMA) other than the fibers used in the imager was used as a source fiber. Detector Fibers 1-8 were used as detectors to measure the intensity of the light from the white sample (i.e., the calibration standard reference sample). The white sample, source fiber and the detector fiber were held in place by lens holders. This ensured that the geometry remained identical throughout the measurement for all the fibers under test. Channel-1 (Master channel) of the spectrometer was used to make all the measurements to prevent further additions of heterogeneities.

Measurement from fiber-1 was selected as the standard spectral measurement, and all other fiber measurements are calibrated at respective wavelengths against this standard fiber. Figure 5.8(a) displays the measurement of spectra made from eight fibers. The differences in spectral intensities are evident. Figure 5.8(b) indicates the ratios of spectral intensities between fibers 2-8 and fiber-1. Larger deviations from unity indicate larger differences between the fibers. The ratios are relatively constant for each of the respective pairs in the spectral range of 500-900 nm. The ratios then are used as calibration factors for each respective fiber to eliminate differences due to heterogeneity in fibers at respective wavelengths.
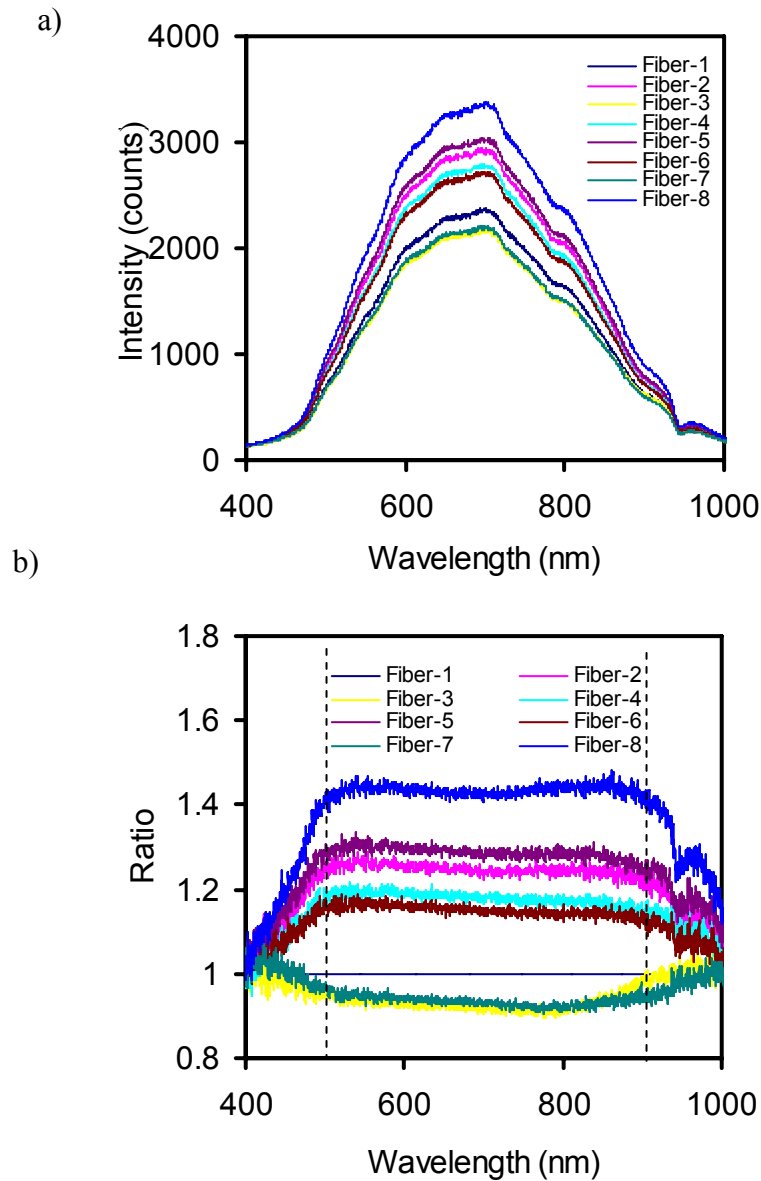
Figure 5.8 Illustration of heterogeneities in optical fibers and method to compensate for heterogeneities. a) Spectra measured from all 8 fibers with identical measurement conditions. Differences in measured intensity are clearly seen from the graph. b) Ratios of intensities measured from fibers 2-8 to those measured from fiber-1. These ratios are used as multiplication factors to compensate for fiber heterogeneities.

5.6.2 Spectrometer channels

The experimental procedure to calibrate the spectrometer channels was similar to that for the optical fibers. The same set of source and detector fibers were used in all measurements. The source fiber (Innova Quartz Inc, Phoenix, Arizona, 3mm core diameter, SMA) was the same as the one used in the fiber calibration (see Section 5.6.1). Fiber 1 was chosen as the detector fiber. Measurements were made by connecting the detector fiber to all channels in the spectrometer in sequence.

Figure 5.9(a) displays the measurement of spectra made from 8 channels of the 8-channel spectrometer. The differences in spectral intensities are evident. Figure 5.9(b) indicates the ratios of spectral intensities between Channels 2-8 and Channel-1. The calibration factors at respective wavelengths were obtained for all the spectrometer channels with respect to channel-1 of the spectrometer. All measurements were made using identical geometry and the same set of source and detector fibers.

a)

b)
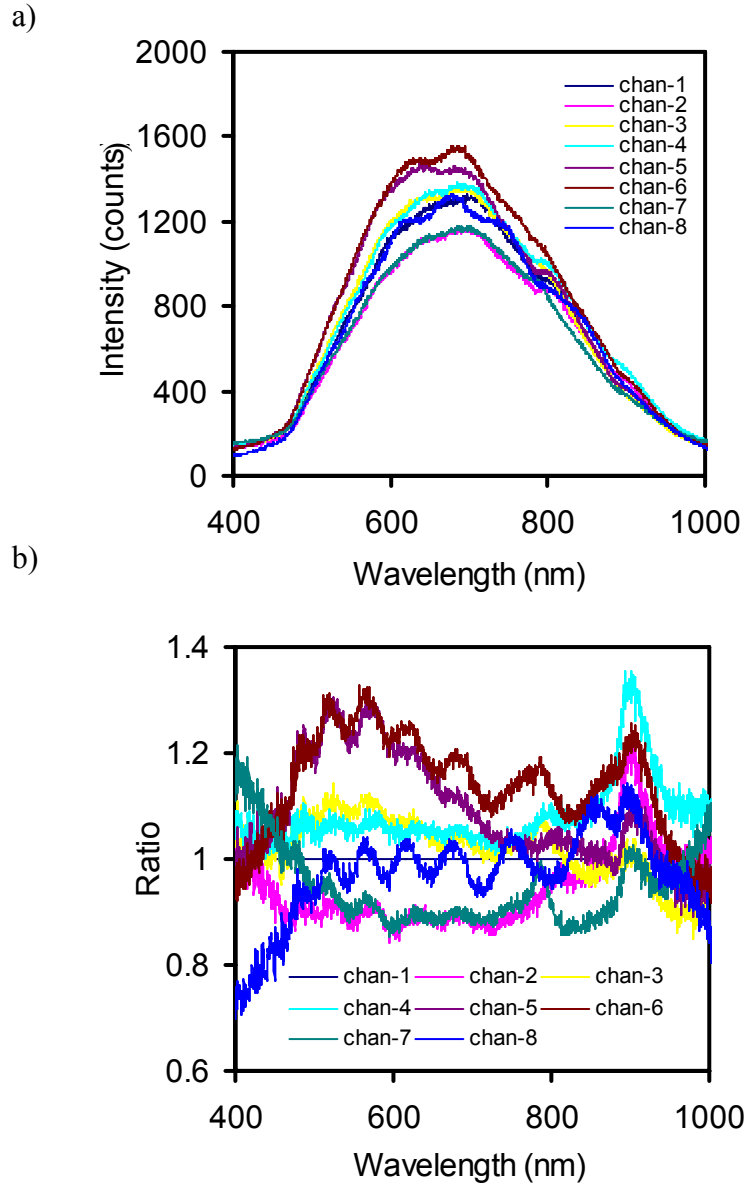
Figure 5.9 Illustration of heterogeneities in 8-channel spectrometer channels and the method to compensate for the heterogeneities. (a) Spectra measured from all 8 channels with identical measurement conditions. Differences in measured intensity are clearly seen from the graph. (b) Ratios of intensities measured from channels 2-8 to those measured from channel-1. Ratios are not constant and are used as multiplication factors to compensate for channel heterogeneities.

5.6.3 Optical multiplexer channels

In this case, the source and the detector fiber set up were identical to the setup used to calibrate the spectrometer channels. Channel-1(Master) of the spectrometer was used to make all measurements to prevent further additions of heterogeneities. The source fiber was firstly connected to channel-1 of the multiplexer. The measurement of light intensity was made by the spectrometer. The multiplexer was then switched to the next channel by connecting the source fiber to channel-2 of the multiplexer. This procedure was repeated for all multiplexer channels.

Figure 5.10(a) displays the measurement of spectra made from 8 channels of the multiplexer. Figure 5.10(b) indicates ratios of the spectral intensities between Channels 2-8 and channel-1. Calibration factors at respective wavelengths were obtained for all multiplexer channels with respect to channel-1 of the multiplexer.
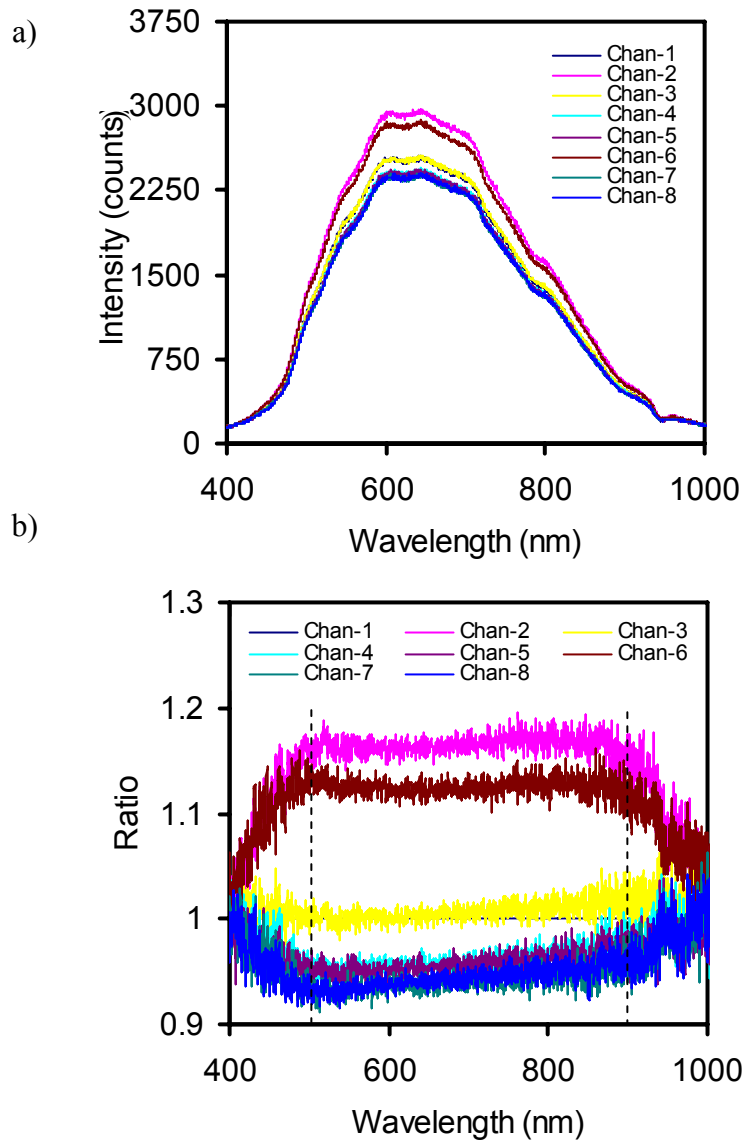
Figure 5.10 Illustration of heterogeneities in multiplexer channels and method to compensate for heterogeneities. (a) Spectra measured using light delivered from all channels of multiplexer. Differences in measured intensity are clearly seen from the graph. (b) Ratios of intensities measured from channels 2-8 to those from channel-1. Ratios seem relatively constant for each respective channel in the range of 500-900 nm, and they are used as multiplication factors to compensate for channel heterogeneities for the multiplexer.

5.7 Model calibration

Model calibration is a mandatory step for image reconstruction to minimize errors due to imperfection in the mathematical model, such as boundary conditions and discretization errors. The measurement in reality is always slightly different from the data simulated by the model, and this could become a systematic error in image reconstruction. One critical parameter, the source strength S_0, must be accurately determined to achieve high accuracy in the quantifications of chromophore concentrations.

5.7.1 Source strength

A set of measurements made on a homogeneous, blood-intralipid phantom were used to determine the source strength. The phantom has a very similar geometry to the inhomogeneous experimental phantoms used for image reconstruction. The phantoms were similar to those described in details in Section 4.3. The smaller glass tube (marked as target in Figure 5.2) that was placed inside the large glass tube was not present for this set of measurements. The blood-intralipid phantoms were made with different intralipid concentrations (for different reduced scattering coefficients) and hemoglobin concentrations, all of which were measured by the ISS Oximeter for calculating the source strength.

In Equation (5.10), $K_{ff}U_f = -K_{fs}U_s$, where the subscript f indicates a free or unknown node and subscript s indicates a specified or a known node. In the conventional forward problem described in Section 5.4.2, the spatial distribution of optical properties (μ_a and μ_s' at every node) is known and source photon densities, $u=u_s$

, at source nodes is known. The detector intensities at the boundary are calculated using Equation (5.10). In the determination of source strength from a particular phantom measurement, source strengths are unknown and are free nodes. The detector nodes are specified nodes, as photon densities at these nodes are measured. The optical properties (μ_a and μ_s') are measured by the ISS Oximeter and are known. The photon density at all the source nodes or the source strength $S(r)$ is computed by using Equation (5.10). The procedure is repeated for all phantom measurements to calculate a set of source strengths for each measurement $S_j(r)$.

Using the finite element model described in Section 5.4.1 and source strengths $S_j(r)$ determined as mentioned above, sum of squared errors between the computed photon densities at the detectors and measured photon densities are evaluated for each set of source strengths $S_j(r)$ as shown in Equation (5.32).

$$\chi^2 = \sum_{j=1}^{n} \sum_{i=1}^{M} \left[\Phi_{ji}^{(m)} - \Phi_{ji}^{(c)} \right]^2 , \qquad (5.32)$$

where M is the number of boundary measurements, $\Phi_{ji}^{(m)}$ is the measured photon density from j^{th} homogeneous phantom at the particular measurement wavelength, and $\Phi_{ji}^{(c)}$ is the corresponding computed photon density using finite element model described in Section 5.4.1 of a homogeneous phantom with identical geometry as the experimental phantom at the respective measurement wavelength. $\Phi_{ji}^{(m)}$ is the intensity measured at the detectors on the boundary by the instrument. χ^2 in Equation (5.32) is also evaluated for the average of source strengths determined from all homogenous

phantom measurements. The set of source strengths $S_j(r)$ that returns the least χ^2 is chosen for image reconstruction.

Measurements are made with 3 intralipid-blood phantoms to obtain the source strengths and boundary coefficients. The same measurements are used to determine the boundary coefficients described in the next Section. Source strengths are determined at each measurement wavelength chosen for reconstruction separately. Measurement wavelengths from the continuous band of wavelengths are chosen using the algorithm for optimal selection of wavelengths described in Section 5.5. The measurement wavelengths chosen for image reconstruction are listed in Section 5.5.4. Calculation of source strength at each measurement wavelength chosen for reconstruction is necessary to account for spectral characteristics of light source.

5.7.2 Boundary coefficients

$$-D\nabla\Phi_{\lambda_1}^{(c)}(r)\bullet\hat{n}=\alpha\Phi_{\lambda_1}^{(m)}(r) \tag{5.33}$$

Equation (5.33) describes the type-3 boundary conditions [115]. $\hat{n}$ is a unit vector for the boundary surface. α is a vector, which is a set of calibration coefficients that are related to internal reflection and imperfections in boundary conditions (practically achievable vs assumed boundary conditions) at the boundary. $\Phi_{\lambda_1}^{(m)}$ are photon densities measured by detectors on the boundary as mentioned in the previous section. The same sets of experimental data used to obtain the source strength are used. The quantities of $\Phi_{\lambda_1}^{(c)}(r)$ are the computed photon densities at detectors on the boundary at a wavelength λ_1. They are computed by using finite element models

162

described in the Section 5.4. The optical properties of the phantom were measured with the ISS Oximeter as mentioned previously in the earlier section. Measured absorption and scattering coefficients were used to compute intensities at detectors, i.e., $\Phi_{\lambda_1}^{(c)}(r)$. Source strengths determined as described in the earlier section are used in computation of photon densities $\Phi_{\lambda_1}^{(c)}(r)$ detected theoretically at the boundary. Again, Equation (5.32) is solved by minimizing χ^2 for set of coefficients, i.e., α, that relate $\Phi_{\lambda_1}^{(m)}$ and $\Phi_{\lambda_1}^{(c)}$. This scheme is based on the argument that the minimum of χ^2 corresponds to the value of source strength associated with experimental inhomogeneous medium [115]. After obtaining the set of coefficients α, they are used to calibrate the measurements made from heterogeneous and dynamic phantoms. The coefficients of α are specific to a measurement wavelength and are determined separately at each measurement wavelength.

The boundary coefficients computed at each measurement wavelength are used to calibrate the data from non-homogenous phantoms. Detected intensities at the boundary detectors (after calibration for system components such as optical multiplexers, spectrometer channels and optical fibers) from the non-homogenous phantoms or test phantoms are multiplied by the boundary coefficients to calibrate for the mismatches described at the beginning of this section. The calibrated intensities are used in the single wavelength reconstructions using HRBF function as described in Section 5.4.5. Indeed, the same data sets were used for the computations of source strengths and boundary coefficients.

5.8 Procedures to obtain optical tomography

This section describes the sequence of procedures followed to obtain tomographic maps of hemoglobin derivative concentrations and scattering coefficients. The first step of obtaining tomographic maps is the calibration. The system calibration was made as described in Section 5.6 to minimize the errors due to non uniformity of the optical fibers, spectrometer channels, and optical multiplexer channels.

Secondly, the measurements were made on homogenous blood intralipid phantoms for determination of the source strength and boundary coefficients. The construction of the blood-intralipid phantoms has been described in Section 5.3.1. The measurements were repeated with several different concentrations of blood and reduced scattering coefficients. The reduced scattering coefficients, hemoglobin derivatives and absorption coefficients were also measured with the ISS Oximeter as expected values for comparison.

Thirdly, the measurements were made on the test blood-intralipid phantoms or dynamic phantoms as described in Sections 5.3.1 and 5.3.2. Calibration factors were applied to compensate for optical components' inhomogeneity or non-uniformity. Boundary coefficients calculated using the calibration measurements mentioned in earlier paragraphs were applied to calibrate for mismatch in boundary conditions. These calibrated measurements were used to obtain the tomographic maps.

Fourthly, single wavelength reconstructions using HRBF were used to determine the spatial extent and initial guesses for multi wavelength reconstructions. The region was divided into background and perturbations as shown in Figure 5.11.

164

Initial guesses of spatial distribution of optical properties obtained from the single-wavelength reconstructions were further iteratively updated using spectral constraints to minimize a weighted sum of squared differences between the computed and measured intensities at detectors and at all measurement wavelengths simultaneously (8 wavelengths listed in Section 5.5.4). Specifically, χ^2 shown in Equation (5.34) expresses the weighted sum of squared differences and will be minimized.

$$\chi^2 = \sum_{k=1}^{p} \sum_{j=1}^{m} \sum_{i=1}^{n} \left(u_{ijk}^{measured} - u_{ijk}^{calculated} \right)^2 \qquad (5.34)$$

where $p=8$ is the number of measurement wavelengths, m is the number of sources, n is the number of boundary detectors. $u_{ijk}^{measured}$ is the measured light intensity by the ith detector with the jth source at the kth measurement wavelength, and $u_{ijk}^{calculated}$ is the corresponding intensity calculated with the finite element model described in Section 5.4.1.

5.9 Results

The ability to characterize an embedded scattering or absorbing object was evaluated with tissue simulating phantoms described in Section 5.3. The phantoms were built with intralipid and horse blood with 95% water. By controlling the amount of blood, concentration of intralipid and oxygenation state, absorption or scattering property of the phantom could be modulated, respectively. Images of static and dynamic multi-tube phantoms were reconstructed. Reconstructed chromophore concentrations were compared with the measurements made with ISS Oximeter (ISS Inc, Urbana Champaign, IL).

5.9.1 Static phantoms

These phantoms were concentric cylinders of diameter 4.5 cm with a 1-cm inclusion offset from the center, which has optical properties different from the background with geometry similar to tissues within the cranium of a rat. Figure 5.11 shows the geometry of the target and background media used in the static phantoms. Region 1 indicates the background, and region 2 indicates the inclusion within the background. Heterogeneity in chromophore concentrations was obtained by differentially oxygenating mixtures of intralipid and animal blood (horse).
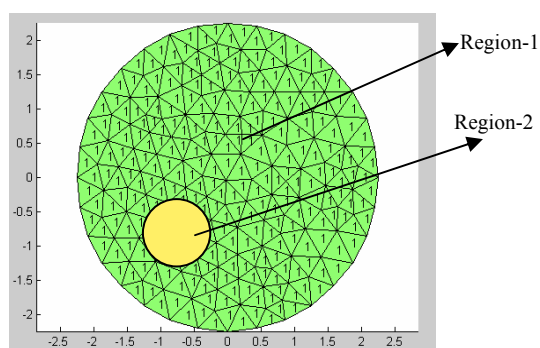
Figure 5.11 Illustration of laboratory phantom geometry and heterogeneity in the spatial distribution of hemoglobin derivatives and reduced scattering coefficients. Sources and detectors will be placed on the periphery.

Three types of heterogeneities were used in the static phantoms within a homogenous background: (A) an inclusion with higher deoxygenated hemoglobin (Hb) concentration, (B) inclusion with higher total hemoglobin concentration (HbT), and (C) inclusion with higher scattering amplitude (μ_s'). The values of [Hb], [HbT] and μ_s' calculated from the algorithm and those measured by the ISS Oximeter are compared in

Table 5.1. The water concentrations in the phantoms are calculated as described in Section 4.3.1.

(A) Inclusion with higher deoxygenated hemoglobin concentration

Oxygen saturation in the intralipid-blood mixture was varied by deoxygenating the blood by bubbling it with pure nitrogen. Pure oxygen was bubbled through the mixture to increase the oxygen saturation. The contrasts in deoxygenated hemoglobin concentrations are evident in Figure 5.12(a). The total hemoglobin concentrations in background and target regions were the same. The two regions varied spatially in their oxygen saturations. The concentrations of lipid and water were spatially homogenous. The scattering amplitude and power were constant spatially as same concentrations of intralipid were used in the background and heterogeneity. All of these points are evident from the reconstructed images from the third and fifth row in Figure 5.12(a).

(B) Inclusion with higher total hemoglobin concentration

Oxygen saturation in the intralipid-blood mixture was maintained spatially constant in this case. The heterogeneity had twice the total hemoglobin concentration in comparison with the background. Reconstructed images of chromophore concentrations are shown in Figure 5.12(b). Equal increases in oxygenated hemoglobin and deoxygenated hemoglobin are evident by the first two rows in Figure 5.12(b). As in the previous case, same concentration of intralipid was used in both background and target regions; therefore, scattering amplitude and power were maintained constant spatially in this phantom. Reconstructed images of oxygenated hemoglobin, deoxygenated hemoglobin, water, lipid and scattering amplitude are shown in Figure 5.12(b).

167
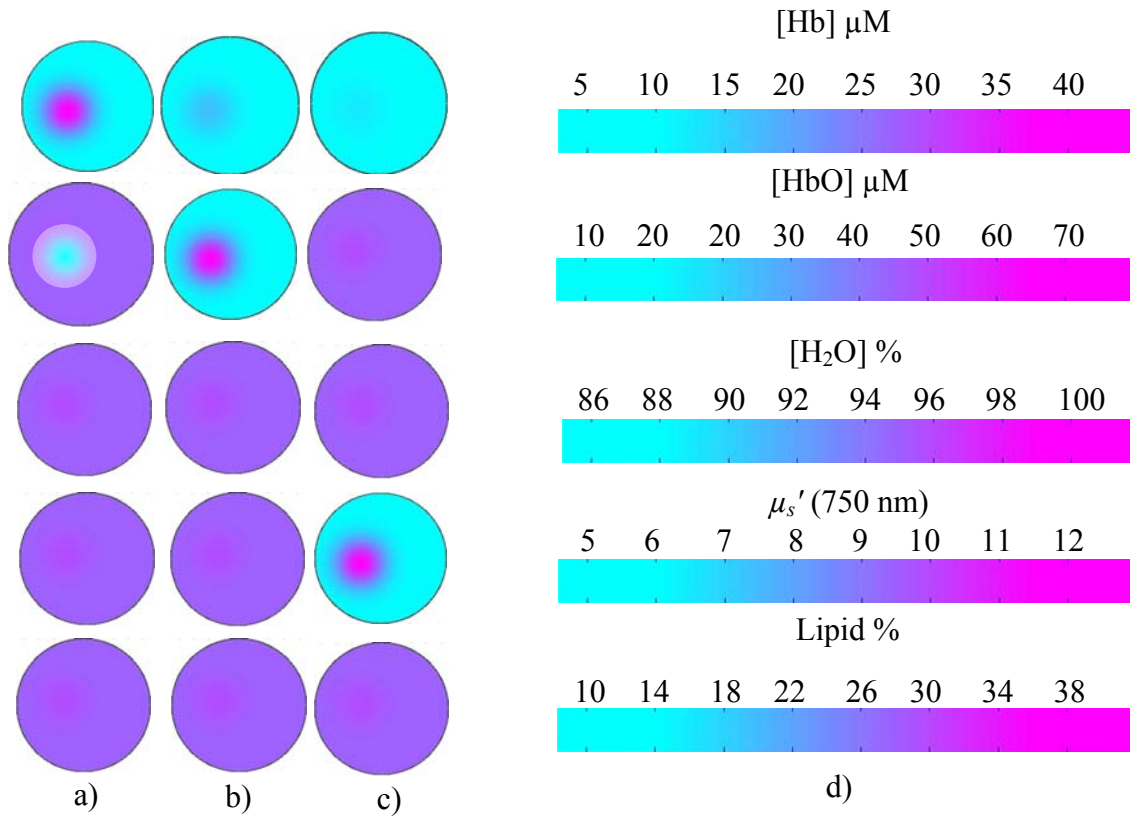
Figure 5.12 Optical tomographic images reconstructed from laboratory phantoms. Spatial distributions of [*Hb*], [*HbO*], water concentration, scattering parameter, and lipid concentration are shown for (a) an inclusion with higher [*Hb*], (b) an inclusion with higher [*HbT*] = [*Hb*]+[*HbO*], and (c) an inclusion with higher scattering coefficients. (d) Color bars depicting respective scales of reconstructed parameters. All diameters are 4.5 cm, and all concentrations are in μM.

(C) Inclusion with higher scattering amplitude.

The earlier paragraphs in this section demonstrated the capability of the broadband imager to make accurate reconstructions of chromophore concentrations in turbid media. In this sub-section, I investigate the imager's ability to reconstruct spatial heterogeneities in scattering amplitude. Specifically, I investigate the ability of the previously developed, spectral-constrained, reconstruction techniques [74, 107] on

direct-current measurements to separate the effects of scatter amplitude and scatter power. To test the cross talk and noise in scatter parameters with experimental measurements and to follow their variation, the intralipid concentration was varied in the liquid phantom. 1% intralipid was used in a small cylinder as the scattering heterogeneity.

Measurements were taken for each concentration, and the spectrally constrained reconstruction was applied to the data. The total hemoglobin and oxygen saturation were constant during the process of varying only concentrations of Intralipid. The scatter amplitude varies linearly with intralipid concentration and shows more variation in comparison with scatter power. The reconstructed images, shown in Figure 5.12(c), indicate a homogenous distribution of oxygenated and deoxygenated hemoglobin, as expected. Concentrations of lipid and water were found to be spatially homogenous in the reconstructed images as seen from Figure 5.12(c). The increase in lipid concentration is only by 0.5 %. (~0.5% when μ_s'(750nm)~5 cm^{-1} and ~1.0% when μ_s'(750nm)~10 cm^{-1}). This increase is very small to appear as heterogeneity in image reconstruction. Hence no spatial heterogeneity in concentrations of lipid are visible, although there is an increase in lipid concentration with increase in μ_s'.

Table 5.1 Comparison of measured and reconstructed chromophore concentrations. Hemoglobin concentrations and reduced concentrations were measured using the ISS Oximeter for comparison. Water volume fraction was calculated from measurement volumes.

Oxygenated Hemoglobin Heterogeneity					
	Actual Concentrations			Reconstructed Concentrations	
	Region-1	Region-2		Region-1	Region-2
Oxygenated Hemoglobin	35.4 μM	14.8 μM	Oxygenated Hemoglobin	44.5 μM	23.3 μM
Deoxygenated Hemoglobin	4.9 μM	27.0 μM	Deoxygenated Hemoglobin	5.7 μM	34.4 μM
Water Fraction	97% (calculated)	97% (calculated)	Water Fraction	94%	94%
μ_s' (750 nm)	5.1 cm^{-1}	5.1 cm^{-1}	μ_s' (750 nm)	5.4 cm^{-1}	5.4 cm^{-1}
Total Hemoglobin Heterogeneity					
	Actual Concentrations			Reconstructed Concentrations	
	Region-1	Region-2		Region-1	Region-2
Oxygenated Hemoglobin	26.4 μM	44.8 μM	Oxygenated Hemoglobin	30.5 μM	49.3 μM
Deoxygenated Hemoglobin	4.9 μM	..10.0 μM	Deoxygenated Hemoglobin	5.7 μM	7.4 μM
Water Fraction	97% (calculated)	97% (calculated)	Water Fraction	94%	94%
μ_s' (750 nm)	5.1 cm^{-1}	5.1 cm^{-1}	μ_s' (750 nm)	5.7 cm^{-1}	5.7 cm^{-1}
Scattering Amplitude Heterogeneity					
	Actual Concentrations			Reconstructed Concentrations	
	Region-1	Region-2		Region-1	Region-2
Oxygenated Hemoglobin	20.4 μM	20.4 μM	Oxygenated Hemoglobin	23.4 μM	18.6 μM
Deoxygenated Hemoglobin	5.0 μM	5.0 μM	Deoxygenated Hemoglobin	5.7 μM	5.4 μM
Water Fraction	97% (calculated)	97% (calculated)	Water Fraction	94%	94%
μ_s' (750 nm)	5.1 cm^{-1}	10.1 cm^{-1}	μ_s' (750 nm)	5.4 cm^{-1}	11.4 cm^{-1}

5.9.2 Dynamic multi tube phantoms

Multi-tube heterogeneous phantoms were used to further evaluate effectiveness and the accuracy of the developed reconstruction algorithms. Reconstructions from these phantoms are more significant than the static phantoms as the heterogeneous phantoms mimic tissue vasculature in a more realistic manner. Reconstructed chromophore concentrations were compared very closely with the concentration values measured from a Co-Oximeter. Animal blood was drawn from a sampling port for the purpose of verification. All absorption and scattering properties were also measured the by ISS Oximeter. Scattering coefficients and hemoglobin concentrations within the multi-tube phantoms were chosen similar to the real tissue conditions. Reconstructed cross-sectional images were generated with a two-dimensional reconstruction format.

In this experiment, there were 4 stages for the measurements Stage 1: As mentioned in Section 5.3.2 blood diluted with PBS has an oxygen saturation of ~75%. This blood in the reservoir was pumped into the small multi-tubes embedded in the surrounding medium. The blood is pumped at a slow rate of 5ml/min to prevent settling of blood cells within the tubes. Stage 2: Pure nitrogen was bubbled in the blood reservoir to deoxygenate the blood, which was pumped into the multi-tubes for the measurement. Stages 3 and 4 corresponded to the time when the blood was reoxygenated and after the blood was completely oxygenated, respectively. At each stage, the total hemoglobin concentration and oxygen saturation of blood were measured by a Co-Oximeter. All reconstructed images of multi-tube phantoms for the four stages are shown in Figure 5.13. From Figures 5.13(a) to 5.13(b), we observe a

clear increase in [*Hb*] and simultaneous decrease in [*HbO*] during the course of

deoxygenation. From Figures 5.13(b) to 5.13(d), we observe the opposite behavior: a

gradual increase in [*HbO*] and eventual decrease in [*Hb*], as expected.
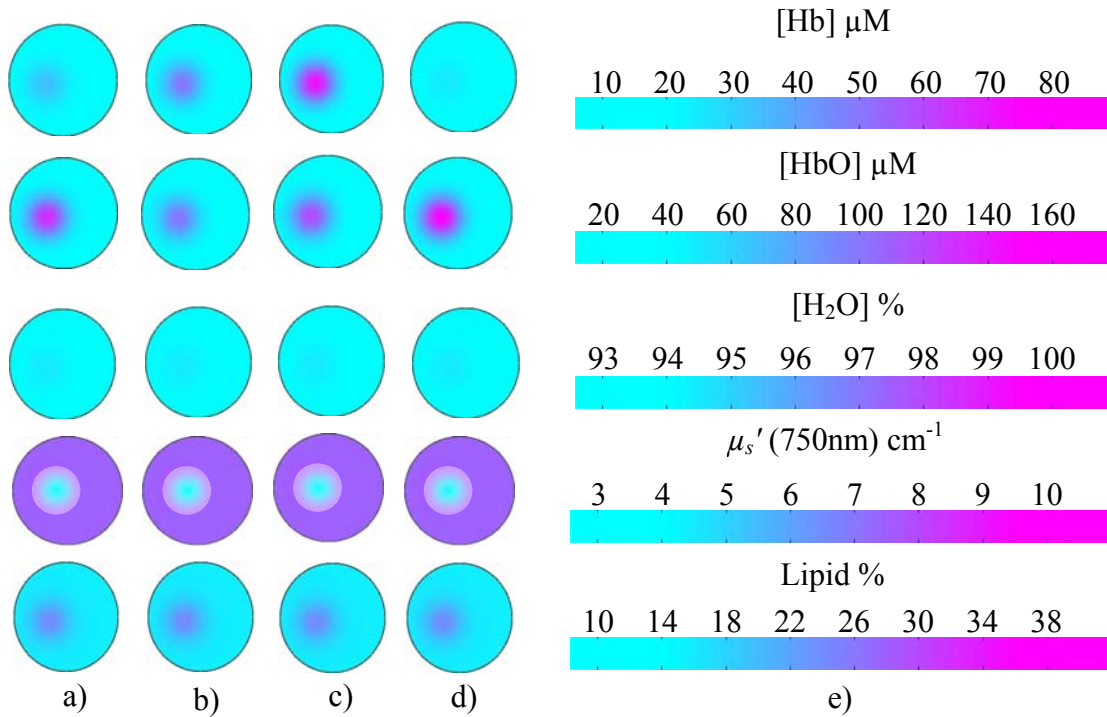
Figure 5.13 Optical tomographic images reconstructed from laboratory phantoms with heterogeneities made of multi-tubes. Sources and detectors are placed on the periphery. All diameters are 4.5 centimeters, and all concentrations are in μM. Reconstructed spatial distributions of [Hb], [*HbO*], water concentration, scattering parameter, and lipid concentration are shown for an inclusion (a) with oxygenated blood, (b) while the blood was deoxygenated, (c) while the blood was reoxygenated, and (d) after the blood was completely oxygenated. (e) Color bars depicting respective scales of the reconstructed parameters. In case (d), oxygen saturation was about 98%, and the [Hb] map is almost zero evenly throughout in region I.

As observed in the previous case, water concentrations in the entire area of

phantom were similar. Heterogeneity in lipid concentrations within the blood

circulating tubes and its surrounding is evident from the fifth row in Figure 5.13.

Heterogeneity in the scattering amplitude is more evident in the reconstruction maps, but it remained unchanged throughout all four stages when the circulating blood was under oxygenation and deoxygenation. Contrasts in lipid concentrations were more pronounced as compared to the previous static phantoms. Blood in the tubes had a lower scattering as well as a larger total hemoglobin concentration in comparison with those determined in the surrounding intralipid suspension. The reduced scattering coefficient of blood in the tubes could not be measured by the ISS Oximeter. The reduced scattering coefficients indicated in Table 5.2 were calculated from the reconstruction algorithm. All the measured and reconstructed concentrations are tabulated in Table 5.2.

Table 5.2 Comparison of measured and reconstructed chromophore concentrations in dynamic multi-tube phantoms. The concentrations and μ_s' of the surrounding blood-intralipid suspension was measured by the ISS Oximeter. A co-Oximeter was used to measure the concentrations of blood in the small tubes.

Stage-1						
	Actual Concentrations		Reconstructed Concentrations		Relative Errors	
	Background	Blood-tubes	Background	Blood-tubes	Background	Blood-tubes
Oxygenated Hemoglobin	15.4 μM	118.8 μM	10.5 μM	140.3 μM	31.8 %	18.1 %
Deoxygenated Hemoglobin	4.9 μM	37.0 μM	5.7 μM	27.4 μM	16.3%	25.9 %
Water Fraction	97% (calculated)	97% (calculated)	94%	94%	3.1%	3.1%
μ_s' (750 nm)	5.10 cm^{-1}		5.04 cm^{-1}	2.3 cm^{-1}	1.2%	
Stage-2						
	Actual Concentrations		Reconstructed Concentrations		Relative Errors	
	Background	Blood-tubes	Background	Blood-tubes	Background	Blood-tubes
Oxygenated Hemoglobin	15.4 μM	88.8 μM	10.5 μM	92.3 μM	31.8 %	3.9%
Deoxygenated Hemoglobin	4.9 μM	80.0 μM	5.7 μM	84.4 μM	16.3%	5.5%
Water Fraction	97% (calculated)	97% (calculated)	94%	94%	3.1%	3.1%
μ_s' (750nm)	5.10 cm^{-1}		5.04 cm^{-1}	2.3 cm^{-1}	1.2%	
Stage-3						
	Actual Concentrations		Reconstructed Concentrations		Relative Errors	
	Background	Blood-tubes	Background	Blood-tubes	Background	Blood-tubes
Oxygenated Hemoglobin	15.4 μM	125.0 μM	10.5 μM	121 μM	31.8 %	3.2%
Deoxygenated Hemoglobin	4.9 μM	42.5 μM	5.7 μM	46.3 μM	16.3%	8.9%
Water Fraction	95% (calculated)	97% (calculated)	94%	94%	3.1%	3.1%
μ_s' (750nm)	5.10 cm^{-1}		5.04 cm^{-1}	2.3 cm^{-1}	1.2%	
Stage-4						
	Actual Concentrations		Reconstructed Concentrations		Relative Errors	
	Background	Blood-tubes	Background	Blood-tubes	Background	Blood-tubes
Oxygenated Hemoglobin	15.4 μM	163.8 μM	10.5 μM	163.3 μM	31.8 %	0.3%
Deoxygenated Hemoglobin	4.9 μM	7.60 μM	5.7 μM	3.3 μM	16.3%	56.5%
Water Fraction	97% (calculated)	97% (calculated)	94%	94%	3.1%	3.1%
μ_s' (750nm)	5.10 cm^{-1}		5.04 cm^{-1}	2.3 cm^{-1}	1.2%	

5.10 Discussion

A broadband white light source provides a relatively simple and inexpensive alternative to discrete wavelength optical tomography techniques for the determination of absorption and reduced scattering coefficients over a large continuous range of wavelengths. The acquisition time per wavelength is significantly reduced in the design presented here. A significant advantage of the method described here is the fact that a spectrum spanning a broad (>500 nm) wavelength range is obtained in a single acquisition. This fact enables the least squares and spectrally constrained optimization algorithms to extract information regarding the spatial distribution of hemoglobin derivatives which are accurate to acceptable levels. The quantifications are less susceptible to errors caused by uncharacterized absorbers. The experimental results from the measurements on dynamic phantoms have verified and evaluated the functionality of our broad band imaging system to be used for measuring the spatial distribution of hemoglobin derivatives and other tissue properties.

5.10.1 Scalability

The system can be easily scaled to house a 32 source-detectors arrangement with simple addition of modular components and little change in the operating software and hardware. The addition of multiplexer unit and spectrometer channels scales the imager. Additions of spectrometer channels, although it is an expensive option, provide higher spatial resolution in image reconstruction. These factors make the hardware very flexible and scalable to application accuracy and complexity.

5.10.2 Test Bed

A plethora of available reconstruction techniques could be utilized and compared for their merits and demerits. My system can be used to evaluate other algorithms and reconstruction paradigms for their efficacy and accuracy. Although a simple available reconstruction algorithm is used to reconstruct image from measured data, detailed and intensive algorithms such as NIRFAST ntensive algorithms such as NIRFAST [116] could be used to elicit required accuracy in image reconstruction. The imager and developed phantoms in my study can function as a reliable test bed to test other developed algorithms and image reconstruction paradigms. The imager records a continuous spectra between 650-1000 nm. This permits the quantitative evaluation of effects of choosing or excluding particular wavelengths on quality of image reconstructions.

The dynamic phantom models attempt to model the tissue vasculature more realistically. Use of multiple small tubes and flowing oxygenated/deoxygenated blood through them in place of static blood is an attempt to mimic the blood flow through vessels and diffused blood in surrounding tissues. Phantoms form a reliable tool to evaluate the performance of image reconstruction algorithms and imager hardware. Use of realistic phantoms described in earlier sections enhances reproducibility and repeatability of optical properties for imager testing. Ability of built phantoms to mimic blood flow and modulate optical properties dynamically in response to change in oxygenation state is particularly useful attributes.

5.10.3 Reconstruction algorithm

The ability of the developed image reconstruction algorithm to obtain tomographic maps was demonstrated by quantitative maps of hemoglobin derivatives on static and dynamic phantoms. The accuracy of quantified concentrations was higher in reconstructions with static phantoms in comparison with the dynamic phantoms. The dynamic phantoms had blood flowing through small tygon tubes as in Figure (5.4). The presence of the small tubes containing the whole blood instead of homogenous blood-intralipid suspension might be one of the sources of error in quantification. The blood in tubes has a low scattering in comparison with the surrounding blood-intralipid suspension.

Intralipid at a higher concentration was used to achieve scattering heterogeneity in static phantoms as described in Section 5.9.1. The contrast in lipid is not visible from Figure 5.12(c). As mentioned in Section 5.9.1 the increase in concentration was ~0.5%, magnitude of which was very small. Moreover, the color bar shown in Figure 5.12(d) indicates a large error in the quantification of lipid concentrations in static phantoms. The specific absorption of lipids is significantly less compared to other tissue chromophores (like Hb and HbO) in the wavelength range 650-850nm [29] [lipid extinction coefficient]. The concentrations of lipid in phantoms is about 1% , making their absorption insignificant. Additionally, the relative sensitivity of the CCD detector in the spectrometer is significantly reduced after 850 nm (The detector data sheet is attached in Appendix G). This may be the reason for large errors in the quantification of

lipids. The quantification of water concentrations may not be effected as much as the lipids, as the water content in phantoms is very high(~97%).

5.10.4 Hardware limitations in the developed imaging system

The components of the imaging system are described in Section 5.2. The diameters of source and detector fibers are restricted by core diameter of the optical multiplexer and slit width of spectrometer channels respectively. This restriction significantly reduces the amount of light delivered to the tissue by the light source and the amount of light that can be collected from the tissue. This leads to a low signal to noise ratio and reduction in rate of measurements. This reduction in signal to noise ratio is a detrimental factor in the accuracy of achieved reconstruction of chromophore concentrations and scattering parameters. Further improvement needs to be explored.

Relaxation of wavelength resolution constraints can improve the speed of the imager significantly as larger slit sizes can be used. Larger slit sizes result in more light entering the CCD detector with a simultaneous reduction of spectral resolution. This reduction in spectral resolution may be admissible as the approach presented used only 8 wavelengths out of the available spectrum.

The optical fibers used in the imaging system were rigid and delicate. Each bifurcated fiber described in Section 5.2.3, had a single fiber of core diameter 1 mm. This made the fiber very rigid and delicate. This can be easily eliminated by the use of fiber bundles instead of single fibers.

5.10.5 Practical constraints in phantom model

Practical limitations in construction of phantoms limit achievable contrasts in water and lipid concentrations. This confines the testing of the developed hardware and reconstruction algorithms for accurate water and lipid quantification. Water forms a significant part of blood and intralipid, hence achieving significant contrasts in water concentrations are practically difficult in liquid phantoms. A change in lipid concentration brings about a bigger change in scattering properties of the phantom. Increase in intralipid concentration beyond 2.5 % -5 % by volume increases the reduced scattering coefficient beyond those found in tissues [33].

5.11 Conclusions

This chapter presented the development of a new broadband, multi source-detector imaging system, which can quickly collect spectra of diffuse reflected light from tissue surface automatically in a short period of time for a spectral range of 650 - 900 nm. The collected spectral data can be used for image reconstruction to extract the concentrations of tissue chromophores and reduced scattering coefficients of turbid media. Calibration techniques for this imaging system were also developed to eliminate the systematic errors due to mismatches or non-uniformities among the individual fibers, setup geometries, spectrometer and multiplex channels. Model calibrations were made to eliminate systematic errors due to mismatch in boundary conditions and deviations from theoretical assumptions in experimental conditions. The experimental measurements using the in house developed hemodynamic phantoms have verified our design of the imaging system and the image reconstruction algorithm. This device and

179

its corresponding reconstruction algorithm has provided the "proof of principle" for a broadband NIR imaging system that can be used to obtain spatial distributions of hemoglobin derivative concentrations and light scattering coefficients. The developed work through my dissertation research has potential applications in the areas of non-invasive, real-time monitoring of animal tumors and animal brain functions and may find additional applications in other fields related to imaging through turbid media.

CHAPTER 6

CONCLUSIONS AND FUTURE WORK

The first part of this dissertation (Chaps. 2-4) described the development, validation and applications of broadband, steady-state, optical spectroscopic systems and algorithms to quantify reduced scattering coefficients and absolute concentrations of tissue chromophores, such as hemoglobin derivatives using (1) thin optical probes with small (100 μm – 1 mm) source-detector separations and (2) a large separation (< 4 cm) probe. In the second stage of my doctoral research development (Chap. 5), image hardware and reconstruction algorithms to quantify spatial distributions of chromophore concentrations and scattering coefficients were developed. The developed algorithms and hardware were successfully validated by making measurements on static and dynamic multi-tube phantoms.

6.1 Conclusions

6.1.1 Quantification of hemoglobin derivative concentration with single very short source-detector separations

Steady-state, spectroscopic reflectance measurements at single short source-detector separation were used to quantify chromophore concentrations and reduced scattering coefficients of the tissues under study. My approach was based on a recently

published analytical model by Zonios and Dimou that expresses the reflectance measured with thin optical probes having short source-detector separations.

Constants k_1 and k_2 were determined through experimental calibrations with blood-intralipid phantoms for three thin fiber optical probes with short source-detector separations, respecgtively: a 7-fiber-array probe and two single source-detector fibers. The values of constants k_1 and k_2 determined at 50, 75 and 100 ms did not show significant differences at 0.05 level of significance, indicating that the determined k_1 and k_2 are independent of integration times. Sensitivity of reflectance with respect to k_1 and k_2 was investigated. k_1 was found to be more sensitive to reflectance in the 600-850 nm range and hence more sensitive to changes in μ_s', as described in Section 2.6.2. k_2 was found to be more sensitive to reflectance in the wavelength range of 500-600 nm and hence more sensitive to changes in μ_a as mentioned in Section 2.6.2.

I have developed a semi-empirical approach in tandem with a heuristic ant colony optimization algorithm to quantify concentrations of hemoglobin derivatives and non-hemoglobin tissue absorbers with acceptable levels of accuracy. The developed technique was validated through measurements with blood-intralipid phantoms. The maximum error in quantification of hemoglobin derivatives was less than 15% (Table 2.7). The calculated reduced scattering coefficients were within ± 1 cm^{-1} from measured values determined by the ISS Oximeter (Table 2.6). Furthermore, all hemoglobin concentrations and reduced scattering coefficients calculated were within error ranges of the instrument taken as gold standard. The probes calibrated can directly be used to quantify optical properties and concentrations of hemoglobin derivatives of living

tissue. The constants calculated are valid for the life of the optical probe and measurement system.

6.1.2 Non-invasive optical monitoring of peripheral hemodynamic changes during formalin-induced pain response

The model and the developed algorithms to quantify hemoglobin derivative concentrations and reduced scattering coefficients in Chapter 2 were further applied to quantify hemodynamic changes during formalin-induced pain behaviors using animal models. The technique developed has the ability to decouple the effects in absorption from those in scattering. Hemodynamic parameters were quantified during the temporal evolution of formalin-induced pain response. Significant ($p<0.001$) increases in $[Hb_{Total}]$, $[HbO]$ and $[Hb]$ after injection of formalin were seen in the ipsilateral side (i.e., the injection side) (Table 3.2). Significant ($p<0.01$) differences were seen in $[Hb_{Total}]$ $[HbO]$ and $[Hb]$ between the ipsilateral and contralateral side during the formali- induced pain response: the values of $[Hb_{Total}]$, $[HbO]$, and $[Hb]$ on the ipsilateral side are much greater than those on the contralateral side. On the other hand, I did not observe any significant changes in light scattering before and after the injection, averaged over 5 experimental animals on either side of the paws. A novel optical non-invasive technique, which could be a valuable tool for the quantitative, objective evaluation of changes in hemoglobin concentrations caused by peripheral noxious stimulation, is presented in this sub-study of my research development.

6.1.3 Quantification of hemoglobin derivative concentrations with single large source-detector separation

Multi-wavelength, steady state reflectance techniques are described for quantification of tissue chromophores and scattering coefficients wish a large source-detector separation. The beneficial aspects and shortcomings of the technique have been mentioned: with broadband, steady-state spectroscopy, the wavelength coverage is continuous. This technique requires only a single source–detector separation, making it suitable to report volume-averaged values of optical properties for heterogeneous tissues. Furthermore, the source–detector separation can be large (1-4 cm, even 5-6 cm if stronger light sources are used), allowing for mean probing depths to be in centimeters that cannot be achieved with multi-source-detector, steady state techniques [26]. This advantage permits to probe deep tissues and thus is significant for many clinical purposes. The developed technique was validated by making simultaneous measurements with the ISS Oximeter. The calculated concentrations of Hb and HbO correlated well with the expected values. The μ_s' values calculated from the algorithm were within $\pm$ 1 cm^{-1} of those measured by the ISS Oximeter.

The feasibility of using the technique that I developed in this study to quantify optical properties of human prostate lesions and during the growth of orthotropic brain tumors in rats has been demonstrated, with spectral acquisition time of less than 500 ms. The total hemoglobin content, oxygen saturation, and water fraction of ex vivo human prostate lesions and of rat brain tumors in vivo have been quantified and shown to have physiological meanings for respective applications. This technique is relatively

inexpensive and could prove valuable in improving accuracy and for developing online monitoring techniques.

One deficiency of my method is the inability to accurately quantify water content or percentage in tissues because of the intrinsic approach of the second derivative method. With the second derivative spectra of the NIR reflectance from tissues, [*Hb*] can be quantified only by having known or assumed water percentage. In the case of tumors, water content or percentage can be a sensitive parameter and can serve as a physiological parameter for monitoring tissue/tumor status. Further study should be carried out in order to overcome this shortcoming of the method.

6.1.4 Imaging of hemoglobin derivative concentrations with multi-large source detector separations

Chapters 2 and 4 described the methods to quantify optical properties of tissue at small (100 μm – 1 mm) and large (1-4 cm) source-detector separations. In Chapter 4 spatial heterogeneities in hemoglobin derivative concentrations and reduced scattering coefficients were ignored, and volume-averaged parameters were computed. This approach is not accurate in real biological tissues when the investigated volumes are large as measured with large source-detector separations. To overcome this limitation, Chapter 5 presented the development of a new broadband, steady-state, multi- source-detector imaging system, which can quickly collect spectra of diffuse reflected light from tissue surface automatically in a short period of time for a spectral range of 650 - 930 nm. The collected spectral data were used for image reconstructions to extract the concentrations of tissue chromophores and reduced scattering coefficients of turbid media. Calibration techniques for this imaging system were also developed to eliminate

the systematic errors due to mismatches or non-uniformities among the individual fibers, setup geometries, spectrometer and multiplex channels. Model calibrations were also made to eliminate systematic errors due to mismatch in boundary conditions and deviations of experimental conditions from theoretical assumptions. The experimental measurements using the in-house developed hemodynamic phantoms have verified our design of the imaging system and the image reconstruction algorithm. This device and its corresponding reconstruction algorithm has provided us with the "proof of principle" for a broadband NIR imaging system that can be used to obtain spatial distributions of hemoglobin derivative concentrations and light scattering coefficients. This developed work through my dissertation research has potential applications in the areas of non-invasive, real-time monitoring of animal tumors and animal brain functions, also finding additional applications in other fields related to imaging through turbid media.

<u>6.2 Future work</u>

6.2.1 Accuracy in quantification of water and lipid concentrations

The water and lipid content in tissues can be quantified with greater quantitative accuracy with the use of longer wavelengths, i.e., > 900 nm. Water [79] and lipids [117] have specific absorptions, orders of magnitude lower than hemoglobin in the wavelength range of 650-850 nm. The specific absorptions of water and lipid become significant only after wavelengths > 875 nm. Use of light sources and detectors with high sensitivity in this wavelength range may result in significant increase in the accuracy of quantified water and lipid concentrations. Water and lipid content or

186

percentage can be sensitive parameters to living tissues and thus can serve as a physiological parameter for monitoring tissue/tumor status.

6.2.2 Extending broadband NIRS Imager developed in Chapter 5 to in vivo studies

The broadband imager developed in Chapter 5 and its corresponding reconstruction algorithm has provided the "proof of principle" for a broadband NIR imaging system that can be used to obtain spatial distributions of hemoglobin derivative concentrations and light scattering coefficients. Modifications would be required to overcome limitations in the system for in vivo animal imaging. The light intensity delivered by the source and that collected by the detector would need to drastically increased. This can be achieved by using optical fibers of larger diameter, which would require building custom designed optical multiplexers. In the present design, the core diameter of optical fibers used in the system is limited by the diameters of optical multiplexer entrance and the slit widths of the multi-channel spectrometer. Increasing the diameter of optical multiplexer entrance and exit would significantly increase the light delivered by source fibers, and thus greatly increasing signal to noise ratios. This increase in signal to noise ratios would allow in vivo studies for the quantification of tissue chromophores and reduced scattering coefficients.

6.2.3 Monitoring of hemodynamic changes in brain and spinal cord during formalin-induced pain responses

This dissertation presented a technique to monitor peripheral hemodynamic changes during formalin-induced pain responses in rats. Such in vivo monitoring of hemodynamic changes could be extended for the studies in the brain and spinal cord to

elicit information leading to better understanding of pain responses. Point measurements, such as those described in Chapter 3, or images of hemodynamic changes obtained by using NIRS imagers (DYNOT) [118] could provide valuable information leading to better understanding of pain mechanisms, which would be further useful in the development of techniques for the management of pain.

APPENDIX A

k_1/k_2 DATA FOR INTEGRATION TIME OF 75 AND 100ms

Table 1 Range of variation of k_1 and k_2 for optical fiber probe computed using measurements from blood-intralipid phantoms. Measurements were made at a integration time of 75 ms

	$[Hb_{Total}]$ μM	Intralipid concentration	μ_s' (750 nm) cm^{-1}	μ_s' (830 nm) cm^{-1}	k_1	k_2
Measurement-1	31	0.5 %	5.8	4.5	30.8	11.8
Measurement-2	48	0.5 %	5.8	4.5	32.5	11.0
Measurement-3	20	0.8 %	8.2	7.5	31.9	11.3
Measurement-4	28	0.8 %	8.2	7.5	32.1	10.6
Measurement-5	37	0.8 %	8.2	7.5	38.1	14.2
Measurement-6	56	0.8 %	8.2	7.5	31.1	17.1
Measurement-7	33	1.25 %	14.2	13.2	39.1	12.3
Measurement-8	48	1.25 %	14.2	13.2	39.7	14.7
		Average			37.6±.2.3	13.4±1.4

Table 2 Range of variation of k_1 and k_2 for optical fiber probe computed using measurements from blood-intralipid phantoms. Measurements were made at a integration time of 100 ms

	[HbTotal] μM	Intralipid concentration	μs′ (750 nm) cm-1	μs′ (830 nm) cm-1	k1	k2
Measurement-1	31	0.5 %	5.8	4.5	35.6	11.8
Measurement-2	48	0.5 %	5.8	4.5	35.4	11.0
Measurement-3	20	0.8 %	8.2	7.5	39.0	11.3
Measurement-4	28	0.8 %	8.2	7.5	40.9	10.6
Measurement-5	37	0.8 %	8.2	7.5	37.7	14.2
Measurement-6	56	0.8 %	8.2	7.5	31	17.1
Measurement-7	33	1.25 %	14.2	13.2	37.8	13.4
Measurement-8	48	1.25 %	14.2	13.2	39.1	12.7
		Average			37.0±.3.05	11.4±3.4

APPENDIX B

SPSS OUTPUT FOR RAT STUDY

Output for Rat 1- Contralateral side

Source	Type III Sum of Squares	df	Mean Square	F	Sig.	Partial Eta Squared	Noncent. Parameter	Observed Power(a)
Corrected Model	1229012.968(b)	13	94539.459	1152.519	.000	.782	14982.747	1.000
Intercept	773785.880	1	773785.880	9433.129	.000	.693	9433.129	1.000
group	7835.998	1	7835.998	95.528	.000	.022	95.528	1.000
parameters	1212830.524	6	202138.421	2464.245	.000	.779	14785.469	1.000
group * parameters	8346.446	6	1391.074	16.958	.000	.024	101.751	1.000
Error	343371.495	4186	82.029					
Total	2346170.343	4200						
Corrected Total	1572384.463	4199						

Tests of Between-Subjects Effects

Dependent Variable: concentration1
a Computed using alpha = .05
b R Squared = .782 (Adjusted R Squared = .781)

Pairwise Comparisons

Dependent Variable: concentration1

parameters	(I) group	(J) group	Mean Difference (I-J)	Std. Error	Sig.(a)	95% Confidence Interval for Difference(a)	
						Lower Bound	Upper Bound
HbO	baseline	5 mins after inj	-4.134(*)	.739	.000	-5.584	-2.684
	5 mins after inj	baseline	4.134(*)	.739	.000	2.684	5.584
Hb	baseline	5 mins after inj	-1.630(*)	.739	.028	-3.080	-.180
	5 mins after inj	baseline	1.630(*)	.739	.028	.180	3.080
Total Hb	baseline	5 mins after inj	-5.763(*)	.739	.000	-7.213	-4.314
	5 mins after inj	baseline	5.763(*)	.739	.000	4.314	7.213
Oxygen Sat	baseline	5 mins after inj	-7.403(*)	.739	.000	-8.853	-5.954
	5 mins after inj	baseline	7.403(*)	.739	.000	5.954	8.853
melanin	baseline	5 mins after inj	-.017	.739	.981	-1.467	1.432
	5 mins after inj	baseline	.017	.739	.981	-1.432	1.467
Mus-min	baseline	5 mins after inj	-.307	.739	.678	-1.757	1.143
	5 mins after inj	baseline	.307	.739	.678	-1.143	1.757
particle size	baseline	5 mins after inj	.132	.739	.858	-1.318	1.582
	5 mins after inj	baseline	-.132	.739	.858	-1.582	1.318

Based on estimated marginal means
* The mean difference is significant at the .05 level.
a Adjustment for multiple comparisons: Bonferroni.

Output for Rat 1 Ipsilateral side

Source	Type III Sum of Squares	df	Mean Square	F	Sig.	Partial Eta Squared	Noncent. Parameter	Observed Power(a)
Corrected Model	1932454.727(b)	13	148650.364	1826.879	.000	.850	23749.423	1.000
Intercept	1522573.099	1	1522573.099	18712.073	.000	.817	18712.073	1.000
group	9702.408	1	9702.408	119.240	.000	.028	119.240	1.000
parameters	1903856.552	6	317309.425	3899.660	.000	.848	23397.958	1.000
group * parameters	18895.767	6	3149.294	38.704	.000	.053	232.225	1.000
Error	340608.501	4186	81.368					
Total	3795636.327	4200						
Corrected Total	2273063.228	4199						

Tests of Between-Subjects Effects

Dependent Variable: concentration1inj
a Computed using alpha = .05
b R Squared = .850 (Adjusted R Squared = .850)

Pairwise Comparisons

Dependent Variable: concentration1inj

parameters	(I) group	(J) group	Mean Difference (I-J)	Std. Error	Sig.(a)	95% Confidence Interval for Difference(a) Lower Bound	Upper Bound
HbO	baseline	5 mins after inj	-7.025(*)	.737	.000	-8.469	-5.581
	5 mins after inj	baseline	7.025(*)	.737	.000	5.581	8.469
Hb	baseline	5 mins after inj	-4.107(*)	.737	.000	-5.551	-2.663
	5 mins after inj	baseline	4.107(*)	.737	.000	2.663	5.551
Total Hb	baseline	5 mins after inj	-11.132(*)	.737	.000	-12.576	-9.688
	5 mins after inj	baseline	11.132(*)	.737	.000	9.688	12.576
Oxygen Sat	baseline	5 mins after inj	.673	.737	.361	-.771	2.117
	5 mins after inj	baseline	-.673	.737	.361	-2.117	.771
melanin	baseline	5 mins after inj	-.009	.737	.990	-1.453	1.435
	5 mins after inj	baseline	.009	.737	.990	-1.435	1.453
Mus-min	baseline	5 mins after inj	.240	.737	.745	-1.204	1.683
	5 mins after inj	baseline	-.240	.737	.745	-1.683	1.204
particle size	baseline	5 mins after inj	.081	.737	.912	-1.363	1.525
	5 mins after inj	baseline	-.081	.737	.912	-1.525	1.363

Based on estimated marginal means
* The mean difference is significant at the .05 level.
a Adjustment for multiple comparisons: Bonferroni.

Output for Rat 2 Contralateral side

Source	Type III Sum of Squares	df	Mean Square	F	Sig.	Partial Eta Squared	Noncent. Parameter	Observed Power(a)
Corrected Model	3993433.486(b)	13	307187.191	5349.588	.000	.943	69544.643	1.000
Intercept	4968742.978	1	4968742.978	86529.414	.000	.954	86529.414	1.000
group	13.205	1	13.205	.230	.632	.000	.230	.077
parameters	3992205.589	6	665367.598	11587.210	.000	.943	69523.260	1.000
group * parameters	1214.692	6	202.449	3.526	.002	.005	21.154	.953
Error	240370.958	4186	57.423					
Total	9202547.423	4200						
Corrected Total	4233804.445	4199						

Tests of Between-Subjects Effects

Dependent Variable: concentration2
a Computed using alpha = .05
b R Squared = .943 (Adjusted R Squared = .943)

Pairwise Comparisons

Dependent Variable: concentration2

parameters	(I) group	(J) group	Mean Difference (I-J)	Std. Error	Sig.(a)	95% Confidence Interval for Difference(a) Lower Bound	Upper Bound
HbO	baseline	5 mins after inj	1.005	.619	.104	-.208	2.218
	5 mins after inj	baseline	-1.005	.619	.104	-2.218	.208
Hb	baseline	5 mins after inj	-2.080(*)	.619	.001	-3.293	-.867
	5 mins after inj	baseline	2.080(*)	.619	.001	.867	3.293
Total Hb	baseline	5 mins after inj	-1.075	.619	.082	-2.288	.138
	5 mins after inj	baseline	1.075	.619	.082	-.138	2.288
Oxygen Sat	baseline	5 mins after inj	1.300(*)	.619	.036	.087	2.513
	5 mins after inj	baseline	-1.300(*)	.619	.036	-2.513	-.087
melanin	baseline	5 mins after inj	.048	.619	.938	-1.165	1.261
	5 mins after inj	baseline	-.048	.619	.938	-1.261	1.165
Mus-min	baseline	5 mins after inj	.038	.619	.951	-1.175	1.251
	5 mins after inj	baseline	-.038	.619	.951	-1.251	1.175
particle size	baseline	5 mins after inj	-.021	.619	.973	-1.234	1.192
	5 mins after inj	baseline	.021	.619	.973	-1.192	1.234

Based on estimated marginal means
* The mean difference is significant at the .05 level.
a Adjustment for multiple comparisons: Bonferroni.

Output for Rat 2 Ipsilateral side

Tests of Between-Subjects Effects

Source	Type III Sum of Squares	df	Mean Square	F	Sig.	Partial Eta Squared	Noncent. Parameter	Observed Power(a)
Corrected Model	2559154.418(b)	13	196858.032	2408.627	.000	.882	31312.150	1.000
Intercept	2575770.848	1	2575770.848	31515.458	.000	.883	31515.458	1.000
group	94888.048	1	94888.048	1160.988	.000	.217	1160.988	1.000
parameters	2342412.061	6	390402.010	4776.705	.000	.873	28660.231	1.000
group * parameters	121854.310	6	20309.052	248.488	.000	.263	1490.930	1.000
Error	342123.438	4186	81.730					
Total	5477048.704	4200						
Corrected Total	2901277.856	4199						

Dependent Variable: concentration2inj
a Computed using alpha = .05
b R Squared = .882 (Adjusted R Squared = .882)

Pairwise Comparisons

Dependent Variable: concentration2inj

parameters	(I) group	(J) group	Mean Difference (I-J)	Std. Error	Sig.(a)	95% Confidence Interval for Difference(a)	
						Lower Bound	Upper Bound
HbO	baseline	5 mins after inj	-23.890(*)	.738	.000	-25.337	-22.443
	5 mins after inj	baseline	23.890(*)	.738	.000	22.443	25.337
Hb	baseline	5 mins after inj	-2.985(*)	.738	.000	-4.432	-1.537
	5 mins after inj	baseline	2.985(*)	.738	.000	1.537	4.432
Total Hb	baseline	5 mins after inj	-26.874(*)	.738	.000	-28.322	-25.427
	5 mins after inj	baseline	26.874(*)	.738	.000	25.427	28.322
Oxygen Sat	baseline	5 mins after inj	-11.927(*)	.738	.000	-13.374	-10.479
	5 mins after inj	baseline	11.927(*)	.738	.000	10.479	13.374
melanin	baseline	5 mins after inj	-.010	.738	.989	-1.458	1.437
	5 mins after inj	baseline	.010	.738	.989	-1.437	1.458
Mus-min	baseline	5 mins after inj	-.912	.738	.217	-2.360	.535
	5 mins after inj	baseline	.912	.738	.217	-.535	2.360
particle size	baseline	5 mins after inj	.054	.738	.941	-1.393	1.502
	5 mins after inj	baseline	-.054	.738	.941	-1.502	1.393

Based on estimated marginal means
* The mean difference is significant at the .05 level.
a Adjustment for multiple comparisons: Bonferroni.

Output for Rat 3 Contralateral side

Source	Type III Sum of Squares	df	Mean Square	F	Sig.	Partial Eta Squared	Noncent. Parameter	Observed Power(a)
Corrected Model	1171072.434(b)	13	90082.495	4561.322	.000	.934	59297.192	1.000
Intercept	907362.915	1	907362.915	45944.274	.000	.916	45944.274	1.000
group	503.186	1	503.186	25.479	.000	.006	25.479	.999
parameters	1168913.245	6	194818.874	9864.644	.000	.934	59187.862	1.000
group * parameters	1656.003	6	276.000	13.975	.000	.020	83.852	1.000
Error	82670.174	4186	19.749					
Total	2161105.524	4200						
Corrected Total	1253742.608	4199						

Tests of Between-Subjects Effects

Dependent Variable: concentration3
a Computed using alpha = .05
b R Squared = .934 (Adjusted R Squared = .934)

Pairwise Comparisons

Dependent Variable: concentration3

parameters	(I) group	(J) group	Mean Difference (I-J)	Std. Error	Sig.ᵃ	95% Confidence Interval for Difference Lower Bound	95% Confidence Interval for Difference Upper Bound
HbO	baseline	5 mins after inj	1.432*	.363	.000	.721	2.144
	5 mins after inj	baseline	-1.432*	.363	.000	-2.144	-.721
Hb	baseline	5 mins after inj	1.560*	.363	.000	.848	2.271
	5 mins after inj	baseline	-1.560*	.363	.000	-2.271	-.848
Total Hb	baseline	5 mins after inj	2.992*	.363	.000	2.281	3.703
	5 mins after inj	baseline	-2.992*	.363	.000	-3.703	-2.281
Oxygen Sat	baseline	5 mins after inj	-.967*	.363	.008	-1.678	-.255
	5 mins after inj	baseline	.967*	.363	.008	.255	1.678
melanin	baseline	5 mins after inj	-.013	.363	.971	-.724	.698
	5 mins after inj	baseline	.013	.363	.971	-.698	.724
Mus-min	baseline	5 mins after inj	-.153	.363	.674	-.864	.559
	5 mins after inj	baseline	.153	.363	.674	-.559	.864
particle size	baseline	5 mins after inj	-.006	.363	.987	-.717	.706
	5 mins after inj	baseline	.006	.363	.987	-.706	.717

Based on estimated marginal means

*. The mean difference is significant at the .05 level.

a. Adjustment for multiple comparisons: Bonferroni.

Output for Rat 3 Ipsilateral side

Tests of Between-Subjects Effects

Source	Type III Sum of Squares	df	Mean Square	F	Sig.	Partial Eta Squared	Noncent. Parameter	Observed Power(a)
Corrected Model	2879185.825(b)	13	221475.833	3360.933	.000	.913	43692.124	1.000
Intercept	2503255.234	1	2503255.234	37987.315	.000	.901	37987.315	1.000
group	28417.390	1	28417.390	431.239	.000	.093	431.239	1.000
parameters	2737369.758	6	456228.293	6923.340	.000	.908	41540.042	1.000
group * parameters	113398.676	6	18899.779	286.807	.000	.291	1720.844	1.000
Error	275845.410	4186	65.897					
Total	5658286.469	4200						
Corrected Total	3155031.235	4199						

Dependent Variable: concentration3inj
a Computed using alpha = .05
b R Squared = .913 (Adjusted R Squared = .912)

Pairwise Comparisons

Dependent Variable: concentration3inj

parameters	(I) group	(J) group	Mean Difference (I-J)	Std. Error	Sig.(a)	95% Confidence Interval for Difference(a) Lower Bound	Upper Bound
HbO	baseline	5 mins after inj	-12.971(*)	.663	.000	-14.271	-11.672
	5 mins after inj	baseline	12.971(*)	.663	.000	11.672	14.271
Hb	baseline	5 mins after inj	-10.583(*)	.663	.000	-11.882	-9.283
	5 mins after inj	baseline	10.583(*)	.663	.000	9.283	11.882
Total Hb	baseline	5 mins after inj	-23.554(*)	.663	.000	-24.853	-22.254
	5 mins after inj	baseline	23.554(*)	.663	.000	22.254	24.853
Oxygen Sat	baseline	5 mins after inj	10.507(*)	.663	.000	9.207	11.806
	5 mins after inj	baseline	-10.507(*)	.663	.000	-11.806	-9.207
melanin	baseline	5 mins after inj	-.018	.663	.979	-1.317	1.282
	5 mins after inj	baseline	.018	.663	.979	-1.282	1.317
Mus-min	baseline	5 mins after inj	.103	.663	.877	-1.197	1.402
	5 mins after inj	baseline	-.103	.663	.877	-1.402	1.197
particle size	baseline	5 mins after inj	.100	.663	.880	-1.200	1.399
	5 mins after inj	baseline	-.100	.663	.880	-1.399	1.200

Based on estimated marginal means
* The mean difference is significant at the .05 level.
a Adjustment for multiple comparisons: Bonferroni.

Output for Rat 4 Contralateral side

Source	Type III Sum of Squares	df	Mean Square	F	Sig.	Partial Eta Squared	Noncent. Parameter	Observed Power(a)
Corrected Model	2374994.162(b)	13	182691.859	4222.735	.000	.929	54895.558	1.000
Intercept	1914263.314	1	1914263.314	44246.236	.000	.914	44246.236	1.000
group	33.520	1	33.520	.775	.379	.000	.775	.142
parameters	2374084.904	6	395680.817	9145.757	.000	.929	54874.541	1.000
group * parameters	875.738	6	145.956	3.374	.003	.005	20.242	.943
Error	181102.552	4186	43.264					
Total	4470360.028	4200						
Corrected Total	2556096.714	4199						

Tests of Between-Subjects Effects

Dependent Variable: concentration4
a Computed using alpha = .05
b R Squared = .929 (Adjusted R Squared = .929)

Pairwise Comparisons

Dependent Variable: concentration4

parameters	(I) group	(J) group	Mean Difference (I-J)	Std. Error	Sig.(a)	95% Confidence Interval for Difference(a)	
						Lower Bound	Upper Bound
HbO	baseline	5 mins after inj	-.503	.537	.349	-1.556	.550
	5 mins after inj	baseline	.503	.537	.349	-.550	1.556
Hb	baseline	5 mins after inj	-.946	.537	.078	-1.999	.107
	5 mins after inj	baseline	.946	.537	.078	-.107	1.999
Total Hb	baseline	5 mins after inj	-1.450(*)	.537	.007	-2.502	-.397
	5 mins after inj	baseline	1.450(*)	.537	.007	.397	2.502
Oxygen Sat	baseline	5 mins after inj	1.677(*)	.537	.002	.624	2.730
	5 mins after inj	baseline	-1.677(*)	.537	.002	-2.730	-.624
melanin	baseline	5 mins after inj	-.007	.537	.990	-1.060	1.046
	5 mins after inj	baseline	.007	.537	.990	-1.046	1.060
Mus-min	baseline	5 mins after inj	-.020	.537	.970	-1.073	1.033
	5 mins after inj	baseline	.020	.537	.970	-1.033	1.073
particle size	baseline	5 mins after inj	-.001	.537	.999	-1.054	1.052
	5 mins after inj	baseline	.001	.537	.999	-1.052	1.054

Based on estimated marginal means
* The mean difference is significant at the .05 level.
a Adjustment for multiple comparisons: Bonferroni.

Output for Rat 4 Ipsilateral side

Tests of Between-Subjects Effects

Source	Type III Sum of Squares	df	Mean Square	F	Sig.	Partial Eta Squared	Noncent. Parameter	Observed Power(a)
Corrected Model	3247691.900(b)	13	249822.454	7654.012	.000	.960	99502.155	1.000
Intercept	1919170.748	1	1919170.748	58799.181	.000	.934	58799.181	1.000
group	8821.712	1	8821.712	270.278	.000	.061	270.278	1.000
parameters	3220353.428	6	536725.571	16444.094	.000	.959	98664.564	1.000
group * parameters	18516.760	6	3086.127	94.552	.000	.119	567.313	1.000
Error	136628.581	4186	32.639					
Total	5303491.229	4200						
Corrected Total	3384320.482	4199						

Dependent Variable: concentration4inj
a Computed using alpha = .05
b R Squared = .960 (Adjusted R Squared = .960)

Pairwise Comparisons

Dependent Variable: concentration4inj

parameters	(I) group	(J) group	Mean Difference (I-J)	Std. Error	Sig.(a)	95% Confidence Interval for Difference(a) Lower Bound	Upper Bound
HbO	baseline	5 mins after inj	-8.920(*)	.466	.000	-9.834	-8.005
	5 mins after inj	baseline	8.920(*)	.466	.000	8.005	9.834
Hb	baseline	5 mins after inj	-.521	.466	.264	-1.436	.393
	5 mins after inj	baseline	.521	.466	.264	-.393	1.436
Total Hb	baseline	5 mins after inj	-9.441(*)	.466	.000	-10.356	-8.526
	5 mins after inj	baseline	9.441(*)	.466	.000	8.526	10.356
Oxygen Sat	baseline	5 mins after inj	-3.187(*)	.466	.000	-4.101	-2.272
	5 mins after inj	baseline	3.187(*)	.466	.000	2.272	4.101
melanin	baseline	5 mins after inj	.061	.466	.896	-.853	.976
	5 mins after inj	baseline	-.061	.466	.896	-.976	.853
Mus-min	baseline	5 mins after inj	1.770(*)	.466	.000	.855	2.684
	5 mins after inj	baseline	-1.770(*)	.466	.000	-2.684	-.855
particle size	baseline	5 mins after inj	-.052	.466	.911	-.967	.862
	5 mins after inj	baseline	.052	.466	.911	-.862	.967

Based on estimated marginal means
* The mean difference is significant at the .05 level.
a Adjustment for multiple comparisons: Bonferroni.

Output for Rat 5 Contralateral side

Tests of Between-Subjects Effects

Source	Type III Sum of Squares	df	Mean Square	F	Sig.	Partial Eta Squared	Noncent. Parameter	Observed Power(a)
Corrected Model	624410.570(b)	13	48031.582	12845.844	.000	.976	166995.978	1.000
Intercept	953030.435	1	953030.435	254883.978	.000	.984	254883.978	1.000
group	664.547	1	664.547	177.730	.000	.041	177.730	1.000
parameters	621978.324	6	103663.054	27724.247	.000	.975	166345.484	1.000
group * parameters	1767.700	6	294.617	78.794	.000	.101	472.764	1.000
Error	15651.770	4186	3.739					
Total	1593092.775	4200						
Corrected Total	640062.340	4199						

Dependent Variable: concentration5
a Computed using alpha = .05
b R Squared = .976 (Adjusted R Squared = .975)

Pairwise Comparisons

Dependent Variable: concentration5

parameters	(I) group	(J) group	Mean Difference (I-J)	Std. Error	Sig.(a)	95% Confidence Interval for Difference(a)	
						Lower Bound	Upper Bound
HbO	baseline	5 mins after inj	.506(*)	.158	.001	.196	.815
	5 mins after inj	baseline	-.506(*)	.158	.001	-.815	-.196
Hb	baseline	5 mins after inj	2.377(*)	.158	.000	2.068	2.687
	5 mins after inj	baseline	-2.377(*)	.158	.000	-2.687	-2.068
Total Hb	baseline	5 mins after inj	2.883(*)	.158	.000	2.573	3.192
	5 mins after inj	baseline	-2.883(*)	.158	.000	-3.192	-2.573
Oxygen Sat	baseline	5 mins after inj	-1.140(*)	.158	.000	-1.450	-.830
	5 mins after inj	baseline	1.140(*)	.158	.000	.830	1.450
melanin	baseline	5 mins after inj	.039	.158	.804	-.270	.349
	5 mins after inj	baseline	-.039	.158	.804	-.349	.270
Mus-min	baseline	5 mins after inj	.832(*)	.158	.000	.522	1.141
	5 mins after inj	baseline	-.832(*)	.158	.000	-1.141	-.522
particle size	baseline	5 mins after inj	.072	.158	.647	-.237	.382
	5 mins after inj	baseline	-.072	.158	.647	-.382	.237

Based on estimated marginal means
* The mean difference is significant at the .05 level.
a Adjustment for multiple comparisons: Bonferroni.

Output for Rat 5 Ipsilateral side

Tests of Between-Subjects Effects

Dependent Variable: concentration5inj

Source	Type III Sum of Squares	df	Mean Square	F	Sig.	Partial Eta Squared	Noncent. Parameter
Corrected Model	3488525.246(b)	13	268348.096	8218.144	.000	.962	106835.868
Intercept	2244326.974	1	2244326.974	68732.373	.000	.943	68732.373
group	64141.735	1	64141.735	1964.337	.000	.319	1964.337
parameters	3324867.079	6	554144.513	16970.641	.000	.961	101823.847
group * parameters	99516.433	6	16586.072	507.947	.000	.421	3047.685
Error	136685.993	4186	32.653				
Total	5869538.213	4200					
Corrected Total	3625211.239	4199					

a Computed using alpha = .05
b R Squared = .962 (Adjusted R Squared = .962)

Pairwise Comparisons

Dependent Variable: concentration5inj

parameters	(I) group	(J) group	Mean Difference (I-J)	Std. Error	Sig.(a)	95% Confidence Interval for Difference(a) Lower Bound	95% Confidence Interval for Difference(a) Upper Bound
HbO	baseline	5 mins after inj	-22.075(*)	.467	.000	-22.990	-21.160
	5 mins after inj	baseline	22.075(*)	.467	.000	21.160	22.990
Hb	baseline	5 mins after inj	-1.897(*)	.467	.000	-2.812	-.982
	5 mins after inj	baseline	1.897(*)	.467	.000	.982	2.812
Total Hb	baseline	5 mins after inj	-23.972(*)	.467	.000	-24.887	-23.057
	5 mins after inj	baseline	23.972(*)	.467	.000	23.057	24.887
Oxygen Sat	baseline	5 mins after inj	-4.417(*)	.467	.000	-5.331	-3.502
	5 mins after inj	baseline	4.417(*)	.467	.000	3.502	5.331
melanin	baseline	5 mins after inj	.039	.467	.933	-.876	.954
	5 mins after inj	baseline	-.039	.467	.933	-.954	.876
Mus-min	baseline	5 mins after inj	-2.446(*)	.467	.000	-3.360	-1.531
	5 mins after inj	baseline	2.446(*)	.467	.000	1.531	3.360
particle size	baseline	5 mins after inj	.056	.467	.904	-.858	.971
	5 mins after inj	baseline	-.056	.467	.904	-.971	.858

Based on estimated marginal means
* The mean difference is significant at the .05 level.
a Adjustment for multiple comparisons: Bonferroni.

APPENDIX C

PHOSPHATE BUFFERED SALINE

Phosphate Buffered Saline (PBS)

10X PBS (0.1M PBS, pH 7.2):

Na2HPO4 (anhydrous) --------------------- 10.9 g

NaH2PO4 (anhydrous) ---------------------- 3.2 g

NaCl -- 90 g

Distilled water ---------------------------- 1000 ml

Mix to dissolve and adjust pH to 7.2

Store this solution at room temperature. Dilute 1:10 with distilled water before use and adjust pH if necessary

APPENDIX D

REGIONS IN THE PROSTATE GLAND

Area on Excised Prostate	Description	Classification in Figure 4.18
abottom1	Apex-bottom Measurement-1	Region-1
abottom2	Apex-bottom Measurement-2	Region-1
abottomb1	Apex-bottom Measurement-3	Region-1
abottomb2	Apex-bottom Measurement-4	Region-1
abottomb3	Apex-bottom Measurement-5	Region-1
atop1	Apex-Top Measurement-1	Region-2
atop2	Apex-Top Measurement-2	Region-2
atopb1	Apex-Top Measurement-3	Region-2
atopb2	Apex-Top Measurement-4	Region-2
atopb3	Apex-Top Measurement-5	Region-2
b	Base	Region-1
lb1	Left Base-1	Region-1
lb2	Left Base-2	Region-1
lb	Left Base-3	Region-1
lbase1	Left Base-4	Region-1
lbase2	Left Base-5	Region-1
lbaseb3	Left Base-6	Region-1
lbaseb	Left Base-7	Region-1
ls2	Left Side-1	Region-1
ls1	Left Side-2	Region-1
lvertical2	Left Vertical -1	Region-1
lvertical	Left Vertical -2	Region-1
phard	Pressure-Hard	Region-1
plight	Pressure-Light	Region-1
rb	Right Base	Region-1
rbase1	Right Base-1	Region-1
rbase2	Right Base-2	Region-1
rs1	Right side-1	Region-1
rs2	Right side-2	Region-1
rs3	Right side-3	Region-1
rt1	Right side-4	Region-1
rt2	Right side-5	Region-1
rver1	Right Vertex-1	Region-1
rver2	Right Vertex-2	Region-1

APPENDIX E

MATLAB CODE

```matlab
function [] = NeuroPlotCB(action)
% Code to run the GUI.
% Requires folder for all measured files - no files other than
measured
% files.presence of other files in the folder results in an error.
% Required folder for calibration files. Store all files such as
extinction
% coeffcients and dark files if significant dark signal needs to be
taken
% in to account. include water, and the hemoglobin exticntion
coeffcients
% of required animal coeffceints or human coeffcients.
% using Ant-Hill Optimization for optimization


% global ehb02_ext;
% global ehb_ext;
%global ewater_ext;

global lambda_low    % Lower limit of Wavelength
global lambda_high   % Higher Limit of Wavelength
global oxygenation
global rho            % Source detector Separation
global XDATA
global YDATA

lambda_low = 500.00;
lambda_high = 850.00;
rho=1.50;

A=2.984128;
flag = 0;
clc
ewater_ext=[];
Data='aa_data3_FAEA';
Type='multiple solutions ';

VTR = 1.e-8;

% D      number of parameters of the objective function
D_algo = 4;

y=[];
% NP             number of population members
NP = 40;
% itermax        maximum number of iterations (generations)
itermax = 1000;
% F              DE-stepsize F ex [0, 2]
F_algo = 0.005;
CR = 0.9;

switch(action)
```

```
case 'Start'
    % ----------------------------------------
    [F, P] = uigetfile('*.*', 'Select one of the files in the
folder');
    if F == 0
        return;
    end
    Folder = P;
    proc_flag=0;
    Contents = dir(Folder);
    for i = 1:length(Contents)
        if strcmp(Contents(i).name,'Slope.txt')==1
            proc_flag=1;
            break;
        end
    end
    if proc_flag==0
        x = 1;

        for i = 1:length(Contents)
            if Contents(i).isdir == 0
                FileNames(x) = str2num(Contents(i).name);
                x = x+1;
            end
        end
        SortFileNames = sort(FileNames);
        Files='';
        for i = 1:length(SortFileNames)
            Files = strvcat(Files, strcat(Folder,
num2str(SortFileNames(i))));
        end


        for i=1:length(Files(:, 1))
            i
            deblank(Files(i,:));
            fr=fopen(deblank(Files(i,:)));
            aaa=fscanf(fr,'%g',[1,inf]);
            fclose(fr);
            for p=1:2048
                aa(p)=aaa(p*2);
                lam(p)=aaa(p*2-1);
            end
            bbb(:,i)=aa';
            maxintensity(i)=max(aa);

        end
        sss=0;
        count=1;
        for j=1:length(Files(:, 1))
            sss=0;
            for i=441:879
```

```matlab
                sss=sss+bbb(i,j);
            end
            aver550(j)=sss;
            sump1=0;
            sump2=0;
            sump3=0;
            sump4=0;

            for jj=1:471
                sump1=sump1 +(lam(jj+1030)*bbb(jj+1030,j));
                sump2=sump2 + lam(jj+1030);
                sump3=sump3+ bbb(jj+1030,j);
                sump4=sump4 + (lam(jj+1030)^2);
            end
            slope1(count)=-(((471*sump1)-
(sump2*sump3))/((471*sump4)-(sump2*sump2)));

            %Determine slope of the two wavelength Ranges
            sump1=0;
            sump2=0;
            sump3=0;
            sump4=0;

            for jj=1:62
                sump1=sump1 +(lam(jj+1092)*bbb(jj+1092,j));
                sump2=sump2 + lam(jj+1092);
                sump3=sump3+ bbb(jj+1092,j);
                sump4=sump4 + (lam(jj+1092)^2);
            end
            slope_715(count)=-(((62*sump1)-
(sump2*sump3))/((62*sump4)-(sump2*sump2)));

            sump1=0;
            sump2=0;
            sump3=0;
            sump4=0;
            for jj=1:80
                sump1=sump1 +(lam(jj+1386)*bbb(jj+1386,j));
                sump2=sump2 + lam(jj+1386);
                sump3=sump3+ bbb(jj+1386,j);
                sump4=sump4 + (lam(jj+1386)^2);
            end
            slope_815(count)=-(((80*sump1)-
(sump2*sump3))/((80*sump4)-(sump2*sump2)));

            % array_1: 720 nm - 740 nm
            array_1 =bbb(1092:1153,j);
            lam_array1=lam(1092:1153);

            % array-2= 815 nm - 850 nm
            array_2 =bbb(1386:1465,j);
            lam_array2=lam(1386:1465);
```

```
                % Fit a single degree polynomial so as to obtain the
slopes for the wavelength ranges
                % Estimate intensity at required wavelength from the
relation so deterimed
                % Least Squred Estimate of the coeffcients. LInear
curve fitting techniques
                % P= Coeffceint Array
                % S= Structure to get regression statistics
                size(array_1);
                size(lam_array1);

                [P,S] = polyfit(lam_array1,array_1',1);
                [P_2,S_2]= polyfit(lam_array2,array_2',1);

                % Evaluate the polynomials obtained for intensity
values
                func_715 = polyval(P,lam_array1);
                func_815 = polyval(P_2,lam_array2);

                % retrieve the evaluated value at 730 nm and 830 nm
                intensity_730(count)=func_715(30);
                intensity_830(count)=func_815(41);

                % Process Data to get oxygenation information
                % Read the Average Reference Data from the File
                % Read data from user data of axes8 to get the path :
if flag set to else prompt user to
                % show path of calibration data
                % Avoids user to enter the path for each run
                if flag == 0
                    [F, P] = uigetfile('*.*', 'Select one of the files
in the folder : Folder for calibration and coeffcients ');
                    if F == 0
                        return;
                    end
                    set(findobj(gcbf, 'Tag', 'axes7'),'UserData',P);
                    oxy_folder = P;
                    flag=1;
                end
                set(findobj(gcbf, 'Tag', 'axes8'),'UserData',flag);
                fname=strcat(oxy_folder,'calib.txt');

                fid = fopen(fname,'r');
                Ref3 = read_sort(fid);
                Ref_avg = Ref3(:,2);

                %Load Exctinction Coeefcients from Text File
                fname = strcat(oxy_folder,'human-extinct.txt');
                extict = load(fname);
                lambda = extict(:,1);
                ehb02 = extict(:,3);
```

210

```matlab
                ehb = extict(:,2);

                %Load Melanin Exctinction Coeefcients from Text File
                fname = strcat(oxy_folder,'extinct_melanin.txt');
                extict = load(fname);
                eMelanin=extict(:,2);

                %Load Fat Exctinction Coeefcients from Text File
                fname = strcat(oxy_folder,'extinct_fat.txt');
                extict_fat = load(fname);
                eFat = extict_fat(:,2);

                %Create a vector comprising of only wavelength, we
assume that the
                %step length in lambda remains the same for all the
reference data and
                %test data

                XDATA = Ref3(:,1);

                %Interpolate extinction coefficients
                ehb_ext= interp1(lambda,ehb,XDATA);
                ehb02_ext = interp1(lambda,ehb02,XDATA);
                eMelanin_ext= interp1(extict(:,1),eMelanin,XDATA);
                eFat_ext= interp1(extict_fat(:,1),eFat,XDATA);

                fname = strcat(oxy_folder,'ewater_ucl.txt');
                extict_water = load(fname);
                ewater_ext =
interp1(extict_water(:,1),extict_water(:,2),XDATA);

                deblank(Files(count,:));
                fid=fopen(deblank(Files(count,:)));
                Hb = read_sort(fid);

calib_fac=str2num(get(findobj(gcbf,'Tag','OD'),'String'));

                %Eliminate spectral effects
                Hb_spectral = Hb(:,2)./ Ref_avg;
                YDATA = Hb_spectral*(1/calib_fac);

                % Scale the values between 1 & 0 .Eliminates the
effect of diffrent integration times
                % Read in values from GUI screen for K1 & K2

                K1=str2num(get(findobj(gcbf,'Tag','mua'),'String'));
                K2=str2num(get(findobj(gcbf,'Tag','mus'),'String'));

                FUN='func_simp_small';

NumAnts=30;Nmoves=60;LocalMoves=30;NONLNCON=[];rpmax=[];
```

```matlab
            % read lower and upper bounds

            %     if particular component consideration is not
required
            %     please set bounds to non-significant values. ex -
            %     0.0002-upperbound
            %     0.0001-lower bound
            %     avoid using zero values

            %     HbO     Hb      Melanin   mus' p'tcle-size  water
fat
            UB =[0.90    0.90    0.01      55       2.00      0.80
0.002];   % -----   Upper bounds
            LB =[0.0001  0.0001  0.01      3.5      0.10      0.80
0.001];   % -----   Lower bounds

            XVmin=LB;
            XVmax=UB;


            opt =
optimset('LargeScale','on','DerivativeCheck','on','Display','iter','Le
venbergMarquardt','on','MaxFunEvals',10000,'MaxIter',10000,'TolFun',1e
-20,'TolX',1e-22,'TolCon',1e-10);


            y=[];

            [Estimates, resnorm] =
api(FUN,XVmin,XVmax,NumAnts,Nmoves,LocalMoves,NONLNCON,rpmax,y,ehb02_e
xt,ehb_ext,ewater_ext,eMelanin_ext,eFat_ext,rho,XDATA,YDATA,K1,K2);

            a(count)=(Estimates(1));
            b(count)=(Estimates(2));
            mel_conc(count)=(Estimates(3));
            c(count)=(Estimates(4));
            d(count)=(Estimates(5));
            e(count)=(Estimates(6));
            f(count)=(Estimates(7));

            count
            oxy_level(count)= (a(count)/(b(count)+a(count)))*100;
            oxygenation = oxy_level(count);

            set(findobj(gcbf,'Tag','count'),'String',count);
            count=count+1;
        end

        fid=fopen(strcat(Folder, 'FileNames.txt'),'w');
        fprintf(fid,'%10d\n',SortFileNames);
        fclose(fid);
```

```matlab
        % Generate mudata.txt file to read from it for later stage
        fid=fopen(strcat(Folder,'mudata.txt'),'w');
        for i = 1: count-1
            fprintf(fid,'%12.6f\t %12.6f\t %12.6f\t %12.6f\t
%12.6f\t %12.6f\t
%12.6f\n',a(i),b(i),mel_conc(i),c(i),d(i),e(i),f(i));
        end
        fclose(fid);

        fid=fopen(strcat(Folder,'oxydata.txt'),'w');
        fprintf(fid,'%12.f\n',oxy_level);
        fclose(fid);
    else
        slope1=load(strcat(Folder, 'Slope.txt'));
        slope_715=load(strcat(Folder, 'slope_715.txt'));
        slope_815=load(strcat(Folder, 'slope_815.txt'));
        maxintensity=load(strcat(Folder, 'maxintensity.txt'));
        oxy_level=load(strcat(Folder, 'oxydata.txt'));
        intensity_830=load(strcat(Folder, 'intensity_830.txt'));
        intensity_730=load(strcat(Folder, 'intensity_730.txt'));
    end

    AxisHndl = findobj(gcbf, 'Tag', 'axes1');
    axes(AxisHndl);
    plot(slope1,'*-');
    xLabel('Steps');
    yLabel('Slope');
    title('Slope 700-850');
    grid;
    set(AxisHndl, 'Tag', 'axes1');
    set(AxisHndl, 'ButtonDownFcn', 'NeuroPlotCB(''click'');');
    set(gcbo,'UserData',Folder);
    % Flag to see whether calibration data was accessed
    % set to 1 if path is set
    flag = 0;
    AxisHnd8 = findobj(gcbf, 'Tag', 'axes8');
    set(AxisHnd8, 'UserData',flag);
    set(AxisHnd8, 'Tag', 'axes8');

    AxisHnd2 = findobj(gcbf, 'Tag','axes2');
    axes(AxisHnd2);
    plot(maxintensity,'*-');
    xLabel('Steps');
    yLabel('Maximum Intensity');
    title('Maximum Intensity Plot');
    grid;
    set(AxisHnd2, 'ButtonDownFcn', 'NeuroPlotCB(''click_Max'');');
    set(AxisHnd2, 'Tag', 'axes2');

    AxisHnd4 = findobj(gcbf, 'Tag', 'axes4');
    axes(AxisHnd4);
    plot(oxy_level,'*-');
```

213

```
        xLabel('Steps');
        yLabel('Oxygenation- Level');
        title('Oxygenation Level Graph');
        grid;
        set(AxisHnd4, 'ButtonDownFcn', 'NeuroPlotCB(''click_730'');');
        set(AxisHnd4, 'Tag', 'axes4');

        AxisHnd5 = findobj(gcbf, 'Tag', 'axes5');
        axes(AxisHnd5);
        plot(intensity_830,'*-');
        xLabel('Steps');
        yLabel('Intensity at 830 nm');
        title('Intensity Plot');
        grid;
        set(AxisHnd5, 'ButtonDownFcn', 'NeuroPlotCB(''click_830'');');
        set(AxisHnd5, 'Tag', 'axes5');

        AxisHnd11 = findobj(gcbf, 'Tag', 'axes11');
        axes(AxisHnd11);
        plot(slope_715,'*-');
        xLabel('Steps');
        yLabel('Slope 715-740 nm');
        title('Slope 715-740 Plot');
        grid;
        set(AxisHnd11, 'ButtonDownFcn',
'NeuroPlotCB(''click_slope_715'');');
        set(AxisHnd11, 'Tag', 'axes11');

        AxisHnd12 = findobj(gcbf, 'Tag', 'axes12');
        axes(AxisHnd12);
        plot(slope_815,'*-');
        xLabel('Steps');
        yLabel('Slope 815-850 nm');
        title('Slope 815-850 Plot');
        grid;
        set(AxisHnd12, 'ButtonDownFcn',
'NeuroPlotCB(''click_slope_815'');');
        set(AxisHnd12, 'Tag', 'axes12');

        fid=fopen(strcat(Folder, 'Slope.txt'),'w');
        fprintf(fid,'%12.6f\n',slope1);
        fclose(fid);

        fid=fopen(strcat(Folder, 'maxintensity.txt'),'w');
        fprintf(fid,'%12.6f\n',maxintensity);
        fclose(fid);

        fid=fopen(strcat(Folder, 'intensity_730.txt'),'w');
        fprintf(fid,'%12.6f\n',intensity_730);
        fclose(fid);

        fid=fopen(strcat(Folder, 'intensity_830.txt'),'w');
```

```matlab
        fprintf(fid,'%12.6f\n',intensity_830);
        fclose(fid);

        fid=fopen(strcat(Folder, 'Slope_815.txt'),'w');
        fprintf(fid,'%12.6f\n',slope_815);
        fclose(fid);

        fid=fopen(strcat(Folder, 'Slope_715.txt'),'w');
        fprintf(fid,'%12.6f\n',slope_715);
        fclose(fid);

    case 'click'
        %-- Get co-ordinates----
        disp('InCB');

        cord_data=get(findobj(gcbf,'Tag','axes1'),'CurrentPoint');
        filepoint=floor(cord_data(1,1));
        set(gcbo,'UserData',filepoint) ;
        Folder=get(findobj(gcbf,'Tag','Start'),'UserData');
        set(findobj(gcbf,'Tag','point'),'String',filepoint);
        %disp(Folder);
        filenames=load(strcat(Folder,'FileNames.txt'));
        specfile=strcat(Folder,num2str(filenames(filepoint)));
        fid=fopen(specfile,'r');
        aaa=fscanf(fid,'%g',[1,inf]);
        fclose(fid);
        for p=1:2048
            aa(p)=aaa(p*2);
            lam(p)=aaa(p*2-1);
        end
        % array_1: 720 nm - 740 nm
        array_1 =aa(1092:1153);
        lam_array1=lam(1092:1153);

        % array-2= 815 nm - 850 nm
        array_2 = aa(1386:1465);
        lam_array2=lam(1386:1465);

        % Fit a single degree polynomial so as to obtain the slopes
for the wavelength ranges
        % Estimate intensity at required wavelength from the relation
so deterimed
        % Least Squred Estimate of the coeffcients. LInear curve
fitting techniques
        % P= Coeffceint Array
        % S= Structure to get regression statistics

        [P,S] = polyfit(lam_array1,array_1,1);
        [P_2,S_2]= polyfit(lam_array2,array_2,1);

        % Evaluate the polynomials obtained for intensity values
        func_715 = polyval(P,lam_array1);
```

215

```
        func_815 = polyval(P_2,lam_array2);

        AxisHnd3 = findobj(gcbf, 'Tag', 'axes3');
        axes(AxisHnd3);
        plot(lam,aa,'*-');
        xLabel('Lambda -nm');
        yLabel('Intensity');
        title('Spectrum');
        grid;
        set(AxisHnd3, 'ButtonDownFcn',
'NeuroPlotCB(''click_spectrum'');');
        set(AxisHnd3, 'Tag', 'axes3');

        AxisHnd6 = findobj(gcbf, 'Tag', 'axes6');
        axes(AxisHnd6);
        plot(lam_array1,array_1,'*-',lam_array1,func_715,'y+');
        xLabel('Lambda -nm');
        yLabel('Intensity');
        title('Spectrum : 715-740 nm');
        grid;
        set(AxisHnd6, 'ButtonDownFcn',
'NeuroPlotCB(''click_spec_715'');');
        set(AxisHnd6, 'Tag', 'axes6');

        AxisHnd7 = findobj(gcbf, 'Tag', 'axes7');
        axes(AxisHnd7);
        plot(lam_array2,array_2,'*-',lam_array2,func_815,'y+');
        xLabel('Lambda -nm');
        yLabel('Intensity');
        title('Spectrum : 815 - 850 nm');
        grid;
        set(AxisHnd7, 'ButtonDownFcn',
'NeuroPlotCB(''click_spec_815'');');
        set(AxisHnd7, 'Tag', 'axes7');

        main_figure=gcbf;
        slope1=load(strcat(Folder, 'Slope.txt'));
        figure(1);
        plot(slope1,'*-');
        xLabel('Steps');
        yLabel('Slope- 700-850nm');
        title('Slope- 700-850nm');
        grid;

        figure(main_figure);
        AxisHndl = findobj(gcbf, 'Tag', 'axes1');
        set(AxisHndl, 'ButtonDownFcn', 'NeuroPlotCB(''click'');');
        set(AxisHndl, 'Tag', 'axes1');

        % Plot Oxy-deoxy Curve on axes8
        % Extract values of a,b,c,d,e from the file : muadata.txt
        % filepoint index to pick specific a,b,c,d,e values
```

216

```
        % Read the Average Reference Data from the File
        % Read data from user data of axes8 to get the path : if flag
set to else prompt user to
        % show path of calibration data
        % Avoids user to enter the path for each run
        AxisHnd8 = findobj(gcbf, 'Tag', 'axes8');
        flag = (get(findobj(gcbf, 'Tag', 'axes8'),'UserData'));
        set(AxisHnd8, 'Tag', 'axes8');
        if(flag==0)
            [F, P] = uigetfile('*.*', 'Select one of the files in the
folder : For Calibration & Dark Signals');
            if F == 0
                return;
            end
            set(findobj(gcbf, 'Tag', 'oxy_folder'),'String',P);
            Folder = P;
            flag=1;
            set(findobj(gcbf, 'Tag', 'axes8'),'UserData',(flag));
        end
        Folder=get(findobj(gcbf, 'Tag', 'oxy_folder'),'String');
        fname=strcat(Folder,'calib.txt');
        fid = fopen(fname,'r');
        Ref3 = read_sort(fid);
        Ref_avg = Ref3(:,2);

        %Load Exctinction Coeefcients from Text File
        fname = strcat(Folder,'human-extinct.txt');
        extict = load(fname);
        lambda = extict(:,1);
        ehb02 = extict(:,3);
        ehb = extict(:,2);

        %Load Melanin Exctinction Coeefcients from Text File
        fname = strcat(Folder,'extinct_melanin.txt');
        extict = load(fname);
        eMelanin=extict(:,2);

        %Load Fat Exctinction Coeefcients from Text File
        fname = strcat(Folder,'extinct_fat.txt');
        extict_fat = load(fname);
        eFat = extict_fat(:,2);

        %Create a vector comprising of only wavelength, we assume that
the
        %step length in lambda remains the same for all the reference
data and
        %test data

        XDATA = Ref3(:,1);
```

```matlab
        %Interpolate extinction coefficients
        ehb_ext= interp1(lambda,ehb,XDATA);
        ehb02_ext = interp1(lambda,ehb02,XDATA);
        eMelanin_ext= interp1(extict(:,1),eMelanin,XDATA);
        eFat_ext= interp1(extict_fat(:,1),eFat,XDATA);

        fname = strcat(Folder,'ewater_ucl.txt');
        extict_water = load(fname);
        ewater_ext =
interp1(extict_water(:,1),extict_water(:,2),XDATA);

        Folder1=get(findobj(gcbf,'Tag','Start'),'UserData');
        disp(Folder1);
        filenames=load(strcat(Folder1,'FileNames.txt'));
        specfile=strcat(Folder1,num2str(filenames(filepoint)));
        fid=fopen(specfile,'r');
        Hb = read_sort(fid);
        calib_fac=str2num(get(findobj(gcbf,'Tag','OD'),'String'));
        %Eliminate spectral effects
        Hb_spectral = Hb(:,2)./ Ref_avg;
        % Scale the values between 1 & 0 .Eliminates the effect of
diffrent integration times
        %YDATA = (Hb_spectral-min(Hb_spectral))/(max(Hb_spectral)-
min(Hb_spectral));
        YDATA = Hb_spectral*(1/calib_fac);

        K1=str2num(get(findobj(gcbf,'Tag','mua'),'String'));
        K2=str2num(get(findobj(gcbf,'Tag','mus'),'String'));

        % Read a,b,c,d,e values from mudata.txt
        fname=strcat(Folder1,'mudata.txt');
        mudata = load(fname);

        a=mudata(filepoint,1);
        b=mudata(filepoint,2);
        mel_conc=mudata(filepoint,3);
        musatlambdamin=mudata(filepoint,4);
        ds=mudata(filepoint,5);
        e=mudata(filepoint,6);
        fat_conc=mudata(filepoint,7);

        %Define numerator terms
        A=2.984128;
        % Degree of polynomial fits required
        d0=0.0625;
        lambdamin = 450;
        lambdamax = 900;

        % Define Scattering and absorption coeefcient
        mua =
(a.*ehb02_ext)+(b.*ehb_ext)+(mel_conc.*eMelanin_ext)+(fat_conc.*eFat_e
xt);
```

218

```
        % Assume scattering coeffcient to follow the classic weak
exponential model
        % with wavelength. instead of linearly decreasing model as
used before to
        % see the senstivity to optimization. Use the same parameters
c and d but
        % set differnt upper and lower bounds

        d=(d0^0.5)/(ds^0.5);
        lambdadiff= XDATA-lambdamin;
        lambdarange= (lambdamax-lambdamin);
        lam_term=lambdadiff./lambdarange;
        term1 = (1-(d.*lam_term));

        mus = term1.*musatlambdamin;
        mus(1:300)= 1.7303*mus(1:300);
        lambdarange = XDATA(301)-XDATA(1);
        mus_diff = (mus(1))-mus(301);
        XDATA_seg = XDATA(1:300);
        term_mus = -((mus_diff/lambdarange).*(XDATA_seg-XDATA(1)));
        mus_seg = (mus(1))+ term_mus;
        mus(1:300)=mus_seg(1:300);

        term2= (K1./mus);
        term3= K2.*mua;
        term4=term3./mus;
        Fitt_curve = term2+term4;
        Fitt_curve = 1./Fitt_curve;

        AxisHnd8 = findobj(gcbf,'Tag','axes8');
        axes(AxisHnd8);
        length(XDATA)
        length(YDATA)
        plot(XDATA,YDATA,'o',XDATA,Fitt_curve,'r+','LineWidth',2);
        hold off
        xLabel('Lambda -nm');
        yLabel('Normalized Reflectance');
        title('Oxygenation - Comparison');
        legend('Measured Data','Fitted Data');
        oxy_level= (a/(a+b))*100;
        grid;

        set(findobj(gcbf,'Tag','aval'),'String',a);
        set(findobj(gcbf,'Tag','bval'),'String',b);
        set(findobj(gcbf,'Tag','melconc'),'String',mel_conc);
        set(findobj(gcbf,'Tag','fat_conc'),'String',fat_conc);
        set(findobj(gcbf,'Tag','cval'),'String',musatlambdamin);
        set(findobj(gcbf,'Tag','dval'),'String',ds);
        set(findobj(gcbf,'Tag','eval'),'String',e);

        set(findobj(gcbf,'Tag','oxylevel'),'String',oxy_level);
        set(AxisHnd8, 'ButtonDownFcn','NeuroPlotCB(''click_Oxy'');');
```

```
        set(AxisHnd8, 'Tag', 'axes8');

        figure(main_figure);
        AxisHndl = findobj(gcbf, 'Tag', 'axes1');
        set(AxisHndl, 'ButtonDownFcn', 'NeuroPlotCB(''click'');');
        set(AxisHndl, 'Tag', 'axes1');

    case 'click_spectrum'

        disp('In click spectrum');
        filepoint=get(findobj(gcbf,'Tag','axes1'),'UserData');
        Folder=get(findobj(gcbf,'Tag','Start'),'UserData');
        disp(Folder);
        main_figure=gcbf;
        filenames=load(strcat(Folder,'FileNames.txt'));
        specfile=strcat(Folder,num2str(filenames(filepoint)));
        fid=fopen(specfile,'r');
        aaa=fscanf(fid,'%g',[1,inf]);
        fclose(fid);
        for p=1:2048
            aa(p)=aaa(p*2);
            lam(p)=aaa(p*2-1);
        end
        figure(1);
        plot(lam,aa,'*-');
        xLabel('Lambda -nm');
        yLabel('Intensity');
        title('Spectrum');
        grid;

        figure(main_figure);
        AxisHnd3 = findobj(gcbf, 'Tag', 'axes3');
        set(AxisHnd3, 'ButtonDownFcn',
'NeuroPlotCB(''click_spectrum'');');
        set(AxisHnd3, 'Tag', 'axes3');

    case 'PlotOd'
        disp('In Plot Od');
        Folder=get(findobj(gcbf,'Tag','Start'),'UserData');
        disp(Folder);
        main_figure=gcbf;
        filenames=load(strcat(Folder,'FileNames.txt'));
        intensity_730=load(strcat(Folder, 'intensity_730.txt'));
        intensity_830=load(strcat(Folder, 'intensity_830.txt'));
        ref=get(findobj(gcbf,'Tag','num_init'),'String');
        ref_od=str2num(ref);
        % Calculate optical density
        % 730 nm Intensities
        ref_intensity_730 = intensity_730(ref_od);
        rel_inten_730= ref_intensity_730./intensity_730;
        od_730=log(rel_inten_730);
        set(findobj(gcbf,'Tag','axes9'),'UserData',od_730);
```

```
        ref_intensity_830 = intensity_830(ref_od);
        rel_inten_830=ref_intensity_830./intensity_830;
        od_830=log(rel_inten_830);
        set(findobj(gcbf,'Tag','axes10'),'UserData',od_830);


        AxisHnd9 = findobj(gcbf, 'Tag', 'axes9');
        axes(AxisHnd9);
        plot(od_730,'*-');
        xLabel('Steps');
        yLabel('Optical Density');
        title('Optical Density 730 nm');
        grid;
        set(AxisHnd9, 'ButtonDownFcn',
'NeuroPlotCB(''click_od_730'');');
        set(AxisHnd9, 'Tag', 'axes9');


        AxisHnd10 = findobj(gcbf, 'Tag', 'axes10');
        axes(AxisHnd10);
        plot(od_830,'*-');
        xLabel('Steps');
        yLabel('Optical Density');
        title('Optical Density 830 nm');
        grid;
        set(AxisHnd10, 'ButtonDownFcn',
'NeuroPlotCB(''click_od_830'');');
        set(AxisHnd10, 'Tag', 'axes10');



        main_figure=gcbf;
        filenames=load(strcat(Folder,'FileNames.txt'));
        slope1=load(strcat(Folder, 'Slope.txt'));
        ref=get(findobj(gcbf,'Tag','num_init'),'String');
        ref_od=str2num(ref);
        % Calculate optical density
        % 730 nm Intensities
        ref_slope = mean(slope1(1:ref_od));
        rel_slope=ref_slope./slope1;
        od_slope=log(rel_slope);

        fid=fopen(strcat(Folder, 'od_slope.txt'),'w');
        fprintf(fid,'%12.6f\n',od_slope);
        fclose(fid);

        AxisHnd13 = findobj(gcbf, 'Tag', 'axes13');
        axes(AxisHnd13);
        plot(od_slope,'*-');
        xLabel('Steps');
        yLabel('Optical Density');
        title('Optical Density - Slope (700- 850nm)');
        grid;
```

```matlab
        set(AxisHnd13, 'ButtonDownFcn',
'NeuroPlotCB(''click_od_slope'');');
        set(AxisHnd13, 'Tag', 'axes13');

        % Normalize the od between 0 & 1
        max_od_slope=max(od_slope);
        min_od_slope=min(od_slope);

        norm_slope_od=(od_slope- min_od_slope)/(max(od_slope)-
min(od_slope));
        fid=fopen(strcat(Folder, 'od_slope_norm.txt'),'w');
        fprintf(fid,'%12.6f\n',norm_slope_od);
        fclose(fid);

        AxisHnd14 = findobj(gcbf, 'Tag', 'axes14');
        axes(AxisHnd14);
        plot(norm_slope_od,'*-');
        xLabel('Steps');
        yLabel('Optical Density');
        title('Optical Density Normalized');
        grid;
        set(AxisHnd14, 'ButtonDownFcn',
'NeuroPlotCB(''click_od_norm'');');
        set(AxisHnd14, 'Tag', 'axes14');


    case 'click_Max'

        disp('In click_Max');
        Folder=get(findobj(gcbf,'Tag','Start'),'UserData');
        disp(Folder);
        main_figure=gcbf;
        maxintensity=load(strcat(Folder, 'maxintensity.txt'));
        figure(1);
        plot(maxintensity,'*-');
        xLabel('Steps');
        yLabel('Maximum Intensity');
        title('Maximum Intensity Plot');
        grid;

        figure(main_figure);
        AxisHnd2 = findobj(gcbf, 'Tag', 'axes2');
        set(AxisHnd2, 'ButtonDownFcn', 'NeuroPlotCB(''click_Max'');');
        set(AxisHnd2, 'Tag', 'axes2');

    case 'click_730'

        disp('In Oxy-Plot');
        Folder=get(findobj(gcbf,'Tag','Start'),'UserData');
        disp(Folder);
        main_figure=gcbf;
```

```
    intensity_730=load(strcat(Folder, 'oxydata.txt'));
    figure(1);
    plot(intensity_730,'*-');
    xLabel('Steps');
    yLabel('Oxygenation- Level');
    title('Oxygenation Level Graph');
    grid;

    figure(main_figure);
    AxisHnd4 = findobj(gcbf, 'Tag', 'axes4');
    set(AxisHnd4, 'ButtonDownFcn', 'NeuroPlotCB(''click_730'');');
    set(AxisHnd4, 'Tag', 'axes4');

case 'click_830'
    disp('In click_830');
    Folder=get(findobj(gcbf,'Tag','Start'),'UserData');
    disp(Folder);
    main_figure=gcbf;
    intensity_830=load(strcat(Folder, 'intensity_830.txt'));
    figure(1);
    plot(intensity_830,'*-');
    xLabel('Steps');
    yLabel('Intensity at 830 nm');
    title('830 nm Intensity Plot');
    grid;

    figure(main_figure);
    AxisHnd5 = findobj(gcbf, 'Tag', 'axes5');
    set(AxisHnd5, 'ButtonDownFcn', 'NeuroPlotCB(''click_830'');');
    set(AxisHnd5, 'Tag', 'axes5');

case 'click_od_730'
    disp('In click_od_730');
    Folder=get(findobj(gcbf,'Tag','Start'),'UserData');
    disp(Folder);
    filenames=load(strcat(Folder,'FileNames.txt'));
    intensity_730=load(strcat(Folder, 'intensity_730.txt'));
    ref=get(findobj(gcbf,'Tag','num_init'),'String');
    ref_od=str2num(ref);
    % Calculate optical density
    % 730 nm Intensities
    ref_intensity_730 = intensity_730(ref_od);
    rel_inten_730=ref_intensity_730./intensity_730;
    od_730=log(rel_inten_730);

    main_figure=gcbf;
    figure(1);
    plot(od_730,'*-');
    xLabel('Steps');
    yLabel('Optical Density');
    title('Optical Density 730 nm');
    grid;
```

```matlab
        figure(main_figure);
        AxisHnd9 = findobj(gcbf, 'Tag', 'axes9');
        set(AxisHnd9, 'ButtonDownFcn',
'NeuroPlotCB(''click_od_730'');');
        set(AxisHnd9, 'Tag', 'axes9');

    case 'click_od_830'
        disp('In click_od_830');
        Folder=get(findobj(gcbf,'Tag','Start'),'UserData');
        disp(Folder);
        filenames=load(strcat(Folder,'FileNames.txt'));
        intensity_830=load(strcat(Folder, 'intensity_830.txt'));
        ref=get(findobj(gcbf,'Tag','num_init'),'String');
        ref_od=str2num(ref);
        % Calculate optical density
        % 730 nm Intensities
        ref_intensity_830 = intensity_830(ref_od);
        rel_inten_830=ref_intensity_830./intensity_830;
        od_830=log(rel_inten_830);

        main_figure=gcbf;
        figure(1);
        plot(od_830,'*-');
        xLabel('Steps');
        yLabel('Optical Density');
        title('Optical Density 830 nm');
        grid;

        figure(main_figure);
        AxisHnd10 = findobj(gcbf, 'Tag', 'axes10');
        set(AxisHnd10, 'ButtonDownFcn',
'NeuroPlotCB(''click_od_830'');');
        set(AxisHnd10, 'Tag', 'axes10');

    case 'click_spec_715'

        disp('In click spec_715');
        filepoint=get(findobj(gcbf,'Tag','axes1'),'UserData');
        Folder=get(findobj(gcbf,'Tag','Start'),'UserData');
        disp(Folder);
        main_figure=gcbf;
        filenames=load(strcat(Folder,'FileNames.txt'));
        specfile=strcat(Folder,num2str(filenames(filepoint)));
        fid=fopen(specfile,'r');
        aaa=fscanf(fid,'%g',[1,inf]);
        fclose(fid);
        for p=1:2048
            aa(p)=aaa(p*2);
            lam(p)=aaa(p*2-1);
        end
```

```matlab
        % array_1: 720 nm - 740 nm
        array_1 =aa(1092:1153);
        lam_array1=lam(1092:1153);

        [P,S] = polyfit(lam_array1,array_1,1);
        func_715 = polyval(P,lam_array1);

        figure(1);
        plot(lam_array1,array_1,'*-',lam_array1,func_715,'y+');
        xLabel('Lambda -nm');
        yLabel('Intensity');
        title('Spectrum : 715-740 nm');
        grid;

        figure(main_figure);
        AxisHnd6 = findobj(gcbf, 'Tag', 'axes6');
        set(AxisHnd6, 'ButtonDownFcn',
'NeuroPlotCB(''click_spec_715'');');
        set(AxisHnd6, 'Tag', 'axes6');

    case 'click_spec_815'

        disp('In click spec_815');
        filepoint=get(findobj(gcbf,'Tag','axes1'),'UserData');
        Folder=get(findobj(gcbf,'Tag','Start'),'UserData');
        disp(Folder);
        main_figure=gcbf;
        filenames=load(strcat(Folder,'FileNames.txt'));
        specfile=strcat(Folder,num2str(filenames(filepoint)));
        fid=fopen(specfile,'r');
        aaa=fscanf(fid,'%g',[1,inf]);
        fclose(fid);
        for p=1:2048
            aa(p)=aaa(p*2);
            lam(p)=aaa(p*2-1);
        end

        % array-2= 815 nm - 850 nm
        array_2 = aa(1386:1465);
        lam_array2=lam(1386:1465);

        [P_2,S_2]= polyfit(lam_array2,array_2,1);
        func_815 = polyval(P_2,lam_array2);

        figure(1);
        plot(lam_array2,array_2,'*-',lam_array2,func_815,'y+');
        xLabel('Lambda -nm');
        yLabel('Intensity');
        title('Spectrum : 815 - 850 nm');
        grid;
```

```matlab
        figure(main_figure);
        AxisHnd7 = findobj(gcbf, 'Tag', 'axes7');
        set(AxisHnd7, 'ButtonDownFcn',
'NeuroPlotCB(''click_spec_815'');');
        set(AxisHnd7, 'Tag', 'axes7');

    case 'click_slope_815'
        disp('In click_815');
        Folder=get(findobj(gcbf,'Tag','Start'),'UserData');
        disp(Folder);
        main_figure=gcbf;
        slope_815=load(strcat(Folder, 'slope_815.txt'));
        figure(1);
        plot(slope_815,'*-');
        xLabel('Steps');
        yLabel('Slope 815-850 nm');
        title('Slope 815-850 nm Plot');
        grid;

        figure(main_figure);
        AxisHnd12 = findobj(gcbf, 'Tag', 'axes12');
        set(AxisHnd12, 'ButtonDownFcn',
'NeuroPlotCB(''click_slope_815'');');
        set(AxisHnd12, 'Tag', 'axes12');

    case 'click_slope_715'
        disp('In click_715');
        Folder=get(findobj(gcbf,'Tag','Start'),'UserData');
        disp(Folder);
        main_figure=gcbf;
        slope_715=load(strcat(Folder, 'slope_715.txt'));
        figure(1);
        plot(slope_715,'*-');
        xLabel('Steps');
        yLabel('Slope 715-740 nm');
        title('Slope 715-740 nm Plot');
        grid;

        figure(main_figure);
        AxisHnd11 = findobj(gcbf, 'Tag', 'axes11');
        set(AxisHnd11, 'ButtonDownFcn',
'NeuroPlotCB(''click_slope_715'');');
        set(AxisHnd11, 'Tag', 'axes11');

    case 'click_od_slope'
        disp('In click_slope');
        Folder=get(findobj(gcbf,'Tag','Start'),'UserData');
        disp(Folder);
        main_figure=gcbf;
        od_slope=load(strcat(Folder, 'od_slope.txt'));
        figure(1);
        plot(od_slope,'*-');
```

```
        xLabel('Steps');
        yLabel('Optical Density Norm');
        title('Optical density Slope 700- 850nm');
        grid;

        figure(main_figure);
        AxisHnd13 = findobj(gcbf, 'Tag', 'axes13');
        set(AxisHnd13, 'ButtonDownFcn',
'NeuroPlotCB(''click_od_slope'');');
        set(AxisHnd13, 'Tag', 'axes13');

    case 'click_od_norm'
        disp('In click_slope_norm');
        Folder=get(findobj(gcbf,'Tag','Start'),'UserData');
        disp(Folder);
        main_figure=gcbf;
        od_slope=load(strcat(Folder, 'od_slope_norm.txt'));
        figure(1);
        plot(od_slope_norm,'*-');
        xLabel('Steps');
        yLabel('Optical Density Normalized');
        title('Optical density Slope 700- 850nm Normalized');
        grid;

        figure(main_figure);
        AxisHnd14 = findobj(gcbf, 'Tag', 'axes14');
        set(AxisHnd14, 'ButtonDownFcn',
'NeuroPlotCB(''click_od_norm'');');
        set(AxisHnd14, 'Tag', 'axes14');

    case 'click_Oxy'
        disp('In Click Oxy');
        main_figure = gcbf;

        % Read the Average Reference Data from the File
        % Read data from user data of axes8 to get the path : if flag
set to else prompt user to
        % show path of calibration data
        % Avoids user to enter the path for each run

        flag = (get(findobj(gcbf, 'Tag', 'axes8'),'UserData'));

        if(flag==0)
            [F, P] = uigetfile('*.*', 'Select one of the files in the
folder');
            if F == 0
                return;
            end
            set(findobj(gcbf, 'Tag', 'oxy_folder'),'String',P);
            Folder = P;
            flag=1;
            set(findobj(gcbf, 'Tag', 'axes8'),'UserData',(flag));
```

```
        end
        Folder=get(findobj(gcbf, 'Tag', 'oxy_folder'),'String');
        fname=strcat(Folder,'calib.txt');
        fid = fopen(fname,'r');
        Ref3 = read_sort(fid);
        Ref_avg = Ref3(:,2);


        %Create a vector comprising of only wavelength, we assume that
the
        %step length in lambda remains the same for all the reference
data and
        %test data

        XDATA = Ref3(:,1);

        %Load Exctinction Coeefcients from Text File
        fname = strcat(Folder,'human-extinct.txt');
        extict = load(fname);
        lambda = extict(:,1);
        ehb02 = extict(:,3);
        ehb = extict(:,2);


        fname = strcat(Folder,'ewater_ucl.txt');
        extict_water = load(fname);
        ewater_ext =
interp1(extict_water(:,1),extict_water(:,2),XDATA);

       %Load Melanin Exctinction Coeefcients from Text File
        fname = strcat(Folder,'extinct_melanin.txt');
        extict = load(fname);
        eMelanin=extict(:,2);
        eMelanin_ext= interp1(extict(:,1),eMelanin,XDATA);

        %Load Fat Exctinction Coeefcients from Text File
        fname = strcat(Folder,'extinct_fat.txt');
        extict_fat = load(fname);
        eFat = extict_fat(:,2);
        eFat_ext= interp1(extict_fat(:,1),eFat,XDATA);


        %Create a vector comprising of only wavelength, we assume that
the
        %step length in lambda remains the same for all the reference
data and
        %test data

        XDATA = Ref3(:,1);

        %Interpolate extinction coefficients
        ehb_ext= interp1(lambda,ehb,XDATA);
        ehb02_ext = interp1(lambda,ehb02,XDATA);
```

```matlab
        Folder1=get(findobj(gcbf,'Tag','Start'),'UserData');
        filepoint=str2num(get(findobj(gcbf,'Tag','point'),'String'));
        disp(Folder1);
        filenames=load(strcat(Folder1,'FileNames.txt'));
        specfile=strcat(Folder1,num2str(filenames(filepoint)));
        fid=fopen(specfile,'r');
        Hb = read_sort(fid);
        calib_fac=str2num(get(findobj(gcbf,'Tag','OD'),'String'));
        %Eliminate spectral effects
         Hb_spectral = Hb(:,2)./ Ref_avg;
        YDATA = Hb_spectral*(1/calib_fac);
       % Scale the values between 1 & 0 .Eliminates the effect of
diffrent integration times
        %YDATA = (Hb_spectral-min(Hb_spectral))/(max(Hb_spectral)-
min(Hb_spectral));
        % Read a,b,c,d,e values from mudata.txt
        fname=strcat(Folder1,'mudata.txt');
        mudata = load(fname);

        a=mudata(filepoint,1);
        b=mudata(filepoint,2);
        mel_conc=mudata(filepoint,3);
        musatlambdamin=mudata(filepoint,4);
        ds=mudata(filepoint,5);
        e=mudata(filepoint,6);
        fat_conc=mudata(filepoint,7);

        %Define numerator terms
        A=2.984128;
        % Degree of polynomial fits required
        d0=0.0625;
        lambdamin = 450;
        lambdamax = 900;

        % Define Scattering and absorption coeefcient
        mua = (a.*ehb02_ext)+(b.*ehb_ext)+(mel_conc.*eMelanin_ext);mua
=
(a.*ehb02_ext)+(b.*ehb_ext)+(mel_conc.*eMelanin_ext)+(fat_conc.*eFat_e
xt);
        % Assume scattering coeffcient to follow the classic weak
exponential model
        % with wavelength. instead of linearly decreasing model as
used before to
        % see the senstivity to optimization. Use the same parameters
c and d but
        % set differnt upper and lower bounds

        d=(d0^0.5)/(ds^0.5);
        lambdadiff= XDATA-lambdamin;
        lambdarange= (lambdamax-lambdamin);
        lam_term=lambdadiff./lambdarange;
        term1 = (1-(d.*lam_term));
```

229

```
        mus = term1.*musatlambdamin;

        mus(1:300)= 1.7303*mus(1:300);
        lambdarange = XDATA(301)-XDATA(1);
        mus_diff = (mus(1))-mus(301);
        XDATA_seg = XDATA(1:300);
        term_mus = -((mus_diff/lambdarange).*(XDATA_seg-XDATA(1)));
        mus_seg = (mus(1))+ term_mus;
        mus(1:300)=mus_seg(1:300);

        K1=str2num(get(findobj(gcbf,'Tag','mua'),'String'));
        K2=str2num(get(findobj(gcbf,'Tag','mus'),'String'));
        term2= (K1./mus);
        term3= K2.*mua;
        term4=term3./mus;
        Fitt_curve = term2+term4;
        Fitt_curve = 1./Fitt_curve;

        main_figure=gcbf;
        figure(1);

        plot(XDATA,YDATA,'o',XDATA,Fitt_curve,'r+');
        xLabel('Lambda -nm');
        yLabel('Normalized Reflectance');
        title('Oxygenation - Comparison');
        legend('Measured Data','Fitted Data');
        grid;

        figure(main_figure);
        AxisHnd8 = findobj(gcbf, 'Tag', 'axes8');
        set(AxisHnd8, 'ButtonDownFcn', 'NeuroPlotCB(''click_Oxy'');');
        set(AxisHnd8, 'Tag', 'axes8');
    end


% Function returns the sum of the squares of the diffrences between
the Fitted and Actual Experiemntal Data
% Experimental curve
% Fits for parameters a,b,c,d,e
% Input Arguements :
% params: array of fittiing parameters
%       a=params[1]
%       b=params[2]
%       c=params[3]
%       d=params[4]
%       e=params[5]
% Input : array of wavelengths :
params,y,ehb02_ext,ehb_ext,ewater_ext,rho,XDATA,YDATA,oxygenation
```

```
% params- from optimization function
% ehb02_ext,ehb_ext,ewater_ext- interpolated extinction ceoffcinets of
% chrmophores
% rho-source detector seperation in cms
% XDATA - Wavelength array
% YDATA - Actual normalized measurement array
% Actual_Output : Reflectance value at corresponding wavelengths
% diff : Sum of Squares of  Difference between Measured Reflectance
Curve & Fitted Curve
% All comparsions are made with Normalized Data

function [diff,Fitt_curve] =
func_simp_small(params,y,ehb02_ext,ehb_ext,ewater_ext,eMelanin_ext,eFa
t_ext,rho,XDATA,YDATA,K1,K2)

% Extract from params array
a=abs(params(1));
b=abs(params(2));
mel_conc=abs(params(3));
musatlambdamin=abs(params(4));
ds=abs(params(5));
water_conc=abs(params(6));
fat_conc=abs(params(7));

d0=0.0625;


% Assume prior information about oxygenation level and mus' parameter.
% Lump mus' paprameter variration to one parameter or give a very
small
% range of variation of mus' exponent as found in realistically in
tissues
% Assume all other information as required

A=2.984128;
% Degree of polynomial fits required
N = 4;
d0=0.0625;
lambdamin = 450;
lambdamax = 900;

% Define Scattering and absorption coeefcient
mua =
(a.*ehb02_ext)+(b.*ehb_ext)+(mel_conc.*eMelanin_ext)+(fat_conc.*eFat_e
xt);
% Assume scattering coeffcient to follow the classic weak exponential
model
% with wavelength. instead of linearly decreasing model as used before
to
% see the senstivity to optimization. Use the same parameters c and d
but
% set differnt upper and lower bounds
```

231

```
d=(d0^0.5)/(ds^0.5);
lambdadiff= XDATA-lambdamin;
lambdarange= (lambdamax-lambdamin);
lam_term=lambdadiff./lambdarange;
term1 = (1-(d.*lam_term));

mus = term1.*musatlambdamin;

mus(1:300)= 1.7303*mus(1:300);
lambdarange = XDATA(301)-XDATA(1);
mus_diff = (mus(1))-mus(301);
XDATA_seg = XDATA(1:300);
term_mus = -((mus_diff/lambdarange).*(XDATA_seg-XDATA(1)));
mus_seg = (mus(1))+ term_mus;
mus(1:300)=mus_seg(1:300);

term2= (K1./mus);
term3= K2.*mua;
term4=term3./mus;
Fitt_curve = term2+term4;
Fitt_curve = 1./Fitt_curve;

diff = (Fitt_curve)-YDATA;
diff = (diff.^2);
diff = sum(diff);
```
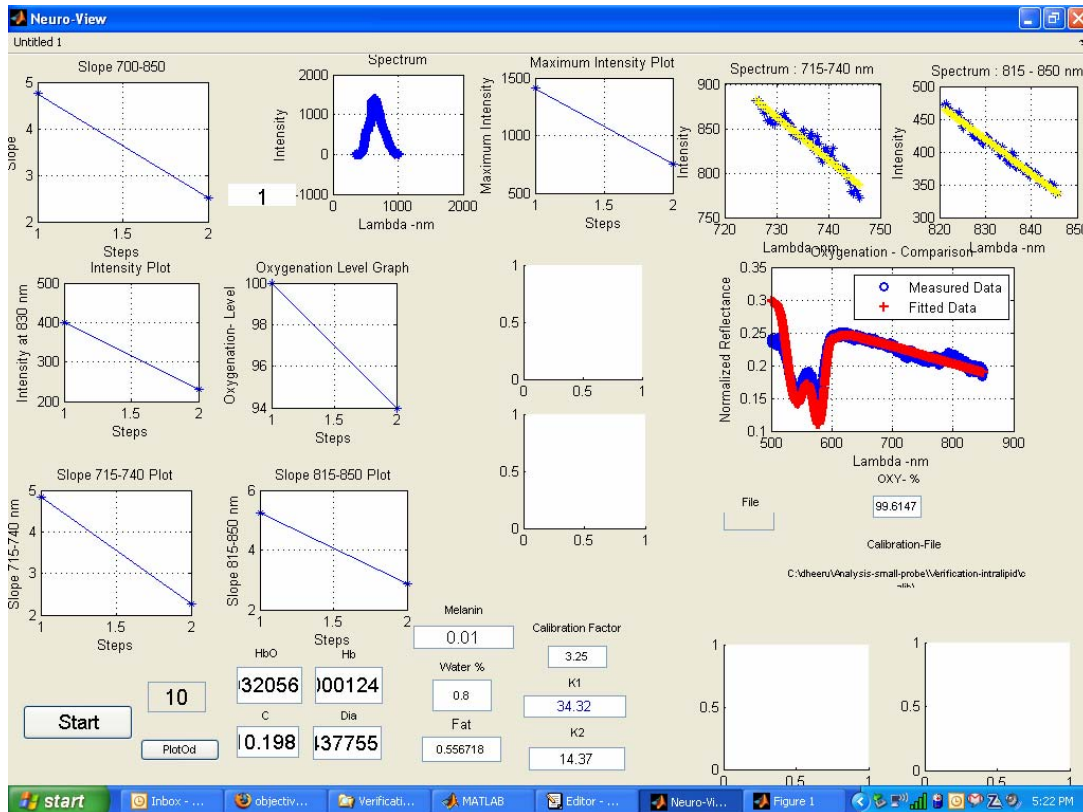
```
function [] = NeuroPlotCB(action)
% Code to run the GUI. First round to find the saturation
% and in the second round fit the other concentrations of chromophores
% Requires folder for all measured files - no files other than
measured
% files.presence of other files in the folder results in an error.
% Required folder for calibration files. Store all files such as
extinction
% coeffcients and dark files if significant dark signal needs to be
taken
% in to account. include water, and the hemoglobin exticntion
coeffcients
% of required animal coeffceints or human coeffcients.
% using Ant-Hill Optimization for optimization

global lambda_low    % Lower limit of Wavelength
global lambda_high   % Higher Limit of Wavelength
global oxygenation
global rho           % Source detector Separation
global XDATA
global YDATA

lambda_low = 650.00;
lambda_high = 845.00;
 rho=1.50;
% rho=0.95;
A=2.984128;
flag = 0;
clc
ewater_ext=[];
Data='aa_data3_FAEA';
Type='multiple solutions ';

switch(action)

case 'Start'
    % -------------------------------------------
    [F, P] = uigetfile('*.*', 'Select one of the files in the
folder');
    if F == 0
        return;
    end
    Folder = P;
    proc_flag=0;
    Contents = dir(Folder);
    for i = 1:length(Contents)
        if strcmp(Contents(i).name,'Slope.txt')==1
            proc_flag=1;
            break;
        end
    end
    if proc_flag==0
```

```
        x = 1;

        for i = 1:length(Contents)
            if Contents(i).isdir == 0
                FileNames(x) = str2num(Contents(i).name);
                x = x+1;
            end
        end
        SortFileNames = sort(FileNames);
        Files='';
        for i = 1:length(SortFileNames)
            Files = strvcat(Files, strcat(Folder,
num2str(SortFileNames(i))));
        end


        for i=1:length(Files(:, 1))
            i
            deblank(Files(i,:));
            fr=fopen(deblank(Files(i,:)));
            aaa=fscanf(fr,'%g',[1,inf]);
            fclose(fr);
            for p=1:2048
                aa(p)=aaa(p*2);
                lam(p)=aaa(p*2-1);
            end
            bbb(:,i)=aa';
            maxintensity(i)=max(aa);

        end
        sss=0;
        count=1;
        for j=1:length(Files(:, 1))
            sss=0;
            for i=441:879
                sss=sss+bbb(i,j);
            end
            aver550(j)=sss;
            sump1=0;
            sump2=0;
            sump3=0;
            sump4=0;

            for jj=1:471
                sump1=sump1 +(lam(jj+1030)*bbb(jj+1030,j));
                sump2=sump2 + lam(jj+1030);
                sump3=sump3+ bbb(jj+1030,j);
                sump4=sump4 + (lam(jj+1030)^2);
            end
            slope1(count)=-(((471*sump1)- (sump2*sump3))/((471*sump4)-
(sump2*sump2)));
```

234

```
        %Determine slope of the two wavelength Ranges
        sump1=0;
        sump2=0;
        sump3=0;
        sump4=0;

        for jj=1:62
            sump1=sump1 +(lam(jj+1092)*bbb(jj+1092,j));
            sump2=sump2 + lam(jj+1092);
            sump3=sump3+ bbb(jj+1092,j);
            sump4=sump4 + (lam(jj+1092)^2);
        end
        slope_715(count)=-(((62*sump1)-
(sump2*sump3))/((62*sump4)-(sump2*sump2)));

        sump1=0;
        sump2=0;
        sump3=0;
        sump4=0;
        for jj=1:80
            sump1=sump1 +(lam(jj+1386)*bbb(jj+1386,j));
            sump2=sump2 + lam(jj+1386);
            sump3=sump3+ bbb(jj+1386,j);
            sump4=sump4 + (lam(jj+1386)^2);
        end
        slope_815(count)=-(((80*sump1)-
(sump2*sump3))/((80*sump4)-(sump2*sump2)));

        % array_1: 720 nm - 740 nm
        array_1 =bbb(1092:1153,j);
        lam_array1=lam(1092:1153);

        % array-2= 815 nm - 850 nm
        array_2 =bbb(1386:1465,j);
        lam_array2=lam(1386:1465);

        % Fit a single degree polynomial so as to obtain the
slopes for the wavelength ranges
        % Estimate intensity at required wavelength from the
relation so deterimed
        % Least Squred Estimate of the coeffcients. LInear curve
fitting techniques
        % P= Coeffceint Array
        % S= Structure to get regression statistics
        size(array_1);
        size(lam_array1);

        [P,S] = polyfit(lam_array1,array_1',1);
        [P_2,S_2]= polyfit(lam_array2,array_2',1);

        % Evaluate the polynomials obtained for intensity values
        func_715 = polyval(P,lam_array1);
```

235

```matlab
            func_815 = polyval(P_2,lam_array2);

            % retrieve the evaluated value at 730 nm and 830 nm
            intensity_730(count)=func_715(30);
            intensity_830(count)=func_815(41);

            % Process Data to get oxygenation information
            % Read the Average Reference Data from the File
            % Read data from user data of axes8 to get the path : if
flag set to else prompt user to
            % show path of calibration data
            % Avoids user to enter the path for each run
            if flag == 0
                [F, P] = uigetfile('*.*', 'Select one of the files in
the folder : Folder for calibration and coeffcients ');
                if F == 0
                    return;
                end
                set(findobj(gcbf, 'Tag', 'axes7'),'UserData',P);
                oxy_folder = P;
                flag=1;
            end
            set(findobj(gcbf, 'Tag', 'axes8'),'UserData',flag);
            fname=strcat(oxy_folder,'calib.txt');

            fid = fopen(fname,'r');
            Ref3 = read_sort(fid);
            Ref_avg = Ref3(:,2);

            %Load Exctinction Coeefcients from Text File
            fname = strcat(oxy_folder,'human-extinct.txt');
            extict = load(fname);
            lambda = extict(:,1);
            ehb02 = extict(:,3);
            ehb = extict(:,2);

            %Create a vector comprising of only wavelength, we assume
that the
            %step length in lambda remains the same for all the
reference data and
            %test data

            XDATA = Ref3(:,1);

            %Interpolate extinction coefficients
            ehb_ext= interp1(lambda,ehb,XDATA);
            ehb02_ext = interp1(lambda,ehb02,XDATA);

            fname = strcat(oxy_folder,'ewater_ucl.txt');
            extict_water = load(fname);
            ewater_ext =
interp1(extict_water(:,1),extict_water(:,2),XDATA);
```

```
            deblank(Files(count,:));
            fid=fopen(deblank(Files(count,:)));
            Hb = read_sort(fid);

            %Eliminate spectral effects
            Hb_spectral = Hb(:,2)./ Ref_avg;
            % Scale the values between 1 & 0 .Eliminates the effect of
diffrent integration times
            YDATA = (Hb_spectral-min(Hb_spectral))/(max(Hb_spectral)-
min(Hb_spectral));
            % YDATA = (Hb_spectral/Hb_spectral(1));


            %use these set of commands for using
lsqnonlin*******************************************
            opt =
optimset('LargeScale','on','DerivativeCheck','off','Display','iter','L
evenbergMarquardt','on','MaxFunEvals',10000,'MaxIter',10000,'TolFun',1
e-20,'TolX',1e-10,'TolCon',1e-10);
            % Since we are dealing with Ill conditioned problem, turn
off warning messages.
            warning off
            % Load the ratio files containg the ratio of Hb to HbO2
            fname = strcat(oxy_folder,'ratio.txt');
            % ratio = load(fname);

            FUN='fun_simp';
            NumAnts=50;Nmoves=25;LocalMoves=50;NONLNCON=[];rpmax=[];

            UB = [0.50    (ratio(count)*0.97*1.20)    10000    10
0.99];     % -----    Upper bounds
            LB = [0.005   (ratio(count)*0.97*0.90)    1000     5
0.98];   % -----    Lower bounds




            XVmin=LB;
            XVmax=UB;






            opt =
optimset('LargeScale','on','DerivativeCheck','on','Display','iter','Le
venbergMarquardt','on','MaxFunEvals',10000,'MaxIter',10000,'TolFun',1e
-20,'TolX',1e-22,'TolCon',1e-10);
            y=[];
            [Estimates, resnorm] =
api(FUN,XVmin,XVmax,NumAnts,Nmoves,LocalMoves,NONLNCON,rpmax,y,ehb02_e
xt,ehb_ext,ewater_ext,rho,XDATA,YDATA);
```

```
            a(count)=(Estimates(1));
            b(count)=(Estimates(2));
            c(count)=(Estimates(3));
            d(count)=(Estimates(4));
            e(count)=(Estimates(5));

            count
            oxy_level(count)= (a(count)/(b(count)+a(count)))*100;
            oxygenation = oxy_level(count);

% To increase accuracy of estimated value of cencentrations and
assuming
% returned values from previous iterations as intial guesses or
constraints
% and use the normailization at one wavelength to get revised estimate
of
% all values. Assume value of mus' to vary between 20% of intial value
% obtained vary Hb and HbO concentrations but assume ratio from
previous
% calculations.  Allow a small varitations of 20 % on either side of
% oxygensaturation

            YDATA = (Hb_spectral/Hb_spectral(1));
            XDATA = Ref3(:,1);
            FUN='func_simp';

%


            UB = [0.90      0.90     9.7215E5     1.8    0.99  ];
%-------  Upper  Bounds
            LB = [0.0001   0.0001   1.3218E5     1.3    0.65  ];
% -----   Lower Bounds

        XVmin=LB;
        XVmax=UB;

        FUN='func_simp';
        NumAnts=50;Nmoves=30;LocalMoves=50;
        NONLNCON='constraints_oxy';rpmax=1.50;

        [Estimates, resnorm]
=api(FUN,XVmin,XVmax,NumAnts,Nmoves,LocalMoves,NONLNCON,rpmax,y,ehb02_
ext,ehb_ext,ewater_ext,rho,XDATA,YDATA,oxygenation);

            a_rev=(Estimates(1));
            b_rev=(Estimates(2));
            c_rev=(Estimates(3));
            d_rev=(Estimates(4));
            e_rev=(Estimates(5));
```

```matlab
                   oxy_level_rev= (a_rev/(b_rev+a_rev))*100;
%
                   oxy_level(count)=oxy_level_rev;
                   a(count)=a_rev;
                   b(count)=b_rev;
                   c(count)=c_rev;
                   d(count)=d_rev;
                   e(count)=e_rev;

            set(findobj(gcbf,'Tag','count'),'String',count);
            count=count+1;
        end

        fid=fopen(strcat(Folder, 'FileNames.txt'),'w');
        fprintf(fid,'%10d\n',SortFileNames);
        fclose(fid);

        % Generate mudata.txt file to read from it for later stage
        fid=fopen(strcat(Folder,'mudata.txt'),'w');
        for i = 1: count-1
            fprintf(fid,'%12.6f\t %12.6f\t %12.6f\t %12.6f\t
%12.6f\n',a(i),b(i),c(i),d(i),e(i));
        end
        fclose(fid);
        fid=fopen(strcat(Folder,'oxydata.txt'),'w');
        fprintf(fid,'%12.f\n',oxy_level);
        fclose(fid);
    else
        slope1=load(strcat(Folder, 'Slope.txt'));
        slope_715=load(strcat(Folder, 'slope_715.txt'));
        slope_815=load(strcat(Folder, 'slope_815.txt'));
        maxintensity=load(strcat(Folder, 'maxintensity.txt'));
        oxy_level=load(strcat(Folder, 'oxydata.txt'));
        intensity_830=load(strcat(Folder, 'intensity_830.txt'));
        intensity_730=load(strcat(Folder, 'intensity_730.txt'));
    end

    AxisHndl = findobj(gcbf, 'Tag', 'axes1');
    axes(AxisHndl);
    plot(slope1,'*-');
    xLabel('Steps');
    yLabel('Slope');
    title('Slope 700-850');
    grid;
    set(AxisHndl, 'Tag', 'axes1');
    set(AxisHndl, 'ButtonDownFcn', 'NeuroPlotCB(''click'');');
    set(gcbo,'UserData',Folder);
    % Flag to see whether calibration data was accessed
    % set to 1 if path is set
    flag = 0;
    AxisHnd8 = findobj(gcbf, 'Tag', 'axes8');
```

```
    set(AxisHnd8, 'UserData',flag);
    set(AxisHnd8, 'Tag', 'axes8');

    AxisHnd2 = findobj(gcbf, 'Tag','axes2');
    axes(AxisHnd2);
    plot(maxintensity,'*-');
    xLabel('Steps');
    yLabel('Maximum Intensity');
    title('Maximum Intensity Plot');
    grid;
    set(AxisHnd2, 'ButtonDownFcn', 'NeuroPlotCB(''click_Max'');');
    set(AxisHnd2, 'Tag', 'axes2');

    AxisHnd4 = findobj(gcbf, 'Tag', 'axes4');
    axes(AxisHnd4);
    plot(oxy_level,'*-');
    xLabel('Steps');
    yLabel('Oxygenation- Level');
    title('Oxygenation Level Graph');
    grid;
    set(AxisHnd4, 'ButtonDownFcn', 'NeuroPlotCB(''click_730'');');
    set(AxisHnd4, 'Tag', 'axes4');

    AxisHnd5 = findobj(gcbf, 'Tag', 'axes5');
    axes(AxisHnd5);
    plot(intensity_830,'*-');
    xLabel('Steps');
    yLabel('Intensity at 830 nm');
    title('Intensity Plot');
    grid;
    set(AxisHnd5, 'ButtonDownFcn', 'NeuroPlotCB(''click_830'');');
    set(AxisHnd5, 'Tag', 'axes5');

    AxisHnd11 = findobj(gcbf, 'Tag', 'axes11');
    axes(AxisHnd11);
    plot(slope_715,'*-');
    xLabel('Steps');
    yLabel('Slope 715-740 nm');
    title('Slope 715-740 Plot');
    grid;
    set(AxisHnd11, 'ButtonDownFcn',
'NeuroPlotCB(''click_slope_715'');');
    set(AxisHnd11, 'Tag', 'axes11');

    AxisHnd12 = findobj(gcbf, 'Tag', 'axes12');
    axes(AxisHnd12);
    plot(slope_815,'*-');
    xLabel('Steps');
    yLabel('Slope 815-850 nm');
    title('Slope 815-850 Plot');
    grid;
```

```
    set(AxisHnd12, 'ButtonDownFcn',
'NeuroPlotCB(''click_slope_815'');');
    set(AxisHnd12, 'Tag', 'axes12');

    fid=fopen(strcat(Folder, 'Slope.txt'),'w');
    fprintf(fid,'%12.6f\n',slope1);
    fclose(fid);

    fid=fopen(strcat(Folder, 'maxintensity.txt'),'w');
    fprintf(fid,'%12.6f\n',maxintensity);
    fclose(fid);

    fid=fopen(strcat(Folder, 'intensity_730.txt'),'w');
    fprintf(fid,'%12.6f\n',intensity_730);
    fclose(fid);

    fid=fopen(strcat(Folder, 'intensity_830.txt'),'w');
    fprintf(fid,'%12.6f\n',intensity_830);
    fclose(fid);

    fid=fopen(strcat(Folder, 'Slope_815.txt'),'w');
    fprintf(fid,'%12.6f\n',slope_815);
    fclose(fid);

    fid=fopen(strcat(Folder, 'Slope_715.txt'),'w');
    fprintf(fid,'%12.6f\n',slope_715);
    fclose(fid);
```

% Rest code same as small separation code. This code is not included.

```
% Function returns the sum of the squares of the diffrences between
the Fitted and Actual Experiemntal Data
% Experimental curve
% Fits for parameters a,b,c,d,e
% Input Arguements :
% params: array of fittiing parameters
%       a=params[1]
%       b=params[2]
%       c=params[3]
%       d=params[4]
%       e=params[5]
% Input : array of wavelengths :
% Actual_Output : Reflectance value at corresponding wavelengths
% diff : Sum of Squares of  Difference between Measured Reflectance
Curve
% & Fitted Curve
% All comparsions are made with Normalized Data (0-1)

function [diff,Fitt_curve] =
fun_simp(params,y,ehb02_ext,ehb_ext,ewater_ext,rho,XDATA,YDATA)
```

```matlab
% Extract from params array
a=abs(params(1));
b=abs(params(2));
c=abs(params(3));
d=abs(params(4));
e=abs(params(5));


A=2.984128;


% Define Scattering and absorption coeefcient
    mua = (a.*ehb02_ext)+(b.*ehb_ext)+(e.*ewater_ext);
    mus = -(c*XDATA*1E-7)+ d;

    mut = mua + mus;
    D = 1./(3*mut);
    mueff=((mua./D).^0.5);
    z0 = 1./mut;
    const=(z0.^2);
    r1 = sqrt((const+(rho^2)));
    r2 = ((z0+(4*A*D)).^2)+(rho^2);
    r2 =(r2.^0.5);
    zo4ad = z0+(4*A*D);

    %Define numerator terms : The factor 4*pi has been excluded as
division
    %by its own maximum eliminates the
    % Constant term
    num_term1 = z0.*(mueff+(1./r1));
    num_term2 =(exp(-(mueff.*r1)))./(r1.^2);
    num_term_1= num_term1.*num_term2;

    num_term_a = (1./r2)+mueff;
    num_term_b = exp(-(mueff.*r2))./(r2.^2);
    num_term_2=(zo4ad.*num_term_a).*num_term_b;

    num_term_R = num_term_1+num_term_2;
    num_term_aux = exp(-(mut.*z0));
    num_term_R = num_term_R .* num_term_aux;
    num_term_3 =(exp(-(mueff.*r1))./(r1));
    num_term_4 =(exp(-(mueff.*r2))./(r2));
    num_term_phi = (1./D).*(num_term_3-num_term_4);
    num_term = (0.306.*num_term_R) + (0.118.*num_term_phi);
    Fitt_curve = (num_term-min(num_term))/(max(num_term)-
min(num_term));
    diff = (Fitt_curve - YDATA);
    diff = (diff.^2);
    diff = sum(diff);
% ******************************************
% When curvefitting, a typical quantity to
% minimize is the sum of squares error.
%******************************************
```

```
% Function returns the sum of the squares of the diffrences between
the Fitted and Actual Experiemntal Data
% Experimental curve
% Fits for parameters a,b,c,d,e
% Input Arguements :
% params: array of fittiing parameters
%       a=params[1]
%       b=params[2]
%       c=params[3]
%       d=params[4]
%       e=params[5]
% Input : array of wavelengths :
params,y,ehb02_ext,ehb_ext,ewater_ext,rho,XDATA,YDATA,oxygenation
% params- from optimization function
% ehb02_ext,ehb_ext,ewater_ext- interpolated extinction ceoffcinets of
% chrmophores
% rho-source detector seperation in cms
% XDATA - Wavelength array
% YDATA - Actual normalized measurement array
% Actual_Output : Reflectance value at corresponding wavelengths
% diff : Sum of Squares of  Difference between Measured Reflectance
Curve & Fitted Curve
% All comparsions are made with Normalized Data (1 at 600 nm)

function [diff,Fitt_curve] =
func_simp(params,y,ehb02_ext,ehb_ext,ewater_ext,rho,XDATA,YDATA,oxygen
ation)

% Extract from params array
a=abs(params(1));
b=abs(params(2));
c=abs(params(3));
d=abs(params(4));
e=abs(params(5));

% Assume prior information about oxygenation level and mus' parameter.
% Lump mus' paprameter variration to one parameter or give a very
small
% range of variation of mus' exponent as found in realistically in
tissues
% Assume all other information as required

A=2.984128;
% Degree of polynomial fits required
N = 4;

% Define Scattering and absorption coeefcient
    mua = (a.*ehb02_ext)+(b.*ehb_ext)+(e.*ewater_ext);
% Assume scattering coeffcient to follow the classic weak exponential
model
% with wavelength. instead of linearly decreasing model as used before
to
```

243

```matlab
% see the senstivity to optimization. Use the same parameters c and d
but
% set differnt upper and lower bounds
    mus = c*(XDATA.^(-d));
% mus = -(c*XDATA*1E-7)+ d; % Commented to include weak exponential
model
% for mus'

    mut = mua + mus;
    D = 1./(3*mut);
    mueff=((mua./D).^0.5);
    z0 = 1./mut;
    r1 = sqrt((z0.^2)+(rho^2));
    r2 = ((z0+(4*A*D)).^2)+(rho^2);
    r2 =(r2.^0.5);
    zo4ad = z0+(4*A*D);

    %Define numerator terms : The factor 4*pi has been excluded as
division by its own maximum eliminates the
    % Constant term
    num_term1 = z0.*(mueff+(1./r1));
    num_term2 =(exp(-(mueff.*r1)))./(r1.^2);
    num_term_1= num_term1.*num_term2;

    num_term_a = (1./r2)+mueff;
    num_term_b = exp(-(mueff.*r2))./(r2.^2);
    num_term_2=(zo4ad.*num_term_a).*num_term_b;

    num_term_R = num_term_1+num_term_2;
    num_term_aux = exp(-(mut.*z0));
    num_term_R = num_term_R .* num_term_aux;
    num_term_3 =(exp(-(mueff.*r1))./(r1));
    num_term_4 =(exp(-(mueff.*r2))./(r2));
    num_term_phi = (1./D).*(num_term_3-num_term_4);
    num_term = (0.306.*num_term_R) + (0.118.*num_term_phi);

    Fitt_curve = num_term/num_term(1);

    diff = (Fitt_curve) - YDATA;
    diff = (diff.^2);
    diff = sum(diff);

% *******************************************
% When curvefitting, a typical quantity to
% minimize is the sum of squares error.
%*******************************************
```

```
function [Hb_c,Hb02_c,H20_c,Lip_c] = get_extcoff_interp(lamda)
% Program written by Gwen Chu. Gets extinction coefficent of tissue
% chromophores. Hb, HbO, H20, Lipid
% lamda in [nm]
%
% open Hb ,Hb02 extinction coefficent data file
%filename='table_ext_coeff_ Hb_HbO.dat';
filename='table_ext_coeff_ Hb_HbO_hum.dat';
fid = fopen(filename);

% initialize some variables
i = 1;     % number of measured data point (Vd,Id)

 while feof(fid) == 0
     rline = fgetl(fid);
     if ( rline(1) ~= '%' )
         a = sscanf(rline,'%g');
         lamdax(i)  = a(1);
         HbOy(i)    = a(2);
         Hby(i)     = a(3);
         i = i+1;
     end
 end

 fclose(fid);
 % interpolate Hb and Hb0
 if lamda <= max(lamdax) & lamda >=min(lamdax)
    Hb_c   = interp1(lamdax,Hby,lamda,'cubic');
    Hb02_c = interp1(lamdax,HbOy,lamda,'cubic');
 else
    Hb_c   = interp1(lamdax,Hby,lamda,'cubic');
    Hb02_c = interp1(lamdax,HbOy,lamda,'cubic');
 end

 % open H20 extinction coefficent data file
%filename='table_ext_coeff_H20.dat';
filename='table_ext_coeff_H20_ver2.dat';
fid = fopen(filename);

% initialize some variables
i = 1;     % number of measured data point (Vd,Id)

 while feof(fid) == 0
     rline = fgetl(fid);
     if ( rline(1) ~= '%' )
         a = sscanf(rline,'%g');
         lamdax(i)  = a(1);
         H2Oy(i)    = a(2);
         i = i+1;
     end
 end
```

```
 fclose(fid);
 % interpolate Hb and Hb0
 H20_c   = interp1(lamdax,H2Oy,lamda,'cubic');

% open Lipid extinction coefficent data file
 filename='table_ext_coeff_Lip.dat';
fid = fopen(filename);

% initialize some variables
i = 1;      % number of measured data point (Vd,Id)

 while feof(fid) == 0
     rline = fgetl(fid);
     if ( rline(1) ~= '%' )
         a = sscanf(rline,'%g');
         lamdax(i)  = a(1);
         Lipy(i)    = a(2);
         i = i+1;
     end
 end

 fclose(fid);
 % interpolate Hb and Hb0
 Lip_c   = interp1(lamdax,Lipy,lamda,'cubic');




function [bestmem,bestval,nfeval] =
devec3_wave(fname,VTR,D,XVmin,XVmax,y,NP,itermax,F,CR,strategy,refresh
);
% minimization of a user-supplied function with respect to x(1:D),
% using the differential evolution (DE) algorithm of Rainer Storn
% (http://www.icsi.berkeley.edu/~storn/code.html)
%
% Special thanks go to Ken Price (kprice@solano.community.net) and
% Arnold Neumaier (http://solon.cma.univie.ac.at/~neum/) for their
% valuable contributions to improve the code.
%
% Strategies with exponential crossover, further input variable
% tests, and arbitrary function name implemented by Jim Van Zandt
% <jrv@vanzandt.mv.com>, 12/97.
%
% Output arguments:
% ----------------
% bestmem         parameter vector with best solution
% bestval         best objective function value
% nfeval          number of function evaluations
%
% Input arguments:
% --------------
%
% fname           string naming a function f(x,y) to minimize
```

246

```
% VTR            "Value To Reach". devec3 will stop its minimization
%                if either the maximum number of iterations "itermax"
%                is reached or the best parameter vector "bestmem"
%                has found a value f(bestmem,y) <= VTR.
% D              number of parameters of the objective function
% XVmin          vector of lower bounds XVmin(1) ... XVmin(D)
%                of initial population
%                *** note: these are not bound constraints!! ***
% XVmax          vector of upper bounds XVmax(1) ... XVmax(D)
%                of initial population
% y              problem data vector (must remain fixed during the
%                minimization)
% NP             number of population members
% itermax        maximum number of iterations (generations)
% F              DE-stepsize F from interval [0, 2]
% CR             crossover probability constant from interval [0, 1]
% strategy       1 --> DE/best/1/exp          6 --> DE/best/1/bin
%                2 --> DE/rand/1/exp          7 --> DE/rand/1/bin
%                3 --> DE/rand-to-best/1/exp  8 --> DE/rand-to-
best/1/bin
%                4 --> DE/best/2/exp          9 --> DE/best/2/bin
%                5 --> DE/rand/2/exp          else  DE/rand/2/bin
%                Experiments suggest that /bin likes to have a
slightly
%                larger CR than /exp.
% refresh        intermediate output will be produced after "refresh"
%                iterations. No intermediate output will be produced
%                if refresh is < 1
%
%        The first four arguments are essential (though they have
%        default values, too). In particular, the algorithm seems to
%        work well only if [XVmin,XVmax] covers the region where the
%        global minimum is expected. DE is also somewhat sensitive to
%        the choice of the stepsize F. A good initial guess is to
%        choose F from interval [0.5, 1], e.g. 0.8. CR, the crossover
%        probability constant from interval [0, 1] helps to maintain
%        the diversity of the population and is rather uncritical. The
%        number of population members NP is also not very critical. A
%        good initial guess is 10*D. Depending on the difficulty of the
%        problem NP can be lower than 10*D or must be higher than 10*D
%        to achieve convergence.
%        If the parameters are correlated, high values of CR work
better.
%        The reverse is true for no correlation.
%
% default values in case of missing input arguments:
%   VTR = 1.e-6;
%   D = 2;
%   XVmin = [-2 -2];
%   XVmax = [2 2];
%   y=[];
%   NP = 10*D;
%   itermax = 200;
```

```
%   F = 0.8;
%   CR = 0.5;
%   strategy = 7;
%   refresh = 10;
%
% Cost function:    function result = f(x,y);
%                       has to be defined by the user and is minimized
%           w.r. to  x(1:D).
%
% Example to find the minimum of the Rosenbrock saddle:
% ----------------------------------------------------
% Define f.m as:
%                   function result = f(x,y);
%                   result = 100*(x(2)-x(1)^2)^2+(1-x(1))^2;
%                   end
% Then type:
%
%   VTR = 1.e-6;
%   D = 2;
%   XVmin = [-2 -2];
%   XVmax = [2 2];
%   [bestmem,bestval,nfeval] = devec3("f",VTR,D,XVmin,XVmax);
%
% The same example with a more complete argument list is handled in
% run1.m
%
% About devec3.m
% --------------
% Differential Evolution for MATLAB
% Copyright (C) 1996, 1997 R. Storn
% International Computer Science Institute (ICSI)
% 1947 Center Street, Suite 600
% Berkeley, CA 94704
% E-mail: storn@icsi.berkeley.edu
% WWW:    http://http.icsi.berkeley.edu/~storn
%
% devec is a vectorized variant of DE which, however, has a
% propertiy which differs from the original version of DE:
% 1) The random selection of vectors is performed by shuffling the
%    population array. Hence a certain vector can't be chosen twice
%     in the same term of the perturbation expression.
%
% Due to the vectorized expressions devec3 executes fairly fast
% in MATLAB's interpreter environment.
%
% This program is free software; you can redistribute it and/or modify
% it under the terms of the GNU General Public License as published by
% the Free Software Foundation; either version 1, or (at your option)
% any later version.
%
% This program is distributed in the hope that it will be useful,
% but WITHOUT ANY WARRANTY; without even the implied warranty of
% MERCHANTABILITY or FITNESS FOR A PARTICULAR PURPOSE.  See the
```

```
% GNU General Public License for more details. A copy of the GNU
% General Public License can be obtained from the
% Free Software Foundation, Inc., 675 Mass Ave, Cambridge, MA 02139,
USA.

%-----Check input variables--------------------------------------
--
err=[];
if nargin<1, error('devec3 1st argument must be function name'); else
  if exist(fname)<1; err(1,length(err)+1)=1; end; end;
if nargin<2, VTR = 1.e-6; else
  if length(VTR)~=1; err(1,length(err)+1)=2; end; end;
if nargin<3, D = 2; else
  if length(D)~=1; err(1,length(err)+1)=3; end; end;
if nargin<4, XVmin = [-2 -2];else
  if length(XVmin)~=D; err(1,length(err)+1)=4; end; end;
if nargin<5, XVmax = [2 2]; else
  if length(XVmax)~=D; err(1,length(err)+1)=5; end; end;
if nargin<6, y=[]; end;
if nargin<7, NP = 10*D; else
  if length(NP)~=1; err(1,length(err)+1)=7; end; end;
if nargin<8, itermax = 200; else
  if length(itermax)~=1; err(1,length(err)+1)=8; end; end;
if nargin<9, F = 0.8; else
  if length(F)~=1; err(1,length(err)+1)=9; end; end;
if nargin<10, CR = 0.5; else
  if length(CR)~=1; err(1,length(err)+1)=10; end; end;
if nargin<11, strategy = 7; else
  if length(strategy)~=1; err(1,length(err)+1)=11; end; end;
if nargin<12, refresh = 10; else
  if length(refresh)~=1; err(1,length(err)+1)=12; end; end;
if length(err)>0
  fprintf(stdout,'error in parameter %d\n', err);
  usage('devec3
(string,scalar,scalar,vector,vector,any,integer,integer,scalar,scalar,
integer,integer)');
end

if (NP < 5)
   NP=5;
   fprintf(1,' NP increased to minimal value 5\n');
end
if ((CR < 0) | (CR > 1))
   CR=0.5;
   fprintf(1,'CR should be from interval [0,1]; set to default value
0.5\n');
end
if (itermax <= 0)
   itermax = 200;
   fprintf(1,'itermax should be > 0; set to default value 200\n');
end
refresh = floor(refresh);
```

249

```matlab
%-----Initialize population and some arrays--------------------------
----

pop = zeros(NP,D); %initialize pop to gain speed

%----pop is a matrix of size NPxD. It will be initialized------------
%----with random values between the min and max values of the--------
%---parameters------------------------------------------------------

for i=1:NP
   pop(i,:) = XVmin + rand(1,D).*(XVmax - XVmin);
end

popold    = zeros(size(pop));      % toggle population
val       = zeros(1,NP);           % create and reset the "cost array"
bestmem   = zeros(1,D);            % best population member ever
bestmemit = zeros(1,D);            % best population member in
iteration
nfeval    = 0;                     % number of function evaluations

%------Evaluate the best member after initialization-----------------
----

ibest   = 1;                       % start with first population member
val(1)  = feval(fname,pop(ibest,:),y);
bestval = val(1);                  % best objective function value so
far
nfeval  = nfeval + 1;
for i=2:NP                         % check the remaining members
  val(i) = feval(fname,pop(i,:),y);
  nfeval  = nfeval + 1;
  if (val(i) < bestval)            % if member is better
     ibest   = i;                  % save its location
     bestval = val(i);
  end
end
bestmemit = pop(ibest,:);          % best member of current iteration
bestvalit = bestval;               % best value of current iteration

bestmem = bestmemit;               % best member ever

%------DE-Minimization-----------------------------------------------
%------popold is the population which has to compete. It is--------
%------static through one iteration. pop is the newly-------------
%------emerging population.------------------------------------------

pm1 = zeros(NP,D);                 % initialize population matrix 1
pm2 = zeros(NP,D);                 % initialize population matrix 2
pm3 = zeros(NP,D);                 % initialize population matrix 3
pm4 = zeros(NP,D);                 % initialize population matrix 4
pm5 = zeros(NP,D);                 % initialize population matrix 5
```

250

```
bm  = zeros(NP,D);               % initialize bestmember  matrix
ui  = zeros(NP,D);               % intermediate population of perturbed
vectors
mui = zeros(NP,D);               % mask for intermediate population
mpo = zeros(NP,D);               % mask for old population
rot = (0:1:NP-1);                % rotating index array (size NP)
rotd= (0:1:D-1);                 % rotating index array (size D)
rt  = zeros(NP);                 % another rotating index array
rtd = zeros(D);                  % rotating index array for exponential
crossover
a1  = zeros(NP);                 % index array
a2  = zeros(NP);                 % index array
a3  = zeros(NP);                 % index array
a4  = zeros(NP);                 % index array
a5  = zeros(NP);                 % index array
ind = zeros(4);

iter = 1;
while ((iter < itermax) & (bestval > VTR))
  popold = pop;                  % save the old population

  ind = randperm(4);             % index pointer array

  a1  = randperm(NP);            % shuffle locations of vectors
  rt = rem(rot+ind(1),NP);       % rotate indices by ind(1) positions
  a2  = a1(rt+1);                % rotate vector locations
  rt = rem(rot+ind(2),NP);
  a3  = a2(rt+1);
  rt = rem(rot+ind(3),NP);
  a4  = a3(rt+1);
  rt = rem(rot+ind(4),NP);
  a5  = a4(rt+1);

  pm1 = popold(a1,:);            % shuffled population 1
  pm2 = popold(a2,:);            % shuffled population 2
  pm3 = popold(a3,:);            % shuffled population 3
  pm4 = popold(a4,:);            % shuffled population 4
  pm5 = popold(a5,:);            % shuffled population 5

  for i=1:NP                     % population filled with the best
member
    bm(i,:) = bestmemit;         % of the last iteration
  end

  mui = rand(NP,D) < CR;         % all random numbers < CR are 1, 0
otherwise

  if (strategy > 5)
    st = strategy-5;             % binomial crossover
  else
    st = strategy;             % exponential crossover
    mui=sort(mui');              % transpose, collect 1's in each column
```

```
    for i=1:NP
      n=floor(rand*D);
      if n > 0
         rtd = rem(rotd+n,D);
         mui(:,i) = mui(rtd+1,i); %rotate column i by n
      end
    end
    mui = mui';              % transpose back
  end
  mpo = mui < 0.5;                    % inverse mask to mui

  if (st == 1)                        % DE/best/1
    ui = bm + F*(pm1 - pm2);          % differential variation
    ui = popold.*mpo + ui.*mui;      % crossover
  elseif (st == 2)                    % DE/rand/1
    ui = pm3 + F*(pm1 - pm2);         % differential variation
    ui = popold.*mpo + ui.*mui;      % crossover
  elseif (st == 3)                    % DE/rand-to-best/1
    ui = popold + F*(bm-popold) + F*(pm1 - pm2);
    ui = popold.*mpo + ui.*mui;      % crossover
  elseif (st == 4)                    % DE/best/2
    ui = bm + F*(pm1 - pm2 + pm3 - pm4);  % differential variation
    ui = popold.*mpo + ui.*mui;          % crossover
  elseif (st == 5)                    % DE/rand/2
    ui = pm5 + F*(pm1 - pm2 + pm3 - pm4);  % differential variation
    ui = popold.*mpo + ui.*mui;           % crossover
  end

%-----Select which vectors are allowed to enter the new population----
--------
range_flag = 0.0;
  for i=1:NP
    tempval = feval(fname,ui(i,:),y);    % check cost of competitor
    nfeval  = nfeval + 1;
    % add constrains to all elements
    len_elem = length(ui(1,:));
    for j=1:len_elem
        if ui(i,j) < XVmin(j) | ui(i,j) > XVmax(j)
            range_flag = 1.0;
        end
    end
    if (tempval <= val(i) & range_flag==0.0)  % if competitor is
better than value in "cost array"
       pop(i,:) = ui(i,:);  % replace old vector with new one (for new
iteration)
       val(i)   = tempval;  % save value in "cost array"

       %----we update bestval only in case of success to save time----
-------
       if (tempval < bestval)     % if competitor better than the best
one ever
          bestval = tempval;      % new best value
          bestmem = ui(i,:);      % new best parameter vector ever
                                    252
```

```
        end
      end
   end %---end for imember=1:NP

   bestmemit = bestmem;         % freeze the best member of this
iteration for the coming
                               % iteration. This is needed for some of
the strategies.

%----Output section-----------------------------------------------
-------

  if (refresh > 0)
     if (rem(iter,refresh) == 0)
        fprintf(1,'Iteration: %d,  Best: %f,  F: %f,  CR: %f,  NP:
%d\n',iter,bestval,F,CR,NP);
        for n=1:D
           fprintf(1,'best(%d) = %f\n',n,bestmem(n));
        end
     end
  end

  iter = iter + 1;
end %---end while ((iter < itermax) ...
_
% The codes calculate condition mumber (kapa) and residue number (R)
% based on "Uniquesness and wavelength optimization in CW
multispectral
% DOT" of Alper Corlu, Turgut Durduran, ...et al.
% Code written by Ngvuvenvu Chu

function [f]=optimal_wave_sen(lamdas,y)
% lamdas : array of wavelengths
% b      : power coefficients of Mie scattering (1.3)
% we use only 3 chromophores and 8 wavelengths in the calculatetion
(m=8,
% n=3)

num_chrom = 3;
num_wave = length(lamdas);

% fill columns of matrix A and K
for ii=1:num_wave
    [Hb_c,Hb02_c,H20_c,lipid] = get_extcoff_interp(lamdas(ii));
    K(ii,:) = [Hb_c,Hb02_c,H20_c,lipid];
    A(ii,:) = K(ii,:)/(lamdas(ii)^1.3);
end
  kapa = cond(K);
 At = A';
X=ones(num_wave,1);
X0 = ((At*A)\At)*X;
```

```matlab
% Residue
R = norm(1-A*X0)+1e-6;


f = kapa/R;
f=1/f;


% Written by nguvenvu Chu
% the codes use DE algorithm to find 8 optimal wavelengths for 3
% chromophores (Hb, Hb0,H20 and lipids) based on based on "Uniquesness
and wavelength
% optimization in CW multispectral DOT" of Alper Corlu, Turgut
Durduran, ...et al.

clear;
% assump that the power coefficeint of Mie scattering
b = 1.3;


FUN='optimal_wave_sen';

 y = [];

 % value to reach
 VTR = 1.0e-6;

%val  = feval(FUN,XVmin,y)

% Set the maximum number of wavelengths which is used in the
calculation
max_wave = 100;

% for ii=4:2:max_wave
for ii=4:2:max_wave
    ii
    XVmin=650*ones(1,ii);
    XVmax=930*ones(1,ii);

    % number of parameters
    D = length(XVmin);

    % problem data vector
    y = [];
    % number of population members (10xnumber of paramters)
    NP = 10*ii;
    % maximum number of iterations (generations)
    itermax = 100;
    % DE stepsize F ex [0,2]
    F = 0.8;
    % cross over probability constant ex [0,1]
    CR = 0.2;
    % strategy
    strategy = 5;
```

```
    %refresh
    refresh = 10;

    [x,f,nf] =
devec3_wave(FUN,VTR,D,XVmin,XVmax,y,NP,itermax,F,CR,strategy,refresh);

    opt_wave = x;

    [kapa,R,f]=get_R_kapa_func(opt_wave);

    filename = strcat('opt_numwave','_',num2str(ii),'.dat');
    fid_opt = fopen(filename,'w+');
    if (fid_opt == -1)
        error('Can''t open file for writting ');
    end
    fprintf(fid_opt,'%% results of optimization \n');

    for jj=1:D
        fprintf(fid_opt,'%6.3e \n',opt_wave(jj));
    end
    fprintf(fid_opt,'kapa = %6.3f \n',kapa);
    fprintf(fid_opt,'Residue = %6.3e \n',R);
    fprintf(fid_opt,'Residue/kapa = %6.3e \n',f);
    fclose(fid_opt);
end
```

```
% This part contains all code for image reconstruction
% all functions are listed one below the other.
% written by Adita Apte
% Modification by Dheerendra Kashyap, Ngvenvu Chu
% Script is for 8 wavelngth reconstruction

% clear memory and close all graphs
clear;
close all;
clc

% array of four wavelengths at which optimization is done
fprintf(' wavelengths [um] used in DOT reconstruction \n');
lambda = [0.650 0.714 0.850 0.886]
%lambda = [650 714 850 886 682 718]

% Ask user for plots
plot_flag = input('Plot the meshed and reconstructued optical
properties [Y/N] : ','s');
fprintf('\n');
% testing mesh gernerated by MATLAB.
% for circular_inv_dot3.m when changing the below two files, users
should
% also go to line 392 & 393 to change file names there.

nodev1;
elemv1;

% After using HRBF to determine locations of tumors.  Normal FEM is
used to
% hopefully to determine more accurate shape of the tumor regions.

EDATA2 = EDATA;

%%% stupid coding here -----------------------------------------------
------
N=100;
R=1;
NN=31; % this is ok
th1=linspace(0,2*pi,NN)';
S1=sin(th1);C1=cos(th1);
S1=S1(1:(NN-1));C1=C1(1:(NN-1));
nc=length(S1);
NN0=NN;
th=linspace(0,2*pi,N);
S=sin(th);C=cos(th);
I=NDATA(:,1);
XY(I,:)=NDATA(:,2:3);
NXY=length(XY(:,1));
```

256

```
%element connectivity
%          Outer ring
I=EDATA2(:,1);              % I : vector stores element indexes
Elec(I,:)=EDATA2(:,7:9);    % get three nodes for triangular element
ith
%Plot mesh
Nelem=length(Elec);         % Nelem : number of elements
for i=1:Nelem
   In=[Elec(i,:)];          % get three nodes for triangular element
ith
   Xe=XY(In,1);             % get x-coordinates the three above nodes.
Xe is a columne vector
   Ye=XY(In,2);
   XC(i)=sum(Xe)/3;
   YC(i)=sum(Ye)/3;
   In=[Elec(i,:) Elec(i,1)];
   Xe=XY(In,1);
   Ye=XY(In,2);
end


NNN=length(XY(:,1))


%----------------------------------------------------------------------
-----
% Get source/detector pair locations from setup for forward problem
% save node numbers of source/detector pair locations for inverse
problem
src_file  = input('Enter filename for source locations [src_loc.m] :
','s');
fprintf('\n');
if isempty(src_file)
    src_file = 'src_loc.m';
end

fid_src = fopen(src_file,'r');
if (fid_src == -1)
    error('Can''t open the source/detector location file');
end

% initilize ii for looping
ii = 1;
while feof(fid_src) == 0
    rline = fgetl(fid_src);
    if (rline(1) ~= '%')
        a = sscanf(rline,'%g');
        IBall(ii) = a(1);
        ii = ii+1;
    end
end
fclose(fid_src);
%----------------------------------------------------------------------
-----
```

```
%
%----------------------------------------------------------------------
-----
% Get light intensity @ detectors for reconstruction at 4 different
% wavelengths
fwd_file  = input('Enter filename for forward data [fwd_data.m] :
','s');
fprintf('\n');
if isempty(fwd_file)
    fwd_file = 'fwd_data.m';
end

% open file to read forward data
fid_fwd = fopen(fwd_file,'r');
if (fid_fwd == -1)
    error('Can''t open the forward data file');
end

ii = 1;
while feof(fid_fwd) == 0
    rline = fgetl(fid_fwd);
        if (rline(1) ~= '%')
        a = sscanf(rline,'%g');
        num_src = length(a);

        if length(IBall) == 8
            mult = 5;
        else
            mult = 13;
        end
        if ceil(ii/(num_src-3))==1
            index = ceil(ii/(num_src-3));
            for is=1:num_src
                Yref1(ii-(index-1)*mult,is) = a(is);
            end
        elseif ceil(ii/(num_src-3))==2
            index = ceil(ii/(num_src-3));
            for is=1:num_src
                Yref2(ii-(index-1)*mult,is) = a(is);
            end
        elseif ceil(ii/(num_src-3))==3
            index = ceil(ii/(num_src-3));
            for is=1:num_src
                Yref3(ii-(index-1)*mult,is) = a(is);
            end
        elseif ceil(ii/(num_src-3))==4
            index = ceil(ii/(num_src-3));
            for is=1:num_src
                Yref4(ii-(index-1)*mult,is) = a(is);
            end
        elseif ceil(ii/(num_src-3))==5
            index = ceil(ii/(num_src-3));
            for is=1:num_src
```

```matlab
                    Yref5(ii-(index-1)*mult,is) = a(is);
                end
            else
                index = ceil(ii/(num_src-3));
                for is=1:num_src
                    Yref6(ii-(index-1)*mult,is) = a(is);
                end
            end
            ii = ii+1;
    end
end
%-----------------------------------------------------------------
-----
%Define Tumor region
II2=EDATA2(:,2);
Ntu=max(II2)-1;   % Ntu number of tumor regions. i.e regions which
have absorption coeff different than the background region.

% looping through all regions which have different optical properties
and
% save number of elements having same optical properties into cell
array
% IT2. for ex. IT{1} stores number of elemnets have material
characteristic
% of 1 (normal region).  IT{2} stores number of elements have material
% characteristic of 2 (1st tumor region) ...

for i=1:(Ntu+1)
    % length of IT2 is the number of regions which have different
optical
    % properties (i.e. normal vs. tumor)
    % IT2{i} stores element indexes of ith regions
    IT2{i}=find(EDATA2(:,2)==i);
end

CLR='yrbgmyrbgmyrbgmyrbgmyrbgmyrbgmyrbgmyrbgmyrbgmyrbgmyrbgmyrbgmyrbg'
;
Nodes=length(NDATA(:,1));   % get number of nodes
nDOF=zeros(Nodes,2);

for i=1:Nelem
    II2=EDATA2(i,2);  % II2 : material property number of element ith
    In=[Elec(i,:)];
    NA=In(1);NB=In(2);NC=In(3);
    i1=(NA-1)*2;i12=(i1+1):(i1+2);
    IA=i12; %% Degrees of freedom of node A
    i1=(NB-1)*2;i12=(i1+1):(i1+2);
    IB=i12;
    i1=(NC-1)*2;i12=(i1+1):(i1+2);
    IC=i12;
    Xe=XY(In,1);
    Ye=XY(In,2);
```

```
    In=[Elec(i, :) Elec(i,1)];
    Xe=XY(In,1);
    Ye=XY(In,2);
    nDOF(NA,:)=IA;
    nDOF(NB,:)=IB;
    nDOF(NC,:)=IC;
end

% plot the phantom in which each element is labled by its material
% properties -- Compare this plot to the plot obtained by HRBF
if plot_flag == 'Y'
    figure
    for ii=1:length(IT2)
        for i=1:length(IT2{ii})
            I=Elec(IT2{ii}(i),:);
            xE=XY(I,1);
            yE=XY(I,2);
            XE=[xE;xE(1)];
            YE=[yE;yE(1)];
            hold on, plot(XE,YE,'b','linewidth',2)
            %text(XC(IT2{ii}(i)),YC(IT2{ii}(i)),int2str(ii))
            if EDATA2(IT2{ii}(i),2) > 1
                % plot only material characteristic of tumor regions

text(XC(IT2{ii}(i)),YC(IT2{ii}(i)),int2str(EDATA2(IT2{ii}(i),2)))
            end
        end
    end
    axis equal
    title('\bfA FE model')
end

%Delete mid-side nodes
IFIXED2=find(nDOF(:,1)==0);

%Generate matrices
Ng=length(XY(:,1));
I=1:Ng;
I(IFIXED2)=[];
Idf=I;
for ii=1:length(IT2)
    KA2=sparse(zeros(Ng,Ng));
    KS2=sparse(zeros(Ng,Ng));
    NE=length(IT2{ii});
    EE=IT2{ii};
    for i=1:NE      % NE number of elements
        ie=EE(i);
        I=Elec(ie,:);
        xE=XY(I,1);
        yE=XY(I,2);
        [Ke,Ce]=t3km2(ie,1,1,Elec,XY);
        Idof=I;
        KS2(I,I)=KS2(I,I)+Ke;
```

```
        KA2(I,I)=KA2(I,I)+Ce;
        IEDOF{i}=Idof;
    end
    Ka2{ii}=KA2(Idf,Idf);   % cell array of [number of different
regions x nodes]
    Ks2{ii}=KS2(Idf,Idf);   % cell array of [number of different
regions x nodes]
end
%-------------------------------------------------------------------
-----
% setting lower/upper bounds for background and tumor region
concentrations
% of Hb, Hb02, H20
% lower bounds
Hb_blb   = 0.01;
Hb02_blb = 0.01;
H20_blb  = 0.89;
if Ntu >=1
    Hb_tulb  = 0.01*ones(1,Ntu);
    Hb02_tulb = 0.01*ones(1,Ntu);
    H20_tulb  = 0.89*ones(1,Ntu);
end
% upper bounds
Hb_bub   = 0.1;
Hb02_bub = 0.1;
H20_bub  = 0.9;
if Ntu >=1
    Hb_tuub  = 0.1*ones(1,Ntu);
    Hb02_tuub = 0.1*ones(1,Ntu);
    H20_tuub  = 0.9*ones(1,Ntu);
end
% setting lower/upper bounds for Mie scattering coefficeints
mul_Mie_blb = 4.5;
pow_Mie_blb = 1.29;
if Ntu >=1
    mul_Mie_tulb = 4.5*ones(1,Ntu);
    pow_Mie_tulb = 1.29*ones(1,Ntu);
end

mul_Mie_bub  = 8;
pow_Mie_bub  = 1.3;
if Ntu >=1
    mul_Mie_tuub = 8*ones(1,Ntu);
    pow_Mie_tuub = 1.3*ones(1,Ntu);
end

% lower/upper bounds for all optimizable parameters (bounds for 2nd
optimization)
if Ntu >=1
    LB2 = [Hb_blb Hb_tulb Hb02_blb Hb02_tulb H20_blb H20_tulb
mul_Mie_blb mul_Mie_tulb pow_Mie_blb pow_Mie_tulb ];
    UB2 = [Hb_bub Hb_tuub Hb02_bub Hb02_tuub H20_bub H20_tuub
mul_Mie_bub mul_Mie_tuub pow_Mie_bub pow_Mie_tuub ];
```

```
else
    LB2 = [Hb_blb Hb02_blb H20_blb mul_Mie_blb pow_Mie_blb];
    UB2 = [Hb_bub Hb02_bub H20_bub mul_Mie_bub pow_Mie_bub];
end

% sources and detectors are at the same locations
IRESP = IBall;
IS = 3e4;   % get source strength from 1st optimization step

FUN1='newobjSen_m2b';
FUN2='newobjSen_m3b';

loop_flag = 1;
loop_cnt  = 1;
Xas=(LB2+UB2)/2;
% data for 4 wavelengths
y = [Yref1(:);Yref2(:);Yref3(:);Yref4(:)];
% data for 6 wavelengths
%y = [Yref1(:);Yref2(:);Yref3(:);Yref4(:);Yref5(:);Yref6(:)];

while (loop_flag)

OPTIONS=optimset('Display','iter','MaxIter',1,'MaxFunEvals',5000000000
0,'GradConstr','on','GradObj','on');

OP2=optimset('GradObj','on','Hessian','on','MaxFunEvals',5000,'MaxIter
',10,'TolX',1e-20,'Display','iter','TolFun',1e-20);
    for jj=1:5
        Aeq=[];beq=[];

X=fmincon(FUN2,Xas,[],[],[],[],LB2,UB2,[],OP2,IBall,Ka2,Ks2,y,lambda,I
S);
        Xas=X;
        [f,df,ddf]=newobjSen_m3b(Xas,IBall,Ka2,Ks2,y,lambda,IS);
        disp([num2str(jj),'     ',num2str(f)])
    end

%OP=optimset('jacobian','on','MaxFunEvals',50000,'MaxIter',500,'TolX',
1e-20,'Display','iter','TolFun',1e-20);

OP=optimset('jacobian','on','LevenbergMarquardt','on','MaxFunEvals',50
00,'MaxIter',20,'TolX',1e-20,'Display','iter','TolFun',1e-30);
    X2=lsqnonlin(FUN1,Xas,LB2,UB2,OP,IBall,Ka2,Ks2,y,lambda,IS)
    Xas = X2;
    [f,df]=newobjSen_m2b(Xas,IBall,Ka2,Ks2,y,lambda,IS);

    loop_cnt = loop_cnt +1;
    if loop_cnt > 10
        loop_flag = 0;
    end
    pause(5);
end
```

```
Xas

fid_opt = fopen('opt_res.dat','w+');
if (fid_opt == -1)
    error('Can''t open file for writting ');
end
% write results to opt_res.dat
fprintf(fid_opt,'%% results of optimization \n');
for ii=1:length(Xas)
    fprintf(fid_opt,'%6.3e \n',Xas(ii));
end
fclose(fid_opt);




function [f,df,ddf]=newobjSen_m3a(paraA,IBall,Ka,Ks,y,lambda,IS)
% for using with lsqnonlin
% spectral constraints bases Srinivasan et al
% get number of tumor regions
nTU = (length(paraA)-5)/5;

% fprintf('Number of tumor region in getProSS_multi =  %i \n',nTU);
% get background and tumor regions optical properties

if nTU >=1
    % background concentration of Hb
    Hb_b      = paraA(1);
    % get background concentration of Hb02
    Hb02_b    = paraA(nTU+2);
    % get background concentration of H20
    H20_b     = paraA(2*nTU+3);
    % get background concentration of lipids
    lipid_b    = paraA(2*nTU+4);
    % get Hb concentrations of tumor regions
    Hb_tu     = paraA(2:1+nTU);
    % get Hb02 concentrations of tumor regions
    Hb02_tu   = paraA(nTU+3:2*nTU+2);
    % get H20 concentration of tumor regions
    H20_tu    = paraA(2*nTU+4:3*nTU+3);
    % get background concentration of lipids
    lipid_tu  = paraA(2*nTU+4);
        % get background multiplication coeff of Mie scattering
    mul_Mie_b  = paraA(3*nTU+4);
    % get multiplication coeffs of Mie scattering
    mul_Mie_tu = paraA(3*nTU+5:4*nTU+4);
    % get background power coeff of Mie scattering
    pow_Mie_b = paraA(4*nTU+5);
    % get power coeffs of Mie scattering
    pow_Mie_tu = paraA(4*nTU+6:5*nTU+5);
else
    Hb_b    = paraA(1);
```

```
    Hb02_b = paraA(2);
    H20_b  = paraA(3);
    lipid_b = paraA(4);
    mul_Mie_b = paraA(4);
    pow_Mie_b = paraA(5);
end


% num_wave: number of wavelength used in reconstruction
num_wave = length(lambda);
ft  = [];
dft = [];
for jj=1:num_wave
% calculate error function and jacobian for each wavelength
    lambda1 = lambda(jj);
    KA=Ka{1};
    n=length(KA(:,1));    % n : numbers of FEM nodes
    nc=length(Ka);        % nc: numbers of different regions in FEM
model
    Kgg=zeros(n,n);
    [Hb_c,Hb02_c,H20_c, lipid_c] = get_extcoff2(lambda1);
    for i=1:nc
        if (i==1)    % background region
            Mua = Hb_b*Hb_c + Hb02_b*Hb02_c + H20_b*H20_c+
lipid_c*lipid_b;
            Mus = mul_Mie_b*((lambda1)^(-pow_Mie_b));;
        else
            Mua = Hb_tu(i-1)*Hb_c + Hb02_tu(i-1)*Hb02_c + H20_tu(i-
1)*H20_c+ lipid_tu(i-1)*lipid_c;;
            Mus = mul_Mie_tu(i-1)*((lambda1)^(-pow_Mie_tu(i-1)));
        end
        k=1/(3*(Mua+Mus));
        Kgg=Kgg+Mua*Ka{i}+k*Ks{i};
    end
    ii=0;
    YC=[];
    df=[];
    for IB=IBall
        ii=ii+1;
        %ii=length(IB);
        Ug=zeros(n,1);
        II=1:n;
        II(IB)=[];
        IDF=II;
        %Specify boundary data
        Ug(IB)=IS*(IB'.^0);
        %Solution with inhomogeneous BC ( specifiet temperature for
this example)
        Kff=Kgg(IDF,IDF);
        Pf=-Kgg(IDF,IB)*Ug(IB);
        Uf=Kff\Pf;
        Ug(IDF,1)=Uf;
        IRESP=IBall;
```

```matlab
        if length(IBall) ==8
            % Neglect measuements near source
            if ii==1
                IRESP([1 2 8])=[];   % ignore detector readings at the
active source, and two closed by% detectors due to intensity aturation
            elseif ii==8
                IRESP([7 8 1])=[];
            else
                IRESP([ii-1 ii ii+1])=[];
            end
        else
            % Neglect measuements near source
            if ii==1
                IRESP([1 2 16])=[];   % ignore detector readings at
the active source, and two closed by
                                      % detectors due to intensity
saturation
            elseif ii==16
                IRESP([15 16 1])=[];
            else
                IRESP([ii-1 ii ii+1])=[];
            end
        end

        U=Ug(IRESP);
        YC=[YC;U];

        %%% Sensitivity %%%
        for ix=1:nc       % Parameter-loop.  nc : number of different
regions in FEM model
            if (ix==1)    % background region
                Mua = Hb_b*Hb_c + Hb02_b*Hb02_c + H20_b*H20_c+
lipid_c*lipid_b;;
                Mus = mul_Mie_b*((lambda1)^(-pow_Mie_b));;
            else
                Mua = Hb_tu(i-1)*Hb_c + Hb02_tu(i-1)*Hb02_c +
H20_tu(i-1)*H20_c+ lipid_tu(i-1)*lipid_c;;
                Mus = mul_Mie_tu(i-1)*((lambda1)^(-pow_Mie_tu(i-1)));
            end
            k=1/(3*(Mua+Mus));

            %For Mus
            %%% newly commented
            dK=-3*k^2*Ks{ix};
            dUg=Ug*0;
            PE=-dK(IDF,:)*Ug;
            dUf=Kff\PE;
            dUg(IDF,1)=dUf;
            dU1(:,ix)=dUg(IRESP);
            %%% end newly commented

            % add jacobian for multipication coeff of Mie scattering
```

```
            if (ix==1)
                dU1_a = dU1*(lambda1)^(-pow_Mie_b);
            else
                dU1_a = dU1*((lambda1)^(-pow_Mie_tu(i-1)));
            end

            % add jacobian for power coeff of Mie scattering
            dU1_b = dU1*Mus*(-log(lambda1));
            %For Mua
            dK=dK+Ka{ix};
            dUg=Ug*0;
            PE=-dK(IDF,:)*Ug;
            dUf=Kff\PE;
            dUg(IDF,1)=dUf;
            dU2(:,ix)=dUg(IRESP);
            % add Jacobian for 3 chomophores (Hb, Hb02, H20)
            ext_coeff = [Hb_c,Hb02_c,H20_c,lipid_c];
            dU2_kr = kron(dU2,ext_coeff);
        end % of      % Parameter-loop
        % 1st derivative when both Mua and Mus are optimizable
paramters
        %df=[df; dU1 dU2];
        %dU1_kr
        %dU2_a
        %dU2_b
        df = [df; dU2_kr dU1_a dU1_b];
    end
    % error function
    f1 = YC;

    ft  = [ft;f1];
    dft = [dft;df];
end
f  = [];
df = [];
% error functions and Jacobian of the 4-wavelength problem
f  = (ft-y)./y;
df = dft;
% approximate Hessian
ddf = 2*df.'*df;
% Jacobian
df = 2*f.'*df;
% error function for optimizationusing fmincon
f = f.'*f;
```

```
% This script plots Hb and HbO maps
% specify Hb of back ground region [uM]
clear all;
Hb_b = 2.5;
% specify Hb of perturbed region in [uM}
% Due to the bugs in the codes please specify the Hb_p 6 unit smaller
than
% the real value
Hb_p = 1.5;
% specify HbO of back ground region [uM]
HbO_b = 10.5 ;
% specify Hb of perturbed region in [uM]
% Due to the bugs in the codes please specify the HbO_p 6 unit smaller
than
% the real value
HbO_p = 110.00;
% specify perturbed location and dimension (for 1 perturbed region
only)
% location of perturbed region for 03/17/2006 dynamic data
SX = 0.694; SY=0.717; XT=-0.698; YT=-0.162; ANG=1.784; IS=3.4e4;
% plot Hb map
Xplot=[Hb_b Hb_p SX SY XT YT ANG 3.4e4];
figure(1), plotMU(Xplot,[Hb_b Hb_p]);
%plotelltu(Xplot,[-2.25 2.25],[-2.25 2.25])
title('\bfReconstructed Hb Map')
% plot HbO map
Xplot=[HbO_b HbO_p SX SY XT YT ANG 3.4e4];
figure(2), plotMU(Xplot,[HbO_b HbO_p]);
% plotelltu(Xplot,[-2.25 2.25],[-2.25 2.25])
title('\bfReconstructed HbO Map');
```

APPENDIX F

DERIVATION FOR JACOBIAN IN CHAPTER 5

$$J_{a,\lambda} = \left.\frac{\partial\phi}{\partial a}\right|_\lambda = \frac{\partial\phi}{\partial k}\left.\frac{\partial k}{\partial a}\right|_\lambda$$

$$k = \frac{1}{3\left(\mu_a + \mu_s'\right)}$$

$$\frac{\partial k}{\partial a} = \frac{\partial k}{\partial \mu_z'}\frac{\partial \mu_z'}{\partial a}$$

$$\frac{\partial \mu_z'}{\partial a} = \lambda^{-b}$$

$$J_{a,\lambda} = \frac{\partial\phi}{\partial a} = \frac{\partial\phi}{\partial k}\bullet\left(-3k^2\right)\lambda^{-b}$$

$$J_{b,\lambda} = \left.\frac{\partial\phi}{\partial b}\right|_\lambda = \frac{\partial\phi}{\partial k}\left.\frac{\partial k}{\partial b}\right|_\lambda$$

$$\frac{\partial k}{\partial b} = \frac{\partial k}{\partial \mu_z'}\frac{\partial \mu_z'}{\partial b}$$

By taking logarithms on both sides,

$\ln\mu_s' - \ln a = -b\ln\lambda$, taking partial derivatives with respect to b

$$\frac{\partial \mu_s'}{\partial b} = -b\ \ln\lambda$$

$$J_{b,\lambda} = \frac{\partial\phi}{\partial k}\bullet\left(-3k^2\right)\left(\mu_s'\right)\left(-b\ln\lambda\right)$$

APPENDIX G

SPECTROMETER CCD DETECTOR DATA SHEET

Spectral Sensitivity (typ.) (Ta = +25°C)
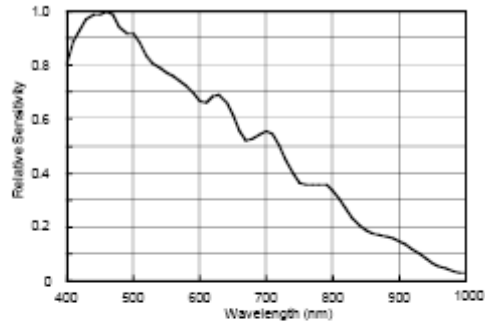
MTF of main scanning direction (typ.)
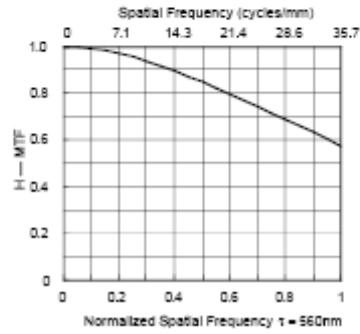
Dark Voltage Rate vs. Ambient Temperature (typ.)
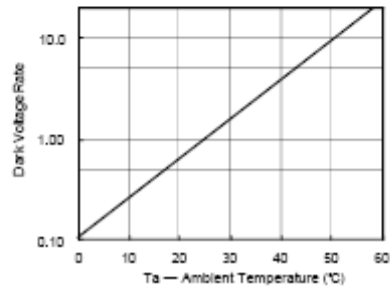
APPENDIX H

EXTINCTION COEFFICIENTS FOR WATER AND LIPID

Absorption Coeffcients of Mammalian Fat

R.L.P. van Veen and H.J.C.M. Sterenborg, A. Pifferi, A. Torricelli
and R. Cubeddu#Determination of VIS- NIR absorption coefficients of
mammalian fat, with time- and spatially resolved diffuse reflectance
and transmission spectroscopy #OSA Annual BIOMED Topical Meeting,
2004.

Wavelength (nm)	Absorption coefficient (m^{-1})
429	8.28
430	8.216
431	8.158
432	8.069
433	7.927
434	7.832
435	7.721
436	7.652
437	7.623
438	7.56
439	7.474
440	7.383
441	7.244
442	7.104
443	7
444	6.899
445	6.811
446	6.729
447	6.659
448	6.571
449	6.464
450	6.375
451	6.291
452	6.21
453	6.135
454	6.049
455	5.95
456	5.837
457	5.751
458	5.663
459	5.593
460	5.523
461	5.413
462	5.288
463	5.144
464	4.985
465	4.846
466	4.72
467	4.594

Wavelength (nm)	Absorption coefficient (m^{-1})
469	4.434
470	4.327
471	4.208
472	4.084
473	3.961
474	3.843
475	3.732
476	3.635
477	3.534
478	3.452
479	3.386
480	3.315
481	3.261
482	3.192
483	3.109
484	3.013
485	2.919
486	2.832
487	2.75
488	2.676
489	2.597
490	2.515
491	2.437
492	2.368
493	2.298
494	2.25
495	2.193
496	2.124
497	2.06
498	1.998
499	1.942
500	1.906
501	1.875
502	1.828
503	1.776
504	1.724
505	1.683
506	1.648
507	1.62
508	1.576
509	1.534
510	1.501
511	1.475
512	1.457
513	1.432
514	1.403

Wavelength (nm)	Absorption coefficient (m^{-1})
516	1.33
517	1.298
518	1.27
519	1.246
520	1.231
521	1.211
522	1.189
523	1.165
524	1.145
525	1.132
526	1.113
527	1.091
528	1.064
529	1.042
530	1.031
531	1.017
532	1.002
533	0.991
534	0.984
535	0.978
536	0.97
537	0.951
538	0.929
539	0.913
540	0.896
541	0.88
542	0.864
543	0.849
544	0.84
545	0.833
546	0.828
547	0.822
548	0.805
549	0.785
550	0.773
551	0.763
552	0.76
553	0.757
554	0.746
555	0.733
556	0.724
557	0.718
558	0.71
559	0.704
560	0.698
561	0.69

Wavelength (nm)	Absorption coefficient (m^{-1})
563	0.673
564	0.662
565	0.653
566	0.647
567	0.641
568	0.636
569	0.63
570	0.629
571	0.633
572	0.639
573	0.632
574	0.613
575	0.589
576	0.573
577	0.562
578	0.563
579	0.566
580	0.566
581	0.564
582	0.562
583	0.562
584	0.557
585	0.548
586	0.541
587	0.53
588	0.52
589	0.512
590	0.502
591	0.493
592	0.488
593	0.485
594	0.486
595	0.487
596	0.479
597	0.472
598	0.467
599	0.462
600	0.466
601	0.471
602	0.479
603	0.487
604	0.487
605	0.484
606	0.48
607	0.475
608	0.47

Wavelength (nm)	Absorption coefficient (m^{-1})
610	0.464
611	0.458
612	0.454
613	0.442
614	0.427
615	0.422
616	0.423
617	0.43
618	0.437
619	0.435
620	0.43
621	0.425
622	0.433
623	0.44
624	0.438
625	0.432
626	0.426
627	0.424
628	0.426
629	0.428
630	0.428
631	0.429
632	0.437
633	0.444
634	0.44
635	0.431
636	0.42
637	0.422
638	0.433
639	0.446
640	0.452
641	0.45
642	0.449
643	0.453
644	0.46
645	0.465
646	0.464
647	0.464
648	0.464
649	0.465
650	0.471
651	0.472
652	0.467
653	0.464
654	0.457
655	0.448

Wavelength (nm)	Absorption coefficient (m^{-1})
657	0.428
658	0.424
659	0.422
660	0.418
661	0.414
662	0.413
663	0.414
664	0.419
665	0.428
666	0.439
667	0.447
668	0.452
669	0.453
670	0.45
671	0.452
672	0.457
673	0.462
674	0.463
675	0.457
676	0.446
677	0.433
678	0.422
679	0.413
680	0.406
681	0.398
682	0.387
683	0.375
684	0.37
685	0.369
686	0.366
687	0.361
688	0.354
689	0.348
690	0.342
691	0.338
692	0.335
693	0.331
694	0.328
695	0.324
696	0.321
697	0.324
698	0.327
699	0.325
700	0.323
701	0.32
702	0.319

Wavelength (nm)	Absorption coefficient (m^{-1})
704	0.326
705	0.323
706	0.318
707	0.313
708	0.31
709	0.311
710	0.315
711	0.32
712	0.321
713	0.32
714	0.321
715	0.326
716	0.334
717	0.343
718	0.351
719	0.358
720	0.367
721	0.376
722	0.383
723	0.39
724	0.401
725	0.415
726	0.43
727	0.447
728	0.463
729	0.48
730	0.499
731	0.516
732	0.535
733	0.552
734	0.564
735	0.576
736	0.589
737	0.6
738	0.616
739	0.636
740	0.654
741	0.68
742	0.707
743	0.735
744	0.768
745	0.801
746	0.837
747	0.874
748	0.908
749	0.941

Wavelength (nm)	Absorption coefficient (m^{-1})
751	1.001
752	1.03
753	1.059
754	1.089
755	1.12
756	1.155
757	1.19
758	1.227
759	1.258
760	1.278
761	1.289
762	1.29
763	1.273
764	1.249
765	1.206
766	1.153
767	1.089
768	1.021
769	0.948
770	0.871
771	0.793
772	0.719
773	0.653
774	0.596
775	0.553
776	0.515
777	0.481
778	0.451
779	0.426
780	0.409
781	0.391
782	0.378
783	0.366
784	0.36
785	0.357
786	0.355
787	0.353
788	0.349
789	0.346
790	0.346
791	0.347
792	0.347
793	0.347
794	0.352
795	0.359
796	0.369

Wavelength (nm)	Absorption coefficient (m^{-1})
797	0.379
798	0.387
799	0.393
800	0.403
801	0.413
802	0.424
803	0.434
804	0.442
805	0.454
806	0.467
807	0.482
808	0.497
809	0.511
810	0.527
811	0.547
812	0.567
813	0.583
814	0.594
815	0.603
816	0.615
817	0.633
818	0.654
819	0.674
820	0.691
821	0.708
822	0.724
823	0.74
824	0.758
825	0.775
826	0.786
827	0.796
828	0.799
829	0.802
830	0.803
831	0.803
832	0.801
833	0.794
834	0.785
835	0.775
836	0.764
837	0.757
838	0.751
839	0.739
840	0.726
841	0.715
842	0.703

Wavelength (nm)	Absorption coefficient (m^{-1})
843	0.692
844	0.685
845	0.678
846	0.669
847	0.661
848	0.651
849	0.643
850	0.637
851	0.633
852	0.632
853	0.631
854	0.633
855	0.639
856	0.647
857	0.656
858	0.662
859	0.666
860	0.674
861	0.68
862	0.69
863	0.705
864	0.724
865	0.751
866	0.786
867	0.822
868	0.86
869	0.899
870	0.938
871	0.979
872	1.022
873	1.074
874	1.133
875	1.198
876	1.264
877	1.345
878	1.43
879	1.527
880	1.636
881	1.752
882	1.867
883	1.992
884	2.121
885	2.262
886	2.414
887	2.581
888	2.754

Wavelength (nm)	Absorption coefficient (m^{-1})
889	2.932
890	3.116
891	3.305
892	3.491
893	3.674
894	3.833
895	3.983
896	4.121
897	4.256
898	4.384
899	4.506
900	4.633
901	4.766
902	4.915
903	5.078
904	5.267
905	5.472
906	5.721
907	5.994
908	6.316
909	6.663
910	7.046
911	7.438
912	7.837
913	8.234
914	8.621
915	8.994
916	9.354
917	9.683
918	10
919	10.32
920	10.65
921	10.99
922	11.33
923	11.67
924	12
925	12.31
926	12.6
927	12.82
928	12.99
929	13.07
930	13.1
931	12.99
932	12.83
933	12.53
934	12.18

283

Wavelength (nm)	Absorption coefficient (m^{-1})
935	11.75
936	11.26
937	10.7
938	10.08
939	9.433
940	8.754
941	8.088
942	7.446
943	6.822
944	6.25
945	5.704
946	5.234
947	4.802
948	4.445
949	4.109
950	3.799
951	3.519
952	3.274
953	3.046
954	2.852
955	2.666
956	2.504
957	2.358
958	2.242
959	2.133
960	2.047
961	1.975
962	1.917
963	1.86
964	1.808
965	1.753
966	1.693
967	1.639
968	1.589
969	1.554
970	1.528
971	1.51
972	1.491
973	1.463
974	1.431
975	1.413
976	1.408
977	1.414
978	1.421
979	1.423
980	1.417

Wavelength (nm)	Absorption coefficient (m^{-1})
981	1.407
982	1.406
983	1.42
984	1.441
985	1.481
986	1.524
987	1.564
988	1.607
989	1.652
990	1.716
991	1.793
992	1.891
993	1.994
994	2.087
995	2.178
996	2.272
997	2.366
998	2.464
999	2.56
1000	2.654
1001	2.751
1002	2.87
1003	2.996
1004	3.136
1005	3.282
1006	3.43
1007	3.579
1008	3.735
1009	3.894
1010	4.057
1011	4.222
1012	4.388
1013	4.554
1014	4.722
1015	4.877
1016	5.024
1017	5.152
1018	5.279
1019	5.386
1020	5.481
1021	5.561
1022	5.631
1023	5.683
1024	5.734
1025	5.79
1026	5.857

Wavelength (nm)	Absorption coefficient (m^{-1})
1027	5.948
1028	6.05
1029	6.164
1030	6.274
1031	6.389
1032	6.503
1033	6.61
1034	6.717
1035	6.799
1036	6.871
1037	6.926
1038	6.97
1039	7.004
1040	7.029
1041	7.018
1042	6.998
1043	6.967
1044	6.904
1045	6.85
1046	6.792
1047	6.719
1048	6.662
1049	6.596
1050	6.504
1051	6.419
1052	6.348
1053	6.281
1054	6.212
1055	6.139
1056	6.045
1057	5.948
1058	5.867
1059	5.789
1060	5.705
1061	5.616
1062	5.534
1063	5.445
1064	5.364
1065	5.303
1066	5.259
1067	5.224
1068	5.18
1069	5.121
1070	5.065
1071	5.032
1072	5.025

Wavelength (nm)	Absorption coefficient (m^{-1})
1073	5.015
1074	5.005
1075	4.947
1076	4.878
1077	4.851
1078	4.841
1079	4.816
1080	4.811
1081	4.813
1082	4.798
1083	4.816
1084	4.804
1085	4.763
1086	4.755
1087	4.762
1088	4.771
1089	4.797
1090	4.801
1091	4.78
1092	4.783
1093	4.783
1094	4.79
1095	4.837
1096	4.876
1097	4.892
1098	4.911

Extinction Coeffcients of water

Wavelngth (nm)	Extinction coefficient (OD per cm)
599	0.00076
600	0.00088
601	0.00099
602	0.00106
603	0.00105
604	0.00105
605	0.00108
606	0.00108
607	0.00108
608	0.00112
609	0.0011
610	0.00117
611	0.00121
612	0.00122
613	0.00126
614	0.00117
615	0.00128
616	0.00122
617	0.00135
618	0.00133
619	0.00131
620	0.00126
621	0.00129
622	0.00128
623	0.00135
624	0.00127
625	0.00133
626	0.00126
627	0.00125
628	0.00124
629	0.00137
630	0.00132
631	0.00135
632	0.00118
633	0.00126
634	0.00127
635	0.00114
636	0.00123
637	0.00119
638	0.0013
639	0.0013
640	0.00137

Wavelngth (nm)	Extinction coefficient (OD per cm)
642	0.00121
644	0.00129
645	0.00137
646	0.0013
647	0.00139
648	0.00139
649	0.00136
650	0.00139
651	0.0014
652	0.00145
653	0.00144
654	0.00147
655	0.00141
656	0.00144
657	0.00142
658	0.00159
659	0.00153
660	0.00166
661	0.00166
662	0.00163
663	0.00164
664	0.00159
665	0.00164
666	0.00164
667	0.00164
668	0.00161
669	0.00167
670	0.00166
671	0.00162
672	0.00168
673	0.00171
674	0.00178
675	0.00166
676	0.00166
677	0.00171
678	0.00172
679	0.00172
680	0.00177
681	0.00183
682	0.0019
683	0.00183
684	0.00181
685	0.00188
686	0.00193
688	0.00204
689	0.00212

Wavelngth (nm)	Extinction coefficient (OD per cm)
690	0.00205
692	0.00225
693	0.00224
694	0.00228
695	0.00238
696	0.00252
697	0.00257
698	0.0026
699	0.00278
700	0.00285
701	0.0028
702	0.00283
703	0.00296
704	0.00301
705	0.00305
706	0.00315
707	0.00338
708	0.00344
709	0.00347
710	0.00365
711	0.00388
712	0.00395
713	0.00415
714	0.00435
715	0.00457
716	0.00475
717	0.00494
718	0.00522
719	0.00552
720	0.00561
721	0.00592
722	0.00622
723	0.00651
724	0.00666
725	0.00707
726	0.00739
727	0.00782
728	0.0082
729	0.00861
730	0.00911
731	0.00969
732	0.01025
734	0.01137
735	0.01182
736	0.0122
737	0.0125

Wavelngth (nm)	Extinction coefficient (OD per cm)
738	0.01274
740	0.01314
741	0.0131
742	0.01315
743	0.0132
744	0.01325
745	0.01312
746	0.01311
747	0.01308
748	0.01304
749	0.01312
750	0.01296
751	0.01306
752	0.01306
753	0.01307
754	0.01304
755	0.01297
756	0.01288
757	0.01296
758	0.01289
759	0.01278
760	0.01275
761	0.01277
762	0.01261
763	0.01252
764	0.01251
765	0.01245
766	0.01249
767	0.01239
768	0.01227
769	0.01217
770	0.01218
771	0.01208
772	0.01201
773	0.01185
774	0.01183
775	0.01191
776	0.0117
777	0.01154
778	0.01149
780	0.01142
781	0.01127
782	0.01118
783	0.01117
784	0.01099
785	0.01087

Wavelngth (nm)	Extinction coefficient (OD per cm)
786	0.01072
788	0.01061
789	0.01053
790	0.01036
791	0.01024
792	0.01022
793	0.01012
794	0.01005
795	0.00983
796	0.00974
797	0.00969
798	0.00964
799	0.00951
800	0.00956
801	0.00951
802	0.00936
803	0.00939
804	0.00935
805	0.00932
806	0.00928
807	0.00923
808	0.00929
809	0.00938
810	0.00942
811	0.00952
812	0.00958
813	0.00969
814	0.00964
815	0.00984
816	0.00995
817	0.01011
818	0.01021
819	0.01019
820	0.01047
821	0.01056
822	0.0106
823	0.01093
824	0.01123
826	0.01218
827	0.0126
828	0.01333
829	0.01384
830	0.01459
831	0.0151
832	0.01586
833	0.01638

Wavelngth (nm)	Extinction coefficient (OD per cm)
834	0.01656
836	0.0174
837	0.0174
838	0.01758
839	0.01773
840	0.01795
841	0.01813
842	0.01805
843	0.01814
844	0.01822
845	0.01835
846	0.01848
847	0.01856
848	0.01883
849	0.01898
850	0.01913
851	0.01908
852	0.01936
853	0.01931
854	0.0193
855	0.01934
856	0.01959
857	0.0196
858	0.01969
859	0.01972
860	0.01981
861	0.02001
862	0.02002
863	0.02008
864	0.01996
865	0.02034
866	0.02021
867	0.02045
868	0.02044
869	0.02085
870	0.02108
871	0.02116
872	0.02111
873	0.02138
874	0.0216
875	0.02172
876	0.02174
877	0.02217
878	0.02236
879	0.02278
880	0.02282

Wavelngth (nm)	Extinction coefficient (OD per cm)
881	0.0229
883	0.02366
884	0.02413
885	0.02421
886	0.02437
887	0.0244
888	0.02447
889	0.02504
890	0.02592
891	0.02579
892	0.02573
893	0.02612
894	0.02602
895	0.02643
896	0.0263
897	0.02667
898	0.0274
899	0.02781
900	0.02858
901	0.02869
902	0.02909
903	0.02938
904	0.02962
905	0.03003
906	0.03042
907	0.03073
908	0.03106
909	0.03155
910	0.032
911	0.03236
912	0.03294
913	0.03352
914	0.0342
915	0.03476
916	0.03558
917	0.03642
918	0.03731
919	0.03822
920	0.03941
921	0.04067
922	0.04191
923	0.04338
924	0.04499
925	0.04674
926	0.04854
927	0.05052

Wavelngth (nm)	Extinction coefficient (OD per cm)
928	0.05266
930	0.0574
931	0.0598
932	0.06248
933	0.0653
934	0.0682
935	0.07118
936	0.07426
937	0.07749
938	0.08087
939	0.08434
940	0.08804
941	0.09178
942	0.09607
943	0.10042
944	0.10503
945	0.11001
946	0.11512
947	0.12066
948	0.12677
949	0.13335
950	0.14015
951	0.14739
952	0.15492
953	0.16251
954	0.17015
955	0.1775
956	0.18438
957	0.19066
958	0.19641
959	0.20144
960	0.20562
961	0.20918
962	0.21194
963	0.21397
964	0.21561
965	0.21687
966	0.2179
967	0.21857
968	0.21913
969	0.21948
970	0.21969
971	0.2198
972	0.21992
973	0.21976
974	0.21959

Wavelength (nm)	Extinction coefficient (OD per cm)
975	0.21926
977	0.21796
978	0.21714
979	0.21609
980	0.21491
981	0.21361
982	0.21211
983	0.21059
984	0.20892
985	0.2071
986	0.20524
987	0.20322
988	0.20111
989	0.19895
990	0.19675
991	0.19451
992	0.19217
993	0.18985
994	0.18732
995	0.18488
996	0.18242
997	0.17985
998	0.17735
999	0.17484
1000	0.17227
1001	0.16973
1002	0.16703
1003	0.16442
1004	0.16173
1005	0.15907
1006	0.15656
1007	0.15394
1008	0.1512
1009	0.14863
1010	0.14602
1011	0.1432
1012	0.1406
1013	0.13796
1014	0.13537
1015	0.13282
1016	0.1302
1017	0.1276
1018	0.1251
1019	0.1227
1020	0.12018
1021	0.11773

Wavelngth (nm)	Extinction coefficient (OD per cm)
1022	0.11526
1024	0.11059
1025	0.10822
1026	0.10583
1027	0.10352
1028	0.1012
1029	0.0991
1030	0.09692
1031	0.09482
1032	0.09276
1033	0.0908
1034	0.08901
1035	0.08721
1036	0.08547
1037	0.08378
1038	0.08222
1039	0.08066
1040	0.07927
1041	0.0779
1042	0.07651
1043	0.07527
1044	0.07397
1045	0.0727
1046	0.07158
1047	0.07041
1048	0.06931
1049	0.06823
1050	0.06724
1051	0.06631

REFERENCES

[1]   B. Chance, S. Nioka, J. Kent, K. McCully, M. Fountain, R. Greenfeld, and G. Holtom, "Time-resolved spectroscopy of hemoglobin and myoglobin in resting and ischemic muscle," *Analytical Biochemistry*, vol. 174, pp. 698-707, 1988.

[2]   S. Homma, T. Fukunaga, and A. Kagaya, "Influence of adipose tissue thickness on near infrared spectroscopic   signal in the measurement of human muscle," *Journal of Biomedical Optics*, vol. 1, pp. 418-424, 1996.

[3]   M. Ferrari, Q. Wei, L. Carraresi, R. A. De Blasi, and G. Zaccanti, "Time-resolved spectroscopy of the human forearm," *Journal of Photochemistry and Photobiology B: Biology*, vol. 16, pp. 141-153, 1992.

[4]   B. Chance, E. Anday, S. Nioka, S. Zhou, L. Hong, K. Worden, C. Li, T. Murray, Y. Ovetsky, D. Pidikiti, and R. Thomas, "A novel method for fast imaging of brain function, non-invasively, with light," *Optics Express*, vol. 2, pp. 411-423, 1998.

[5]   R. Wenzel, H. Obrig, J. Ruben, K. Villringer, A. Thiel, J. Bernarding, U. Dirnagl, and A. Villringer, "Cerebral blood oxygenation changes induced by visual stimulation in humans," *Journal of Biomedical Optics*, vol. 1, pp. 399-404, 1996.

[6]   D. Kashyap, V. Sharma, and H. Liu, "Non-invasive monitoring of hemodynamic changes in orthotropic brain tumor," presented at Optical Tomography and Spectroscopy of Tissue VII, San Jose, CA, USA, 2007.

[7]   R. G. Steen, K. Kitagishi, and K. Morgan, "In vivo measurement of tumor blood oxygenation by near-infrared spectroscopy: Immediate effects of pentobarbital overdose or carmustine treatment," *Journal of Neuro-Oncology*, vol. 22, pp. 209-220, 1994.

[8]   H. D. Sostman, S. Rockwell, A. L. Sylvia, D. Madwed, G. Cofer, C. H. Charles, R. Negro-Vilar, and D. Moore, "Evaluation of ba1112 rhabdomyosarcoma oxygenation with microelectrodes, optical spectrophotometry, radiosensitivity, and magnetic resonance spectroscopy," *Magnetic Resonance in Medicine*, vol. 20, pp. 253-267, 1991.

[9]   H. Liu, Y. Song, K. L. Worden, X. Jiang, A. Constantinescu, and R. P. Mason, "Noninvasive investigation of blood oxygenation dynamics of tumors by near-infrared spectroscopy," *Applied Optics*, vol. 39, pp. 5231-5243, 2000.

[10]   M. S. Patterson, B. Chance, and B. C. Wilson, "Time resolved reflectance and transmittance for the noninvasive measurement of tissue optical properties," *Applied Optics*, vol. 28, pp. 2331-2336, 1989.

[11]   A. Kienle and M. S. Patterson, "Improved solutions of the steady-state and the time-resolved diffusion equations for reflectance from a semi-infinite turbid medium," *JOSA A*, vol. 14, pp. 246-254, 1997.

[12] J. B. Fishkin, O. Coquoz, E. R. Anderson, M. Brenner, and B. J. Tromberg, "Frequency-domain photon migration measurements of normal and malignant tissue optical properties in a human subject," *Applied Optics*, vol. 36, pp. 10-20, 1997.

[13] B. W. Pogue and M. S. Patterson, "Frequency-domain optical absorption spectroscopy of finite tissue volumes using diffusion theory," *Physics in Medicine and Biology*, vol. 39, pp. 1157-1180, 1994.

[14] F. Bevilacqua, A. J. Berger, A. E. Berger, D. Jakubowski, and B. J. Tromberg, "Broadband absorption spectroscopy in turbid media by combined frequency-domain and steady-state methods," *Applied Optics*, vol. 39, pp. 6498-6507, 2000.

[15] L. Reynolds, C. Johnson, and A. Ishimaru, "Diffuse reflectance from a finite blood medium: applications to the modeling of fiber optic catheters," *Applied Optics*, vol. 15, pp. 2059-2067, 1976.

[16] M. Johns, C. Giller, and H. Liu, "Computational and in vivo investigation of optical reflectance from human brain to assist neurosurgery," *Journal of Biomedical Optics*, vol. 3, pp. 437-445, 1998.

[17] M. Johns, C. A. Giller, and H. Liu, "Determination of hemoglobin oxygen saturation from turbid media using reflectance spectroscopy with small source-detector separations," *Applied Spectroscopy*, vol. 55, pp. 1686-1694, 2001.

[18] E. L. Hull, M. G. Nichols, and T. H. Foster, "Quantitative broadband near-infrared spectroscopy of tissue-simulating phantoms containing erythrocytes," *Physics in Medicine and Biology*, vol. 43, pp. 3381-3404, 1998.

[19] S. Nioka, M. Miwa, S. Orel, M. Shnall, M. Haida, S. Zhao, and B. Chance, "Optical imaging of human breast cancer," *Advances in Experimental Medicine and Biology*, vol. 361, pp. 171-179, 1994.

[20] C. A. Giller, H. Liu, P. Gurnani, S. Victor, U. Yazdani, and D. C. German, "Validation of a near-infrared probe for detection of thin intracranial white matter structures," *Journal of Neurosurgery*, vol. 98, pp. 1299-1306, 2003.

[21] H. Liu, Y. Gu, J. G. Kim, and R. P. Mason, "Near-Infrared Spectroscopy and Imaging of Tumor Vascular Oxygenation," *Methods in Enzymology*, vol. 386, pp. 349-378, 2004.

[22] G. Zonios and A. Dimou, "Modeling diffuse reflectance from semi-infinite turbid media: application to the study of skin optical properties," *Optics Express*, vol. 14, pp. 8661-8674, 2006.

[23] Z. Qian, S. Victor, Y. Gu, C. Giller, and H. Liu, "Look-ahead distance of a fiber probe used to assist neurosurgery: Phantom and Monte Carlo study," *Optics Express*, vol. 11, pp. 1844-1855, 2003.

[24] S. J. Matcher and C. E. Cooper, "Absolute quantification of deoxyhaemoglobin concentration in tissue near infrared spectroscopy," *Physics in Medicine and Biology*, vol. 39, pp. 1295-1312, 1994.

[25] M. Dorigo, V. Maniezzo, and A. Colorni, "Ant System: Optimization by a colony of cooperating agents," *IEEE Transactions on Systems, Man, and Cybernetics-Part B*, vol. 26, pp. 29-41, 1996.

[26] T. J. Farrell, M. S. Patterson, and B. Wilson, "A diffusion theory model of spatially resolved, steady-state diffuse reflectance for the noninvasive determination of tissue optical properties in vivo," *Medical Physics*, vol. 19, pp. 879-888, 1992.

[27] E. M. C. Hillman, A. Devor, M. B. Bouchard, A. K. Dunn, G. W. Krauss, J. Skoch, B. J. Bacskai, A. M. Dale, and D. A. Boas, "Depth-resolved optical imaging and microscopy of vascular compartment dynamics during somatosensory stimulation," *NeuroImage*, vol. 35, pp. 89-104, 2007.

[28] H. Liu, "Unified analysis of the sensitivities of reflectance and path length to scattering variations in a diffusive medium," *Applied Optics*, vol. 40, pp. 1742-1746, 2001.

[29] W. G. Zijlstra, V. O. W. Assendelft, and A. Buursma, *Visible and Near Infrared Absorption Spectra of Human and Animal Haemoglobin: Determination and Application*: VSP, 2000.

[30] E. L. Hull and T. H. Foster, "Steady-state reflectance spectroscopy in the P_3 approximation," *Journal of the Optical Society of America A*, vol. 18, pp. 584-599, 2001.

[31] M. Johns, C. A. Giller, D. German, and H. Liu, "Determination of reduced scattering coefficient of biological tissue from a needle-like probe," *Optics Express*, vol. 13, pp. 4828-4842, 2005.

[32] S. J. Matcher, M. Cope, and D. T. Delpy, "In vivo measurements of the wavelength dependence of tissue-scattering coefficients between 760 and 900 nm measured with time-resolved spectroscopy," *Applied Optics*, vol. 36, pp. 386-396, 1997.

[33] S. T. Flock, S. L. Jacques, B. C. Wilson, W. M. Star, and M. J. C. Van Gemert, "Optical properties of intralipid: A phantom medium for light propagation studies," *Lasers in Surgery and Medicine*, vol. 12, pp. 510-519, 1992.

[34] P. Gurnani, "Near infrared spectroscopic measurement of human and animal brain structures," in *Biomedical Engineering*. Arlington, TX: University of Texas at Arlington, 2003, pp. 172.

[35] P. Van der Zee, M. Essenpreis, and D. T. Delpy, "Optical properties of brain tissue," presented at Photon Migration and Imaging in Random Media and Tissues, Los Angeles, CA, USA, 1993.

[36] http://www.oceanoptics.com/Products/ws1diffrefstan.asp, "Diffuse Reflectance Standards," Ocean Optics Inc, 2007.

[37] B. P. Wang and A. Apte, "Design optimization using ant colony system," presented at Chinese Soceity for Mechanical Engineers, Taipei, Taiwan, 2003.

[38] M. Dorigo and L. M. Gambardella, "Ant Colony System: A cooperative learning approach to the traveling salesman problem.," *IEEE Transactions on Evolutionary Computation*, vol. 1, pp. 53-66, 1997.

[39] R. M. Mickey, O. J. Dunn, and C. V. A., *Applied Statistics: Analysis of Variance and Regression*, 3 ed: Wiley, 2004.

[40] S. Fantini, D. Hueber, M. A. Franceschini, E. Gratton, W. Rosenfeld, P. G. Stubblefield, D. Maulik, and M. R. Stankovic, "Non-invasive optical monitoring

of the newborn piglet brain using continuous-wave and frequency-domain spectroscopy," *Physics in Medicine and Biology*, vol. 44, pp. 1543-1563, 1999.

[41] H. J. Van Staveren, C. J. M. Moes, J. v. Marle, S. A. Prahl, and M. J. C. Van Gemert, "Light scattering in Intralipid-10% in the wavelength range of 400-1100 nm," *Applied Optics*, vol. 30, pp. 4507-4514, 1991.

[42] G. Kumar and J. M. Schmitt, "Optimal probe geometry for near-infrared spectroscopy of biological tissue," *Applied Optics*, vol. 36, pp. 2286–2293, 1997.

[43] M. Johns and H. Liu, "Limited possibility for quantifying mean particle size by logarithmic light-scattering spectroscopy," *Applied Optics*, vol. 42, pp. 2968-2971, 2003.

[44] D. Kashyap, C. A. Giller, and H. Liu, "Determination of particle size distribution from tissue using light scattering spectroscopy with small source detector separations," presented at Optical Tomography and Spectroscopy of Tissue VI, San Jose, CA, USA, 2005.

[45] A. M. K. Nilsson, C. Sturesson, D. L. Liu, and S. Andersson-Engels, "Changes in spectral shape of tissue optical properties in conjunction with laser-induced thermotherapy," *Applied Optics*, vol. 37, pp. 1256-1267, 1998.

[46] R. Graaff, J. G. Aarnoudse, J. R. Zijp, P. M. A. Sloot, F. F. M. de Mul, J. Greve, and M. H. Koelink, "Reduced light-scattering properties for mixtures of spherical particles: a simple approximation derived from Mie calculations," *Applied Optics*, vol. 31, pp. 1370-1376, 1992.

[47] A. Tjolsen, O.-G. Berge, S. Hunskaar, J. H. Rosland, and K. Hole, "The formalin test: an evaluation of the method," *Pain*, vol. 51, pp. 5-17, 1992.

[48] D. Dubuisson and S. G. Dennis, "The formalin test: A quantitative study of the analgesic effects of morphine, meperidine, and brain stem stimulation in rats and cats," *Pain*, vol. 4, pp. 161-174, 1978.

[49] C. G. Heapy, A. Jamieson, and N. J. W. Russell, "Affrent C-fibre and A-delta activity in models of inflammation.," *British Journal of Pharmacology*, vol. 90, pp. 164P, 1987.

[50] B. Taylor, M. Peterson, and A. Basbaum, "Persistent cardiovascular and behavioral nociceptive responses to subcutaneous formalin require peripheral nerve input," *Journal of Neuroscience*, vol. 15, pp. 7575-7584, 1995.

[51] E. R. Kandel, J. H. Schwartz, and T. M. Jessell, *Principles of Neural Science*, 4 ed: McGraw-Hill Professional, 2000.

[52] T. Lewis, *The blood vessels of the human skin and their responses*. London: Shaw and Sons Ltd, 1927.

[53] S. D. Brain, T. J. Williams, J. R. Tippins, H. R. Morris, and I. MacIntyre, "Calcitonin gene-related peptide is a potent vasodilator," vol. 313, pp. 54-56, 1985.

[54] G. Majno, S. M. Shea, and M. Leventhal, "Endothelial contraction induced by histamine-type mediators: An Electron Microscopic Study," *The Journal of Cell Biology*, vol. 42, pp. 647-672, 1969.

[55] R. L. Nahin and J. L. K. Hylden, "Peripheral inflammation is associated with increased glutamic acid decarboxylase immunoreactivity in the rat spinal cord," *Neuroscience Letters*, vol. 128, pp. 226-230, 1991.

[56] W. D. Willis Jr, "Dorsal root potentials and dorsal root reflexes: a double-edged sword," *Experimental Brain Research*, vol. 124, pp. 395-421, 1999.

[57] R. Porszasz, N. Beckmann, K. Bruttel, L. Urban, and M. Rudin, "Signal changes in the spinal cord of the rat after injection of formalin into the hindpaw: Characterization using functional magnetic resonance imaging," *Proceedings of the National Academy of Sciences*, vol. 94, pp. 5034-5039, 1997.

[58] P. N. Fuchs, M. Ringkamp, M. Shiotani, and S. N. Raja, "Sympathectomy decreases formalin-induced nociceptive responses independent of changes in peripheral blood flow," *Experimental Neurology*, vol. 155, pp. 95-102, 1999.

[59] B. K. Taylor, M. A. Peterson, R. E. Roderick, J. Tate, P. G. Green, J. O. Levine, and A. I. Basbaum, "Opioid inhibition of formalin-induced changes in plasma extravasation and local blood flow in rats," *Pain*, vol. 84, pp. 263-270, 2000.

[60] N. Vergnolle, N. W. Bunnett, K. A. Sharkey, V. Brussee, S. J. Compton, E. F. Grady, G. Cirino, N. Gerard, A. I. Basbaum, P. Andrade-Gordon, M. D. Hollenberg, and J. L. Wallace, "Proteinase-activated receptor-2 and hyperalgesia: A novel pain pathway," vol. 7, pp. 821-826, 2001.

[61] Y. B. Peng, D. R. Kenshaloa, and R. H. Gracely, "Periaqueductal gray-evoked dorsal root reflex is frequency dependent," *Brain Research*, vol. 976, pp. 217-226, 2003.

[62] M. Zimmermann, "Ethical guidelines for investigations of experimental pain in conscious animals," *Pain*, vol. 16, pp. 109-110, 1983.

[63] R. P. Crippa, V. Cristofoletti, and N. Romeo, "A band model for melanin deduced from optical absorption and photoconductivity experiments," *Biochimica et Biophysica Acta.*, vol. 538, pp. 164-170, 1978.

[64] T. Sarna and R. C. Sealy, "Photoinduced oxygen consumption in melanin systems. Action spectra and quantum yields for eumelanin and synthetic melanin.," *Photochemistry and Photobiology*, vol. 39, pp. 69-74, 1984.

[65] H. Woodard and D. White, "The composition of body tissues," *The British Journal of Radiology*, vol. 59, pp. 1209-1218, 1986.

[66] M. Suh, S. Bahar, A. D. Mehta, and T. H. Schwartz, "Blood volume and hemoglobin oxygenation response following electrical stimulation of human cortex," *NeuroImage*, vol. 31, pp. 66-75, 2006.

[67] G. M. Pitcher and J. L. Henry, "Second phase of formalin-induced excitation of spinal dorsal horn neurons in spinalized rats is reversed by sciatic nerve block," *European Journal of Neuroscience*, vol. 15, pp. 1509-1515, 2002.

[68] Y. Kong, Y. Zheng, D. Johnston, J. Martindale, M. Jones, S. Billings, and J. Mayhew, "A model of the dynamic relationship between blood flow and volume changes during brain activation," vol. 24, pp. 1382-1392, 2004.

[69] B. K. Taylor, A. M. Peterson, and A. I. Basbaum, "Continuous intravenous infusion of naloxone does not change behavioral, cardiovascular, or

inflammatory responses to subcutaneous formalin in the rat," *Pain*, vol. 69, pp. 171-177, 1997.

[70]   B. K. Taylor and A. I. Basbaum, "Early antinociception delays edema but does not reduce the magnitude of persistent pain in the formalin test," *Journal of Pain*, vol. 1, pp. 218-228, 2000.

[71]   J. B. Mandeville, J. J. A. Marota, B. E. Kosofsky, J. R. Keltner, R. Weissleder, B. R. Rosen, and R. M. Weisskoff, "Dynamic functional imaging of relative cerebral blood volume during rat forepaw stimulation," *Magnetic Resonance in Medicine*, vol. 39, pp. 615-624, 1998.

[72]   H. Bortfeld, E. Wruck, and D. A. Boas, "Assessing infants cortical response to speech using near-infrared spectroscopy," *NeuroImage*, vol. 34, pp. 407-415, 2007.

[73]   C. H. Schmitz, D. P. Klemer, R. Hardin, M. S. Katz, Y. Pei, H. L. Graber, M. B. Levin, R. D. Levina, N. A. Franco, W. B. Solomon, and R. L. Barbour, "Design and implementation of dynamic near-infrared optical tomographic imaging instrumentation for simultaneous dual-breast measurements," *Applied Optics*, vol. 44, pp. 2140-2153, 2005.

[74]   S. Srinivasan, B. W. Pogue, S. Jiang, H. Dehghani, and K. D. Paulsen, "Spectrally constrained chromophore and scattering near-infrared tomography provides quantitative and robust reconstruction," *Applied Optics*, vol. 44, pp. 1858-1869, 2005.

[75]   F. E. W. Schmidt, M. E. Fry, E. M. C. Hillman, J. C. Hebden, and D. T. Delpy, "A 32-channel time-resolved instrument for medical optical tomography," *Review of Scientific Instruments*, vol. 71, pp. 256-265, 2000.

[76]   B. Chance, S. Niokab, J. Kenta, K. McCullyb, M. Fountaina, R. Greenfeld, and G. Holtom, "Time-resolved spectroscopy of hemoglobin and myoglobin in resting and ischemic muscle," *Analytical Biochemistry*, vol. 174, pp. 698-707, 1988.

[77]   H. Xu, R. Springett, H. Dehghani, B. W. Pogue, K. D. Paulsen, and J. F. Dunn, "Magnetic-resonance-imaging–coupled broadband near-infrared tomography system for small animal brain studies," *Applied Optics*, vol. 44, pp. 2179-2188, 2005.

[78]   T. Svensson, S. Andersson-Engels, M. Einarsdottir, and K. Svanberg, "In vivo optical characterization of human prostate tissue using near-infrared time-resolved spectroscopy," *Journal of Biomedical Optics*, vol. 12, pp. 014022-10, 2007.

[79]   S. J. Matcher, M. Cope, and D. T. Delpy, "Use of the water absorption spectrum to quantify tissue chromophore concentration changes in near-infrared spectroscopy," *Physics in Medicine and Biology*, vol. 39, pp. 177-196, 1994.

[80]   S. L. Jacques and D. J. McAuliffe, "The melanosome: threshold temperature for explosive vaporization and internal absorption coefficient during pulsed laser irradiation.," *Photochemistry and Photobiology*, vol. 53, pp. 769-775, 1991.

[81]   A. Savitzky and M. J. E. Golay, "Smoothing and differentiation of data by simplified least squares procedures," *Analytical Chemistry*, vol. 36, pp. 1627-1639, 1964.

[82]   J. G. Webster, *Medical Instrumentation: Application and Design*, 3 ed. New York, NY: John Wiley, 1997.

[83]   Y. Nakamura, K. Pilt, N. Kakuta, H. Arimoto, and Y. Yamada, "Optical measurement of water content in tissue," presented at Biophotonics, 2004. APBP 2004. The Second Asian and Pacific Rim Symposium on, 2004.

[84]   T. G. Psarros, B. Mickey, K. Gall, J. Gilio, J. Delp, C. White, J. Drees, M. Willis, D. Pistemmna, and C. A. Giller, "Image-guided robotic radiosurgery in a rat glioma model," *Minimally Invasive Neurosurgery*, vol. 47, pp. 266-272, 2004.

[85]   C. C. Abbou, L. Salomon, A. Hoznek, P. Antiphon, A. Cicco, F. Saint, W. Alame, J. Bellot, and D. K. Chopin, "Laparoscopic radical prostatectomy: preliminary results," *Urology*, vol. 55, pp. 630-633, 2000.

[86]   S. Kaul, "Laparoscopic and robotic radical prostatectomy," in *eMedicine*, 2005, pp. http://www.emedicine.com/med/topic3723.htm.

[87]   L. Tark, S. Deger, B. Winkelmann, B. Schanberger, and S. Loening, "Laparoscopic radical prostatectomy. Technical aspects and experience with 125 cases.," *European urology*, vol. 40, pp. 46-53, 2001.

[88]   J.-U. Stolzenburg, M. C. Truss, M. Do, R. Rabenalt, H. Pfeiffer, M. Dunzinger, B. Aedtner, C. G. Stief, U. Jonas, and W. Dorschner, "Evolution of endoscopic extraperitoneal radical prostatectomy (EERPE)â€"technical improvements and development of a nerve-sparing, potency-preserving approach," *World Journal of Urology*, vol. 21, pp. 147-152, 2003.

[89]   R. F. Van Velthoven, T. E. Ahlering, A. Peltier, D. W. Skarecky, and R. V. Clayman, "Technique for laparoscopic running urethrovesical anastomosis:the single knot method," *Urology*, vol. 61, pp. 699-702, 2003.

[90]   J. G. Kim, D. Zhao, Y. Song, A. Constantinescu, R. P. Mason, and H. Liu, "Interplay of tumor vascular oxygenation and tumor pO[sub 2] observed using near-infrared spectroscopy, an oxygen needle electrode, and [sup 19]F MR pO[sub 2] mapping," *Journal of Biomedical Optics*, vol. 8, pp. 53-62, 2003.

[91]   M. Xia, V. Kodibagkar, H. Liu, and R. P. Mason, "Tumour oxygen dynamics measured simultaneously by near-infrared spectroscopy and F magnetic resonance imaging in rats," *Physics in Medicine and Biology*, vol. 51, pp. 45-60, 2006.

[92]   V. Saxena, J. F. Nielsen, I. Gonzalez-Gomez, G. Karapetyan, V. Khankaldyyan, M. D. Nelson, and W. E. Laug, "A Non-invasive, Multi-modality Approach Based on NIRS and MRI Techniques For Monitoring Intracranial Brain Tumor Angiogenesis," presented at aipr, 2005.

[93]   H. Liu, B. Chance, A. H. Hielscher, S. L. Jacques, and F. K. Tittel, "Influence of blood vessels on the measurement of hemoglobin oxygenation as determined by time-resolved reflectance spectroscopy," *Medical Physics*, vol. 22, pp. 1209-1217, 1995.

[94]   B. J. Tromberg, N. Shah, R. Lanning, A. Cerussi, J. Espinoza, T. Pham, L. Svaasand, and J. Butler, "Non-invasive in vivo characterization of breast tumors using photon migration spectroscopy.," *Neoplasia*, vol. 2, pp. 26–40, 2000.

[95]   Q. Zhu, E. Conant, and B. Chance, "Optical imaging as an adjunct to sonograph in differentiating benign from malignant breast lesions," *Journal of Biomedical Optics*, vol. 5, pp. 229-236, 2000.

[96]   B. W. Pogue, S. P. Poplack, T. O. McBride, W. A. Wells, K. S. Osterman, U. L. Osterberg, and K. D. Paulsen, "Quantitative hemoglobin tomography with diffuse near-infrared spectroscopy: Pilot Results in the Breast," *Radiology*, vol. 218, pp. 261-266, 2001.

[97]   A. Siegel, J. J. Marota, and D. Boas, "Design and evaluation of a continuous-wave diffuse optical tomography system," *Optics Express*, vol. 4, pp. 287-298, 1999.

[98]   C. H. Schmitz, D. P. Klemer, R. Hardin, M. S. Katz, Y. Pei, H. L. Levin, M. B. Levin, R. D. Levina, N. A. Franco, W. B. Solomon, and R. L. Barbour, "Design and implementation of dynamic near-infrared optical tomographic imaging instrumentation for simultaneous dual-breast measurements," *Applied Optics*, vol. 44, pp. 2140-2153, 2005.

[99]   S. R. Arridge, M. Schweiger, M. Hiraoka, and D. T. Delpy, "Performance of an iterative reconstruction algorithm for near-infrared absorption and scatter imaging," presented at Photon Migration and Imaging in Random Media and Tissues, Los Angeles, CA, USA, 1993.

[100]   M. Schweiger and S. R. Arridge, "Near-infrared imaging: photon measurement density functions," presented at Optical Tomography, Photon Migration, and Spectroscopy of Tissue and   Model Media: Theory, Human Studies, and Instrumentation, San Jose, CA, USA, 1995.

[101]   T. D. Yates, J. C. Hebden, A. P. Gibson, L. Enfield, N. L. Everdell, S. R. Arridge, and D. T. Delpy, "Time-resolved optical mammography using a liquid coupled interface," *Journal of Biomedical Optics*, vol. 10, pp. 054011-10, 2005.

[102]   S. Jiang, B. W. Pogue, and K. D. Paulsen, "Dynamic frequency domain tomography system and phantom test," presented at Multimodal Biomedical Imaging II, San Jose, CA, USA, 2007.

[103]   T. O. McBride, B. W. Pogue, S. Poplack, S. Soho, W. A. Wells, S. Jiang, U. L. Osterberg, and K. D. Paulsen, "Multispectral near-infrared tomography: a case study in compensating for water and lipid content in hemoglobin imaging of the breast," *Journal of Biomedical Optics*, vol. 7, pp. 72-79, 2002.

[104]   B. W. Pogue, "Near-infrared characterization of disease via vascular permeability probes," *Academic Radiology*, vol. 13, pp. 1-3, 2006.

[105]   U. Netz, J. Beuthan, H.-J. Cappius, H.-C. Koch, A. D. Klose, and A. H. Hielscher, "Imaging of rheumatoid arthritis in finger joints by sagittal optical tomography," *Medical Laser Application*, vol. 16, pp. 306-310, 2001.

[106]   X. Wang, B. W. Pogue, S. Jiang, H. Dehghani, X. Song, S. Srinivasan, B. A. Brooksby, K. D. Paulsen, C. Kogel, S. P. Poplack, and W. A. Wells, "Image reconstruction of effective Mie scattering parameters of breast tissue in vivo

with near-infrared tomography," *Journal of Biomedical Optics*, vol. 11, pp. 041106-13, 2006.

[107] A. Corlu, T. Durduran, R. Choe, M. Schweiger, E. M. C. Hillman, S. R. Arridge, and A. G. Yodh, "Uniqueness and wavelength optimization in continuous-wave multispectral diffuse optical tomography," *Optics Letters*, vol. 28, pp. 2339-2341, 2003.

[108] R. Ranga, "An in vitro hemodynamic phantom model for near infrared spectroscopy," in *Biomedical Engineering*. Arlington, TX: University of Texas at Arlington, 2005, pp. 92.

[109] A. Apte, "Finite element and numerical methods for inverse problem in optical medical imaging," in *Mechanical Engineering*. Arlington, TX: University of Texas at Arlington, 2004, pp. 56.

[110] S. R. Arridge and W. R. B. Lionheart, "Nonuniqueness in diffusion-based optical tomography," *Optics Letters*, vol. 23, pp. 882-884, 1998.

[111] J. R. Mourant, T. Fuselier, J. Boyer, T. M. Johnson, and I. J. Bigio, "Predictions and measurements of scattering and absorption over broad wavelength ranges in tissue phantoms," *Applied Optics*, vol. 36, pp. 949-957, 1997.

[112] R. L. P. van Veen, H. J. C. M. Sterenborg, A. Pifferi, A. Torricelli, and R. Cubeddu, "Determination of VIS- NIR absorption coefficients of mammalian fat, with time and spatially resolved diffuse reflectance and transmission spectroscopy," presented at OSA Annual BIOMED Topical Meeting, Miami, FL, 2004.

[113] A. Corlu, R. Choe, T. Durduran, K. Lee, M. Schweiger, S. R. Arridge, E. M. C. Hillman, and A. G. Yodh, "Diffuse optical tomography with spectral constraints and wavelength optimization," *Applied Optics*, vol. 44, pp. 2083-2093, 2005.

[114] R. Storn and K. Price, "Minimizing the real functions of the ICEC'96 contest by differential evolution," presented at Proceedings of IEEE International Conference on Evolutionary Computation, 1996.

[115] N. Iftimia and H. Jiang, "Quantitative optical image reconstruction of turbid media by use of direct-current measurements," *Applied Optics*, vol. 39, pp. 5256-5261, 2000.

[116] H. Dehghani, B. W. Pogue, S. Jiang, S. P. Poplack, and K. D. Paulsen, "Optical images from pathophysiological signals within breast tissue using three-dimensional near-infrared light," presented at Optical Tomography and Spectroscopy of Tissue V, San Jose, CA, USA, 2003.

[117] R. L. P. van Veen, H. J. C. M. Sterenborg, A. Pifferi, A. Torricelli, E. Chikoidze, and R. Cubeddu, "Determination of visible near-IR absorption coefficients of mammalian fat using time- and spatially resolved diffuse reflectance and transmission spectroscopy," *Journal of Biomedical Optics*, vol. 10, pp. 054004-6, 2005.

[118] C. H. Schmitz, H. L. Graber, R. D. Levina, M. B. Levin, and R. L. Barbour, "Data integrity assessment and instrument calibration for the DYNOT imaging system," presented at OSA Biomedical Optics Topical Meetings, Advances in Optical Imaging and Photon Migration, (Miami Beach, FL, 2004.

BIOGRAPHICAL INFORMATION

Dheerendra Kashyap was born on January 20, 1977 in Bangalore, India. He received his Bachelor of Engineering degree in Electrical and Electronics Engineering from University Visveswaraya College of Engineering, Bangalore, India in October 1998. In Spring 2000 he started his graduate studies in Electrical Engineering and graduated with a Master of Science in Fall 2001. In Spring 2002 he started his Doctoral studies in Biomedical Engineering from Joint Program of Biomedical Engineering at the University of Texas at Arlington and University of Texas Southwestern Medical Center at Dallas, completing it by spring 2007. His research interests include Near Infrared Spectroscopy and medical imaging techniques.